INTERNATIONAL
HELLENIC
UNIVERSITY

Thermal management of Lithium – ion batteries used in EVs and HEVs

George Georgiadis

Supervisor: Dr. Aikaterini Sardi

SCHOOL OF SCIENCE & TECHNOLOGY

A thesis submitted for the degree of

Master of Science (MSc) in Energy Systems

Date: 23.12.2016

THESSALONIKI – GREECE

“To the perfect, if it be perfect,

there is nothing that can be added.

Therefore, the will is not capable of any other desire,

when that which is of the perfect is present with it,

highest and best.”

Giordano Bruno

Abstract

From 2020 onwards the utilization of conventional gasoline engines is expected to be decreased and it will have been disappeared by 2050. Lithium – ion batteries constitute the most prevalent storage means in EVs and HEVs and their study is attracting more and more interest. Lithium – ion batteries require a proper thermal management system such that overheating phenomena and reduction of power rate capability at low temperatures are averted, as well as thermal losses are minimized and the battery's lifespan is extended. The objective of this thesis includes the understanding of EV and HEV operation, the understanding of the lithium – ion battery's operation, the simulation of common problems relevant to practical applications in EVs and HEVs, proposing solutions for tacking the problems and proposing topics for further research.

An extensive literature review on EVs and HEVs, on batteries, on their operation and on special topics was carried out. As part of the thesis different types of modeling and models were simulated with the aid of software packages such as ANSYS Fluent, Matlab/Simulink, Comsol Multiphysics, LMS ImagineLab and detailed parametric studies were conducted. Last but not least, the results were summarized in the cause and effect form in order for the effects of several parameters on the battery's and the vehicle's performance to be reported.

Acknowledgments

I would like to specially thank Dr. Sardi for supervising this thesis and give special thanks to Dr. Heracleous for her mentoring when that was needed. I would also like to thank all the professors throughout my studies for their teaching.

Of course, I would like to express my sincere gratitude to Dr. Iosiph, Dr. Samaras, Dr. Doukas and to my Colleague for providing me with useful information on this fascinating topic.

This thesis is devoted to the Hope.

List of figures

Nomenclature

Latin symbols

Equation (1.2.1.1), (1.2.1.2), (1.2.1.3)

m_v	Vehicle mass
m_{bat}	Battery mass
m_{fc}	Fuel cell mass
subscript v	Vehicle
subscript bat	Battery
subscript fc	Fuel cell

Equation (1.3.4)

-ΔG	Total work
W_{rev}	Reversible work
PΔV	Volume change work

Equations (1.3.2.2.1) – (1.3.2.2.2)

I_c	Current at the cathode
I_o	Exchange current density at the cathode
a_{Rd}	Charge transfer coefficient during reduction
a_{Ox}	Charge transfer coefficient during oxidation
F	Faraday constant
R	Universal gas constant
$E-E^o$	Actual potential
V_{act}	Activation overpotential
A	Tafel constant

Equation (1.3.5)

E	Cell potential or electromotive force
E^o	Potential in standard conditions
p	Pressure
T	Temperature in K
R	Universal gas constant
F	Faraday's constant
n	Moles of electrons

Equation (1.3.6)

n_{th}	Theoretical efficiency
ΔG	Useful output work
ΔH	Chemical input energy

Equations (2.1.9) – (2.1.10)

c	Total battery capacity
R_o	Battery internal resistance
I	Load current
h_1	Battery SOC
h_2	Bound – charge tank SOC
k	Coefficient

Equations (2.2.1) – (2.2.9)

j	Apparent current density
A	Surface are of the separator area
σ	Electric conductivity
ϕ_α	Anode electric potential
ϕ_c	Cathode electric potential

Y	Reverse of the V-I characteristic slope
a_i	Constant
b_i	Constant
Vol	Computing cell volume
C_i	Model coefficient
S_{Joule}	Joule heating
S_{echem}	Reaction heating

Equations (2.3.1) – (2.3.3)

j	Volumetric current density
q'	Sum of electrochemical release, Joule and entropic heat rates
σ_{+-}	Effective electric conductivities of the electrodes
ϕ_{+-}	Phase potentials of the electrodes

Equations (2.6.1) – (2.6.2)

E_o	Constant voltage
K	Polarization constant (Ah^{-1})
i*	Low frequency current dynamics
i_t	Extracted capacity
i	Battery current
f	Battery open - circuit voltage
A	Exponential voltage
B	Exponential capacity
Exp(s)	Exponential zone dynamics

Equations (2.8.1) – (2.8.4)

r	Molecular radius (m)
ε	Material's permittivity

ε_o	Permittivity of free space
R	Ideal gas constant
d	Molecular radius
F	Faraday constant
I_{sc}	Current
A_I	Interface are between electrolytes and electrodes (m^2)
C_T	Total capacitance
R_{SC}	Total resistance (Ω)
N_e	Number of electrode layers
N_A	Avogadro constant
N_e	Number of parallel supercapacitors
N_s	Number of series supercapacitors
T	Operating temperature (K)
c	Molar concentration (mol/m^3)

Equation (2.17.1)

C_{Li+}	Concentration of lithium ions in the electrolyte (mol/m^3)
$C_{Li+,ref}$	Reference concentration
F	Faraday's constant
n	Overpotential in V

Equation (2.17.2)

M_P	Molar weight = 0.1 kg/mol
P_P	Density of the product = 2100 kg / m^3

1. Introduction

In this chapter the different types of electric vehicles are presented and discussed firstly in terms of their environmental and cost benefits. Then focus is placed in more technical features such as power electronics, electric machines, regenerative braking, hybrid configurations and HV cables. These topics are addressed both for the sake of completeness and also due to their connection and impacts on battery operation. Finally concentration is placed on batteries which comprise the topic of this thesis.

1.1 Overview of EVs and HEVs

Electric Vehicles (EVs) and Hybrid Electric Vehicles (HEVs) nowadays expand over a large variety of categories from bicycles and motorcycles to forklifts and cars. The different types of electric vehicles and some of their typical specifications are summarized in the table following.

Table 1 EV and HEV typical specifications [15]

Type of electric vehicle	Typical specifications
Electric bicycles	Motor ranging from 250-750 W, 12-48 V Pb – acid, NiMH, Li-ion battery
Electric motorcycles	Motor rated approximately at 21 kW, 125 V NiMH or Li-ion battery
Forklifts	Industrial applications, 12-48 V Pb – acid battery with capacity ranging from 10 – 75 kWh
Battery EV	Motor ranging from 100 – 200 kW, 300 – 500 V NiMH or Li-ion batteries with capacity ranging from 15 – 75 kWh, all power derives from the battery
Fuel – cell EV	100 – 400 V NiMH or Li-ion batteries with capacity ranging from 1 – 5 kWh, electrical power converted into motive power derives from the fuel cell, hydrogen or methanol as a fuel
Hybrid EV	ICE engine, no external charging of the battery is needed as in EVs, battery design for high currents of short durations in contrast with EV battery design aiming at constant charging and discharging
Microhybrid EV	Start – stop mechanism without extra electric motor for restarting the engine, 5-10% fuel economy, 12V 500Wh Pb – acid battery not providing motive force

Mild hybrid EV	Start – stop mechanism with extra electric motor of around 15 Kw, 42 - 200V up to 1000Wh NiMH or Li-ion battery for storing the excess and recovered energy, resulting in 10 to 20% improved performance
Full hybrid EV	Start – stop mechanism with extra electric motor, 300 - 500V 2 to 5 kWh NiMH or Li-ion battery for storing the excess and recovered brake energy and for acceleration boosts, low – speed movement
Plug - in Hybrid EV	More similar to EV, 300 - 500V 5 to 20 kWh NiMH or Li-ion battery for providing autonomy for 50 or more kms

Table 2 Typical BMS functions and architectures by vehicle application [15]

Vehicle category	Typical functions	Architecture
LEV	Monitor, control	Centralized
Industrial	Monitor, measure, communicate	Centralized
BEV	Monitor, measure, calculate, communicate, balance	Distributed
FCV	Monitor, measure, calculate, communicate, balance	Centralized or Distributed
HEV – Micro	Monitor, measure, calculate, communicate	Centralized
HEV – Mild	Monitor, measure, calculate, communicate, balance	Centralized or Distributed
HEV – Full	Monitor, measure, calculate, communicate, balance	Centralized or Distributed
PHEV	Monitor, measure, calculate, communicate, balance	Distributed

1.2 Special topics in EVs and HEVs

1.2.1 Environmental and economic aspects of EVs and HEVs

GHG emissions with their corresponding weighting factors (w_{CO2}=1, w_{CH4}=21, w_{N2O}=310, w_{SF6}=24900) and airborne pollutants (AP) with their corresponding weighting factors with respect to NO_x (w_{NOx}=1, w_{SOx}=1.3, w_{CO}=0.017, w_{VOCs}=0.64) are considered two essential factors for evaluating the environmental impact of EVs and HEVs [15]. AP and GHG indices per vehicle curb weight are given by equations (1.2.1.1) and (1.2.1.2), while the same indices for fuel cell – based vehicles are given by equations (1.2.1.3) and (1.2.1.4) respectively [15]. In general, GHG emissions of vehicles may be estimated by multiplying the fuel carbon content by 3.66 [15].

$$AP = (m_v - m_{bat})AP_m + m_{bat}AP_{bat} \quad (1.2.1.1)$$

$$GHG = (m_v - m_{bat})GHG_m + m_{bat}GHG_{bat} \quad (1.2.1.2)$$

$$AP = (m_v - m_{fc})AP_m + m_{fc}AP_{fc} \quad (1.2.1.3)$$

$$GHG = (m_v - m_{fc})GHG_m + m_{bat}GHG_{fc} \quad (1.2.1.4)$$

According to [16] HEVs emit less airborne pollutants than ICVs, PHEVs emit less airborne pollutants than HEVs, whereas EVs have zero emissions. The vehicle environmental impact is accurately evaluated by means of a Life Cycle Analysis from manufacturing to vehicle disposal. Since vehicle operational emissions are in principle the highest, EVs have the lowest environmental impact [15]. Vehicle LCA models such as the LEM and the GREET model have already developed indicating that battery electric and fuel cell vehicles result in the lowest GHG emissions [15]. However, factors such as battery scaling up (larger battery cells) for producing advanced EVs affects other vehicle parts as well. Additively, factors such as the use of various alternative fuels in vehicle applications changing the process efficiencies, the GWP emission rates, the fuel production from biomass affecting the land and the vehicle systems improved efficiencies raise concerns about the environmental impact of new generation vehicles [15]. Thus, LCA studies based on new LCA models or on the GREET model must be conducted. Not to mention that models such as the COBRA model correlate the health effects caused by environmental changes with monetary impacts [16].

According to the study conducted in [15] HEVs and EVs become an advantageous choice provided that RES and nuclear power correspond to approximately 50 of the energy producing electricity, while the hybrid car turns to be the advantageous choice in case more than 50% of the energy producing electricity derives from fossil fuels. The ammonia – hydrogen ICE car is the best solution if scenarios 2 and 3 are implemented.

HEVs are cheaper, have higher rating and emit less pollutants than EVs. In order to make the EV competitive, a gas turbine undergoing a constant pressure thermodynamic cycle and having higher efficiency than an ICE, in conjunction with a SOFC is proposed [15].

Table 3 Emissions of different vehicle types [15] (scenario 1: electricity produced by RES and nuclear power, scenario 2: electricity produced 50% from RES and 50% from NG at 40% efficiency, scenario 3: electricity produced from NG at 40% efficiency)

Vehicle type	Fuel utilization stage		Overall life cycle[a]	
	GHG emissions (kg/100 km)	AP emissions (kg/100 km)	GHG emissions (kg/100 km)	AP emissions (kg/100 km)
Conventional	19.9	0.0564	21.4	0.0600
Hybrid	11.6	0.0328	13.3	0.0370
Electric[b]				
Scenario 1	0.343	0.00131	2.31	0.00756
Scenario 2	5.21	0.0199	7.18	0.0262
Scenario 3	10.1	0.0385	12.0	0.0448
Fuel cell[b]				
Scenario 1	10.2	0.0129	14.2	0.0306
Scenario 2	10.6	0.0147	14.7	0.0324
Scenario 3	11.1	0.0165	15.2	0.0342
H_2-ICE	10.0	0.014	11.5	0.0180
NH_3–H_2-ICE	0.0	0.014	1.4	0.0170

[a] During vehicle lifetime (10 years), an average car drives 241,350 km
[b] Scenarios refer to electricity-generation scenarios.

Table 4 Economic and environmental assessment of 6 vehicle types [15]

Vehicle type	Scenario[a]	Normalized indicators					General indicator	Normalized general indicator
		Car cost	Range	Fuel cost	GHG emissions	AP emissions		
Conventional	1	1	0.581	0.307	0.098	0.126	0.00220	0.2090
Hybrid	1	0.733	1	0.528	0.105	0.204	0.00830	0.0550
Electric	1	0.212	0.177	1	0.610	1	0.02290	0.0200
Fuel cell	1	0.154	0.382	0.532	0.098	0.247	0.00076	0.6050
H_2-ICE	1	0.255	0.322	0.110	0.122	0.42	0.00046	1
NH_3–H_2-ICE	1	0.382	0.462	0.140	1	0.44	0.01087	0.042
Conventional	2	1	0.581	0.307	0.098	0.283	0.00494	0.2085
Hybrid	2	0.733	1	0.528	0.105	0.459	0.01865	0.0552
Electric	2	0.216	0.177	1	0.194	0.649	0.00481	0.2141
Fuel cell	2	0.154	0.382	0.532	0.095	0.525	0.00156	0.6600
H_2-ICE	2	0.255	0.322	0.110	0.122	0.94	0.00103	1
NH_3–H_2-ICE	2	0.382	0.462	0.140	1	1	0.02470	0.0420
Conventional	3	1	0.581	0.307	0.098	0.283	0.00494	0.0210
Hybrid	3	0.733	1	0.528	0.105	0.459	0.01865	0.0557
Electric	3	0.212	0.177	1	0.117	0.379	0.00166	0.6265
Fuel cell	3	0.154	0.382	0.532	0.092	0.497	0.00143	0.7273
H_2-ICE	3	0.255	0.322	0.110	0.122	0.94	0.00104	1
NH_3–H_2-ICE	3	0.382	0.462	0.140	1	1	0.02471	0.0421

[a] Refers to scenario for electricity generation.

In the case of the ammonia – hydrogen ICE vehicle the highest work is produced at the engine shaft, while ammonia has relatively high volumetric and gravimetric energy storage capability [15]. Furthermore,

methanol follows ammonia's values, whereas compressed natural gas needs larger fuel tanks. Batteries present lower gravimetric and volumetric energy density compared to chemical hydrides. This means that their usage in EVs as energy storage means entails lower weight and volume.

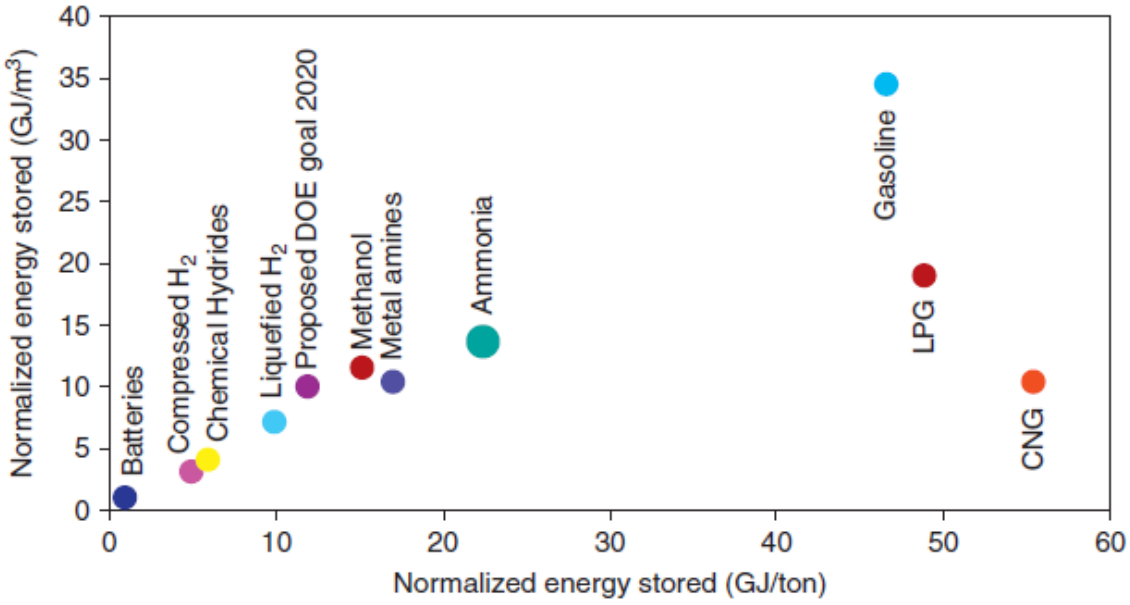

Figure 1 Gravimetric and volumetric energy densities for different fuels [15]

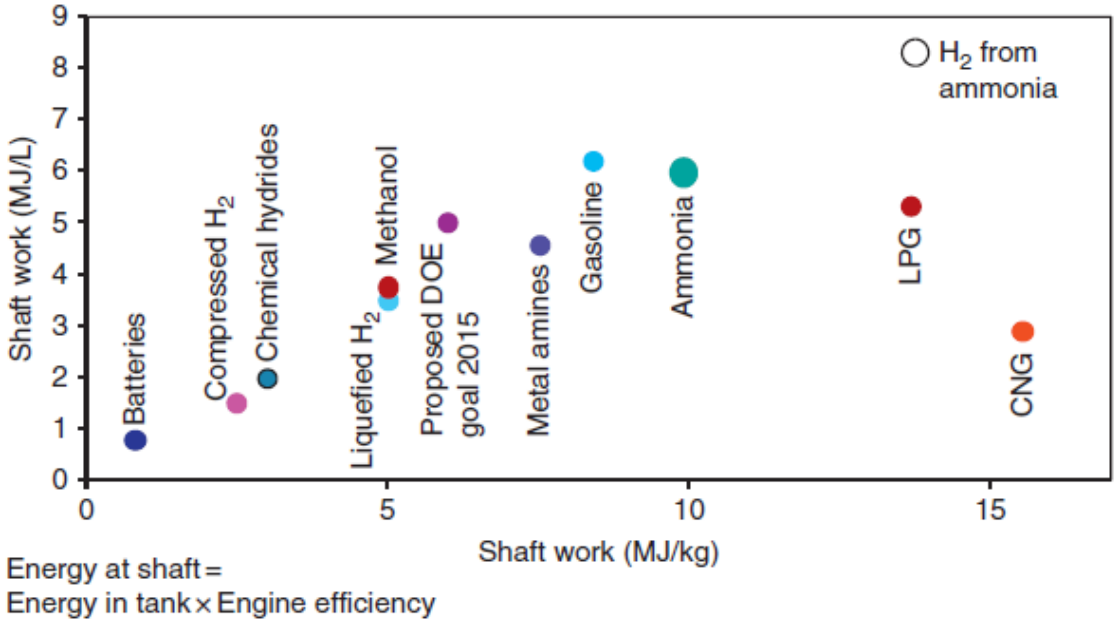

Figure 2 Gravimetric and volumetric energy at shaft for different fuels [15]

The benefit from developing EVs is not only that they have a positive effect on the environment, but they reduce the oil imports enhancing energy security [16]. Studies conducted estimated that 971 million dollars R&D investments in EVs have a NPV of 1294 million dollars and an IRR of 17.7% in 2022 [16].

Lithium ion cell substances pose environmental hazard, as anode metal oxides, $LiPF_6$ and electrolyte organic solvents are carcinogenic [18]. Thus, the disposal of the battery must comply with the EC 2006/66. Furthermore, the recycling of battery materials such as Al, Cu, Ni, Co and Li from the electrodes and gold or silicon from the circuit board is possible [18]. Since recycled batteries retain a considerable amount of their nominal capacity, they can also be utilized for other applications.

1.2.2 Power Electronics and electric machines in EVs

Electric motors of EVs can be classified into DC and AC motors. In the case of AC electric motors, the stator windings are fed with a 3 – phase AC voltage such that a rotary magnetic field is generated [18]. Thus, the DC current of the battery has to be converted by means of an inverter.
Power electronics affecting the efficiency and the cost constitute essential components in EV applications. A typical power electronics topology of an EV is depicted in the figure following.

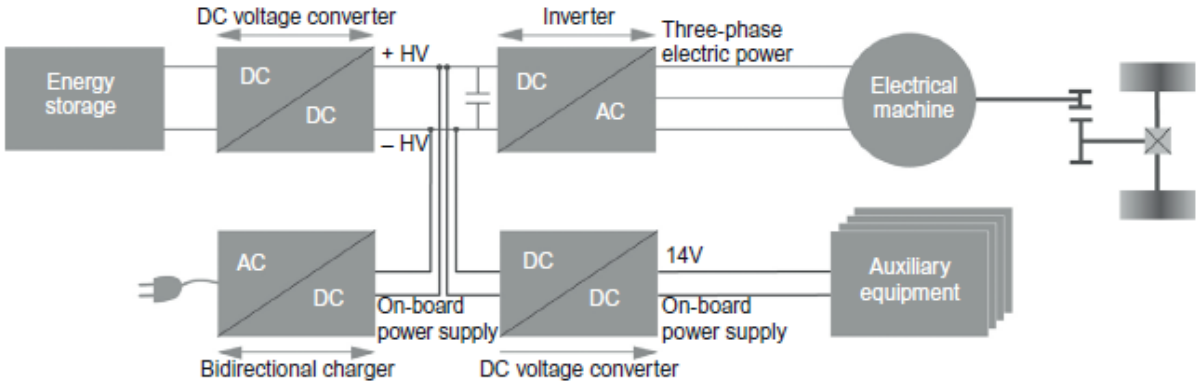

Figure 3 Typical power electronics topology of an EV [18]

The most prevalent type of DC electric motor is the “brushed-dc” motor. Its rotor’s windings are equally distributed, whereas the terminals start from and end to insulated electric contacts, which form the collector [20]. Voltage applied to the rotor via brushes creates a magnetic field, the angle of witch equals the angle between brushes’ and the collector’s positions. The movement of the rotor is the result of the interaction of the aforementioned magnetic field and the stationary magnetic field via permanent magnets [20]. The main problems arise from the brushed – dc motors are the electrical noise, the

production of sparks at high speeds and the need for replacing brushes [20]. In case of the excitation current being separately generated, torque and rotation speed can be controlled, which is the reason why this kind of electric DC motors is preferred in EVs [20]. In general, DC motor application in EVs is considered obsolete [20].

AC electric motors are classified into asynchronous (induction) and synchronous motors. According to Lenz law, stator windings produce a rotating magnetic field interacting with the conductors of the rotor, while simultaneously the magnetic field generated by the induced current in the rotor conductors interacts with the stator magnetic field [20]. The result of the mutual interaction of the magnetic fields is the creation of a torque, which is not equal to zero provided that the rotation speeds of the magnetic fields are unequal or the rotor speed is not equal to the synchronous speed [20]. In synchronous electric motors, permanent magnets or dc excitation current generate the rotor magnetic field and the rotor speed is equal to the synchronous speed [20].

Although electric motors reach high rotational speeds, they produce low torque. Thus, a reduction gear acting as a torque amplifier can be implemented in order for higher torque to be applied to the wheels [22].

Despite the fact DC electric motors are cheaper and their control is simpler, their disadvantages mentioned render them inappropriate for electric vehicles, especially for fuel cell – based EVs. On the other hand, although AC electric motors require more complex control, their robustness along with the fact that the cost of electronic control components is decreasing render them the appropriate solution for the powertrain [20]. Converters, such as inverters, utilized may consist of switching circuits from thyristors or from more advanced semiconductors such as IGBTs being controlled by Pulse Width Modulation [20]. Furthermore, various parameters, such as the variable load, the voltage stability, the power losses reduction requirement and the cooling system selection, should be taken into consideration for the design of the power electronics of an electric vehicle [20].

1.2.3 Regenerative braking

The production of electricity from the conversion of brake power is called regenerative braking. In case an external force is applied to the electric motor, the latter rotates the rotor and behaves as an electric generator [22]. In particular, regenerative brakes force the electric motor of the vehicle to spin backwards and as a result the electric motor functions as a generator [51].

The electricity generated is stored in the battery system saving the energy, which would otherwise be a heat loss by means of friction. In particular, regenerative braking may achieve a considerably high energy recovery ratio under traffic conditions [22]. The regenerative braking system may be compatible with the conventional braking system of the vehicle.

1.2.4 Hybrid configurations

A hybrid vehicle is defined as a vehicle being powered by at least two power sources. The rationale conditioning hybrid vehicles is that the battery system is employed in case the vehicle accelerates or moves slowly such that the power is boosted and the battery life is extended [20]. Hybrid vehicles having an ICE are classified into series hybrid and parallel hybrid configuration [20]. The main differences of the two configurations are summarized in the following table.

Table 5 Hybrid configurations [20] [22]

	Series hybrid configuration	**Parallel hybrid configuration**	**Mixed series/parallel configuration**
Traction power	Derives from electric drive powered by battery or ICE or from both power sources	Derives either from battery or from ICE or directly from both power sources	Derives from both battery and ICE power sources
Pros/Cons	Low cost / One way energy flow	Two energy flows, different operation modes, fuel economy, less emissions / electric motor is off when electricity is generated	The electric motor while the battery is being charged, optimization of energy efficiency depending on the driving conditions

Apart from these configurations, there is a wide variety of hybrid topologies. For instance, the hybrid configuration can be further hybridized by dedicating each power source to a different driving axle [20]. In addition, RES such as solar PVs may constitute a power source in hybrid vehicles. Not to mention that supercapacitors can be combined with batteries for enhancing the battery system [20]. The replacement

of the ICE with a fuel cell would lead to a pure EV having almost zero emissions [20]. A hybrid configuration incorporating three power sources (fuel cell, battery, supercapacitors) is illustrated in Appendix A.

Electric motors utilized in vehicle regenerative braking applications can be induction motors. When the speed of an induction motor becomes greater than the synchronous speed, then the direction of the induced torque changes sign and the motor produces electricity as illustrated in torque – speed curve [52]. Because in this operation mode the electric motor only consumes reactive power, an external source supplying the motor with reactive power in order for the magnetic field of the stator and the voltage to be maintained is required [52]. For this reason, reactive power compensation with capacitors for power factor correction is needed. The simplicity of the induction motor mechanism for producing electricity renders it appropriate for electricity production methods from supplementary power sources in existing applications, such as heat recovery and regenerative braking [52].

1.2.5 Formula E

Automotive brands, such as McLaren, supported the FIA Formula E championship to promote the EV technology as well [34]. Typical specifications of FEVs include 200 kW power and rechargeable energy storage systems consisting of lithium – ion battery and supercapacitors rated up to 800 V[35][36]. Specifically, Williams Advanced Engineering firm set the requirements such that the lithium – ion battery has a maximum voltage of 1000 V, a maximum capacity of 28 kWh, a power peak of 200 kW and the cell weight should not exceed 200 kg [37].

The thermal and electrical behavior of lithium – ion battery raises concerns even in sportscar applications. Challenges regarding the lithium – ion battery remain the improvement of the gravimetric energy density, the increase of the lifespan and the charging time reduction [37].

1.2.6 Atkinson cycle

Automotive brands such as Toyota implemented the thermodynamic Atkinson cycle in their hybrid vehicles so that the intake valves' timing is modified and fuel saving is achieved [42]. The battery – electric motor system provides the conventional engine with extra power and increases the fuel economy [43].

The ideal Atkinson cycle takes advantage of the full expansion of the burned gas and of the heat addition under constant volume. Thus, it has higher efficiency and higher network output compared to Otto and Brayton cycle [44]. If constants expressing the combustion and heat losses are defined in Joule per fuel molecule as in [45], it is found that for a given compression ratio the energy of combustion plays a determinant role in the increase of the power output and of the efficiency. In addition, the specific heat variability during the Atkinson cycle significantly affects the cycle efficiency and should be taken into consideration [44].

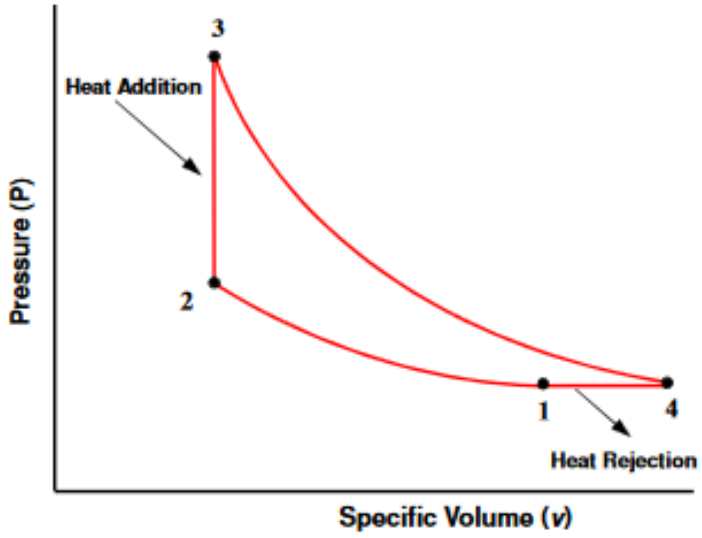

Figure 4 Ideal Atkinson cycle P-V diagram [4]

1.2.7 High Voltage cables

The HV battery bank is usually located under the rear side of the EV or the HEV, while the orange HV cables transferring the stored power to the electric motor are located inside protective cases at the middle of the vehicle near the driver's seat [69]. The orange color of HV cables is a standard of Fluke for HEVs, whereas the blue cable has been used by General Motors in HEVs of 2007 as a middle voltage (30-60 V) in emergency cases. GM and Chevy also utilized the orange high voltage cable (120 V) for hybrid electric trucks [69].

The insufficient cable tightness is an essential challenge in automotive industry. Liquids such as petrol or water penetrating electronic parts may cause short circuits and electrical connect loss owing to corrosion [70]. In order to overcome these problems, Prettl utilizes thermosets being plastics whose shape cannot be changed once hardened and thermoplastics being plastics whose shape can be changed by means of adding heat [70]. The testing of the cable includes heating up to 120 ^{o}C and immersing in ice – cold water with NACl. The temperature difference results in a pressure difference and thus, winter conditions are simulated. If white flecks or salt residues are observed on the inner area of the cable, it is concluded that the cable is not tight enough. However, if white flecks are observed only on the outer part, then the cable is sufficiently sealed and white flecks are produced due to the salt residue being crystallized [70]. Wiring and sensors in a EV is the "vehicle's nervous system" [70]. An example of a system of sensors in an EV is illustrated in Appendix B.

In the following sections some of the battery technologies are presented. For the time being, the most prevalent battery technologies are the lithium – ion and the NiMH batteries. Examples of HEVs being commercially available are: Audi A3 Sportback e-tron, BMW 225 xe, Lexus CT 200h, Mercedes – Benz C350 e, Mitsibushi PHEV, Toyota Yaris Hybrid, VW Golf GTE, Volvo V60 plug – in Hybrid [71]. Examples of EVS being commercially available are: BMW i3 BEV, VW e-Golf, Mercedes – Benz B250 e, VW e-up.

1.3 Storage means for EVs and HEVs

EVs and the electric part of HEVs are based on the so called electrochemical energy production. Systems for electrochemical energy storage and conversion include batteries, fuel cells, and electrochemical capacitors (ECs).

1.3.1 Batteries

The basic reaction taking place in galvanic and electrolytic cells and producing direct current and chemical energy, respectively, is called redox reaction defined as a process in which the oxidation state of the species atoms is modified [20]. The oxidation state is characterized by the oxidation number and signifies the amount and the sign of the atom charge, which is calculated under ideal conditions [20]. Moreover, during oxidation taking place in the anode, the atom oxidation number increases and the atom loses electrons, whereas during reduction taking place in the cathode, the atom oxidation number decreases and the atom gains electrons [20].

The oxidation, reduction and redox reaction between two species A and B are described by equations (1.3.1) – (1.3.3).

$$A_{red} \leftrightarrow A_{ox} + ne^{-} \qquad (1.3.1)$$

$$B_{ox} + ne^{-} \leftrightarrow B_{red} \qquad (1.3.2)$$

$$A_{red} + B_{ox} \leftrightarrow A_{ox} + B_{red} \qquad (1.3.3)$$

Fundamental thermodynamic quantities, such as the free energy change in a reaction, the cell potential in a fuel cell and the theoretical efficiency of a fuel cell, are given by equations (1.3.4) – (1.3.6).

$$-\Delta G = W_{rev} - P\Delta V \qquad (1.3.4)$$

$$E = E^{o} + \frac{RT}{nF} ln \frac{p_{H2} p_{O2}^{0.5}}{p_{H2O}} \qquad (1.3.5)$$

$$n_{th} = \frac{\Delta G}{\Delta H} \qquad (1.3.6)$$

The theoretical efficiency corresponds to open circuit conditions of the fuel cell. As the voltage generated in real fuel cells is lower than the voltage in standard conditions, the main issue in terms of efficiency to be resolved is achieving the highest possible voltage [20].

The battery management systems (BMS) aims at the safe operation of the battery and at the highest efficiency during its lifetime. The fundamental functions of a BMS are [15][18]:

- **Monitoring** battery cell quantities such as voltage, pressure, temperature or battery pack quantities such as operating current, leakage current and coolant temperature for safety reasons.
- **Measuring** accurately the magnitudes of the quantities above. Such measurements play an important role. For instance, Li – ion batteries require accurate voltage measurements on the order of mVs in order for SoC to be calculated, as they have approximately constant voltage profiles.
- **Calculating** quantities based on measurement data. For instance, the rate of increase in of the cell temperature can be calculated based on temperature measurement data or the SoC, the SoP and the SoH based on measurement and historical data.
- **Communicating** among the different vehicle subsystems complying with some protocol or standard such as the ISO 11898.
- **Controlling** the battery pack. Control actions include current interruption, modification of the thermal management system and decisions made during the regenerative braking.
- **Balancing** the charging and discharging rates of battery cells.

The BMS architectures are divided into two major categories, the centralized and the distributed architecture. As to the centralized architecture, the BMS functions are embedded in a subsystem located in the battery back. The centralized architecture is often utilized in large Battery Electric Vehicles (BEVs), (HEVs) and Fuel Cell Vehicles (FCVs) for taking advantage of the less cost and size, since less wiring and circuits are required [15]. The distributed architecture divides the battery pack into subsystems and provides flexibility in case the vehicle application is to be compatible with different battery pack sizes or a battery pack is to be compatible with vehicle applications of different size [15].

1.3.1.1 Lithium – Ion battery

The new generation of lithium – ion batteries for EV and HEV vehicles focuses on the increase of energy and power density preserving the safety and the sustainable cost of the overall system. Replacing the conventional anode from carbon with materials such as germanium or silicon being capable of hosting larger amounts of lithium, can result in the increase of energy and power density, while at the same time such materials have too low cycling performance and suffer from irreversible phenomena during charging and discharging [2]. The previous problems can be tackled by means of utilizing nanomaterials as electrodes. Fast lithium diffusion along with the lattice relaxation may confine structural changes. Electrodes in nano – scale exhibit improved chemical kinetics, reversibility and higher gravimetric capacity compared to electrodes of conventional size [2]. In particular, assuming complete lithiation, the gravimetric capacities of germanium and silicon may reach up to 1620 mAh/g and 4010 mAh/g respectively, while commercial graphitic carbons have a typical capacity of 372 mAh/g [2].

Considering lithium cobalt oxide ($LiCoO_2$) and graphite representative electrode materials, the fundamental operation of lithium – ion batteries is described by the chemical equations below [1]:

- Positive electrode : $LiCoO_2 \leftrightarrow Li_{1-x}CoO_2 + xLi^+ + xe^-$ (1.3.1.1.1)
- Negative electrode : $6C + xLi^+ + xe^- \leftrightarrow Li_xC_6$ (1.3.1.1.2)
- Overall reaction: $6C + LiCoO_2 \leftrightarrow Li_xC_6 + Li_{1-x}CoO_2$ (1.3.1.1.3)

Lithium cobalt oxide's structure consists of an octahedral lattice with overlapping lithium and carbon trioxide positive ion layers. According to equation (1.2.1.1) during battery charging lithium ions are removed from the positive electrode releasing electrons and Co^{3+} is oxidized into Co^{4+}, whereas during battery discharging positive lithium ions are intercalated into the lithium cobalt oxide lattice and Co^{4+} is deoxidized into Co^{3+} increasing the number of electrons by one [1]. According to equation (1.2.1.2), during battery charging lithium ions are intercalated into the graphene layer and electrons are also inserted into the lattice such that atomic state lithium is formed, whereas during battery discharging positive lithium ions are deintercalated from the graphene layers and electrons are released [1]. Due to lithium atoms oscillating between the positive and the negative electrode, lithium – ion battery was called "the rocking chair battery" [1].

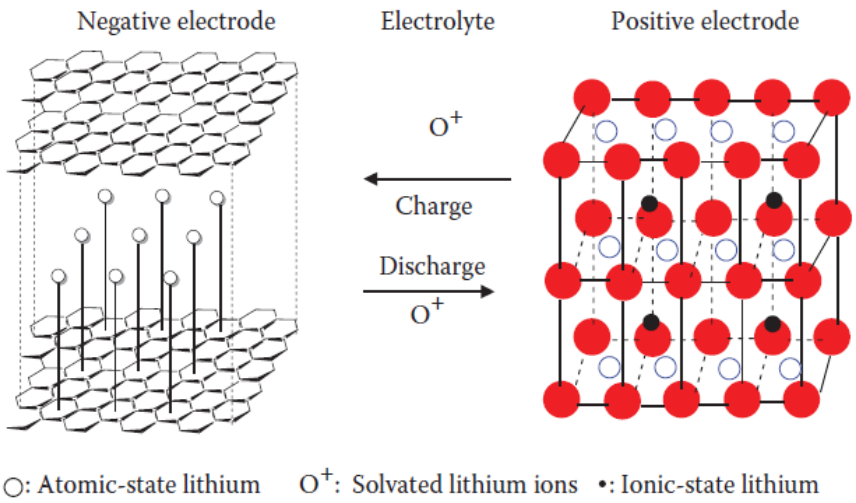

Figure 5 Lithium - ion battery charging and discharging process (Oxygen atoms = red circles, cobalt atoms -> blue circles, lithium atoms -> black circles) [1]

Typical automotive Li – ion cells consists of "jelly rolls" being spirals of positive and negative electrodes (See Appendix A). Cell designs can be either "stacked electrode" or cylindrical [18].

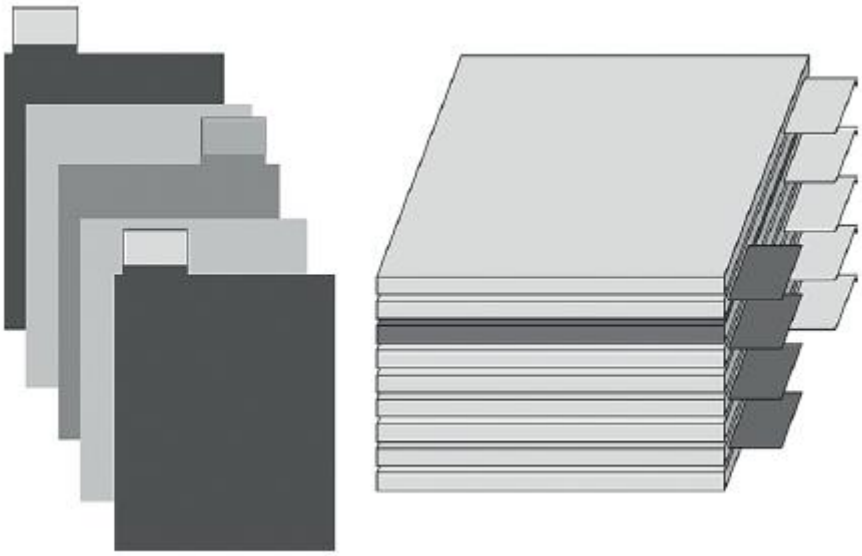

Figure 6 "Stack electrode" Li - ion battery [18]

Table 6 Material requirements of lithium - ion battery components [1]

Positive Electrode	Negative Electrode	Liquid Electrolyte	Inorganic - Solid Electrolyte	Polymer – Solid Electrolyte
The metal ion should have high reduction and stable potential to generate high voltage and stable output	Low and stable reduction potential	Stable Lithium – ion conductivity from 0.003 to 0.02 S/cm	As high ionic conductivity as possible even at low temperatures	As high ionic conductivity as possible even at low temperatures
As large number lithium ions as possible in the intercalation compound to achieve high capacity	Large number of lithium ions, chemical stability	Thermal stability	Phase stability	Chemical stability, prevention of reactions with the electrodes
Reversibility of intercalation – deintercalation process	Reversibility of intercalation – deintercalation process	Relatively high electrochemical window / voltage range, up to 4.5 V	Chemical stability, prevention of reduction reactions during charging	Relatively high electrochemical window
Decent conductivity of the intercalation compound for polarization reduction and for high current density	Decent conductivity of the intercalation compound for polarization reduction and for high current density	Chemical stability, ion solvation capability for ions	Relatively high electrochemical window / voltage range, greater than 4.2 V	Processability and mechanical strength of the membrane
Intercalation compound stability so as not to react with the electrolyte	Appropriate surface structure for decent interface formation with liquid electrolyte	Low vapor pressure, environmental – friendly, low cost	-	Low cost, environmental - friendly
High diffusion coefficient of lithium ions for high current density	High diffusion coefficient of lithium ions for high current density	Facilitation of the reversibility of electrode reactions	-	-
Low cost, environmental - friendly	Low cost, environmental - friendly	Phase stability over a wide range of temperature changes	-	-

$LiNi_xM_yO_2$ materials exhibit higher energy than lithium cobalt oxide positive electrodes. Different chemical compounds such as nickel – cobalt – aluminum and nickel – cobalt – manganese (NMC) oxides are becoming more and more attractive with a view to replacing lithium cobalt oxide batteries [15]. However, due to their low stability, they face safety problems under extreme delithiation.

$LiMn_2O_2$ materials provide better performance in terms of safety, but they have lower energy density than the previous alternative materials and they result in short cycle life owing to the reduced stability of the negative electrode cause by the manganese solubility under high temperatures [15]. Moreover, $LiFePO_4$ exhibits improved stability under extreme delithiation and the capability of reducing the cost because of the iron utilization. On the other hand, $LiFePO_4$ has lower density and lower but stable operating voltage meaning that its energy density is lower as well [15]. As the anode material plays an essential and must comply with the requirements of the applications, different materials are compared on parameters such as the safety, the energy density, the cost, the power density, the SoC and the cycles [56] (Appendix A).

Despite the fact that the lithium metal electrode's high energy density, its short life due to charging and discharging cycles renders the necessity of using graphitized carbon as the negative electrode host material, as carbon is capable of reversibly carrying out the intercalation process [16]. Carbon materials are capable of reversibly exchanging lithium ions without their electrical and structural properties being affected [18]. In addition, amorphous carbon offered higher capacity and stability in the first Li – ion battery applications [16]. The titanium oxide $Li_4T_5O_{12}$ is an alternative solution to the common negative electrode from graphite due to its improved power density, durability and safety [2]. Titanium dioxide (T_iO_2) is a material attracting interest since it has a remarkably greater theoretical capacity than $Li_4T_5O_{12}$ (335 mAh/g > 175 mAh/g). In general titanium oxides exhibit appropriate properties, such as high ionic diffusion and high current density, for applications requiring high power [2], which can further enhanced in case nanostructures are implemented [2]. Neglecting the energy density criterion, titanium oxides negative electrodes are preferable to graphite ones on the grounds that they provide safety and the lithium intercalation is carried out at lower voltage (approximately 1.5 V) preventing lithium from depositing on the electrode surface [2]. Hence, titanium oxides provide higher power density.

Materials currently used for the negative electrode in HEVs, PHEVs and EVs are the coated natural graphite, the synthetic graphite, the hard carbon and lithium titanate (LTO) [18]. Synthetic graphite carbon atoms have the advantage of the thermodynamic stability due to the synthetic graphite being produced by organic compounds in high temperature on the order of 3000 ^oC. Although hard carbon having hydrogen to carbon ratios lower than 0.1, exhibits may store greater amounts of lithium, it suffers from

irreversibilities and hysteresis phenomena (between charging and discharging process) [18]. On the other hand, LTO provides the best possible cycling stability and power efficiency, but its low energy density renders it appropriate for specific applications [18].

1.3.1.2 Ammonia battery

The "thermally regenerative ammonia battery" (TRAB) constitutes an innovative mechanism for the conversion of low – quality waste heat to electricity in the frame of thermoelectrochemical systems based on liquid electrolytes [3]. TRAB consists of copper electrodes and of an ammonia electrolyte allowing for charging at higher and discharging at lower temperatures [3]. Specifically, copper gains electrons at the cathode, while at the same time the copper anode is being corroded with the aid of the ammonia solution [3]. Once the electrical power is discharged, ammonia is dissociated from the anolyte by means of distillation, regenerating the electrolyte composition [3]. Subsequently, ammonia being placed in the electrolyte chamber, is utilized such that the initial anode electrode acts as a cathode electrode. That flexibility of ammonia allows the regenerative corrosion – oxidation cycle or charging – discharging process of the battery [3]. The ammonia battery efficiency can increase by enhancing the copper ion conductivity, by increasing ammonia concentration, by utilizing ion – selective polymer membranes and heat exchangers for recovering heat [3]. TRAB experiments along with modeling ammonia with ASPEN HYSYS software showed that [3]:

- Open circuit voltage is stable with the operating temperature.
- Instantaneous power density increases with the operating temperature.
- Total charge inversely decreases with the temperature at close to room temperature levels.
- Energy density is higher at low currents.
- Discharge energy efficiency is maximum at low temperatures (50-55%).
- Ammonia requires high temperature to improve its efficiency.
- The thermal efficiency is approximately 10% of the corresponding Carnot efficiency.
- The cathode potential rapidly decreases in a couple of hours.
- The highest volumetric energy density achieved was 650 Wh/m^3.
- The competitive advantage of the ammonia battery is that it is charged exploiting a waste heat source which makes ammonia battery unique, while typical charging of batteries requires electrical power.

Since liquid ammonia's hydrogen content equals 1.7 times the hydrogen content of pure liquid hydrogen for the same volume, ammonia is considered a precious energy carrier [4]. In addition, ammonia is abundant in nature and accessible in terms of cost, light, evaporates fast, has a characteristic odor and is recycled via the nitrogen cycle, that is to say ammonia is not environmentally harmful [4]. The known fuel cells used or having the potential of being used in vehicle applications utilize directly or indirectly hydrogen as a fuel. In order to incorporate fuel blending into a medium – scale fuel cell – based vehicle, a reformer along with a rechargeable battery for starting up and covering peak loads are required [4]. Due to bad chemical kinetics and high activation energy of ammonia's reforming to hydrogen and nitrogen, appropriate catalysts such as the nickel – oxide with ruthenium salt are needed [4]. As the aforementioned reaction is exothermic occurring at high temperatures, the selection of the appropriate fuel cell is essential.

The electrochemical reactions of an ammonia battery consisting of copper electrodes sunk in nitrate solutions are explained by equations (1.3.1.2.1) – (1.3.1.2.3) [10]:

- Positive electrode : $Cu^{2+}\ (aq) + 2e^{-} \rightarrow Cu\ (s)$ (1.3.1.2.1)
- Negative electrode : $Cu\ (s) + 4NH_3\ (aq) \rightarrow Cu(4NH_3)_4^{2+}\ (aq) + 2e^{-}$ (1.3.1.2.2)
- Overall reaction: $Cu^{2+}\ (aq) + 4NH_3\ (aq) \rightarrow Cu(4NH_3)_4^{2+}\ (aq)$ (1.3.1.2.3)

After discharging, ammonia is dissociated from the effluents in the distillation column utilizing waste heat and recomposing the electrolyte [10].

TRAB is currently not applied in EVs due to practical implications such as the need for an external source providing thermal energy. However, it remains a topic of research.

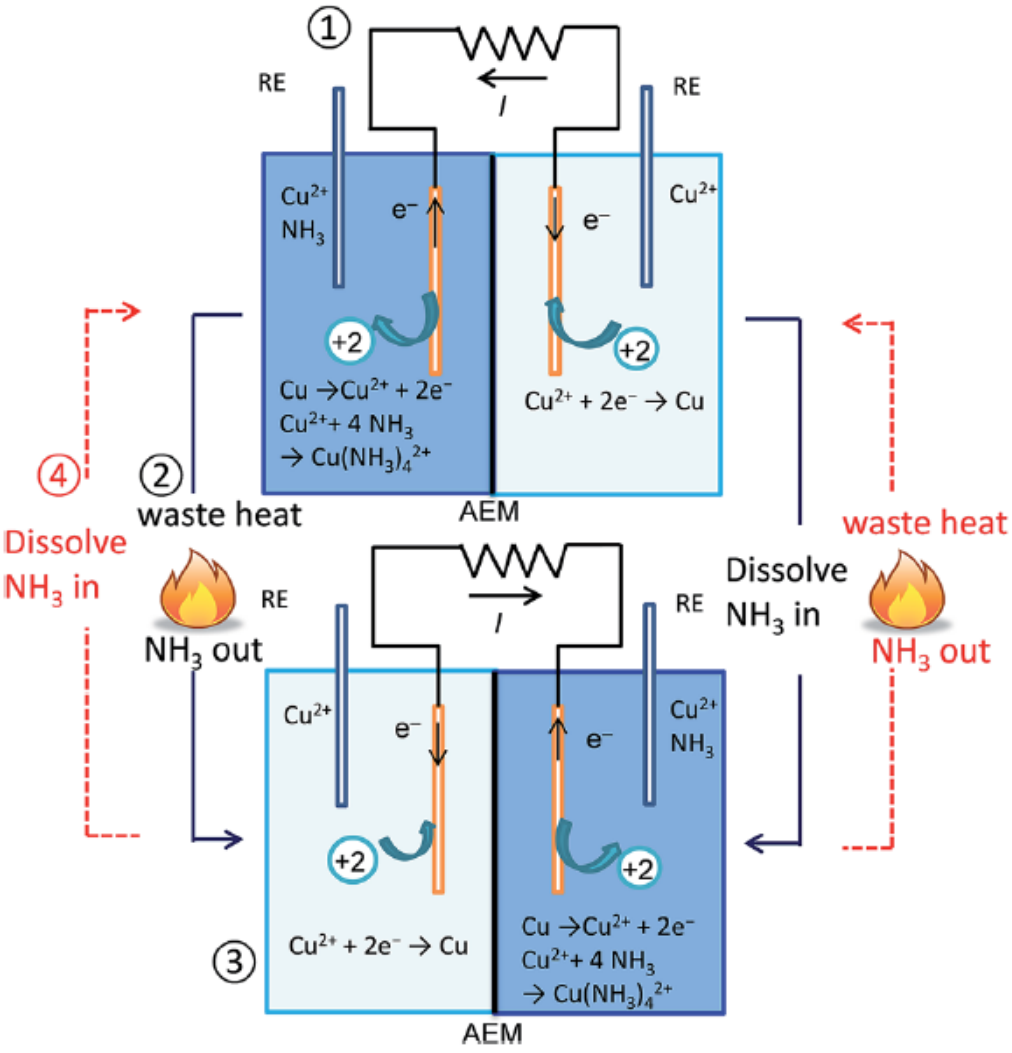

Figure 7 Waste heat conversion to electricity process in TRAB [10]

1.3.1.3 NiMH and NiZn batteries

NiMH batteries are currently prevalent in the hybrid vehicle market [18]. The overall reactions taking place during charging and discharging in NiMH and NiZn batteries under standard potentials of 1.35 and 1.76 V are described by equations (1.3.1.3.1) and (1.3.1.3.2) respectively [18].

$$M + Ni(OH)_2 \leftrightarrow MH + NiOOH \quad (1.3.1.3.1)$$

$$2Ni(OH)_2 + Zn(OH)_2 \leftrightarrow Zn + 2NiOOH + Zn \quad (1.3.1.3.2)$$

The metal hydride can be from different alloys listed in [18], which may face difficulties in the activation process and suffer from high self – discharging rates. Concentration of additives such as Mg, Co, Sn or Aluminum have an effect on the battery life cycle and on the activation and formation processes [18]. Additionally, NiZn batteries exhibit the highest energy density and the lowest cost among the batteries based on Ni [18]. However, they are prone to recombination issues, short – circuits and they have short life cycles [18].

1.3.1.4 Halide and Proton batteries

Halide batteries have halide ions such as fluorine or chloride ions moving through the electrolyte. As the fluorine is the most electronegative element, the fluorine battery can reach cell voltages up to 6V in case it combined with metals, whereas their specific capacity on the order 400 mAh/g is considerably low [18]. The charging and discharging process of the fluoride battery is depicted in Appendix A.

As the main drawback of batteries involving chemical reactions is the relatively low power rate, future trends aim at improving the power rates based on electrode materials conducting protons. Proton battery or “inverse mass ratio battery” follows an energy conversion process according to which energy derives from the segregation of charged species immersed in saline solutions [18]. In other words, an AC current electrolyzes water generating redox reaction similar to those of fuel cells so that proton gradients are formed in the solution [18]. The charging and discharging process of proton battery is described by equation (1.3.1.4.1) [18].

$$2H_2O + Cl^- + energy \leftrightarrow H_2 + 0.5O_2 + HCl + OH^- \quad (1.3.1.4.1)$$

1.3.1.5 Graphene battery

Graphene being a 2-D atomic crystal exhibits particularly significant performance owing to its unique structure, as it is the only 2-D atomic sheet with carbon atoms being connected with sp^2 bonds in hexagonal arrangement [59] (Appendix A). The carbon – carbon bond renders graphene mechanically strong and very flexible at the same time [59]. Despite the fact that the increase in the number of the graphene layers decreases the curved surface of graphene, graphene is still not perfectly flat. The states of the graphene's surface and edges constitute a determinant factor concerning the material's performance [59]. The edge state can have either the zigzag or the armchair arrangement. The type of edge state can be so essential that it can determine the electronic properties of "Graphene Quantum Dots" (GQD) and "graphene nanoribbons" (GNRs). Another example is that the increase in the number of the zigzag edges in GNRs reduces the energy gap. Hence, controlling the edge states is of great interest. According to [59], modifying the reaction precursors controls the zigzag to armchair configuration during the graphene growth. Additionally, armchair edges are found to grow faster than zigzag edges [59].

Among the enhanced properties of graphene, the Dirac point [1] being the zero – state intersection point of the conduction and valence bands renders graphene a semiconductor with zero energy gap. Since the effective mass at the Dirac point equals zero, graphene electrons acts as Dirac fermions resulting in very high carrier mobility [59]. According to the "ambipolar electric field" effect of graphene, when graphene is negatively biased, the Fermi level [2]is lower than the Dirac point and the number of holes in the valence band increases, whereas when graphene is positively biased, the Fermi level is greater than the Dirac point and the number of electrons in the conduction band increases [59]. The carrier mobility may become higher than 15000 cm^2/Vs even and it slightly depends on the temperature [59]. Moreover, electron transport in graphene is confined in a two dimensional plane and results in phenomena such as the Hall effect, which is approximately a thousand times stronger in graphene under low temperature conditions than in other metals [57][59]. Not to mention that the chiral electron transport in graphene (Klein tunneling) results in a full transmission rate through any barrier regardless of its size [59].

Graphene exhibits the greatest intrinsic thermal conductivity ever found in materials. Its thermal conductivity reaches up to 6000 W/mK, even higher than that of its allotrope nanotube from carbon, which equals 3500 W/mK [59]. The superior performance of graphene derives from its incomparable

[1] Dirac points in graphene are points in the momemtum space on the Brillouin zone edge and they indicate the transition between the conduction and the valence band. There are 2 sets of 3 Dirac points.
[2] Fermi level in graphene is located within the conduction or the valence band.

electronic and topographic characteristics, while its thermal conductivity is predominantly determined by diffusive conduction of phonons at high temperatures and ballistic conduction of phonons at low temperatures [59].

Graphene is currently being investigated in lithium – ion batteries, since lithium ion battery electrode materials may suffer from slow lithium ion diffusion, low electron transport and high internal resistance at high charge and discharge rates [59]. Hence, graphene – based electrodes, either anode or cathode materials, may significantly improve the lithium – ion battery's electrochemical performance [59]. Furthermore, graphene is proposed as material for heat dissipation and for improving electrical conductivity. Thus, graphene is a promising material for thermal management [59]. In [58] it is proved that the addition of graphene in phase change materials based on hydrocarbons not only increases the material's thermal conductivity by two orders of magnitude, but the latent heat storage capability of the material also remains the same. As a result incorporation of graphene in lithium ion batteries enhances the battery's thermal management by averting overheating and thermal runaway [58].

Lithium – oxygen or air batteries can achieve 90% efficiency, can be recharged more than two thousand time and an energy density ten times higher than conventional lithium chemistries, which means that lithium – oxygen battery has an energy density approaching that of gasoline and if utilized in an EV could reduce the cost and the weight up to 5 times [68]. The lithium – oxygen battery constructed in Cambridge consists of a porous single – atom graphene electrode having the carbon atoms arranged in a honeycomb lattice. The addition of water and of a lithium iodide mediator to the lithium – oxygen battery contributes to the stability of the battery and to its slower degradation [68]. Even though lithium – air batteries are considered promising, there are several obstacles described in [68] regarding their realization.

Graphene's unique properties render it appropriate for supercapacitor energy storage devices in EVs, since it extremely increases the power density of the storage device as it shown in the comparative table below.

Table 7 Graphene - based supercapacitor specific energy and power density [57]

Storage Device	Maximum Specific Energy Density (Wh/Kg)	Maximum Specific Power Density (W/Kg)
Alkaline battery	85	50
Lithium battery	250	350
Graphene-Based Supercapacitor	33	1184

1.3.2 Fuel Cells

An appropriate energy carrier for vehicle applications should simultaneously fulfill the requirements of sustainability, of scalability and of providing sufficiently high power and energy density [21]. "Hydrogen economy" concept envisages a based on hydrogen energy network consisting of production, distribution, storage, conversion and application steps [11]. Although hydrogen possesses some critical advantages such as high gravimetric energy density, abundance, wide flammability limits, zero emissions, low combustion temperature, high compression ratios and providing high efficiency in and compatibility with vehicle applications, various concerns are raised about treating hydrogen as an energy carrier through the hereinabove steps [11].

Regarding the hydrogen production, vapor reforming is the most prevalent process for converting hydrocarbons to hydrogen [14]. Initially, mixing of the hydrocarbon with water vapor takes place under low pressure of a few bar units, temperature of approximately 850 ^{o}C (300 ^{o}C in the methanol case) and the effect of a nickel – based catalyst [14]. Subsequently, the hydrocarbon undergoes an endothermic reaction and is oxidized producing carbon monoxide and hydrogen [14]. Since carbon monoxide is undesirable as a product, it undergoes an exothermic "shift – reaction" producing both carbon dioxide and hydrogen under 400 – 500 ^{o}C temperature [14]. Finally, carbon dioxide can be isolated from the gas mixture product for further environmental treatment [14].

Due to the long duration of this process on the order of a few minutes, cold start issues may arise [14] and the presence of a battery is necessary in order for the fuel cell to operate properly. Another drawback of vapor reforming is the difficulty in isolating carbon monoxide from hydrogen, which renders the hydrogen fuel inappropriate for the fuel cell. In order to keep the aforementioned concentration in the hydrogen – CO mixture lower than 10 ppm, filters containing costly chemical elements such as palladium must be utilized [14].

First and second stage hydrocarbon and overall methanol vapor reforming reactions are described by equations (1.3.2.1) – (1.3.2.3) [14] [11].

$$C_xH_y + yH_2O \rightarrow xCO + (x+0.5y)H_2 \qquad (1.3.2.1)$$

$$CO + H_2O \rightarrow CO_2 + H_2 \qquad (1.3.2.2)$$

$$CH_3OH + H_2O \rightarrow CO_2 + 3H_2 \qquad (1.3.2.3)$$

The hydrogen storage method is essential in vehicle applications utilizing hydrogen as a fuel. As hydrogen in the gas form has considerably low volumetric energy density, its storage in gas cylinder can be achieved under extreme pressures on the order of hundreds of bars, which causes safety and practical impediments [11][20]. On the other hand, liquid cryogenic hydrogen may achieve higher volumetric energy density (10.1 instead of 5.6 MJ/L in at 700 bar in gaseous form) [20]. Hydrogen undergoing the Linde cycle is liquefied. In particular, gaseous hydrogen is initially compressed. Subsequently, it is cooled liquid nitrogen passing through a heat exchanger. Finally, it flows through an throttle valve undergoing the Joule – Thomson effect and as a result liquid hydrogen is produced and the remaining gaseous hydrogen undergoes the same cycle [20] (See Appendix A). The overall process results in the loss of the 30% of the hydrogen's LHV.

Hydrogen storage in solid materials can be achieved either by means of physisorption (carbon nanostructures, metal organic frameworks) or chemisorption (metal or chemical hydrides) providing larger energy capacity [11]. The adsorption and absorption processes occur in physisoprtion and chemisorption, respectively. The absorption process is comprised of the successive stages: hydrogen gas molecules come in contact with the solid material surface, gas molecule are dissociated, hydrogen atoms form bonds with the solid material lattice, which build a hydride in case the pressure is sufficiently high

[20]. The operating temperature and pressure have a strong effect on metal hydrides in vehicle applications [20].

1.3.2.1 Direct Methanol Fuel Cell (DMFC)

DMFCs are regarded as an attractive alternative solution to batteries as to light traction applications [12]. They can function longer, they do not require recharging, they save space and face no refueling issues [12]. DMFC – battery hybrid systems can be implemented in traction applications with a view to enhancing the dynamic performance of the DMFC, reducing system size, recovering energy from braking and providing power at start-up [12]. As in every hybrid energy system there is a distinct power source and a distinct energy source, in DMFC – battery hybrid systems DMFC is the fundamental source supplying power and the battery is the power source covering peak loads and storing the recovered energy [12]. Furthermore the energy management of such a system is of utmost importance, since controlling the power flow between the battery and the DMFC plays an essential role in both guaranteeing normal operation and averting damages such as the corrosion of the catalyst in case of impermissibly low voltage [12].

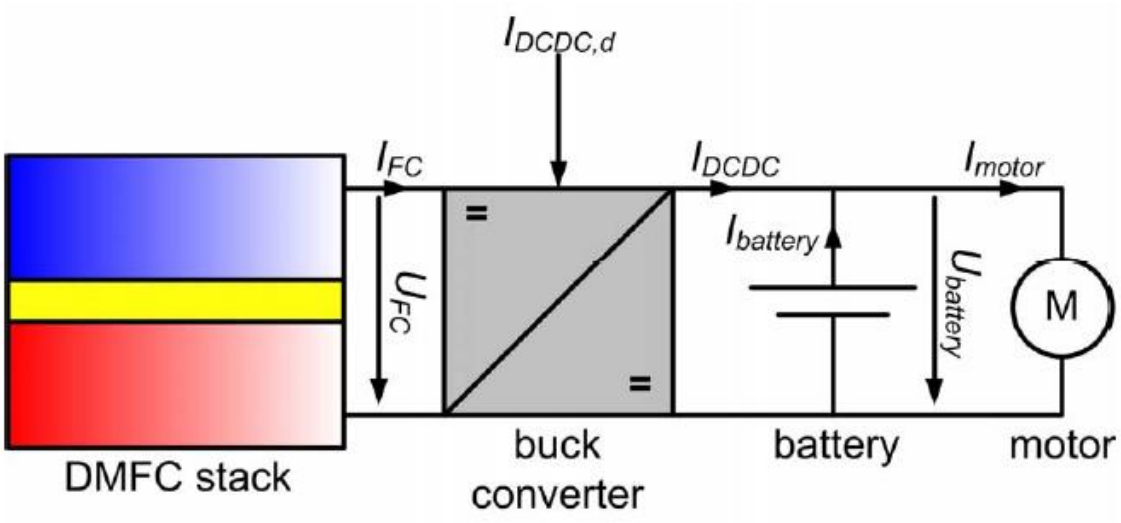

Figure 8 DMFC - battery hybrid system [12]

The major difference of the DMFC with respect to the PEMFC is that DMFC overrides the fuel to hydrogen reforming process, as methanol is directly converted to hydrogen at the anode [11][13]. Methanol as a liquid fuel provides at low temperatures being equal approximately to 130 ^{o}C production – storage – transportation convenience, and relatively high energy density and high efficiency [13].

A typical DMFC consists of two electrodes separated with a "membrane electrode assembly (MEA)", which is the most determinant factor of the fuel cell and comprises of two diffusion layers and two catalysts [13]. Methanol along with water is supplied to the positive electrode producing CO_2, hydrogen protons passing through the MEA and electrons flowing to the cathode via the external bus. At the negative electrode the electrons and the protons react with the oxygen and water is formed [13].

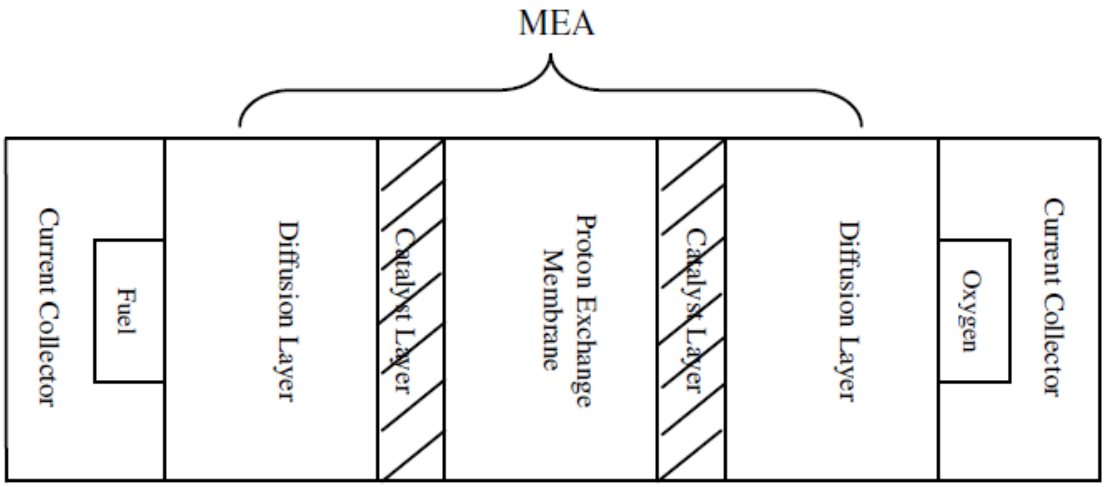

Figure 9 Typical DMFC structure [13]

The electrochemical reactions taking place in the DMFC are described by equations (1.3.2.1.1) – (1.3.2.1.3) [11] [13]:

- Positive electrode : $CH_3OH + H_2O \rightarrow CO_2 + 6H^+ + 6e^-$ (1.3.2.1.1)
- Negative electrode : $1.5O_2 + 6H^+ + 6e^- \rightarrow 3H_2O$ (1.3.2.1.2)
- Overall reaction: $CH_3OH + 1.5O_2 \rightarrow CO_2 + 3H_2O$ (1.3.2.1.3)

1.3.2.2 PEM fuel cell

The utilization of DMFC in vehicles raises some concerns due to the high toxicity of methanol and due to refinements that should be made regarding the low efficiency and the fast degradation of the DMFC [20]. On the other hand, the Proton Exchange Membrane (PEM) fuel cells operating at 40 – 90 °C are another type of low – temperature fuel cell, which constitutes a promising energy source for EVs, since they have relatively high efficiency, acceptable transient response, durability owing to their electrolytes not being corrosive and they achieve quick start – up [20].

In a PEMFC hydrogen positive ions produced at the anode move to the cathode through the electrolyte due to voltage drop across the electrolyte, whereas electrons flow through the external circuit producing electricity. At the cathode hydrogen ions react with oxygen and as a result, water and heat are produced [20].

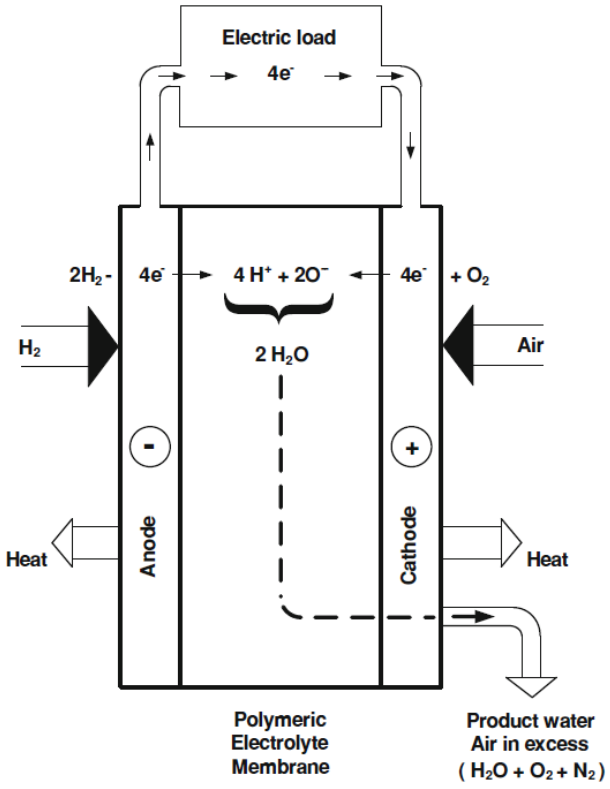

Figure 10 PEMFC operation process [20]

A typical PEMFC is composed of two bipolar plates and of the membrane – electrode assembly, which in turn consists of a polymeric membrane conducting ions, 2 gas diffusion layers and 2 catalysts usually made from platinum [20]. The low operative temperature of the PEMFC denotes that fuel being less reactive than hydrogen cannot be employed. In addition, post - purification of steam containing hydrogen is essential owing to the fact that carbon monoxide may reduce the voltage, as it is adsorbed on platinum catalysts at operative temperatures of the PEMFC [20]. Since the membrane's conductivity plays a significant role in the PEMFC operation, diffused materials such as tetrafluoroethylene with perfluorosulfonate monomers (Teflon) are utilized [20]. The proton conduction through the membrane is a result of protons associating with and disassociating from sulfonic acids and of proton diffusion through the water solvent [20]. The permeability of the membrane should be as low as possible in the sense that only hydrogen species should pass through it. A main challenge in PEMFCs is the realization of independent of water proton conduction through the membrane, which achieves operation at higher temperatures [20].

Carbon powders are utilized along with the platinum catalysts to enhance the dispersion of metal species and to increase the reaction rate. Thus, the ratio of platinum over carbon powder (typically 10-40 wt%) should be optimized so that a trade – off between the increased reaction rate and the active surface are is achieved [20]. Since the reduction at the cathode is significantly slower than the anodic oxidation, the exchange current density at the anode is much higher than the exchange current density at the cathode, which in other words has higher overpotential [20]. The cathode reaction can be described by equation (1.3.2.2.1), whereas the activation overpotential is given by the equation (1.3.2.2.2) [20].

$$i_c = i_o \left(e^{-\frac{a_{Rdc} F (E_c - E_c^o)}{RT}} - e^{-\frac{a_{Oxc} F (E_c - E_c^o)}{RT}} \right) \qquad (1.3.2.2.1)$$

$$V_{act} = A ln \left(\frac{i_c}{i_o} \right) \qquad (1.3.2.2.2)$$

Power losses in PEMFCs are attributed to [20]:

- **Fuel crossover:** Hydrogen having not reacted at the anode reaches the cathode, which results in the loss of two electrons per hydrogen molecule.
- **Internal current:** Hydrogen is oxidized at the anode and passes through the electrolyte, which stands for loss of electrons as well.

- **Ohmic losses:** Cells and membrane present electrical resistance.
- **Mass transport resistance:** At high currents the consumption rate is higher than the fuel supply rate, which results in almost zero reactants' concentration at the electrodes and almost zero voltage.

1.3.3 Supercapacitors

Supercapacitors are capable of responding to rapid load changes and of providing higher power rates than batteries, whereas they are not appropriate for cases in which high energy storage is a key factor [7]. Supercapacitors' charging occurs as fast as their discharging meaning that they constitute an excellent option for storing energy deriving from dynamic recovery. For instance, they could be utilized in vehicles to store the energy recovered from the braking system [7]. Additively, supercapacitors' reversible electrostatic storage process not including chemical reactions and redox phenomena results in greater cycling durability with respect to batteries and in avoiding electrodes' swelling and shrinking [7]. Ragone plot depicts the gravimetric energy and power densities of various storage devices, while it indicates that energy reduces due to internal dissipation and leakage phenomena [7].

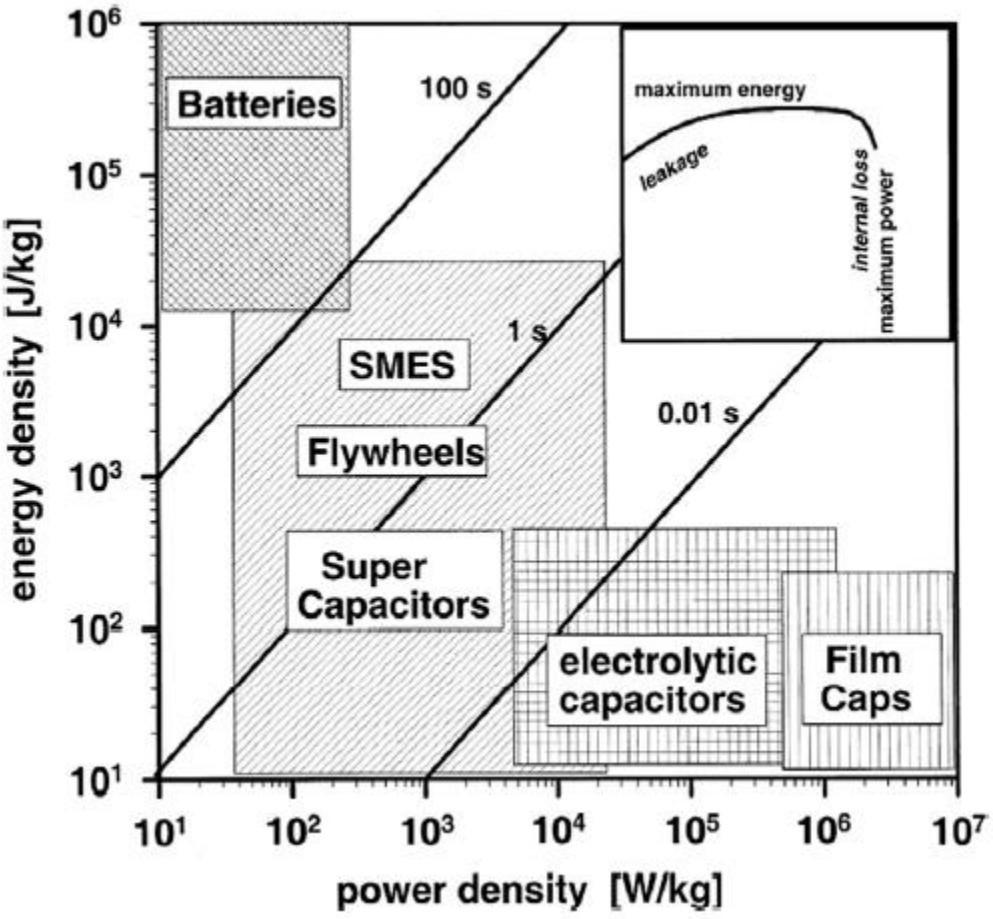

Figure 11 Ragone plot [7]

The major limitations of supercapacitors are their relatively lower energy storage capability, which can be compensated if electrodes with higher surface are implemented such as activated carbon electrodes, and the fact that they should operate at low voltage so as to avert electrolyte decomposition [7].

Supercapacitors can be either symmetric or asymmetric meaning that their electrodes' materials are either same or different [7]. Despite the fact asymmetry significantly increases the capacity, symmetric supercapacitors are preferable to asymmetric ones on the grounds that asymmetric supercapacitors have shorter lifespan [7].

Figure 12 Symmetric supercapacitor [7]

Another type of supercapacitor is the hybrid one, which combines the faradaic and the non – faradaic battery behavior, having gravimetric energy density greater than 10 Wh/kg, 10 – minute charging time on average and being commercially available for vehicle applications [7]. Hybrid supercapacitors constitute an advanced storage device, as they possess both the advantages of supercapacitors and Li-on batteries, which are the lifespan and improved cycle performance [17]. The latter is attributed to the the supercapacitor's simple adsorption – desorption process on the activated carbon area [17]. A hybrid supercapacitor is proposed in [17] having $Li_{4-x}M_xTi_{5-y}N_yO_{12}$ as an anode material and activated carbon as a cathode material, where M and N correspond to dopants, such as Na and Mn respectively, which enhance conductivity, avert the progress of the calcination process and result in fast lithium ion kinetics. As proved in [17], the most efficient hybrid supercapacitor is the one having LTO (pristine $Li_4Ti_5O_{12}$) as an anode material. The equations describing the hybrid supercapacitor's operation [17]:

- Positive electrode : $Li_4Ti_5O_{12} + 3Li^+ + 3e^- \leftrightarrow Li_7Ti_5O_{12}$ (1.3.3.1)
- Negative electrode : $AC + PF_6^- \leftrightarrow AC^+PF_6^- + e^-$ (1.3.3.2)

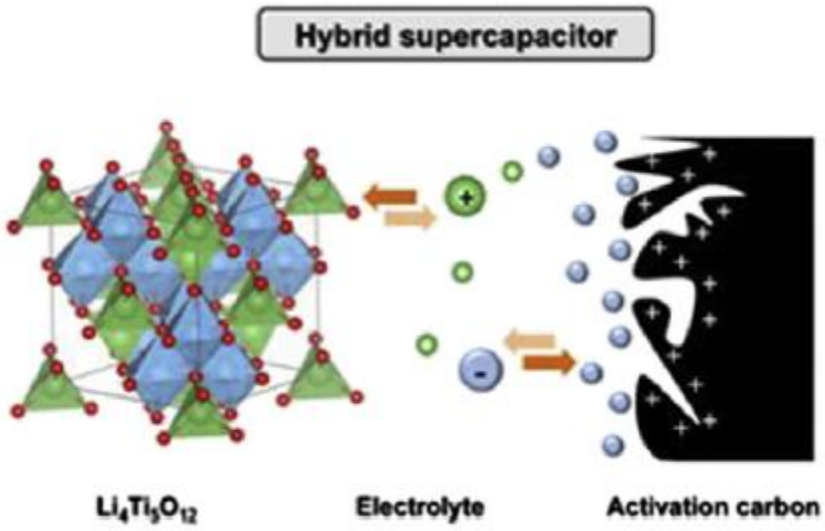

Figure 13 Hybrid supercapacitor structure [17]

Electric double – layer capacitors (EDLCs) have a wide range of applications from portable devices such as camera recorders to electric cars, ships and railway engines [6]. EDLCs have 2 porous polarizable electrodes creating an adequately high voltage. Their operation is described by the electrochemical equations below [6]:

- Positive electrode : $E_s + A^- \leftrightarrow E^+_S // A^- + e^-$ (1.3.3.3)
- Negative electrode : $E_s + C^+ + e^- \leftrightarrow E^-_S // C^+$ (1.3.3.4)
- Overall reaction: $2E_s + C^+ + A^- \leftrightarrow E^-_S // C^+ + E^+_S // A^-$ (1.3.3.5)

Where E_s corresponds to the electrode surface, // corresponds to the electric double – layer signifying that charge occupies both sides, A^- and C^+ correspond to electrolyte anions and cations.

Under the effect of an external energy source, during charging electrons switch places from the positive to the negative electrode, while anions and cations move through the electrolyte medium to the electrode surfaces. Inversely, during discharging electrons switch places from the negative to the positive electrode and ions move from the electrode surfaces to the electrolyte medium affecting the electrolyte concentration and charge density at the electrodes – electrolyte interfaces [6].

1.4 Li – ion battery performance related issues

The thermal management of the battery aims at preventing overheating phenomena, guaranteeing the battery's lifetime, minimizing thermal losses and averting reduction in power rates due to low temperatures [18]. The failure of li – ion battery is classified as a critical factor in comparison with the failure of other types of rechargeable batteries, because on the one hand more heat is released in such case and on the other hand its organic solvent electrolyte is flammable, having as consequences fire outbreaks and explosions being affected by the kinetics of the battery chemical degradation reactions [15][18] . Hence, if certain actions are not taken in time, the vehicle shall be burned to the ground. In case the produced by the lithium ion cell heat is greater than the heat dissipated, an exothermic failure causing fire called "thermal runaway" occurs [15]. Short – circuits, overstresses and overheating are some of the causes of the thermal runaway event [15]. Thus, a battery control system for managing charging, for protection from overvoltages and overcurrents, for controlling the communication between the battery and the ECU and for controlling the battery cooling is required in EVs and in HEVs [15]. In order for the battery control system to be appropriate a series of tests such as overcharge, short circuit, overload, high temperature, crush and drop, asymmetric voltage and chassis fault stresses or system – based abuse tests according to safety standards, such as the ANSI C18.2 and IEEE standards, have to be carried out [15].

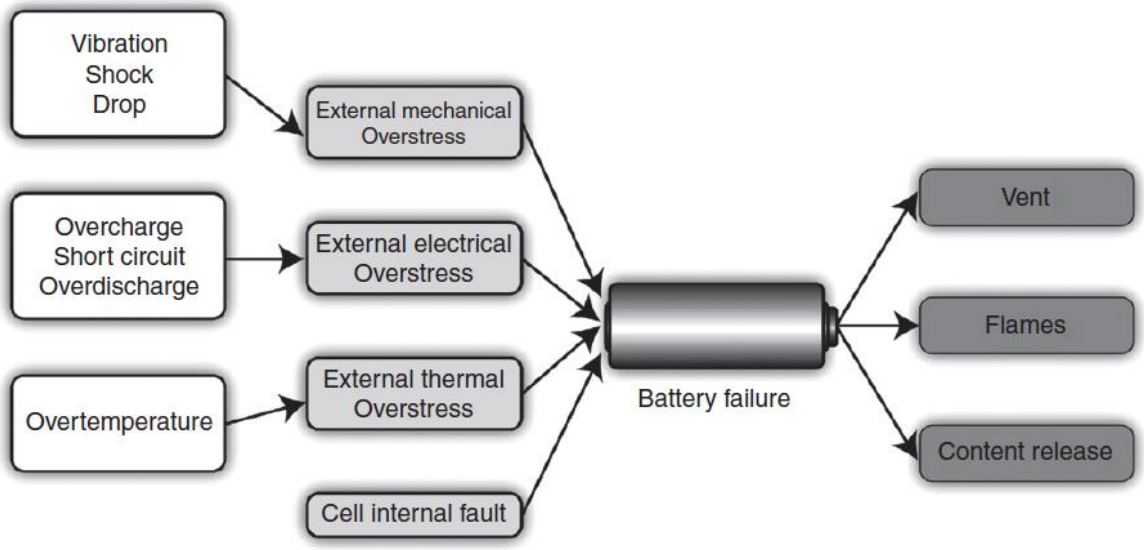

Figure 14 Li - ion cell thermal runaway causes and consquences [15]

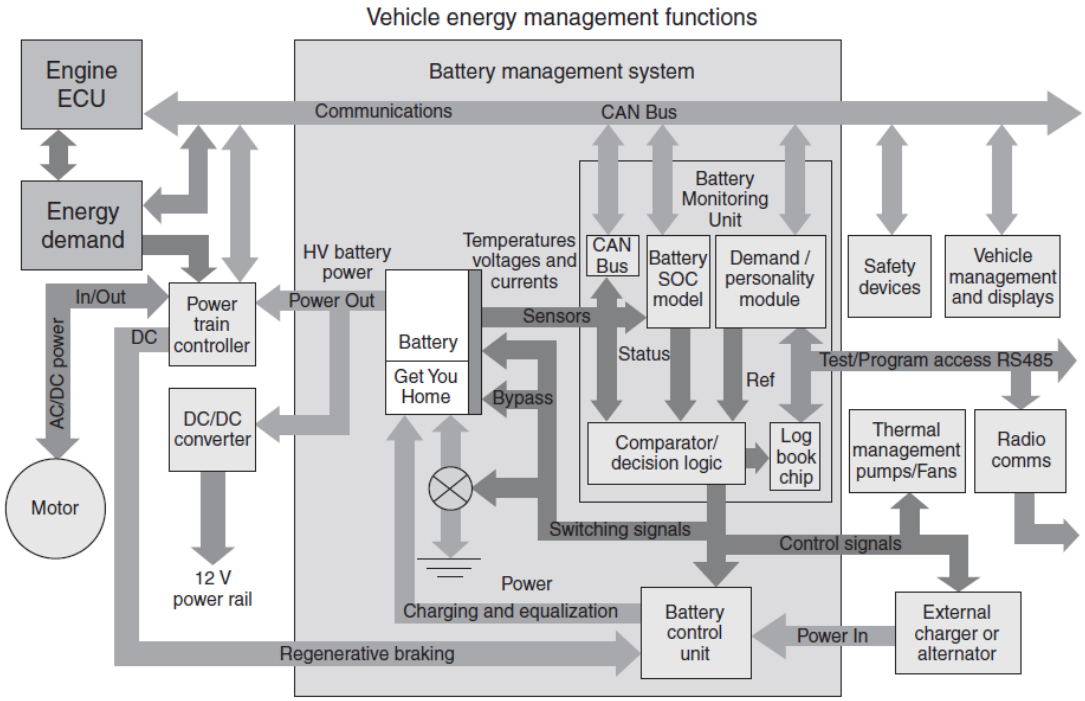

Figure 15 Typical battery control system in HEV [15]

The sizing of the battery is dependent on the minimum driving distance to be achieved and on the cell design taking into account the energy to power ratio [15]. For instance, NREL developed a hybrid mode battery model according to which the engine covers high power loads, that is to say that the battery has a lower energy to power ratios and costs less [15].

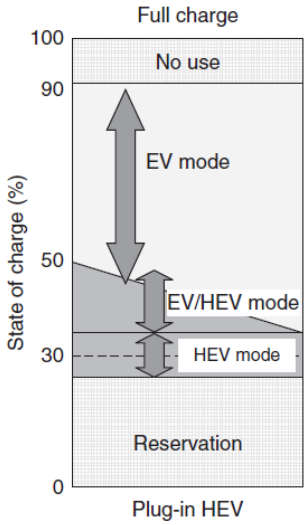

Figure 16 NREL hybrid mode battery model [15]

As Li – ion batteries commercially constitute the top choice for plug – in hybrid electric vehicles, the major challenges about improving their performance are the cost, the duration in EV mode, their calendar life and enhancing their gravimetric energy density for succeeding longer drive ranges [15] [18]. As stated in [18], battery energy densities are going to reach up to 250 Wh/kg until 2020, whereas the design aims at operating temperature limits from -40 to 60 °C and from -40 to 80 °C during charging [18]. Similarly, the lithium – ion cell is to be designed for functioning properly longer than ten years and the battery cost per kWh is to fall within between 200 and 250 € [18]. The following table indicates that EVs require the highest battery capacity and utilization factor, whereas they have the lowest power to energy ratio due to the fact that EVs require almost equal electrical power from the battery to those of both HEVs and PHEVs [18].

Table 8 Battery energy and power specifications for EVs, HEVs and PHEVs [18]

Battery	Energy content (kWh)	Utilization (%)	Power (kW)	P/E ratio
HEV	1–3	40–70	20–60	30–40
PHEV	5–15	60–90	40–150	5–10
EV	20–50	80–100	50–350	3–7

The chemical properties of the Li – ion battery are to provide solutions to the aforementioned challenges [15]. For instance, in EVs LMP (lithium metal polymer) employing metallic lithium negative electrode and polymeric electrolyte offers the advantages of longer cycle life and safety. However, they have lower energy density than lithium ion batteries [15], which can be encountered by means of combining the battery with supercapacitors.

According to [18] standardization of the battery pack components, such BMS, fuses and plugs, is of interest, as well as the cost reduction based on the electronic architecture [18]. Since every application has its own requirements, the goals to be achieved as to the batteries by electric vehicle application are set (See Appendix A). The battery development is also encouraged by the automotive industry target of producing 20,000,000 EVs until 2020 [18].

A side effect of every rechargeable battery is the so called memory effect and it takes place when the user charges the battery at irregular intervals without the battery having completely discharged and without charging leading to full charge. This problem occurs in battery materials which remain inactive for a long time. As a result, free electrons are bound to the material crystal structure forming oxides and they are

not able to move from the cathode to the anode [69]. The battery “remembers” its bad use. The memory effect has been minimized in new battery types, but it can also be found in NiMH and lithium – ion batteries [69].

2. Modeling

Since lithium – ion battery is a promising energy storage in EVs, its specifications should be optimized so as to meet customers’ needs. In particular, VW aims at increasing the driving range from 200 to 700 km by developing solid-state batteries instead of lithium – ion batteries having liquid electrolytes [23], whereas StoreDot is intended to decrease the charging time of lithium – ion battery from a few hours to five minutes and to increase the life cycles from approximately 500 to 1500, as well as increase the charging rate, by means of “multifunction electrodes” consisting of metal oxides and conductive polymers [24].

Decrease of the ambient temperature results in increase in the internal resistance and in decrease in the power extraction rate of the lithium – ion battery [25]. Experiments being verified by a detailed electro – thermal model indicate that there is a strong correlation between thermal and electrical effects [25]. The findings of [25] also indicate under sub - zero temperature conditions both the voltage and the delivered energy of the battery decrease due to the diffusivity of lithium ions increase. For instance, the delivered energy at -20 ^{o}C was found to be up to half that at 25 ^{o}C. As stated in [26], the lithium – ion battery should function from 25 to 40 ^{o}C for achieving the maximum performance and the maximum calendar life. As to thermal management system, the liquid cooling system is proposed, as it efficiently extracts heat and balances the cells [26].

Optimization of the calendar life and the electrical conductivity, confinement of cell degradation and overheating of the lithium – ion battery are all critical points for enhancing performance and avoiding thermal runaway [27]. In [27] a Finite Element Analysis of an electric vehicle 12V 20 Ah lithium – ion battery having Li_2MSiO_4 as a cathode material is performed in ANSYS, the results of which show that Li_2MSiO_4 can reduce the temperature approximately 15 ^{o}C [27]. Furthermore, in [28] a two dimensional iron phosphate Li-ion battery cell is built in ANSYS with a view to verifying experimental results and to simulating the surface thermal distribution at various currents and ambient temperatures. At low charging and discharging rates the heat production is mainly reversible indicating exothermic chemical reactions,

whereas the irreversible heat production indicates endothermic chemical reactions [28]. Internal resistance is found to be significantly at high State of Charge values as well, while the entropy coefficient increases with the State of Charge and is stabilized for State of Charge values higher than 90% [28]. As anticipated, the results of [28] show that the heat transfer coefficient is an essential parameter, since high values of the heat transfer coefficient lead to great heat dissipation to the environment and thus, the surface temperature of the battery decreases [28].

A non – uniform thermal distribution in a lithium – ion battery may cause swelling phenomena. In [29] the model of a prismatic battery cell is simulated in order for the thermal mechanics to be studied. As the results of [29] denote, swelling due to lithium ion intercalation occurs in the direction being perpendicular to the electrodes, gaps are created due to thermal variations, the need for cooling due to the large temperature increase in the central region of the battery, and thermal stresses and strains have a strong effect on the battery safety and lifespan owing to the fact that swelling due to temperature increase follows the trend of the swelling due to intercalation. In [30] CFD analysis and Design Failure Mode and Effect Analysis (DFMEA) were performed considering the electric motor, the battery and motor controller of an EV and making various assumptions in order for the thermal management system to be designed. Water jackets for the electric motor and the motor controller and air cooling system for the battery were selected as thermal management systems [30]. In addition, in [31] the study of the thermal management system of a Li – ion battery for EVs shows that a trade – off between the heat dissipation requirements and the temperature of the cell should be achieved, since lower input temperature of the coolant simultaneously results in lower cell temperature and in higher heat production within the cell. Optimization of the thermal management system also includes the study of the effect of the geometry by means of a sensitivity analysis on the thermal response of the battery, as well as the maximization of the efficiency of the thermal management systems by optimizing the cooling system and minimizing the power consumed for cooling [31].

Several standards, such as ISO 12405 and IEC 62660, aiming at defining requirements for the lithium – ion battery design in traction applications have been published [32]. These standards determine also tests relative to performance, capacity, energy efficiency, internal resistance, SOC loss at storage, cycle life, reliability, temperature change, abuse, thermal shock, vibration, mechanical shock, overcharge and overdischarge protection, that should be conducted so as the safety and the performance of the battery are validated [33].

Battery electric vehicles mainly suffer from power losses due to acceleration and low brake energy recovery [38]. In order for supercapacitors to be controlled, the reference current should be accurate [38]. In [38] a control design based on acceleration is proposed, according to which voltage and current references are obtained from the energy balance of the stored energy and the kinetic energy of the vehicle. According to [38] this control design results in lower battery sizing and in more accurate control of the electric motor, that is to say that higher brake energy can be recovered [38]. Furthermore, in [39] a novel EMS is developed so as to optimize the power control of an EV hybrid storage system consisting of battery and supercapacitors.

As hybrid energy storage systems (HESS) can be implemented so that stress on lithium – ion batteries decreases, in [40] three different energy management control strategies of a battery combined with supercapacitors are studied. Specifically, inversion – based control (IBC), estimation – based control (EBC) and closed loop control (CLC) are evaluated [40]. From the results obtained in [40], IBC is proposed as the most efficient control scheme based on performance and implementation criteria [40].

2.1 Basic battery modelling

The battery cells for electric vehicles rated at 6 or 12 V_{dc} are connected in series to produce the desired voltage. The basic equivalent circuit of the battery is described by equation (2.1.1), where E the battery generated voltage,

$$E = V - IR \quad (2.1.1)$$

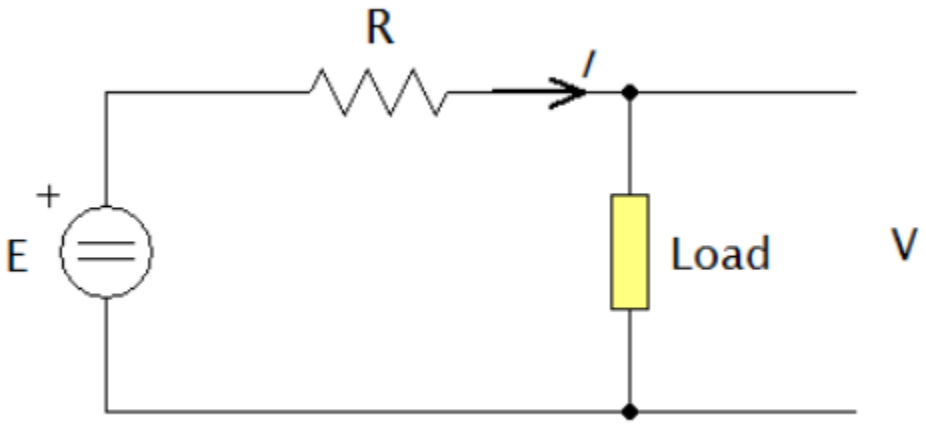

Figure 17 Battery basic equivalent circuit

The battery capacity decreases with the current reduction rate [5], which is essential in electric vehicle applications. The battery capacity can be modeled with the Peukert equation:

$$C_p = I^k T \quad (2.1.2)$$

Where k is the Peukert coefficient and T the number of hours the battery lasts at a constant current I.

Considering time steps of duration equal to dt, the effective charge loss is given by equation (2.1.3).

$$CR = dt\, I^k \quad (2.1.3)$$

Thus, the battery depth of discharge (DoD) is defined as "the ratio of the charge removed to the battery capacity" [5] or as DoD = 1 – SoC, whereas the state of charge (SoC) of the battery is defined as the "ratio between the present capacity and the nominal capacity of the battery" [19].

$$DoD = \frac{CR}{C_p} \quad (2.1.4)$$

In order for the vehicle to achieve a constant speed, a certain amount of power deriving from the battery is required. The current I producing this power is calculated by equation (2.1.5).

$$P = VI = (E - IR)I = EI - I^2R \rightarrow I = \frac{E - \sqrt{E^2 - 4RP}}{2R} \quad (2.1.5)$$

Gaining power from braking is a common mechanism applied to electric vehicles. In such case the battery is being charged. Thus, equation (2.1.6) is modified correspondingly:

$$V = E + IR \quad (2.1.6)$$

Similarly, the current required to charge the battery at power P is calculated from equation (2.1.7):

$$P = VI = (E + IR)I = EI + I^2R \rightarrow I = \frac{-E + \sqrt{E^2 + 4RP}}{2R} \quad (2.1.7)$$

The effective charge loss during a time step is given by equation (2.1.8):

$$CR_{t+1} = CR_t - \frac{Idt}{3600}\, Ah \quad (2.1.8)$$

The efficiency of the battery is defined as “the ratio of the charge extracted during discharge and the amount of charge needed to restore the initial state of charge” [19]. As the battery degrades, its internal resistance increases and the capacity decreases. The state of health (SoH) is defined as the “ratio of the battery capacity that can be discharged with nominal current at nominal temperature under full charge and the nominal battery capacity” [18]. Another battery parameter is the state of function (SoF) being a vague quantity, which describes the extent to which the battery performance responds to the application requirements [18].

The electrochemical battery models are considered very accurate, since the chemical processes occurring inside the battery cell are described by differential equations, the solutions of which are the voltage and current versus time, as well as the electrodes’ and electrolyte potentials, the current density, the reaction rate and the salt concentration versus time and position [46][47].

Chemical kinetics can also be employed as in the Kinetic Battery Model (KiBaM) in order to model the battery behavior. In KiBaM the battery charge is stored in the “available charge” tank supplying the load and in the “bound-charge” tank supplying the first tank [46]. The charge changes in both tanks are described by equations (2.2.1) – (2.2.2) [46][47].

$$\frac{di}{dt} = -I + k(h_2 - h_1) \quad , \qquad i = h_1 c \qquad (2.1.9)$$

$$\frac{dj}{dt} = -k(h_2 - h_1) \, , \qquad j = h_2(1 - c) \qquad (2.1.10)$$

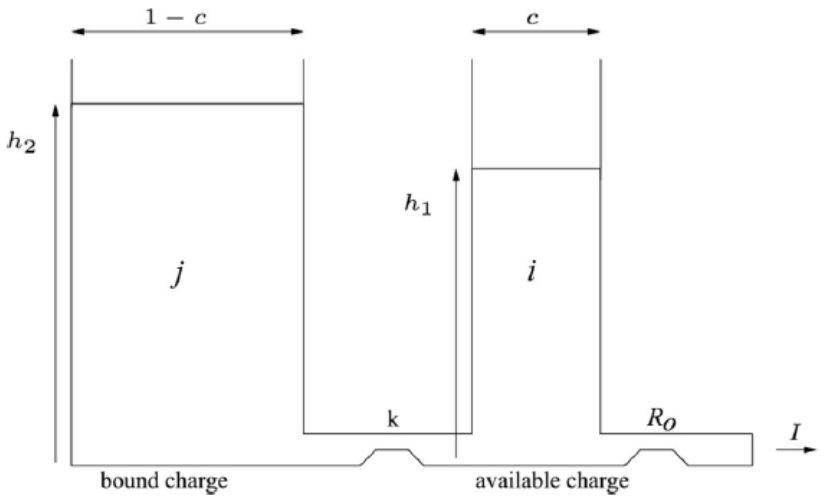

Figure 18 KiBaM "charge tanks" [47]

Although the KiBaM mainly describes lead – acid batteries of large capacity, it can also be utilized for modeling other types of batteries in case the battery lifetime is to be estimated, since the two "charge tanks" model calculates the rate capacity and the recovery effect of the battery [46].

2.2 Single Potential Empirical model

The "Single Potential Empirical" battery model consists of the electrodes and the corresponding current collectors, while a potential drop across the separator layer is considered [8]. The electric potential and the apparent current density (A/m^2) are computed from equation (2.2.1) and (2.2.2).

$$\int_V \nabla \cdot (\sigma \nabla \phi) dV = \int_A j dA \quad (2.2.1)$$

$$j = Y(\phi_c - \phi_a - U) \quad (2.2.2)$$

Regarding the polarization curve of the battery, if U is the point where the V-I characteristic crosses the vertical axis and Y is the inverse of slope of the curve, then based on experimental data, U (2.2.3) and Y (2.2.4) are defined as functions of DoD (2.2.5), whereas the depth of discharge is defined as function of the theoretical capacity of the battery Q_t [8].

$$U = a_0 + a_1 DoD + a_2 DoD^2 + a_3 DoD^3 + a_4 DoD^4 + a_5 DoD^5 \quad (2.2.3)$$

$$Y = b_0 + b_1 DoD + b_2 DoD^2 + b_3 DoD^3 + b_4 DoD^4 + b_5 DoD^5 \quad (2.2.4)$$

$$DoD = \frac{A}{Q_t} \int_0^t j dt \quad (2.2.5)$$

In order for electric and thermal fields to be coupled, temperature is considered being dependent on electric conductivity, on apparent current density in $(\Omega m^2)^{-1}$ (2.2.6) and on voltage (2.2.7) [8]. Moreover,

the assumptions of the Joule heating (2.2.8) and the reaction heating (2.2.9) being volumetric source terms being embedded into the thermal energy equation are made [8].

$$Y = \left(\sum_{n=0}^{5} b_n (DoD)^n \right) e^{C_1 \left(\frac{1}{T_{ref}} - \frac{1}{T} \right)} \quad (2.2.6)$$

$$U = \left(\sum_{n=0}^{5} a_n (DoD)^n \right) - C_2 (T - T_{ref}) \quad (2.2.7)$$

$$S_{joule} = \frac{i^2}{\sigma} = \frac{\sigma^2 \nabla^2 \phi}{\sigma} = \sigma \nabla^2 \phi \quad (2.2.8)$$

$$S_{echem} = j \cdot [U - (\phi_c - \phi_a)] \frac{A}{Vol} \quad (2.2.9)$$

2.3 MSMD model

The "Multi – Scale Multi – Domain" (MSMD) battery model provides the capability of extensively examining the electrochemical and battery phenomena over a wide range of battery topologies and length scales [8]. Despite the obvious competitive advantages mentioned of the Li – ion battery applications in EVs and in HEVs, the battery's safety, performance and life related aspects need further study [8][15]. The major issue with respect to approaching the Li – ion battery modeling is the particularly complicated nature of the lithium - ion battery [8]. The thermal analysis aims at the determination of the temperature distribution on a length scale basis, while the lithium ions movement takes place in the layers of the "anode – separator – cathode" sandwich scheme. Thus, a "multi – scale multi – domain approach" is required to obtain a decent solution.

The governing thermal and electrical equations describing the Li-ion battery model (2.3.1) – (2.3.3):

$$\frac{\partial \rho C_p T}{\partial t} - \nabla \cdot (k \nabla T) = \dot{q} \qquad (2.3.1)$$

$$\nabla \cdot \left(\sigma_+ \nabla \varphi_+ \right) = -j \qquad (2.3.2)$$

$$\nabla \cdot \left(\sigma_- \nabla \varphi_- \right) = j \qquad (2.3.3)$$

2.4 ECM Model

The Equivalent Circuit Model (ECM) describes the battery with a circuit being composed of 2 capacitors and two resistors. In the ECM the V-I characteristic is obtained from equations (2.4.9). Provided that the battery specifications are known, the open – circuit voltage and the circuit components are obtained from equations (2.4.1) – (2.4.6) as functions of state of charge, whereas the volumetric current density and the heat generation are computed from equations (2.4.7) and (2.4.8) respectively [8].

$$R_s = a_0 + a_1 (soc) + a_2 (soc)^2 + a_3 (soc)^3 + a_4 (soc)^4 + a_5 (soc)^5 \qquad (2.4.1)$$

$$R_1 = b_0 + b_1 (soc) + b_2 (soc)^2 + b_3 (soc)^3 + b_4 (soc)^4 + b_5 (soc)^5 \qquad (2.4.2)$$

$$C_1 = c_0 + c_1 (soc) + c_2 (soc)^2 + c_3 (soc)^3 + c_4 (soc)^4 + c_5 (soc)^5 \qquad (2.4.3)$$

$$R_2 = d_0 + d_1 (soc) + d_2 (soc)^2 + d_3 (soc)^3 + d_4 (soc)^4 + d_5 (soc)^5 \qquad (2.4.4)$$

$$C_2 = e_0 + e_1 (soc) + e_2 (soc)^2 + e_3 (soc)^3 + e_4 (soc)^4 + e_5 (soc)^5 \qquad (2.4.5)$$

$$V_{ocv} = f_0 + f_1 (soc) + f_2 (soc)^2 + f_3 (soc)^3 + f_4 (soc)^4 + f_5 (soc)^5 \qquad (2.4.6)$$

$$j = I / Vol \qquad (2.4.7)$$

$$\dot{q} = \sigma_+ \nabla^2 \varphi_+ + \sigma_- \nabla^2 \varphi_- + \frac{I}{Vol} \left[V_{ocv} - (\varphi_+ - \varphi_-) - T \frac{dU}{dT} \right] \qquad (2.4.8)$$

$$
\begin{aligned}
V(t) &= V_{OCV}(soc) + V_1 + V_2 - R_s(soc)I(t) \\
\frac{dV_1}{dt} &= -\frac{1}{R_1(soc)C_1(soc)}V_1 - \frac{1}{C_1(soc)}I(t) \\
\frac{dV_2}{dt} &= -\frac{1}{R_2(soc)C_2(soc)}V_2 - \frac{1}{C_2(soc)}I(t) \\
\frac{d(soc)}{dt} &= I(t)/3600Q_{Ah}
\end{aligned}
\tag{2.4.9}
$$

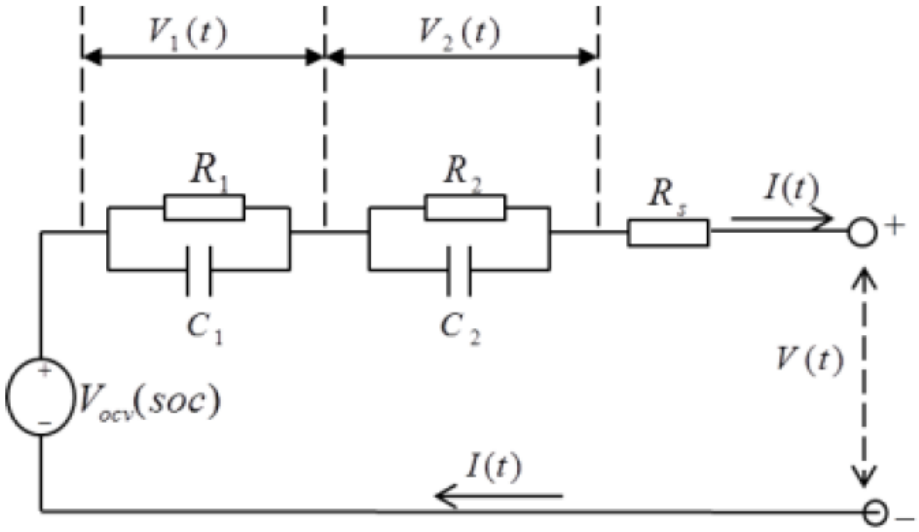

Figure 19 ECM [8]

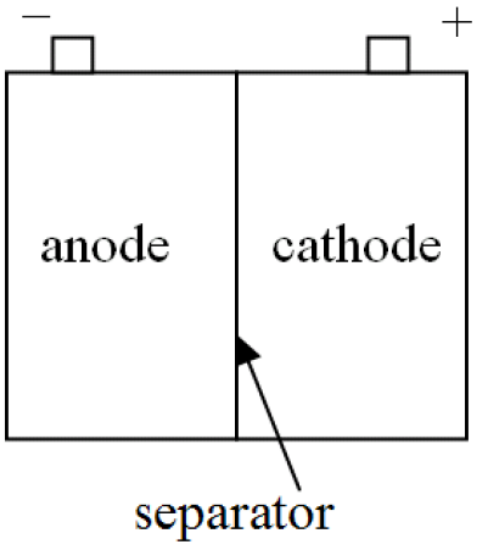

Figure 20 Anode - Cathode - Separator interface (assumed to be infinitely thin) battery assembly [8]

The battery cell 3d model mesh in ANSYS Fluent consists of 1032 cells, 3569 faces and 1552 nodes, while it has minimum orthogonal quality and a maximum orthogonal skewness of 0.999988 and $1.15935 * 10^{-5}$ respectively. The battery cell model dimensions equal 0.237m x 0.145m x 0.0054m.

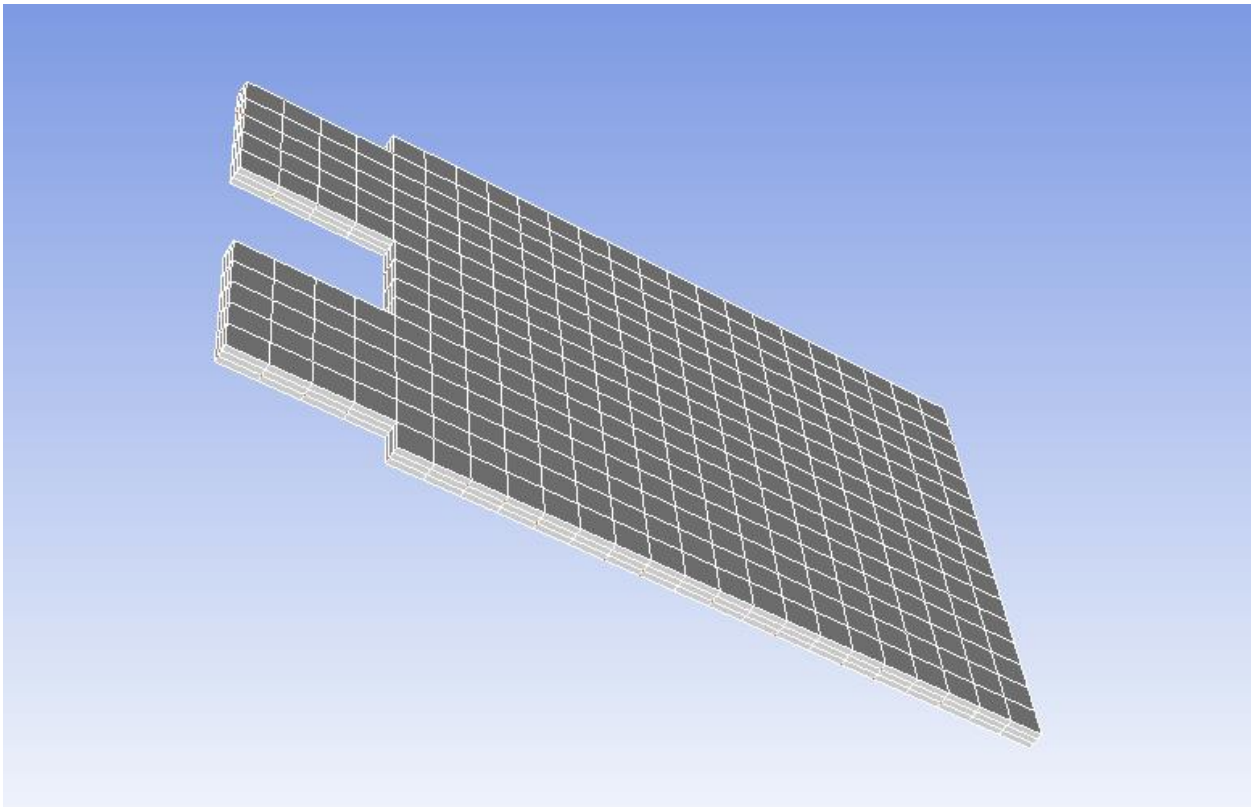

Figure 21 Lithium – ion battery cell 3d model

The battery pack 3d model mesh consists of 39400 cells, 129668 faces and 51245 nodes, while it has minimum orthogonal quality and a maximum orthogonal skewness of 0.8682 and 0.1317 indicating high quality.

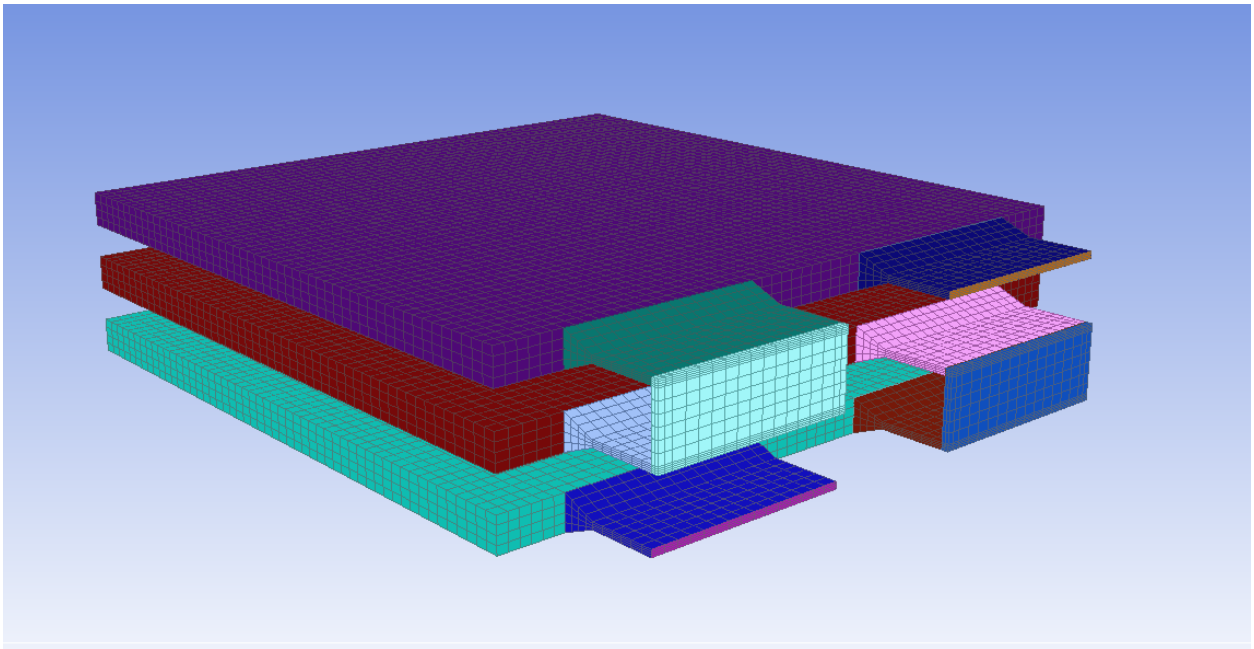

Figure 22 Battery pack 3d model

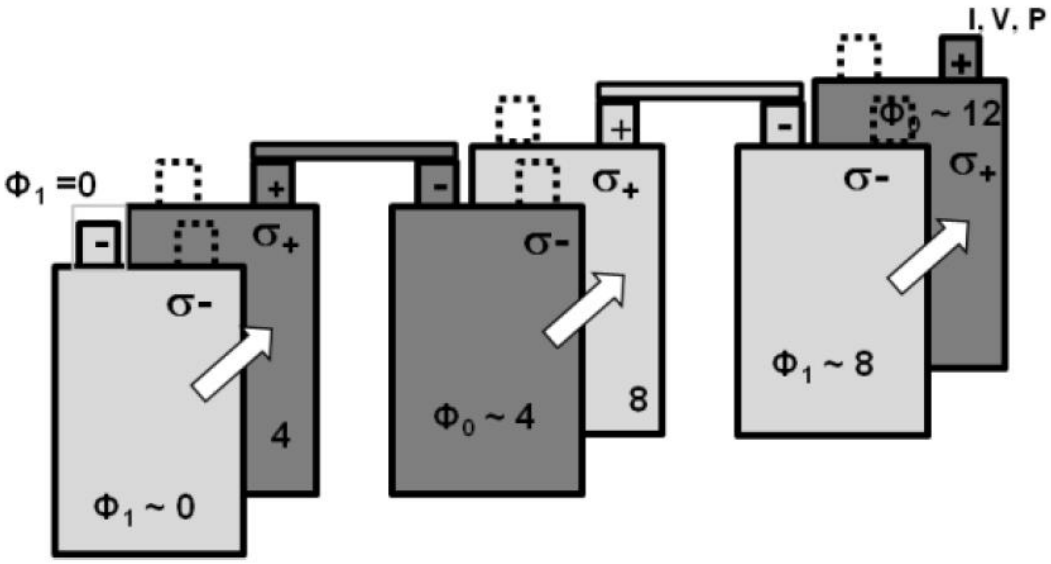

Figure 23 Battery bank circuit [8]

Despite the fact that equivalent circuit EV battery models cannot estimate battery cell properties such as the ion diffusion or the electrolyte potential and they require real data in order to be developed, they have been utilized for Battery Management Systems applications and they are regarded as fast and reliable models [47]. Since the thermal effects play a determinant role in the kinetics of electrochemical systems, thermal dependence is embedded into equivalent circuit models [50]. Moreover, in equivalent

circuit battery models the addition of RC branches increases the model accuracy and the complexity at the same time [47].

2.5 RC branch equivalent circuit models of lithium - ion cell in Matlab/Simulink

In [50] an equivalent circuit model consisting of a voltage source, a resistor in series and a RC branch is built in Matlab/Simulink so as to simulate the discharge dynamics of a lithium – ion battery cell made from $LiNiCoMnO_2$ and graphite electrodes, utilizing pulse discharge experimental data. Parameters such as the terminal voltage, the current, the temperature as well as the SOC are estimated, since it is essential that the battery management system, predominantly based on the SOC estimation, can provide the user with information such as the remaining driving range and the necessity of the battery replacement [49][50]. The circuit component values depend on the SOC and the inner temperature of the cell, which is assumed to uniform [50]. The result of the model parametric study is the creation of look – up tables for non – isothermal models [50]. A similar with 2 RC branches instead of 1 under the assumption that cooling is carried out via convection and heat is generated mainly due to the lithium – ion cell resistance is expected to provide more accurate results [49].

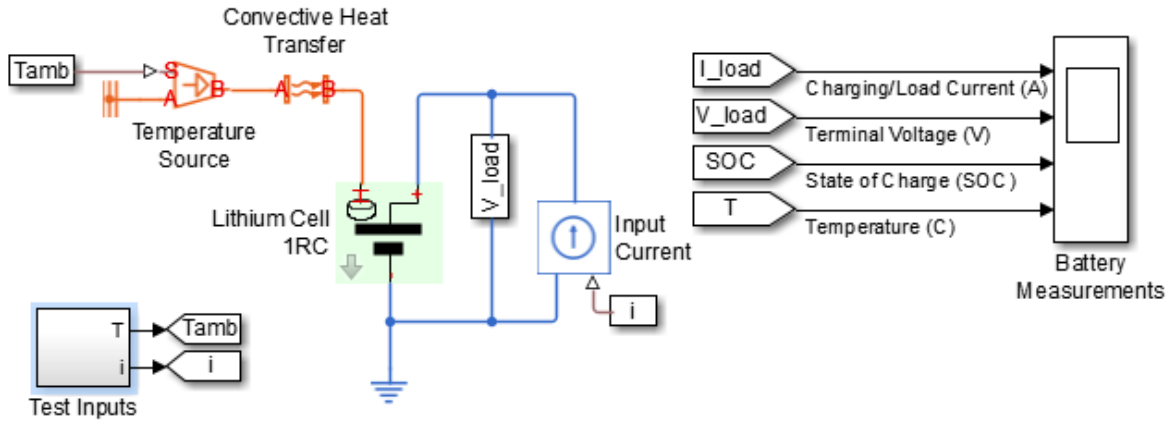

Figure 24 1 RC branch equivalent circuit model of lithium - ion cell (Matlab/Simulink) [49]

2.6 Lithium – ion Temperature Dependent Model in Matlab/Simulink

The "Lithium – ion Temperature Dependent Model" developed in [49][53] may be utilized for showing the effect of the temperature on the lithium – ion battery parameters of a hybrid electric vehicle during charging and discharging. In [53] it is found that the battery voltage depends on the voltage and on the State of Charge. The model is also able to accurately simulate the discharge curves of lithium – ion battery manufacturers and the battery transient phenomena [53]. The charge and discharge models of the lithium - ion battery are described by equations (2.6.1) and (2.6.2), respectively.

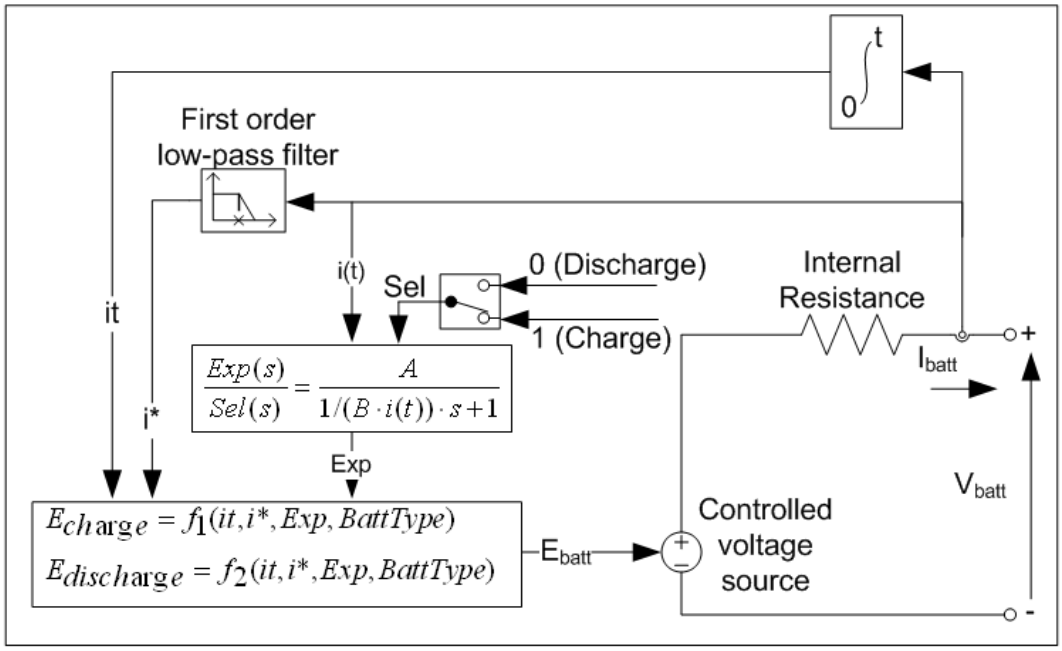

Figure 25 Equivalent circuit of the generic battery model [49]

$$f_1(i_t, i*, i) = E_o - K\frac{Q}{Q - i_t} i* - K\frac{Q}{Q - i_t} i_t + Aexp(-Bi_t) \quad (2.6.1)$$

$$f_2(i_t, i*, i) = E_o - K\frac{Q}{i_t + 0.1Q} i* - K\frac{Q}{Q - i_t} i_t + Ae^{-Bi_t} \quad (2.6.2)$$

The battery model's function f corresponds to a non – linear voltage being dependent only on the SOC. In other words, when the battery charge and the current equal zero, the battery voltage equals zero as well [53]. The following assumptions are made regarding this battery model [49]:

- The battery internal resistance remains constant during charging and discharging regardless of the current. In the case of the lithium-Ion battery, the internal resistance of the battery depends on the temperature.
- The model parameters are obtained from discharge characteristics and hold true during charging.
- There is no Peukert effect meaning that the battery capacity does not depend on the current.
- Although the self – discharge parameter is not included in the model, it can be represented by means of large resistance in parallel with the terminals of the battery.
- There is no memory effect.

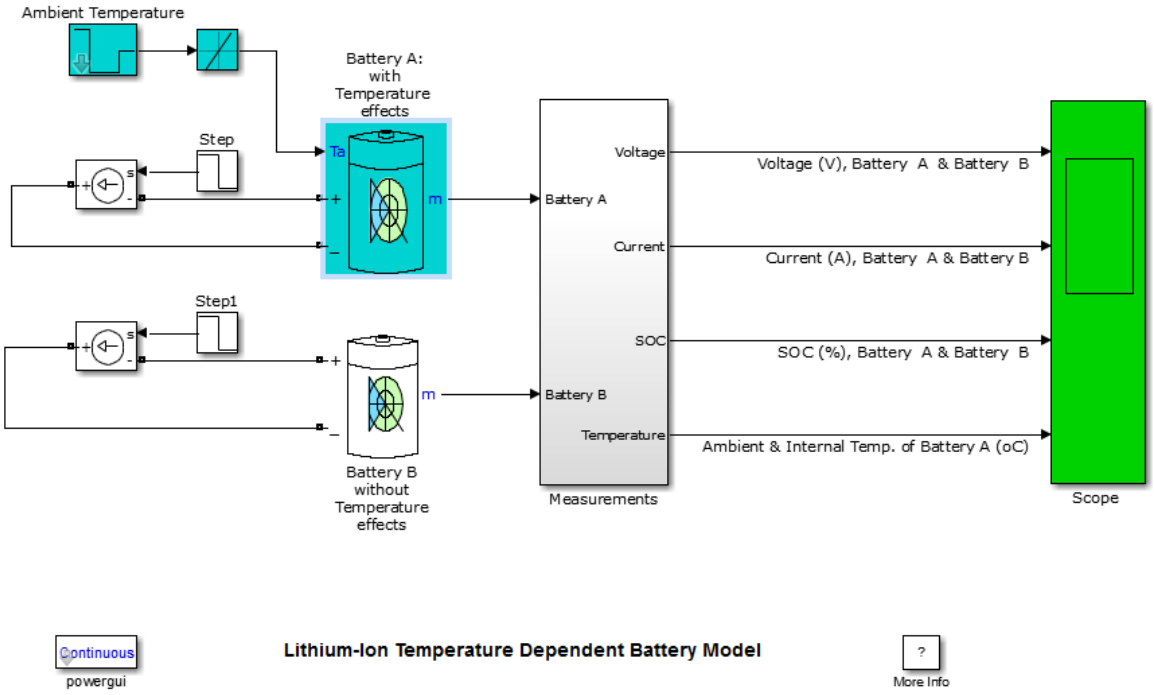

Figure 26 "Lithium - ion Temperature dependent model" [49]

2.7 Lithium – ion battery cell model in Comsol Multiphysics

A lithium – ion battery cell model developed by the team of John Newman at the University of California at Berkeley can be simulated in Comsol Multiphysics with a view to studying the battery from the reaction kinetics view. The 3d model of battery cell consists of a porous positive electrode and a negative electrode from lithium metal, while the current collector is attached to the positive electrode [55]. However, provided that the electrochemical reactions occur only on the surface and that the conductivity is high

enough, a cross – section of the 3d model is sufficient for the simulation neglecting the thickness of the negative electrode [55].

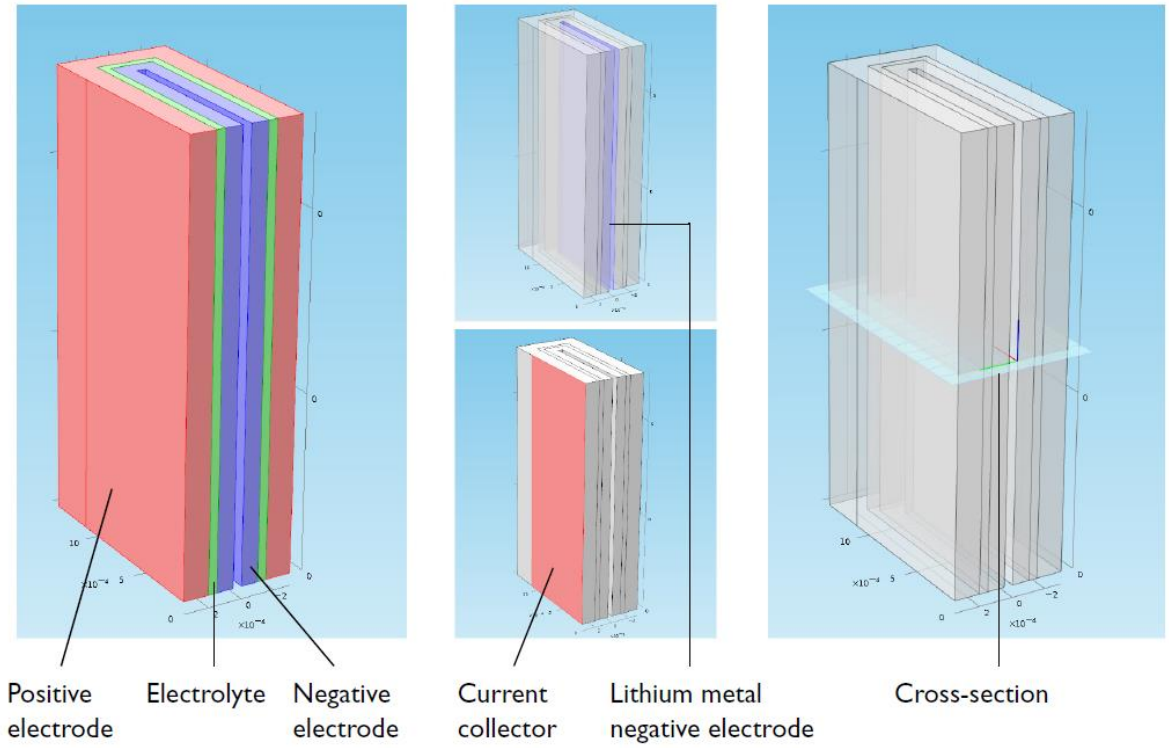

Figure 27 Lithium - ion battery cell 3d geometry (Comsol Multiphysics) [55]

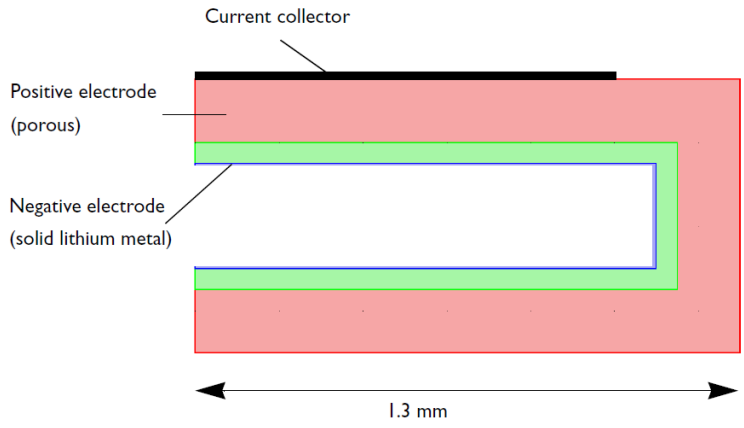

Figure 28 Cross-section of the lithium - ion battery cell 3d geometry (Comsol Multiphysics) [55]

In [55] a 3d model of an air-cooled cylindrical lithium – ion battery consisting of 18650 cells and incorporating the cooling fluid flow is developed. The cell model and the 3d thermal model are coupled

by means of the average temperature and of the average produced heat [55]. The 3d geometry consists of the domain of the active battery's material having a radius of 9mm and a height of 65mm, of a mandrel having a radius equal to 2mm, of and a cylindrical steel connector of thickness equal to 3mm [55]. Since the battery canister does not significantly affect the temperature variations, it is not included in the model.

The thermal conductivity, the heat capacity, the heat source and the density of the 3d thermal model are configured as the same parameters are configured in the 2d thermal model [55]. In addition, the thermal conductivity of the battery's active material exhibits anisotropy owing to the spiral winding placed in the cell layers, while the active material's orthotropic thermal conductivity is controlled by means of a cylindrical coordinate system [55]. As to the boundary conditions, the fluid is assumed to have zero relative to the wall velocity (no – slip condition) and the symmetrical conditions are implemented in the symmetry planes [55]. More information about the thermal model can be found in [55].

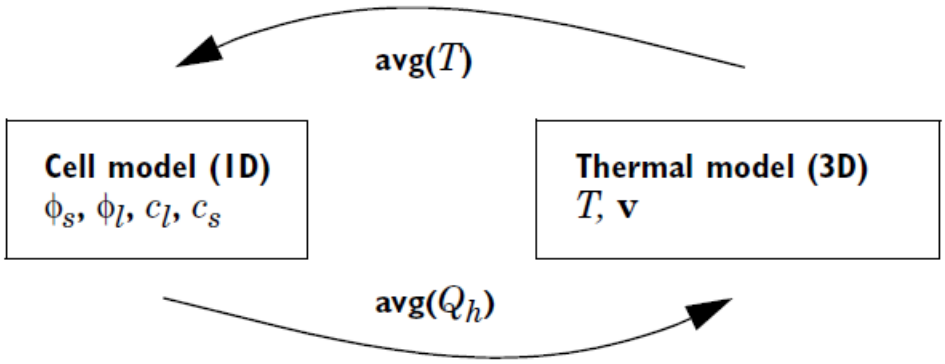

Figure 29 Lithium - ion battery cell and 3d thermal model coupling (Comsol Multiphysics) [55]

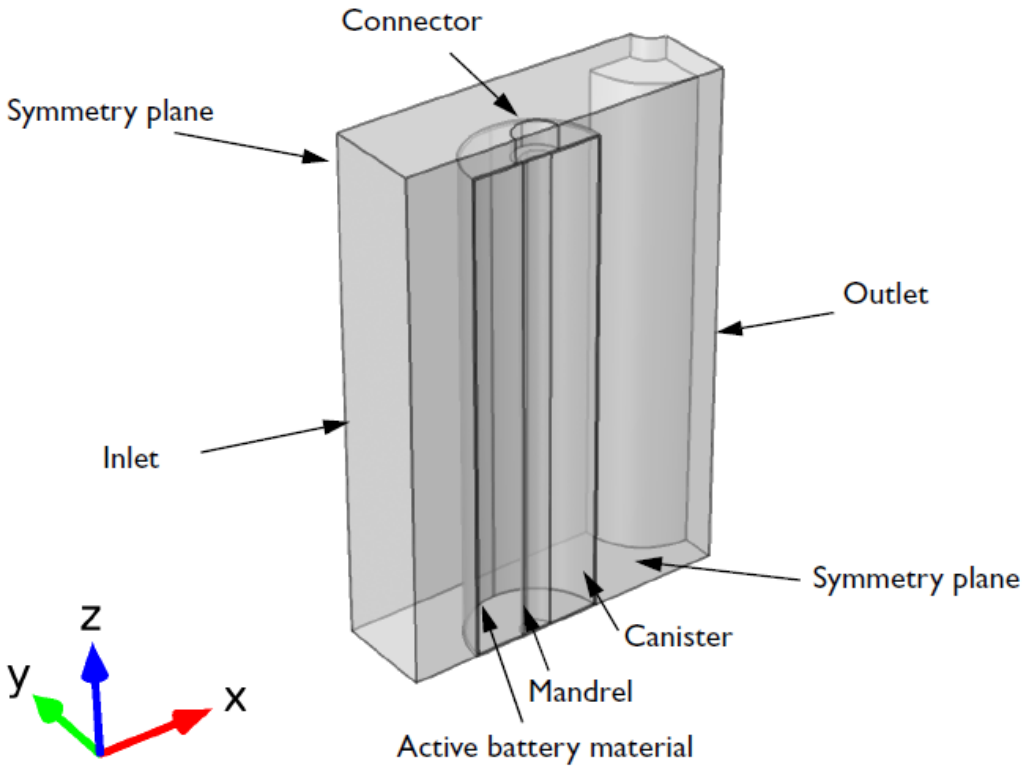

Figure 30 Lithium - ion battery 3d thermal model (Comsol Multiphysics) [55]

2.8 Supercapacitor model in Matlab/Simulink

The generic supercapacitor model is able to represent the majority of the supercapacitor types [49]. The equivalent circuit of the supercapacitor model is illustrated in the figure below.

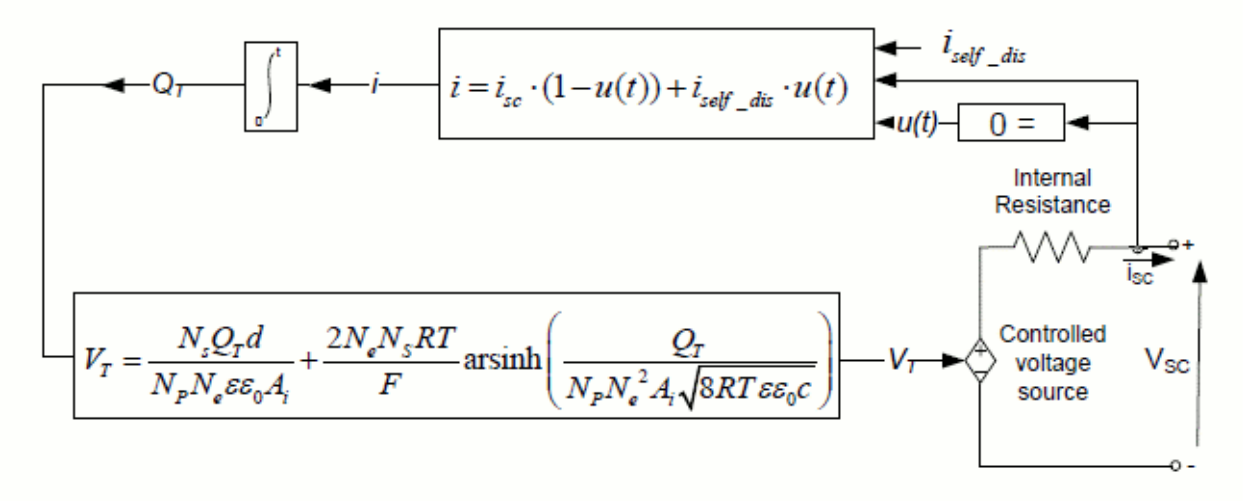

Figure 31 Supercapacitor model equivalent circuit [49]

The governing equations of the supercapacitor's model including the output voltage V_{SC}, the electric charge Q_T, the self-discharge current i_{self_dis} and the SOC are given by equations (3.1.26) – (3.1.29) [49].

$$V_{SC} = \frac{N_s Q_T d}{N_p N_e \varepsilon \varepsilon_0 A_i} + \frac{2N_e N_s RT}{F} \sinh^{-1}\left(\frac{Q_T}{N_p N_e^2 A_i \sqrt{8RT\varepsilon \varepsilon_0 c}}\right) - R_{SC} \cdot i_{SC} \qquad (2.8.1)$$

$$Q_T = \int i_{SC} dt \qquad (2.8.2)$$

$$i_{self\_dis} = \begin{cases} \dfrac{C_T \alpha_1}{1 + sR_{SC}C_T} & if \quad t - t_{oc} \le t_3 \\ \dfrac{C_T \alpha_2}{1 + sR_{SC}C_T} & if \quad t_3 < t - t_{oc} \le t_4 \\ \dfrac{C_T \alpha_3}{1 + sR_{SC}C_T} & if \quad t - t_{oc} > t_4 \end{cases} \qquad (2.8.3)$$

$$SOC = \frac{Qinit - \int_0^t i(\tau)d\tau}{Q_T} \times 100 \qquad (2.8.4)$$

2.9 Electric vehicle model with VCU in LMS Imaginelab

A model for simulating the EV response for different normalized driving cycles can be implemented in LMS ImagineLab [62]. The Vehicle Control Unit (VCU) controls the acceleration and braking actions with a view to reduce the battery consumption [62]. During braking the electric motor charges the battery. However, minimum torque value is taken into account and changed based on motor speed and battery voltage so as regenerative braking to be limited [62]. In particular, this is carried out through a parameter called "electric motor rotary speed threshold to regenerate battery" (speedthr). In case the vehicle speed is greater than speedthr, then VCU provides the battery with regenerative power. On the other hand, if the torque required is greater than the torque during battery regeneration, hydraulics brakes are employed [62]. VCU has five inputs (maximum and minimum electric motor torque, electric rotary velocity, acceleration command from driver, braking command from driver, battery's SOC) and two outputs (electric motor torque command, braking command) [62].

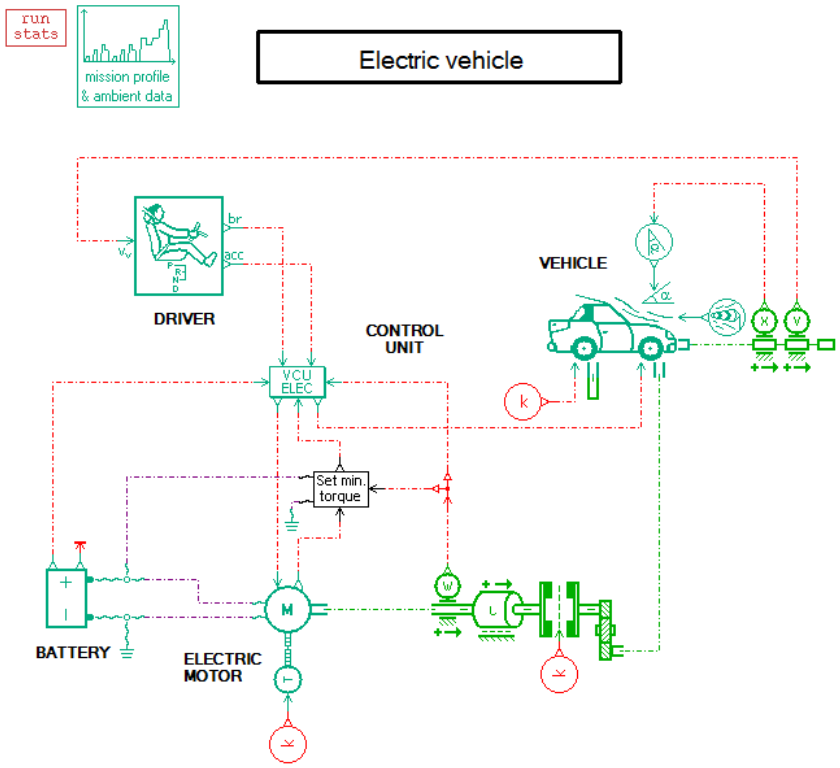

Figure 32 Electric vehicle model with VCU (LMS ImagineLab) [62]

2.10 Electric vehicle model with SCU in LMS ImagineLab

Another model representing a complete automotive power network and including VCU along with Safety Control Unit (SCU) can be implemented in LMS ImagineLab for simulating battery safety management and EV response [62]. The VCU follows the driver input determined by the speed profile taking into account the electric motor and battery safety specifications and it generates the proper torque command for the electric motor, which means that the electric motors require specific amount of energy to generate the torque for the wheels [62]. The lithium – ion battery pack consists of 1000 cells in 10 parallel branches. The battery pack has a total mass of 80 kg and a convective exchange area of $7.35*10^6$ mm^2 with a convection coefficient equal to 20 W/m^2K [62]. On the other hand, convection of the electric motor is carried out through air velocity [62]. The behavior of the SCU is set based on quasi-state data of the manufacturer. In particular, the battery is configured to open circuit when its SOC equals to zero in order to avert overdischarge and the current limits and the pulse time are also determined (30A maximum charge and discharge current with a 30s pulse time, 20 A continuous charge and discharge current) [62].

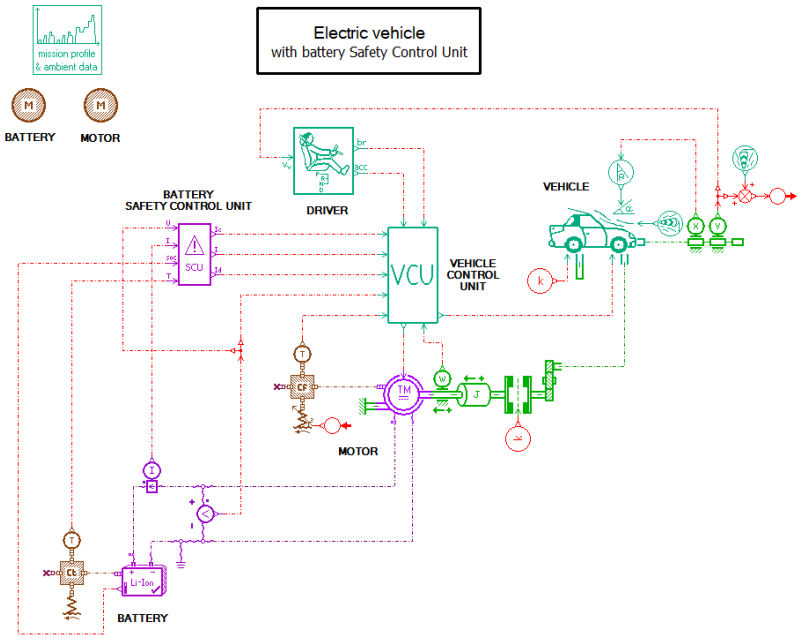

Figure 33 Electric vehicle model with SCU (LMS ImagineLab) [62]

2.11 Battery pack air – cooling model in LMS Imaginelab

In order for assessing the air – cooling performance of a lithium – ion battery pack, a model constituting the one branch of the battery pack is utilized in [62]. The lithium – ion battery is rated at 130 V and 3 kWh, while the battery pack consists of three branches of 40 cells rated at 3.34 V and 8 Ah [62].

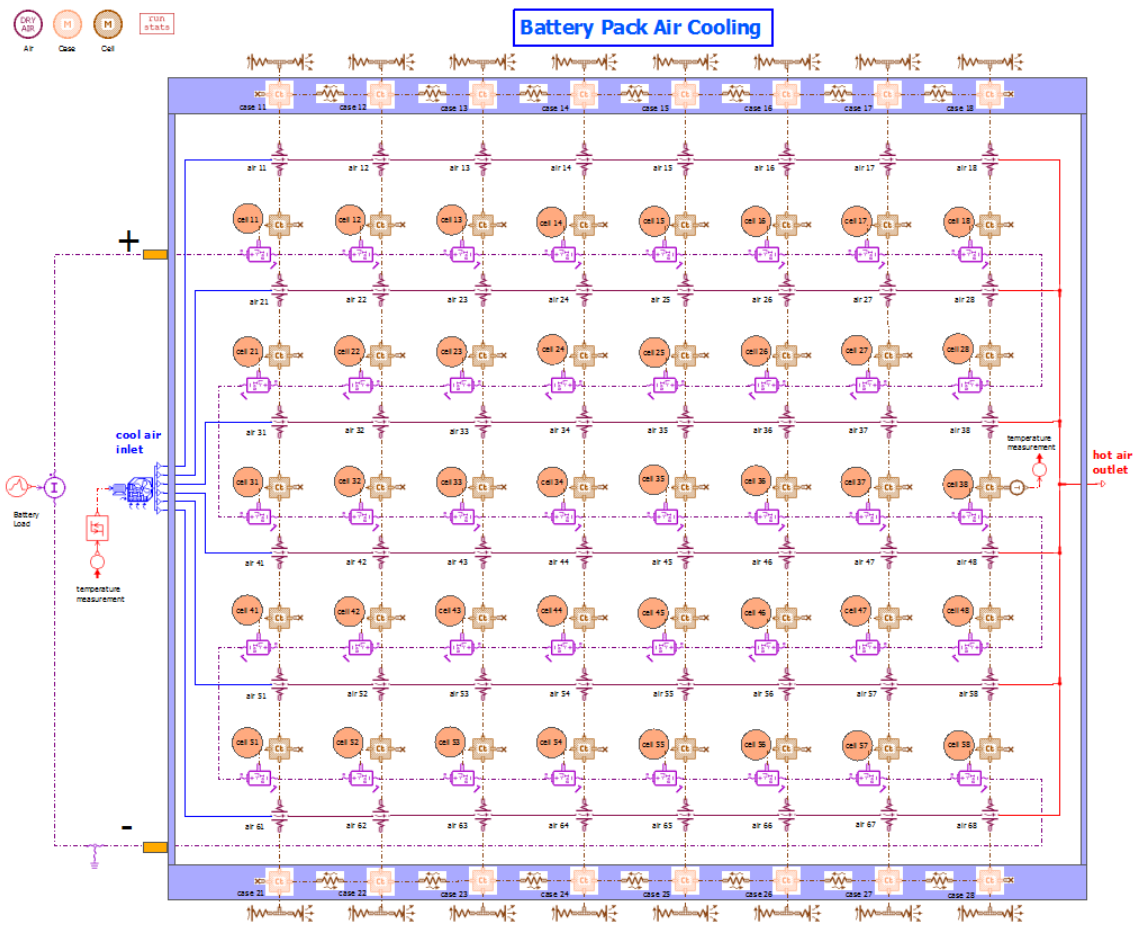

Figure 34 Battery pack air - cooling model (LMS ImagineLab) [62]

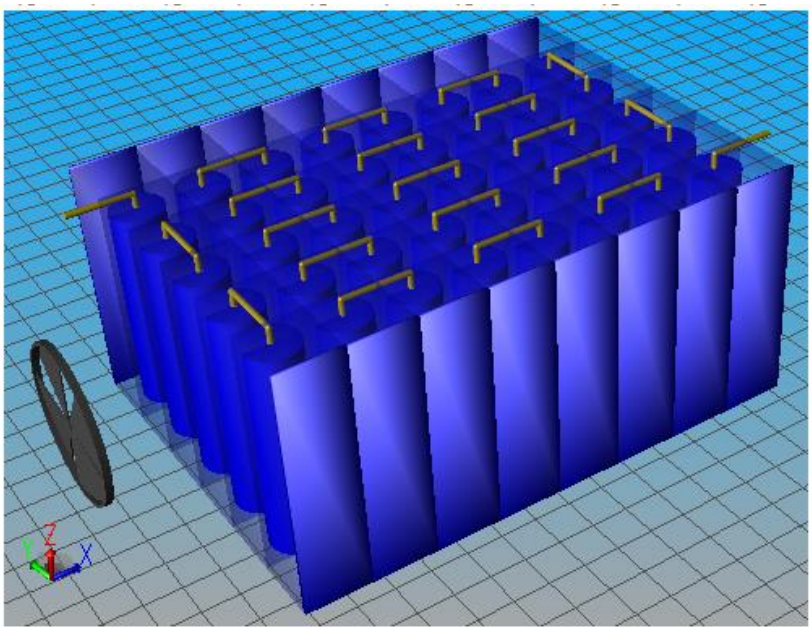

Figure 35 Battery pack air - cooling geometric model (LMS ImagineLab) [62]

Each cell has an electrical and thermal component. The cell average surface temperature is calculated by means of the thermal capacitance, whereas the electrical quantities along with the heat flow rate are calculated by means of the electrical model [62]. Radial thermal exchanges with the air occur on each side of the cells. Each branch consists of forty connected in series cells arranged in 5 rows of 8 cells.

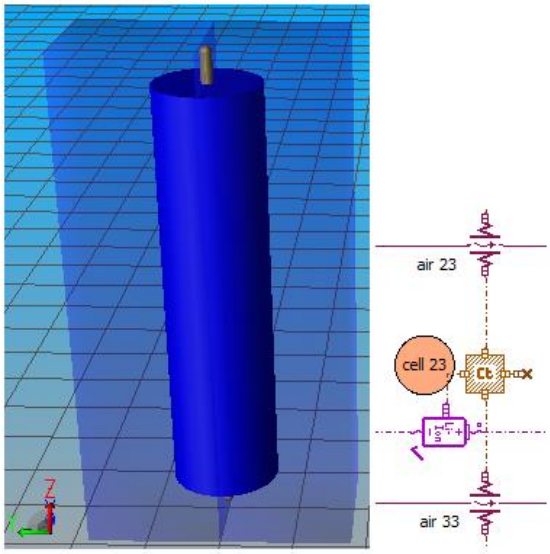

Figure 36 Cell of the battery pack air – cooling model (LMS ImagineLab) [62]

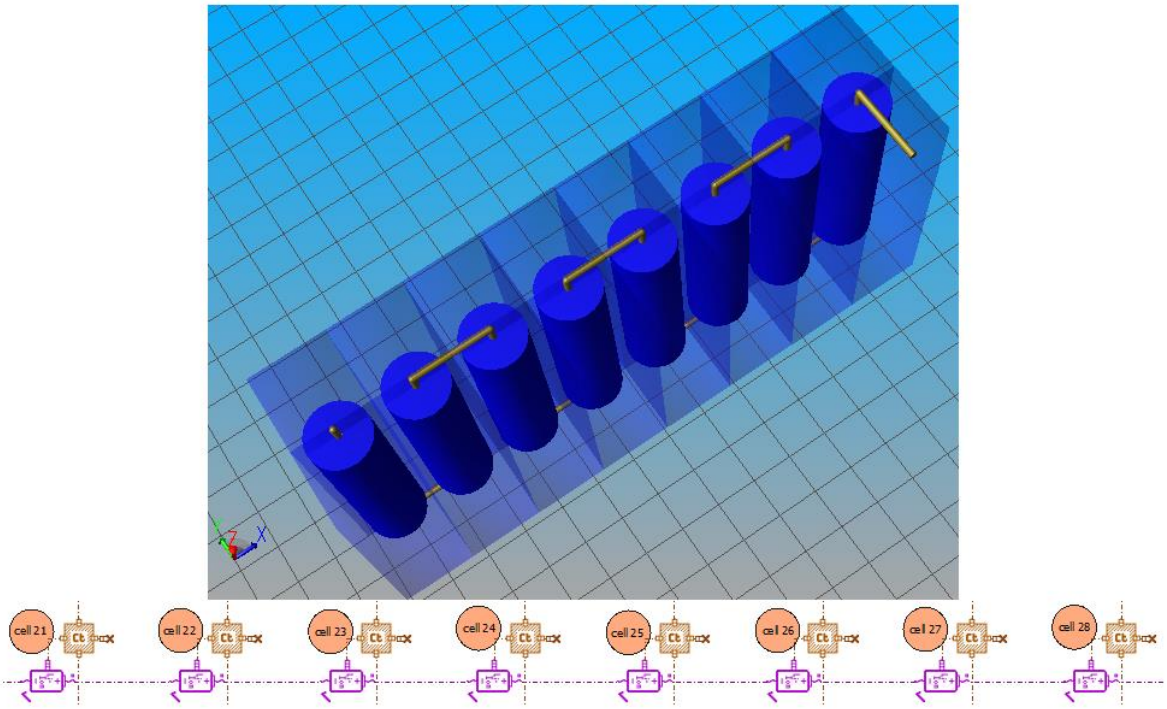

Figure 37 Row of the battery pack air – cooling model (LMS ImagineLab) [62]

2.12 EV battery aging model in LMS ImagineLab

The purpose of the following model developed in LMS ImagineLab is so comparing the response of an EV with an old and a new battery as assessing the aging effect on the vehicle performance [62]. The model represents a complete automotive network consisting of the vehicle, the driver, the battery and its control (VCU and SCU) and the electrical machine [62].

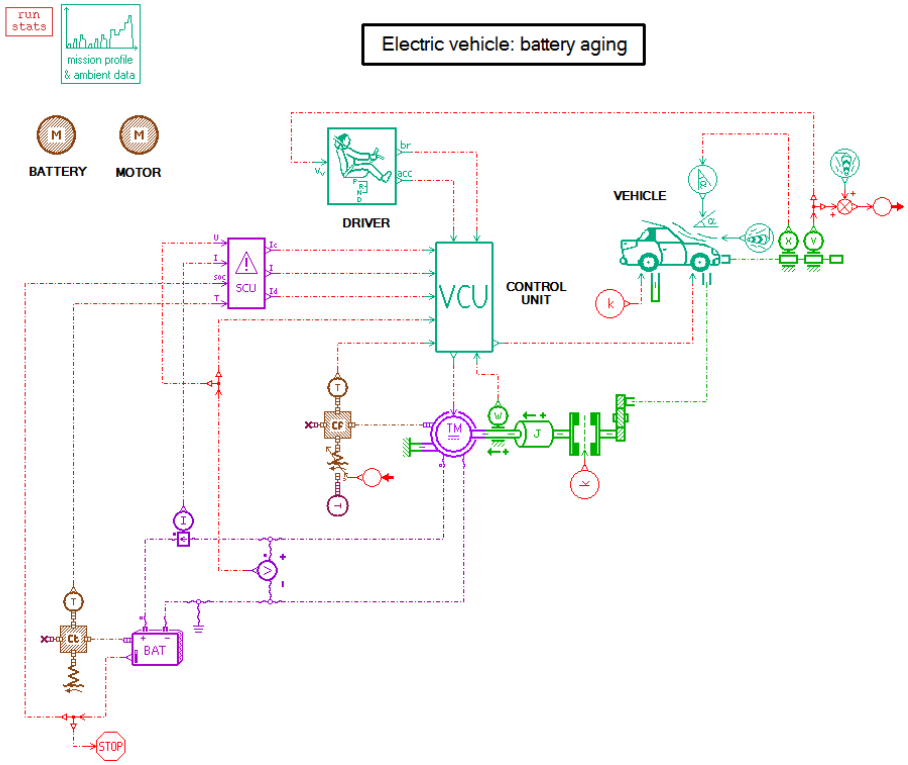

Figure 38 EV battery aging model (ImagineLab) [62]

The vehicle movement is simulated with NEDC cycles under driving conditions in urban (800 s) and extra – urban conditions (800-1200s) until the battery is almost completely discharged, which means that the battery SOC becomes 10%. The battery pack consists of 1000 cells with 100 cells in series in each of the 10 branches. It is assumed that the new battery pack's cells have a nominal capacity of 2.3 Ah, whereas the old battery pack's cells have a nominal capacity of 1.9 Ah due to aging [62]. As stated, the VCU aims at meeting the driver's demand taking into consideration the limits imposed by the SCU which include 10% as the threshold of the battery SOC.

The battery is considered a Li-ion battery with $LiFePO_4$ - Carbon (LFP - C) chemistry. The electrical parameters of the battery are estimated with the proper identification tool in [62].

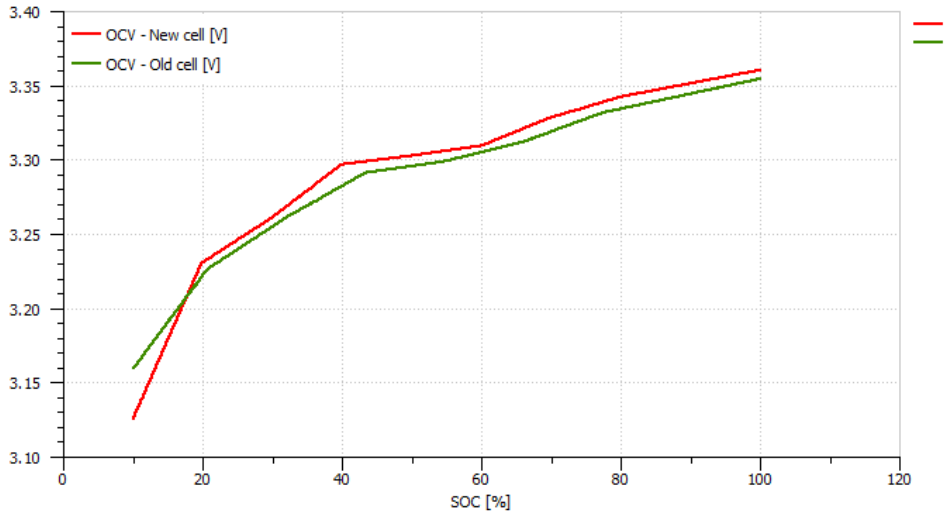

Figure 39 OCV vs SOC for the new and the old battery [62]

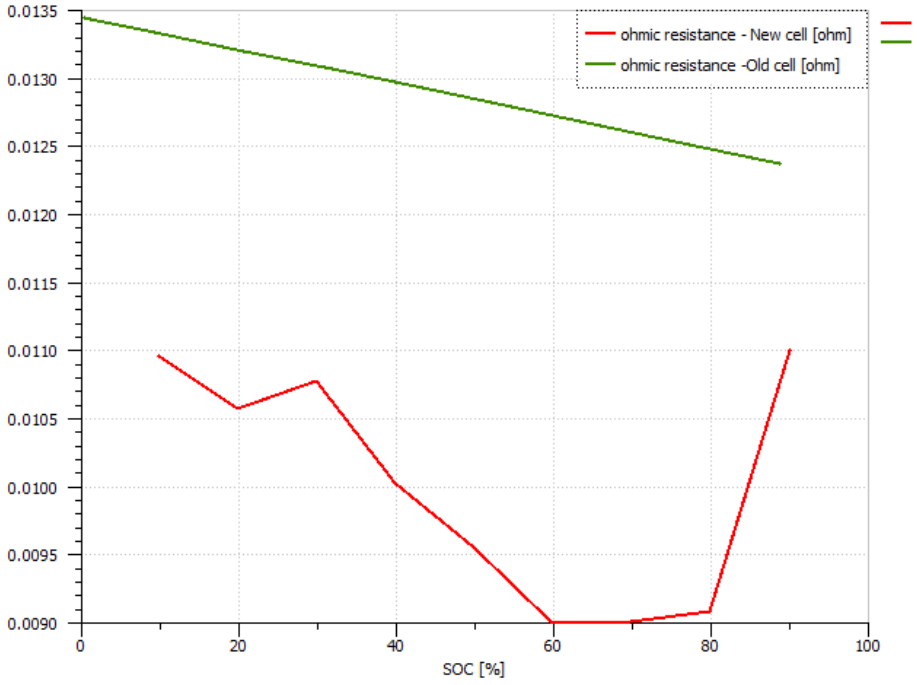

Figure 40 Ohmic resistance vs SOC at current equal to -10A for the new and the old battery [62]

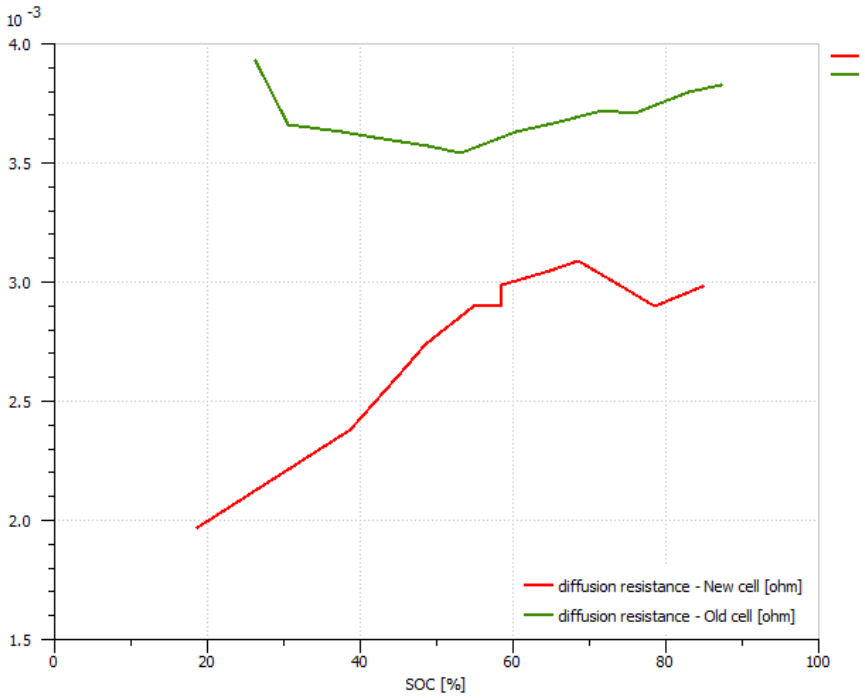

Figure 41 Diffusion resistance vs SOC at current equal to -10A for the new and the old battery [63]

The curves above indicate that OCV is not significantly affected by aging. However, the Ohmic resistance of the cell increases by 30% (from 10 to 13 μΩ) and the diffusion resistance of the cell increases by 25% (from 2.9 to 3.6 μΩ) due to aging [62].

2.13 Model for evaluating charging strategies with respect to aging in LMS ImagineLab

Since battery aging results in capacity loss and reduction of driving range, the investigation of the system's behavior during the whole battery's life is critical [62]. Battery aging can be classified into aging due to use (cycling aging) and aging due to time (calendar aging) [65]. The model below aims at comparing different battery charging strategies.

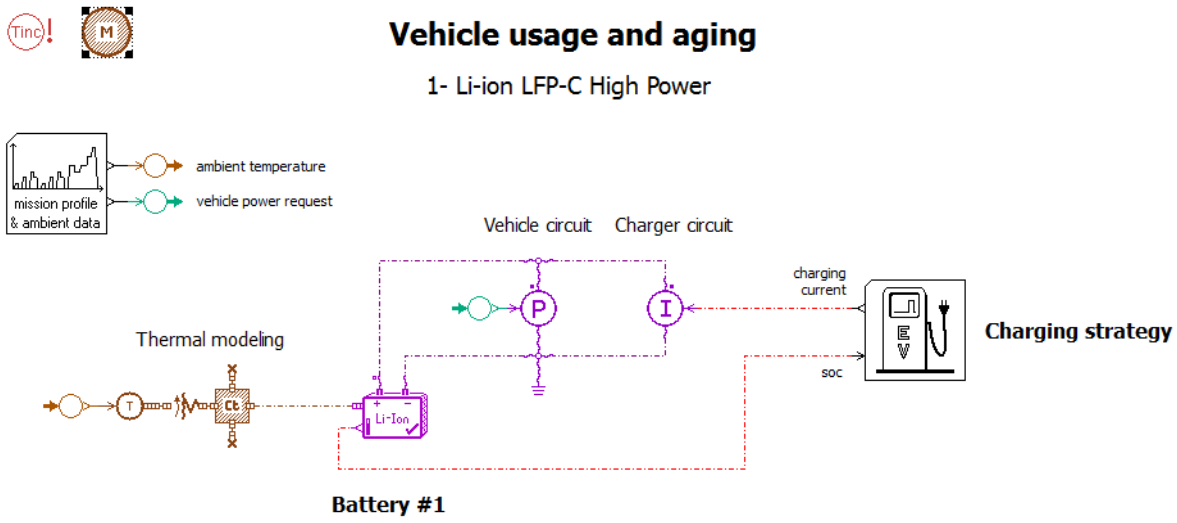

Figure 42 Model for evaluating charging strategies with respect to aging [62]

The LFP – C high power lithium – ion battery is solicited via two sources: the first source corresponds to the power source being the power that vehicle demands during its operation and the second source corresponds to a current source representing the interaction between the vehicle and the grid (the interaction can be either G2V during charging or V2G during discharging) [62].

The ambient temperature profiles simulated constitute a daily and an annual variation. As to the power demand, this derives from an EV simulator simulating a NEDC driving cycle being repeated four times a day at 8 AM, 12 AM, 1 PM and 6 PM [62]. Each power demand cycle represents a home – work trip.

The charging scenarios are assumed as followed: As to the G2V there are the possibilities of recharging the vehicle before leaving home in the morning, at work before and after lunch, and after coming back home. As to the V2G there are the possibilities of discharging the vehicle after arriving at work, after coming back home during lunch break and after coming back home [62]. Both V2G and G2V phase include constant current charging until 90% SOC and constant current discharging until 10% SOC, while the current is set to 40 A [62]. The five scenarios are summarized in table below.

Table 9 Five charging scenarios

Scenario	Details
Reference	Common routes with one recharge at the evening after coming back home.
Just in time	Common routes with one recharge before going to work at 6 AM.

Charge when you can	Common routes with recharges when the driver is able to recharge the vehicle. 9.00 AM after arriving at work, 2.00 PM after coming back from lunch,
Strong V2G	V2G discharges at 9.00 AM after arriving at work, 2.00 after coming back from lunch and at 7.00 PM after coming back home. Recharges at 6.00 AM before leaving home, at 11.00 AM before lunch break and 5.00 PM before leaving work.
Light V2G	Common routes with one recharge before going to work at 6.00 AM and one complete discharge after coming back at 7.00 PM.

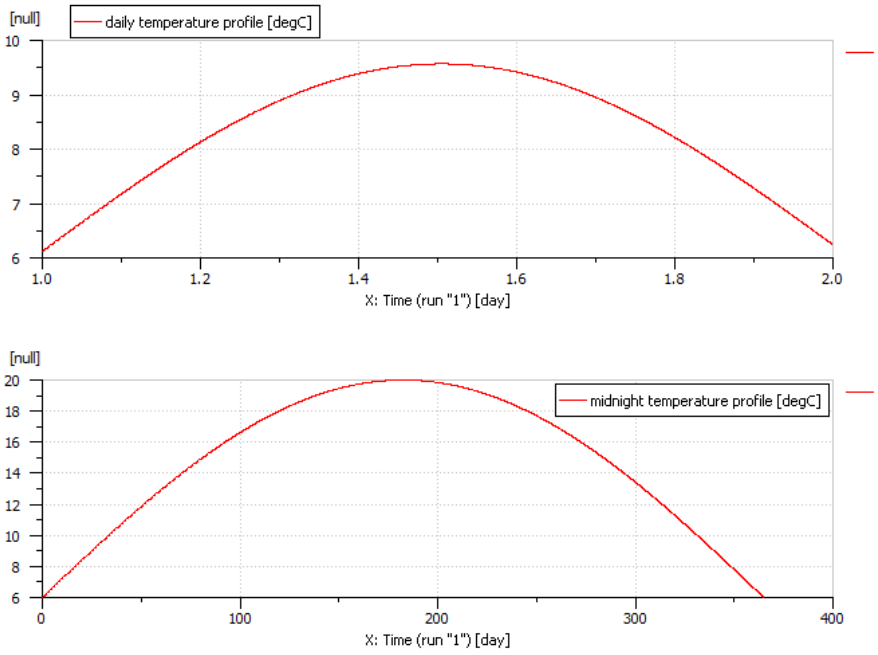

Figure 43 Daily and annual temperature variations (Model for evaluating charging strategies with respect to aging - ImagineLab) [62]

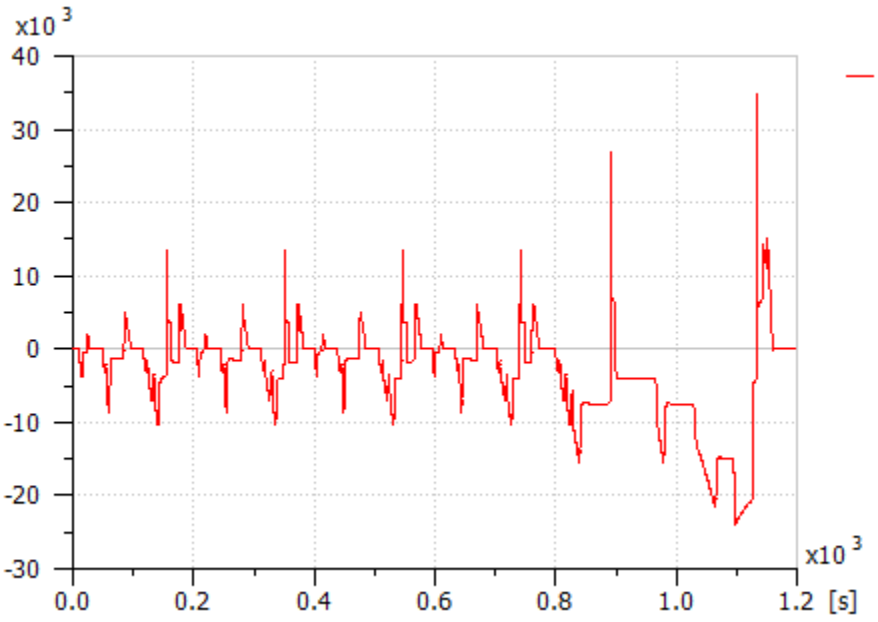

Figure 44 Power demand in W during a NEDC driving cycle (Model for evaluating charging strategies with respect to aging - ImagineLab) [62]

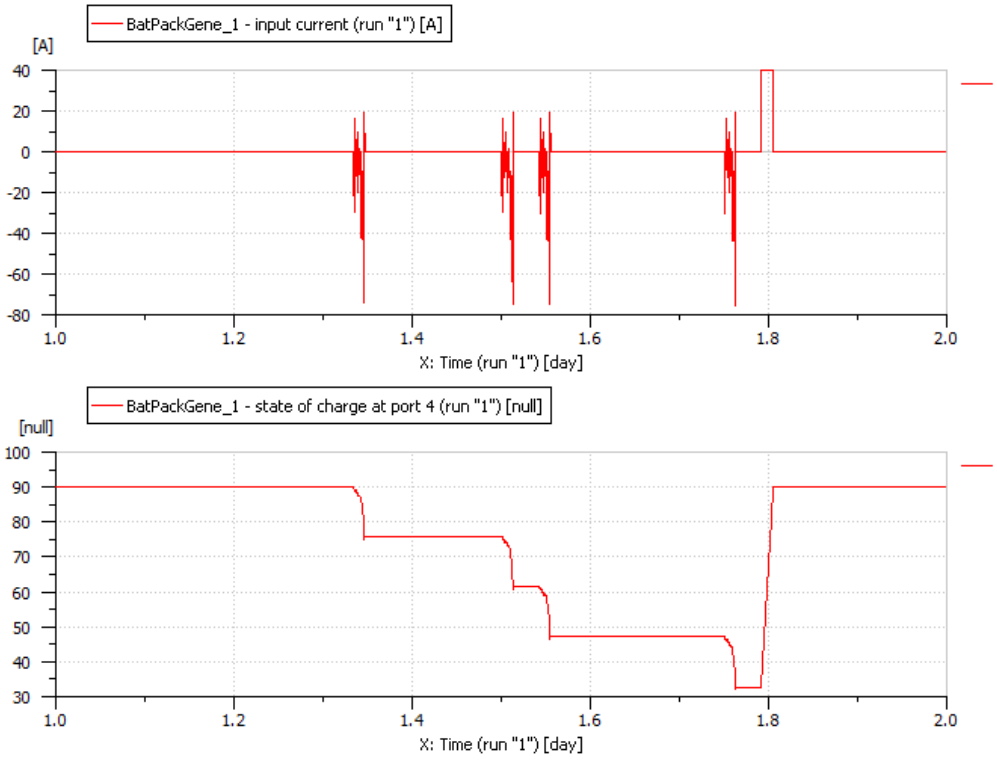

Figure 45 Reference charging scenario (Model for evaluating charging strategies with respect to aging - ImagineLab) [62]

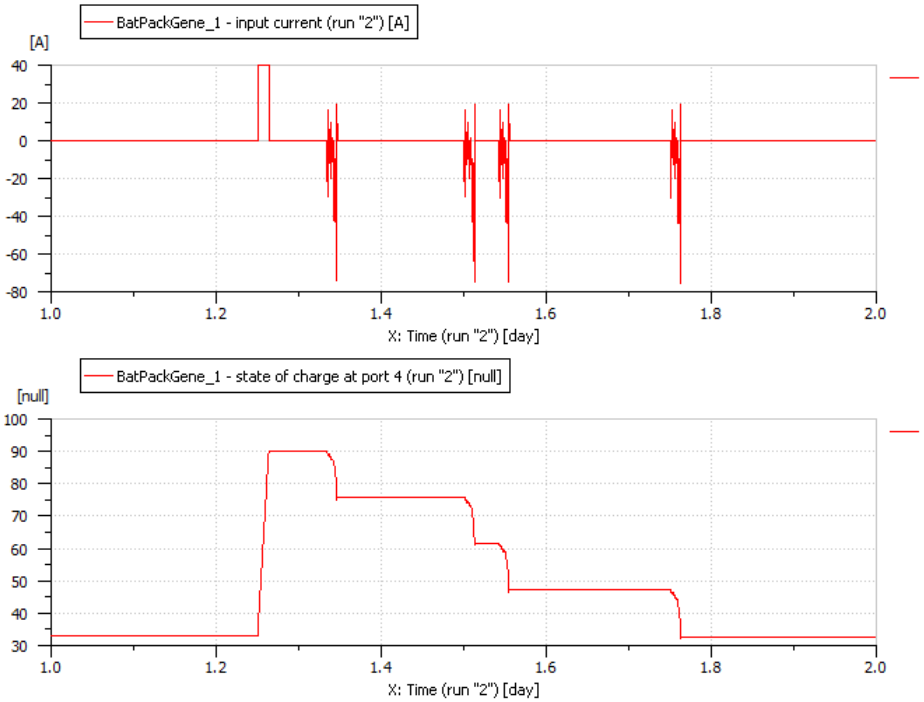

Figure 46 Just in time charging scenario (Model for evaluating charging strategies with respect to aging - ImagineLab) [62]

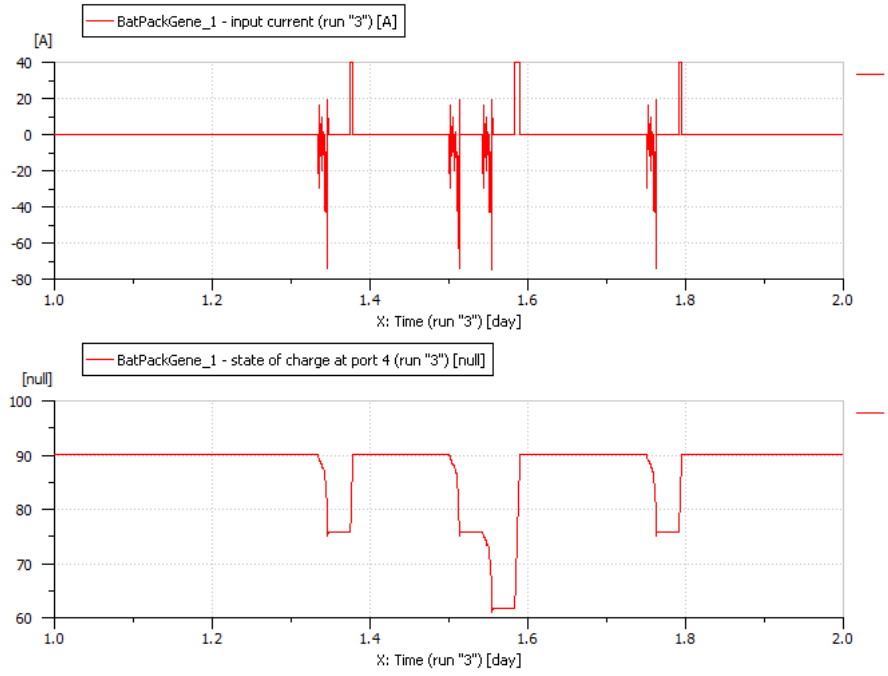

Figure 47 Charge when you can (Model for evaluating charging strategies with respect to aging - ImagineLab) [62]

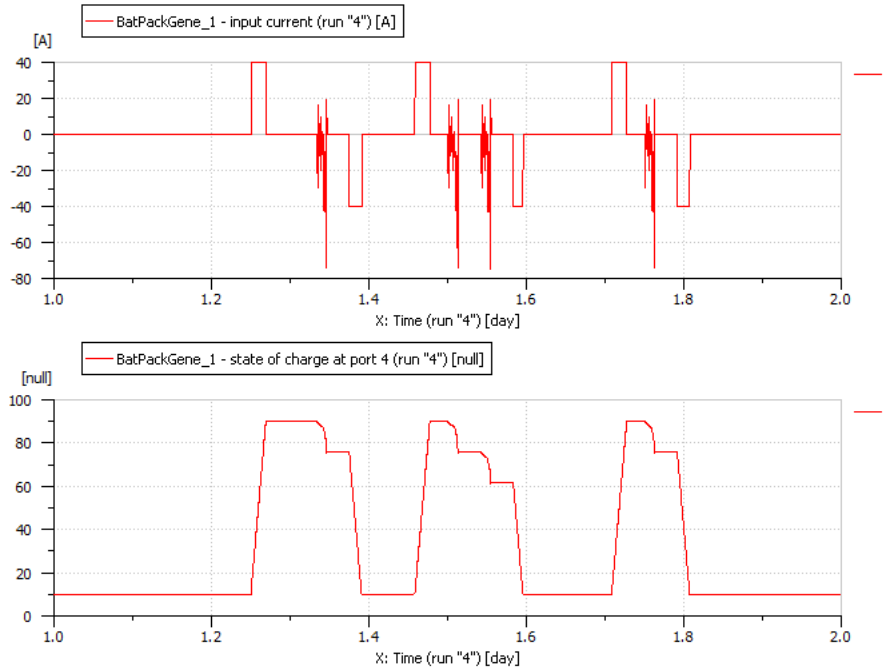

Figure 48 Strong V2G charging scenario (Model for evaluating charging strategies with respect to aging - ImagineLab) [62]

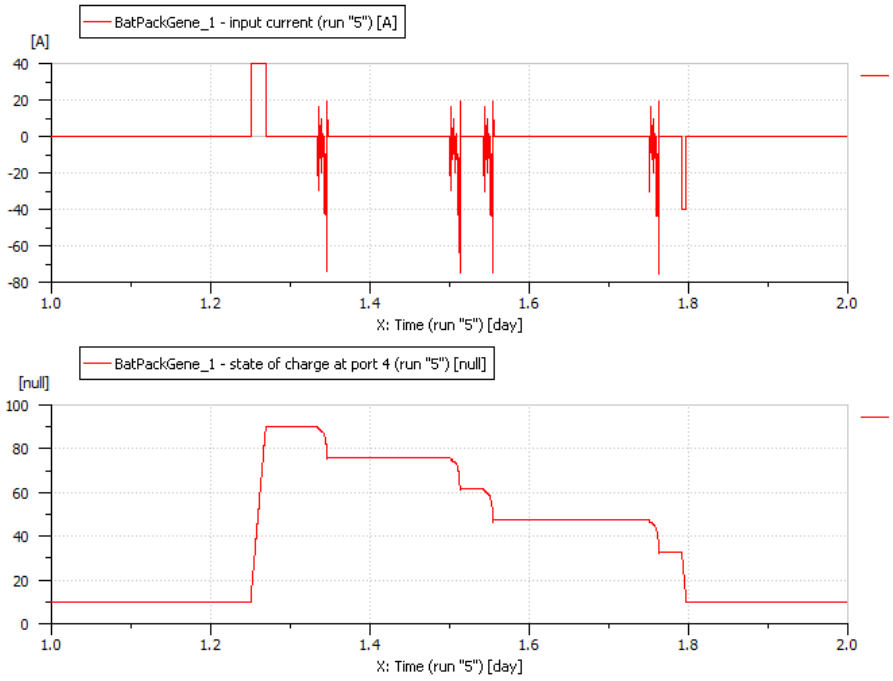

Figure 49 Light V2G charging scenario (Model for evaluating charging strategies with respect to aging - ImagineLab) [62]

2.14 Energy and power storage system model in LMS ImagineLab

As described the combination of a lithium – ion battery and a supercapacitor reaps several benefits. The following model developed in [62] is a circuit consisting of a high energy lithium – ion battery in parallel with a high power supercapacitor being connected with a reversible load such that the lithium – ion battery responds to low power demands and the supercapacitor responds to peak power demands.

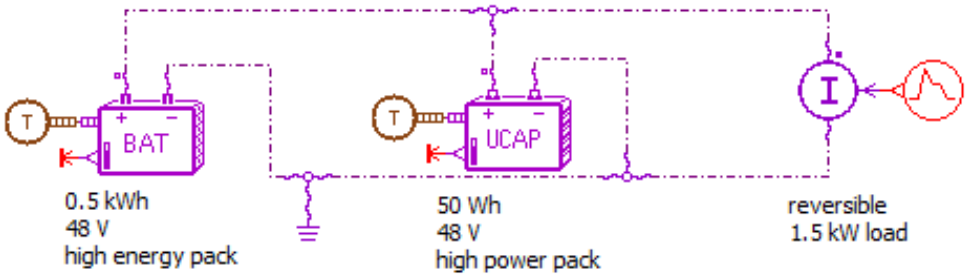

Figure 50 Energy and power storage system model (ImagineLab) [62]

2.15 SCU based on look - up table model in LMS ImagineLab

Since safety is a key factor to the proper design of lithium – ion batteries, the battery has to function within a specified range which is controlled by the SCU [62]. The "SCU based on look – up table" model of [62] aims at the assessment of the current limits taking into account the SOC, the temperature and the duration during charging and discharging [62]. A methodology for the generation of the maximum power tables (look-up tables) is developed in [67] (Appendix A).

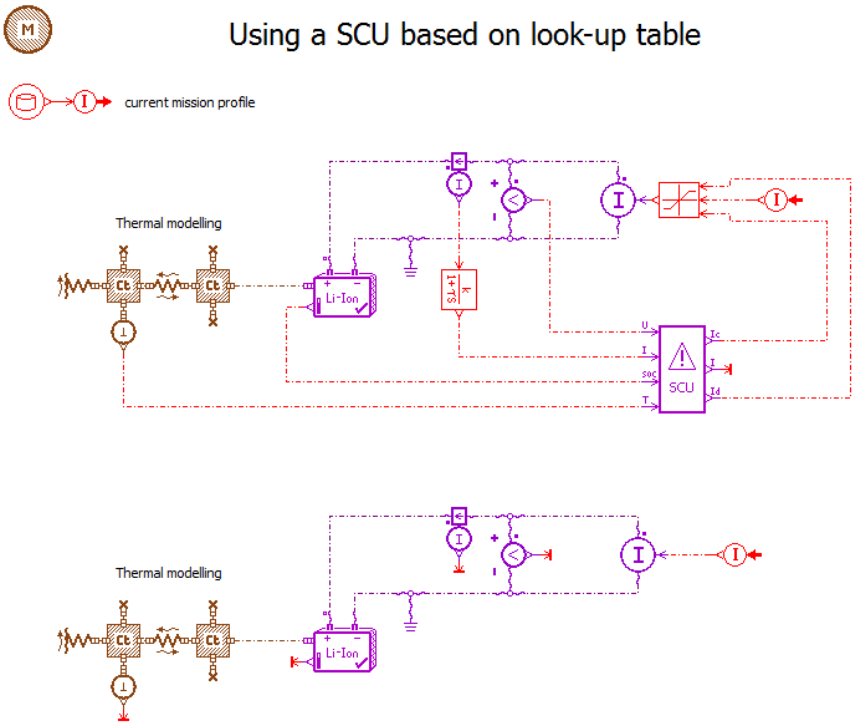

Figure 51 SCU based on look - up table model (ImagineLab) [62]

The lithium – ion battery cell model employed high frequency Ohmic phenomena, low frequency diffusion phenomena and charge transfer phenomena represented by the respective overpotentials (U) in the equivalent circuit [62]. Ohmic and charge resistance are dependent on the temperature as described by the Arrhenius law, whereas the charge transfer phenomena is modeled as static resistance neglecting transient response. Since the mass transport boundary conditions may vary, the diffusive or Warburg impedance Z_{diff}, it is expressed in the frequency domain as in equation (3.1.30) [62].

$$Z_{diff}(s) = R_{diff}\frac{tanh\sqrt{s\tau_{diff}}}{\sqrt{s\tau_{diff}}} \quad (3.1.30)$$

Where R_{diff} is the difussive resistance and $s\tau_{diff}$ the characteristic diffusion time. The lithium – ion battery cell model's parameters are calibrated by means of Electrochemical Impedancemetry Spectroscopy (EIS) measurements so as the equivalent circuit to correspond to low frequency measured impedances as functions of temperature and of SOC [62]. Quantitative results being available for a cell nominal capacity of 2.3 Ah.

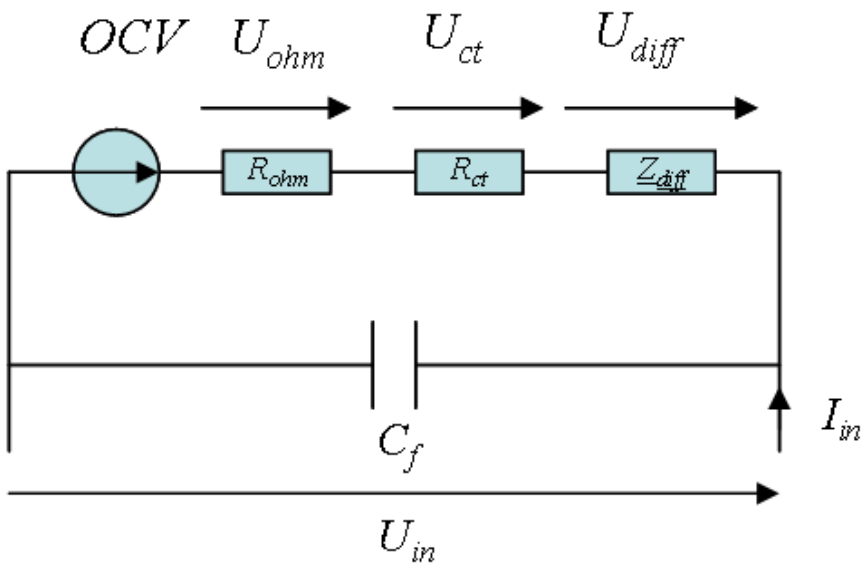

Figure 52 Lithium - ion cell equivalent circuit (SCU based on look - up table model - ImagineLab) [62]

Executing a python script the largest maximum charge and discharge power are obtained [62]. The largest maximum powers are found around 30 ° C and at the middle of the range of the SOC values, which is attributed to the fact that at 30 °C the power is limited both due to overvoltages and due to high temperatures [62]. As time increases, the power is further limited due to longer pulse durations resulting in higher voltage and higher temperature [62].

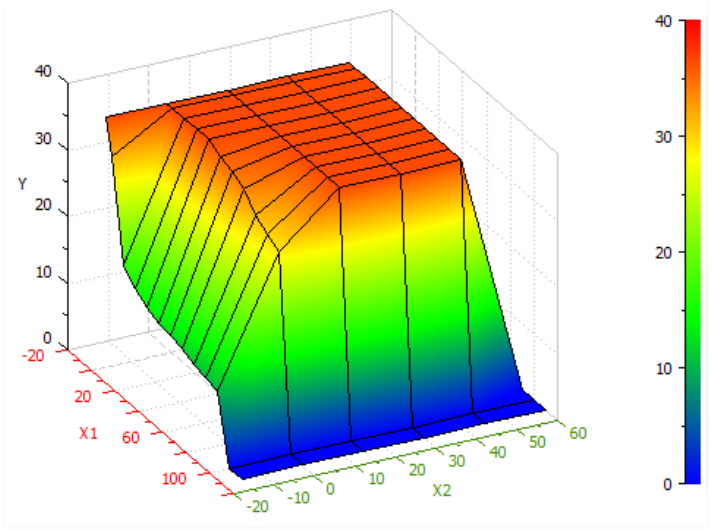

a) after 1s

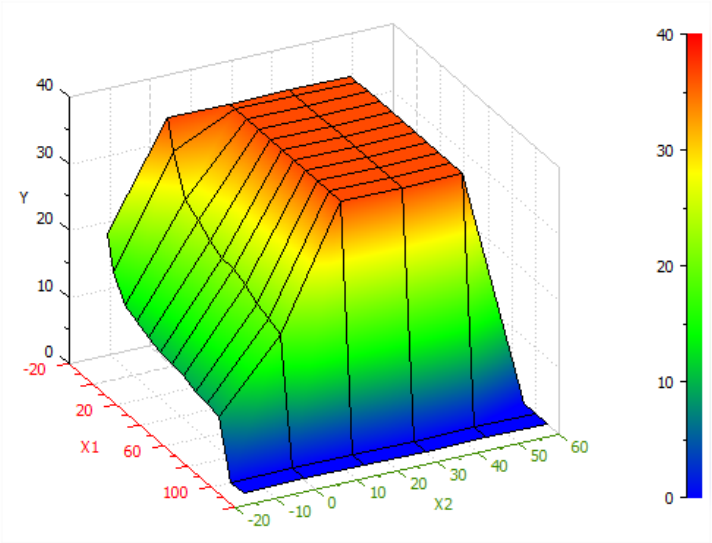

b) after 30s

Figure 53 Maximum charge power(SCU based on look - up table model - ImagineLab) [62]

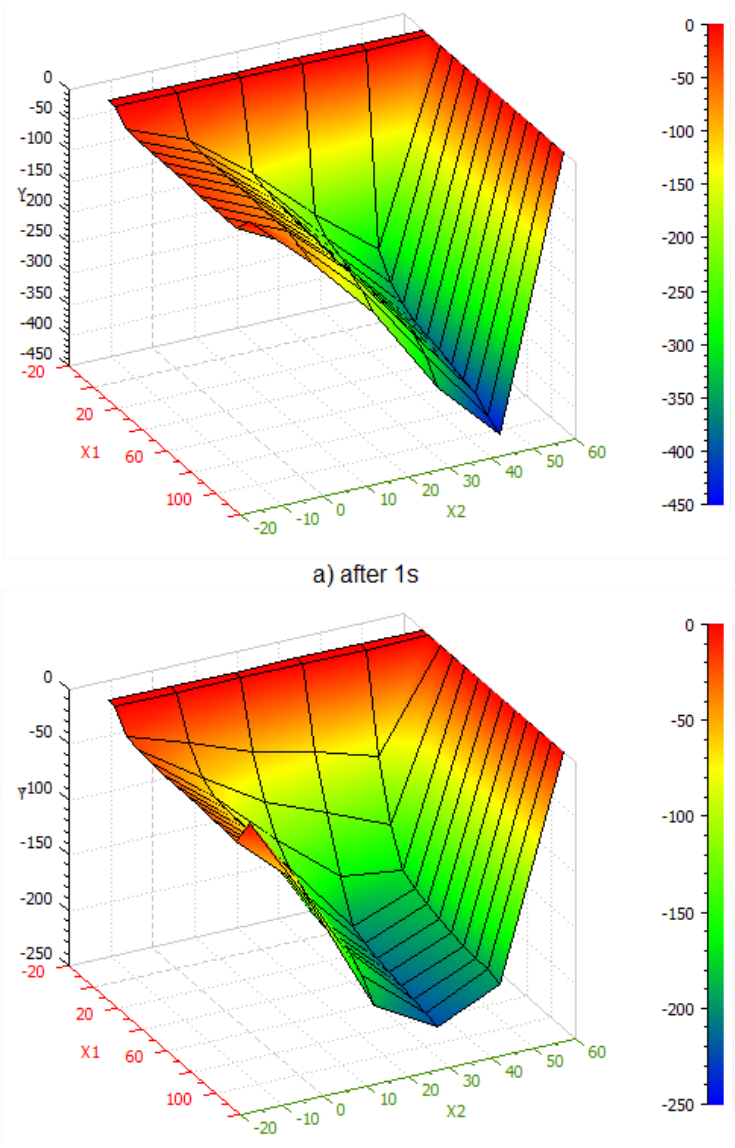

Figure 54 Maximum dicharge power(SCU based on look - up table model - ImagineLab) [62]

Subsequently, the 3D tables are imported into the model and two dynamic Lithium – ion LFP – C cells are supplied with the same current source, one of which is considered saturated so as SCU to be taken into account in the results [62]. The heat transfer coefficient is set to 50 W/m^2K and the current mission profiles represents that of an EV [62].

2.16 Battery cell response to HEV driving cycles model in LMS ImagineLab

The following model developed in Comsol Multiphysics aims at studying the battery cell response to HEV driving cycles. Three components can be characterized as critical in EV BMS, which are the battery, the monitoring and the control. The battery voltage and temperature are monitored during the vehicle operation [55]. The monitoring unit with aid of an algorithm estimates, for instance, the battery SOC, and monitors the temperature for averting overheating. The control unit take certain actions which are the pause of charging and discharging [55].

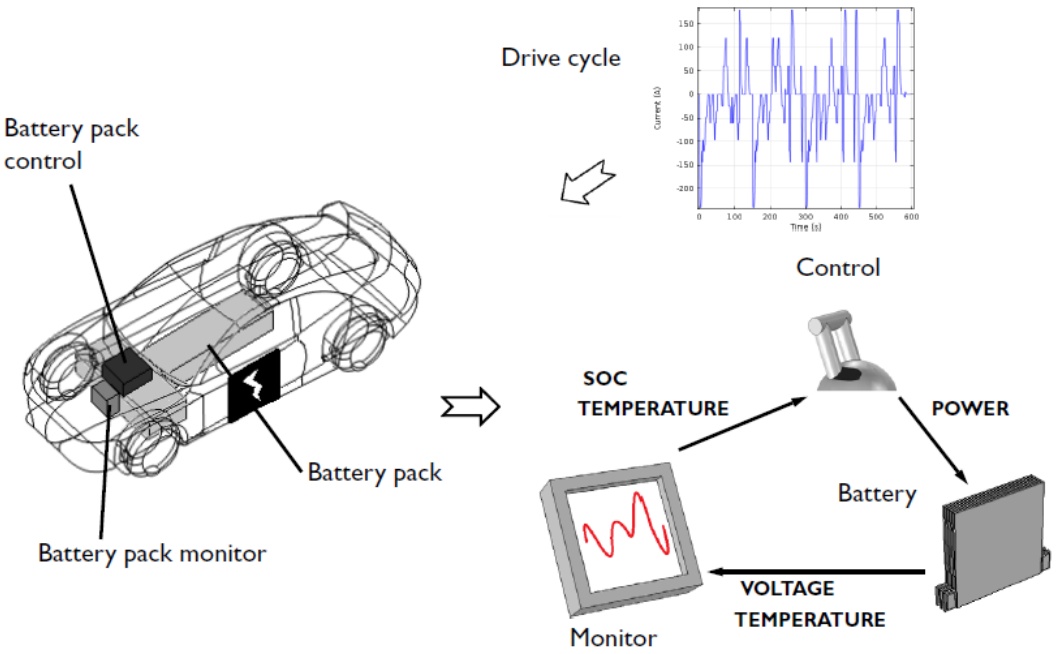

Figure 55 EV BMS system (Comsol) [55]

The model takes into account several physical and is able compute properties being difficult to measure such as each electrode's SOC, more precise cell SOC, internal resistance, polarization effects and local temperatures [55]. The battery is composed of a positive porous electrode having an active material ($LiMn_2O_4$), of a negative porous electrode having an active material (graphite MCMB Li_xC_6) and of an electrolyte $LiPF_6$ [55]. The model takes into consideration conduction in the electrodes, ionic charge transport phenomena, ionic conductivity and overpotential concentrations, mass transport inside spherical particles form by the electrodes and Butler – Volmer kinetics derived from experimental measurements [55].

The one – dimensional geometry represents a flat prismatic battery in which the heat transfer is unidirectional. In addition, the thermal insulation is set as the leftmost boundary and as the battery center, whereas the convective heat flux is set as the rightmost boundary condition and as the battery surface [55]. The heat transfer coefficient being equal to 10 W/m^2K is close to a cell being passively air – cooled. The driving cycle of the HEV is a typical driving cycle having C-rates up to 20 C while 1 C = 12 A. The initial cell voltage is approximately 3.9 V and the values of the cell voltage depend on the SOC [55].

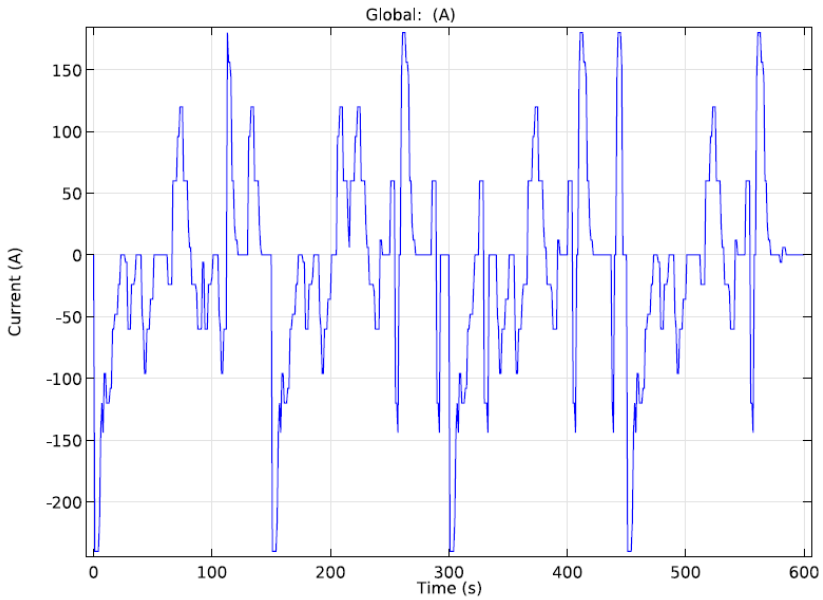

Figure 56 Typical HEV driving cycle - Comsol [55]

2.17 Lithium – ion battery capacity fade model in Comsol Multiphysics

Capacity loss in lithium – ion in batteries during a load cycle can be attributed to side reactions and degradation. Various effects being dependent on the current direction, on the temperature, on concentrations and on the potential take place during a battery load cycle [55]. A battery cell model is employed in Comsol to study those effects [55]. Apart from the basic graphite – lithium intercalation reaction occurring on negative electrode, a parasitic lithium - solvent redox reaction is involved in the model ($S + 2Li^+ + 2e^-$ -> P), where S is the ethylene carbonate and P stand for the product of the reaction. This reaction mainly takes place during the battery charging due to the expansion of the graphite particle owing to intercalation bringing the graphite surface in contact with the electrolyte, whereas during

charging the Solid Electrolyte Interphase (SEI) layer is formed [55]. The product P is translated into lithium losses in the battery and into the increase in the SEI layer resistance. The kinetics of the parasitic reaction is given by the current density in A/m^2 on the particle surface equation.

$$i_{loc} = -i_o \frac{c_{Li+}}{c_{Li+,ref}} e^{\frac{-0.5Fn}{RT}} \qquad (2.17.1)$$

The exchange current density i_o equals 10^{-3} A/m^2 in case lithium intercalates into negative electrode particles and zero during discharging.

The thickness of the SEI layer is given by equation (3.1.32) and the SEI layer resistance in Ωm^2 in the negative electrode is given by equation (3.1.33).

$$\frac{d\delta_{film}}{dt} = -\frac{i_{loc} M_p}{2F\rho_p} \qquad (2.17.2)$$

$$R_{film} = \frac{\delta_{film}}{\kappa} \qquad (2.17.3)$$

The battery cycle consists of the stages below [55]:

- Open circuit for 1 s.
- Constant current discharge at 1 C-rate until cell voltage becomes lower than 3.1 V.
- Constant voltage discharge until the current density becomes lower 0.1 A/m^2.
- Constant current charge at 1 C-rate until cell voltages becomes higher than 4.1 V.
- Constant voltage charge at 4.1 V until the current density becomes lower than 0.1 A/m^2.
- Open circuit until load time cycle equals three hours.

2.18 Liquid – Cooled Li–on Battery Pack model in Comsol Multiphysics

This model is utilized for simulating the temperature profile in a liquid – cooled battery pack and it provides a 3D solution during a load cycle, while an one – dimensional electrochemical lithium – ion battery model calculates the average heat source [55]. On the one hand it is assumed that the material properties can be computed by means of battery pack's average battery provided that the battery pack temperature does not significantly vary, and on the other hand the changes of the heat generated during a cycle occur considerably slower than the heat transfer though the battery pack, which means that the

heat balance is considered quasi – stationary for the given battery acting as a heat source at a specific operational point during the cycle [55].

The battery temperature is assumed to be the same with the cooling fluid inlet temperature, while the C-rate equals 7.5. The Laminar Flow interface is utilized for solving the velocity and pressure fields within the channels and the Heat Transfer interface is utilized for solving the temperature fields [55].

The battery pack is composed of a cooling fin with channels and with one cell on each side as illustrated in the figure following. The thickness of each cooling fin and of each battery cell equals 2 mm Liquid – Cooled Li–on Battery Pack model in Comsol Multiphysics.

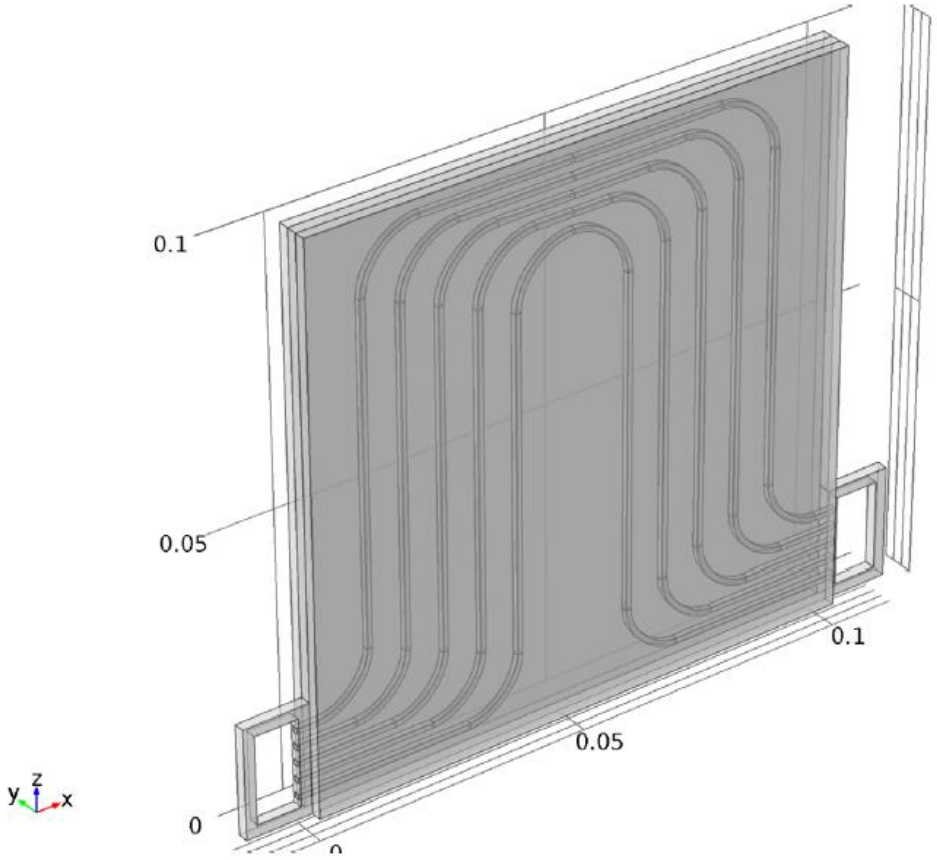

Figure 57 Two prismatic battery cells on each side of a cooling fin plate with five channels (Liquid – Cooled Li-on Battery Pack model in Comsol Multiphysics) [55] .

The battery pack geometry is composed of 3 stacked cells and 2 connector channels one of which is located at the inlet and the second is located at the outlet of the cooling fins [55].

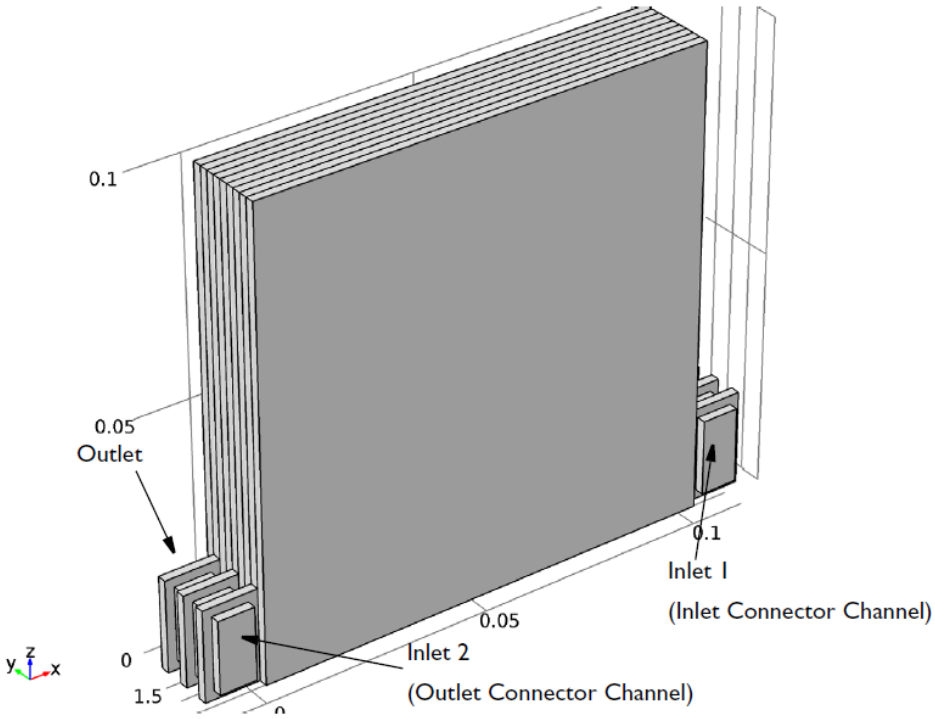

Figure 58 Battery pack geometry (Liquid – Cooled Li-on Battery Pack model in Comsol Multiphysics) [55]

The geometry has two inlets because it represents the last cells of a larger battery pack. The cooling liquid enters inlet 1, whereas the cooling liquid having passed through the cooling fins of the previous cells enters inlet 2 [55]. The modeled cooling fins are assumed to be 3, the pack fins equal to 50 and the average flow equal to 0.5 cm^3/s. The inlet flows, the approximate laminar velocity profile and the inflow velocities are given by equations (2.18.1), (2.18.2), (2.18.3), (2.18.4) and (2.18.5), respectively.

$$\dot{Q}_{\text{inlet 1}} = N_{\text{fins, model}}\dot{Q}_{\text{fin}} \qquad (2.18.1)$$

$$\dot{Q}_{\text{inlet 2}} = (N_{\text{fins, pack}} - N_{\text{fins, model}})\dot{Q}_{\text{fin}} \qquad (2.18.2)$$

$$v_{\text{profile}}(s_1, s_2) = 36 \cdot s_1(1-s_1)s_2(1-s_2) \qquad (2.18.3)$$

$$v_{\text{inlet 1}} = v_{\text{profile}} \dot{Q}_{\text{inlet 1}} / A \qquad (2.18.4)$$

$$v_{\text{inlet 2}} = v_{\text{profile}} \dot{Q}_{\text{inlet 2}} / A \qquad (2.18.5)$$

Where A is the cross – sectional area in m^2 of the connectors channels and s_1 and s_2 are surface parameters.

As to the thermal conductivities of the cells on the xz – plane, they are described by equations (2.18.6) – (2.18.9) [55].

$$k_{T,x} = \frac{\sum L_i k_{T,i}}{\sum L_i} \qquad (2.18.6)$$

$$k_{T,y} = \frac{\sum L_i}{\sum L_i / k_{T,i}} \qquad (2.18.7)$$

$$k_{T,z} = \frac{\sum L_i k_{T,i}}{\sum L_i} \qquad (2.18.8)$$

Where L_i represent the thicknesses of the cell different layer and $k_{T,I}$ the thermal conductivities of the corresponding materials.

Concerning the boundary conditions, the temperature at inlet 1 is set to be 310 K, while the heat flux at inlet 2 is expressed by equation (2.18.9).

$$q_0 = 2Q_h(N_{\text{fins, pack}} - N_{\text{fins, model}})V_{\text{batt}} \cdot 0.99 \qquad (2.18.9)$$

Where Q_h is the average heat generated by the battery, V_{batt} is the volume of each cell, constant 2 represents the two cell per fin and 0.99 is due to the fact that 1% heat losses to the surroundings before the liquid enters the collector are assumed [55]. A heat transfer coefficient of 1 W / m^2K, which represents poor insulation, is also assumed.

3. Simulations

3.1 Overview of cases examined

The cases examined, the models employed, the parameters studied as well as the causes, the effects and the purposes of each simulation are tabulated below.

Table 10 Overview of cases examined

Case	Model	Parameter	Purpose	Cause	Effect
1	ANSYS Fluent ECM	-	Visualization of fundamental physical quantities of a typical Li-ion battery cell for EVs	-	-
	Simulink 1 RC branch model	Discharge current pulse	Study of discharge current on temperature variation and SOC of a lithium – ion battery cell	I.50% increase II.50% decrease III.Variable pulse	I.7 K temperature variation, zero SOC before the end of the simulation II.1 K temperature variation, SOC becomes half at the end III. 6 K temperature variation, SOC becomes 5% at the end
	Simulink 2 RC branches model	Discharge current pulse	Comparison of the results with those of 1 RC branch model	I.50% increase II.50% decrease III.Variable pulse	Higher temperature variations, SOC decreases faster
	Comsol Multiphysics lithium – ion	-	Study of DoD distribution as a function of discharge time in	-	-

	battery cell model		the positive electrode		
2	Simulink lithium – ion temperature dependent battery model	Ambient temperature	Determination of ambient temperature effects on the lithium – ion battery	I.Decrease in ambient temperature II.Increase in ambient temperature	I.Decrease in voltage and SOC during discharging II.Stabilization of SOC during discharging
3	Simulink lithium - ion battery model with fault	Capacity, OCV, Cell resistance	Study of internal fault in lithium – ion battery	I.Capacity reduction II.OCV reduction III.Increase in cell resistance	I. Decrease in the SOC ripple of healthy cells II.No effect III.Cell temperature increase
4	Battery 3d thermal model in Comsol Multiphysics	Inlet air velocity, C-factor, battery radius, reaction rate coefficient	Study of the parameters' effects on the lithium – ion battery	I.Increase in the inlet air velocity II.C-factor decrease III.Increase in the battery radius IV.Doubling of the reaction rate coefficient	I.Battery surface temperature and average temperature reduction II.Voltage reduction,more thermally stable battery III.Lower or higher surface temperature, significantly higher temperature variations, no specific temperature profile trend IV.Surface temperature reduction by 25 K, no change in the temperature profile
5	Electric vehicle model with VCU in LMS Imaginelab	Maximum braking torque, electric motor rotary speed threshold to	Study of parameters determining driver's experience during braking in a EV	I.Increase in the maximum braking torque II.Increase in the electric motor rotary speed threshold to	I.Deviation of the vehicle speed and the braking command from the corresponding reference values II.Fitting of vehicle speed and braking

		regenerate battery		regenerate battery	command curves with corresponding reference curves
6	Electric vehicle model with SCU in LMS ImagineLab	Lithium – ion element nominal capacity	Study of SCU behavior and capacity effects on the EV response in cold environment	I.Increase in element nominal capacity	I.Meeting driver's demands more accurately
7	Battery pack air – cooling model in LMS ImagineLab	Battery load, air flow rate, cell density, SOC	Study of different parameters' effect on the lithium – ion cell temperature	I.Increase in the battery load II.Doubling of the air flow rate III.Doubling of the cell density IV.Increase in the SOC	I.Cell temperature reaching the upper limit faster, fan being not sufficiently efficient II.More efficient heat dissipation III.Temperature decrease becomes slower, fan functions for a longer period IV.No temperature effect, faster charging – discharging transition
8	EV battery aging model in LMS ImagineLab	Nominal cell capacity	Comparison of an old and a new lithium – ion battery	I.Decrease of nominal cell capacity from 2.3 Ah to 1.9 Ah	I.Vehicle's autonomy fade from 60 to 48 km II.Higher internal resistance, higher battery temperature due to Joule effect III.Faster OCV decrease IV.Lower diffusion resistance for low SOC values
9	Model for evaluating charging with		Evaluating charging strategies based on chemistries	I.1000 and 10000 cells	I."Just in time" best charging strategy for both battery chemistries and for 1000 cells

	respect to aging in LMS ImagineLab	Battery chemistry, number of cells	and on the cell number of EV lithium – ion battery for achieving the least capacity loss	II.High power LFP-C and NCA-C batteries	II."Charge when you can" best charging strategy for both chemistries and for 10000 cells III.Best charging strategy based on capacity loss depends on the battery chemistry IV.Best charging strategy based on aging phenomena depends on the battery chemistry
10	Energy and power storage system model in LMS ImagineLab	SOC	Evaluation of lithium – ion battery – supercapacitor system response to Formula – E load	I.Addition of circuit breaker to the system	I.Increase of supercapacitor's SOC from 78% to 89%, decrease of battery's SOC from 48% to 46%, mitigation of transitional phenomena
11	SCU based on look - up table model in LMS ImagineLab	Ambient temperature, initial SOC	Study of ambient temperature and initial SOC effects on battery cell load and voltage response with and without SCU	-	-
12	Lithium – ion battery response to HEV driving cycles in Comsol Multiphysics	Battery heat capacity, battery density, battery thermal conductivity, initial cell voltage	Study of lithium – ion battery response during HEV driving cycles	I.20% increase of positive electrode thickness and positive electrode heat capacity II.20% increase of positive electrode density III.20% increase of cell thickness IV.Increase of initial cell	I.II.III.Minor changes in the cell voltage, polarization curve, no significant response changes IV.Improved battery performance, extension of battery's lifespan, thermal runaway risk reduction

				voltage from 3.9 to 4.5 V	
13	Lithium – ion battery capacity fade model in Comsol Multiphysics	Density of the product of the side reaction	Study of lithium – solvent parasitic redox reaction	I.Increase in the density of the product of the side reaction (30%)	I.Increase in the potential drops by 0.01 V, potential drops not being uniform over the depth of the electrode
14	Liquid – Cooled Li–on Battery Pack model in Comsol Multiphysics	Cooling flow per fin and x,z-axis battery thermal conductivity	Study of a liquid – cooled lithium – ion battery	I.Doubling of cooling flow per fin II.Doubling of x,z – axis thermal conductivity III. Doubling of the electrolyte salt concentration IV.Cooling flow per fin quadruplication	I. Battery surface temperature decreased by 1.5 K, the temperature gradient at the corner near the inlet slightly decreased II. No significant impact on the simulation results, minor changes in the battery surface temperature distribution III. Cooling fluid and battery surface temperature increase by 2 – 2.5 K, more uniform temperature distribution IV.Battery surface temperature decrease by 2 K, uniform temperature distribution

3.2 Cases examined

3.2.1 Case 1 : Lithium – ion battery cell simulation

The purpose of the simulation is to study the behavior of the fundamental component of the lithium – ion battery cell for EVs. A typical lithium – ion battery cell for electric vehicles has a capacity of 4.1 Ah, a nominal voltage of 3.65 V and dimensions equal to 290 mm x 216mm [48]. Thus the battery cell model is transformed using scaling factors 1.49 on x axis and 1.22 on y axis.

The modeling technique initially employed is the ECM simulated in ANSYS Fluent. The initial SOC and the reference capacity are set to 1 and 0.85. The materials' properties are listed in the table following. "Using polynomials" and "using different coefficients for charging and discharging" are also activated. 100 time steps with a step size equal to 30 s are executed.

Table 11 Anode/Cathode and Electrolyte material properties

	Electrodes	**Active material**
Density (kg/m^3)	8978	2092
Specific heat (J/kgK)	381	678
Thermal conductivity (W/mK)	387.6	18.2
Conductivity (S/m)	10^7	$3.541 * 10^7$

In the residuals plot UDS-0 and UDS-1 correspond to electric conductivities in the positive and negative electrodes respectively.

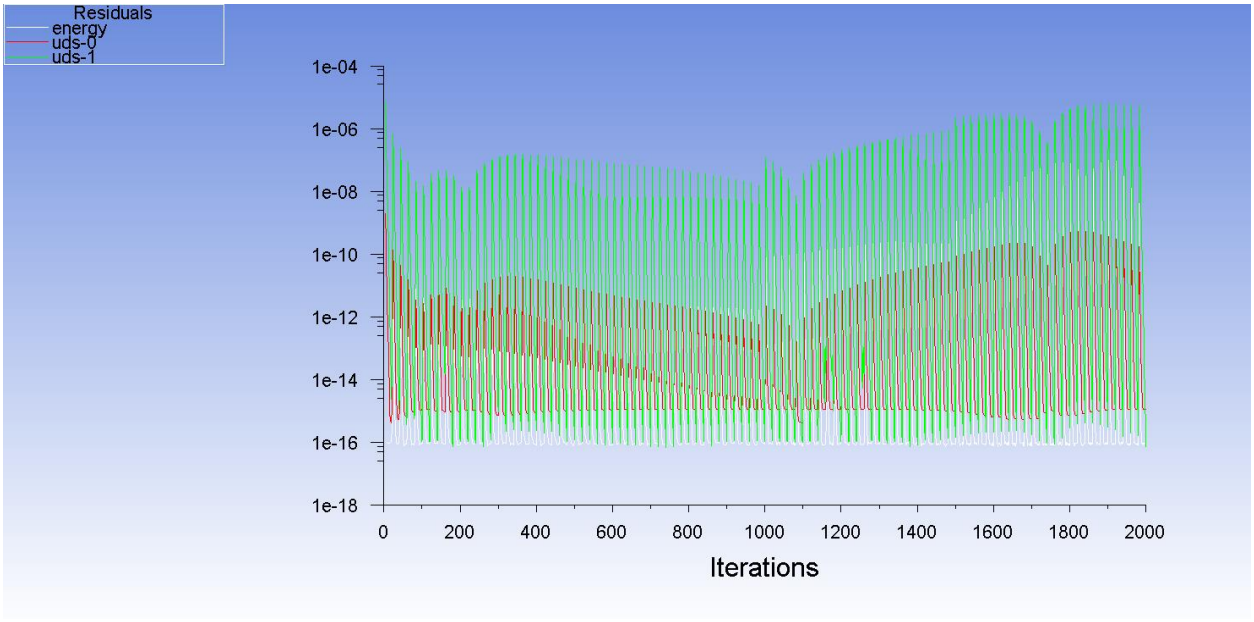

Figure 59 Residuals plot (Li-on battery cell – ECM)

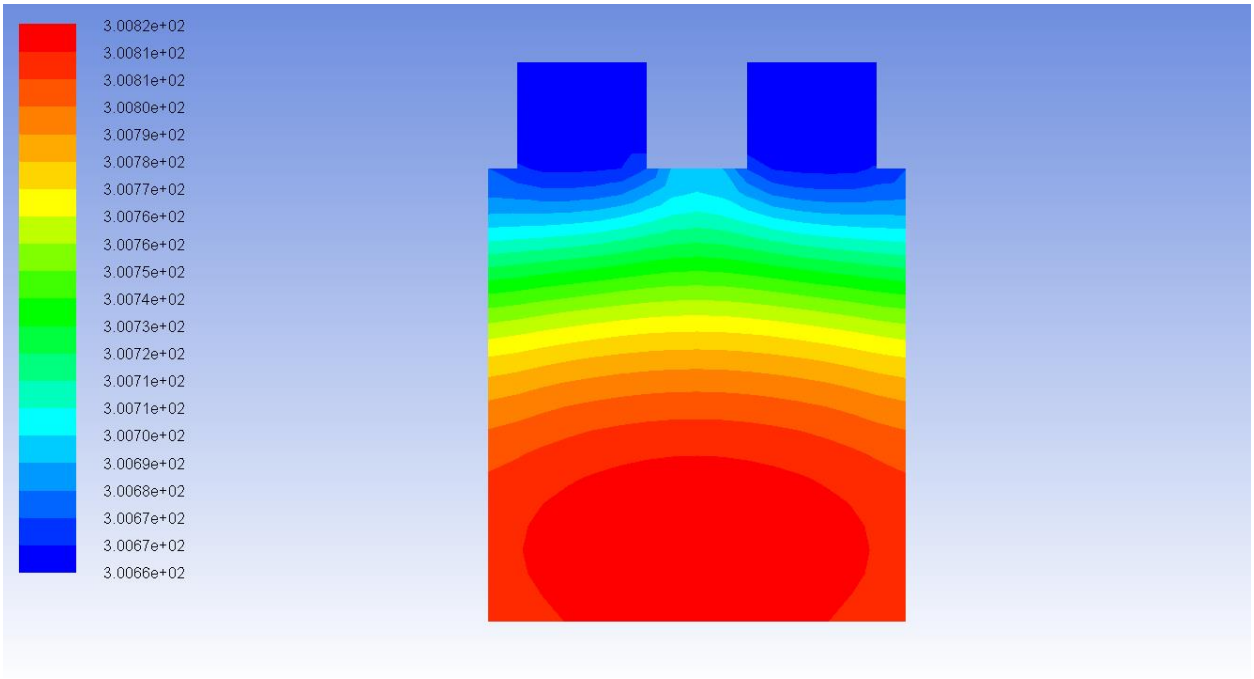

Figure 60 Static temperature (K) (Li-on battery cell – ECM)

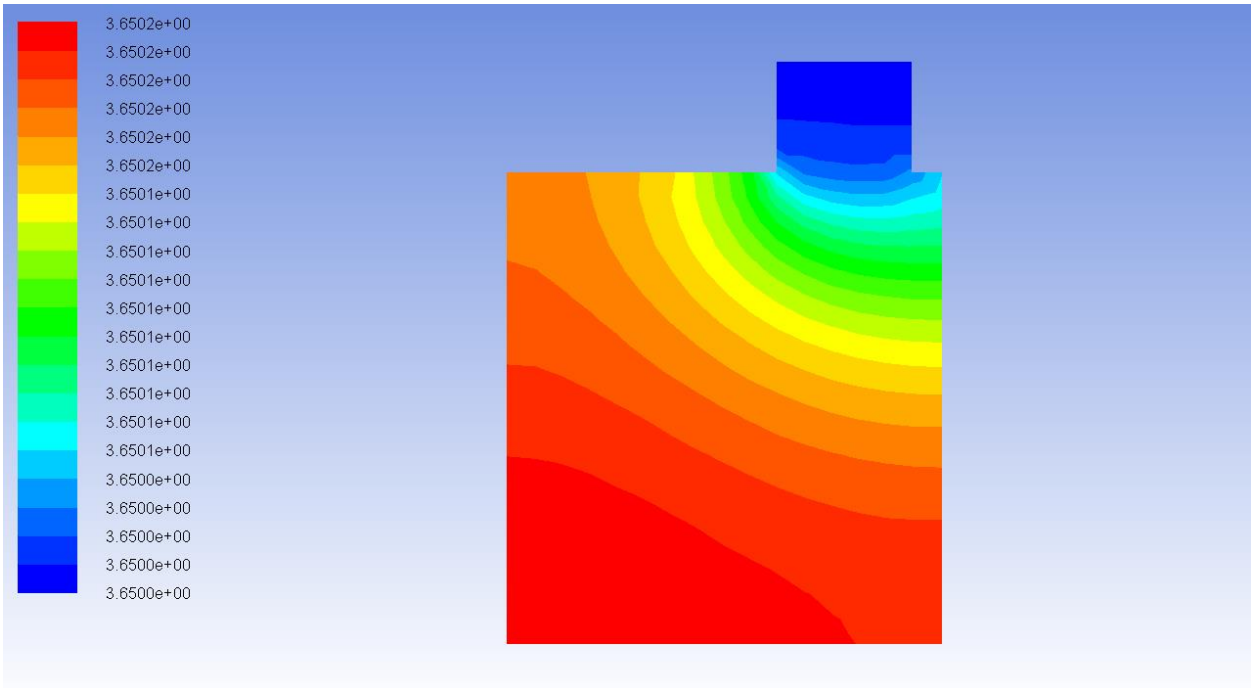

Figure 61 Positive electrode potential (V) (Li-on battery cell – ECM)

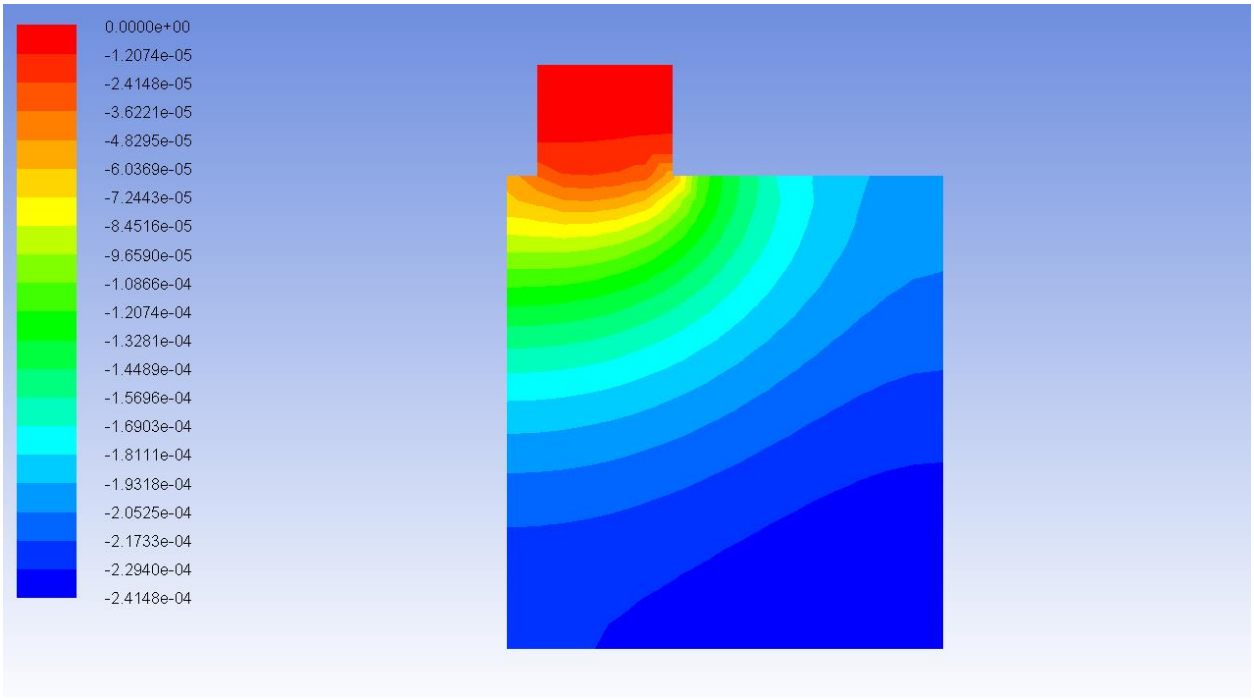

Figure 62 Negative electrode potential (V) (Li-on battery cell – ECM)

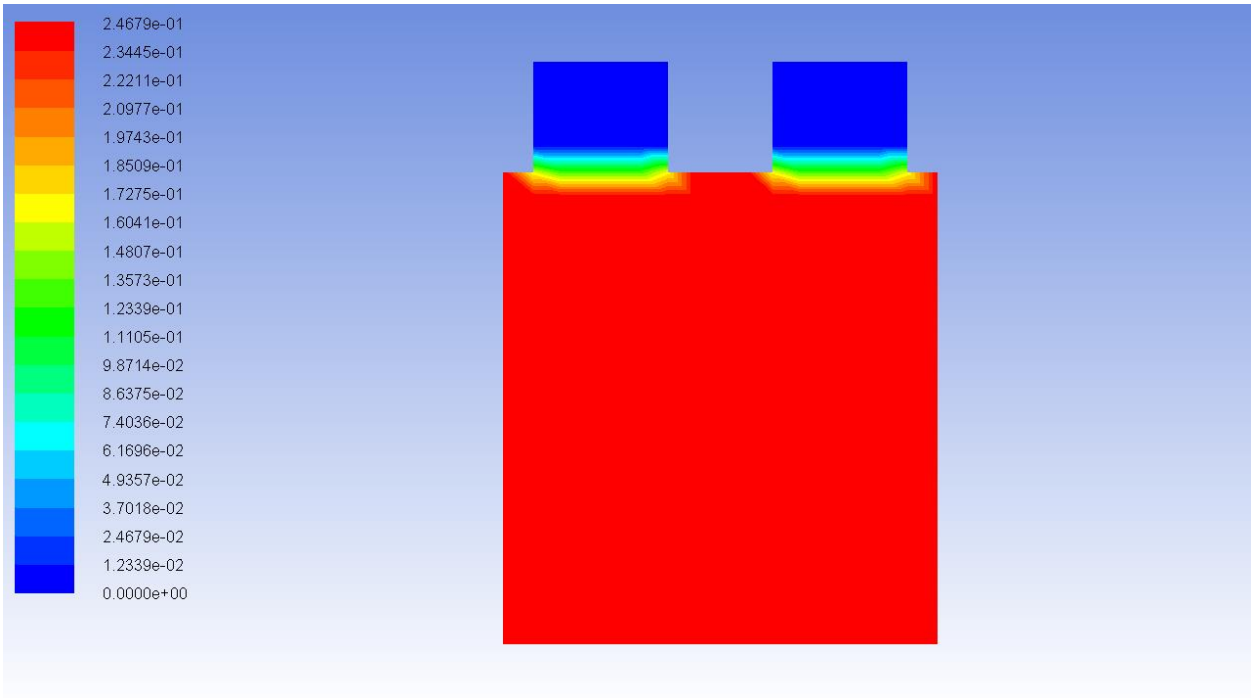

Figure 63 Transfer current density (A/m²) (Li-on battery cell – ECM)

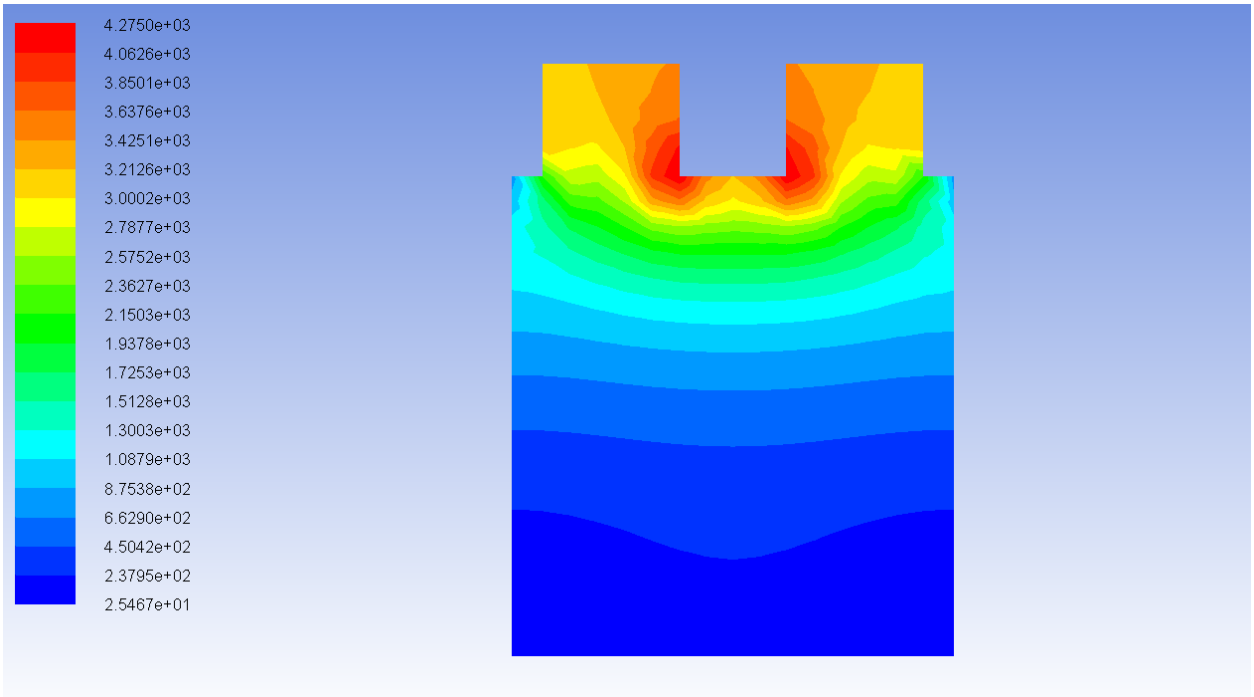

Figure 64 Current density (A/m²) (Li-on battery cell – ECM)

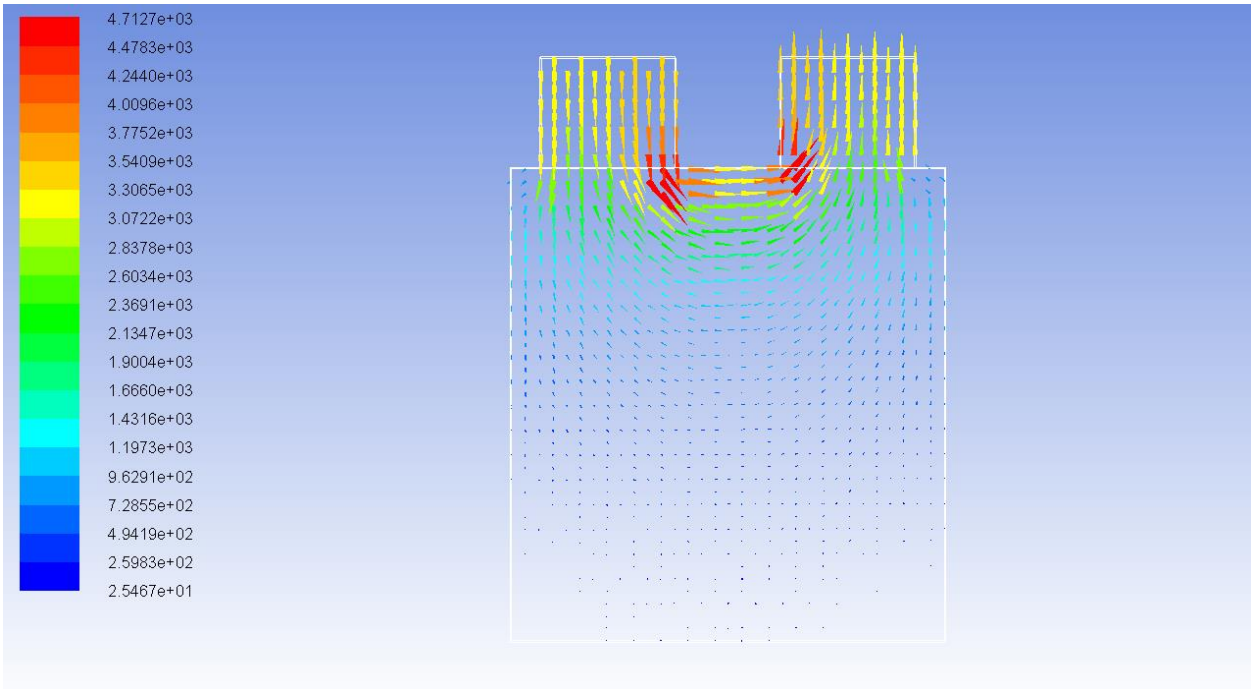

Figure 65 Current density vector plot (Li-on battery cell – ECM)

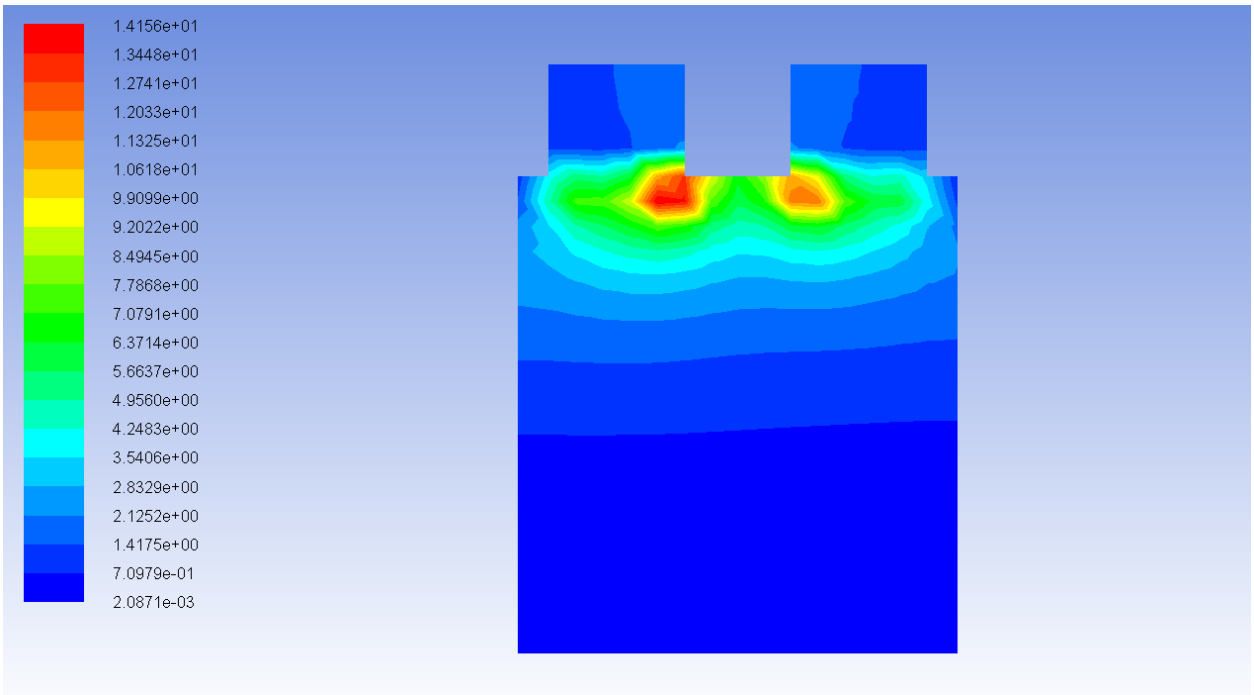

Figure 66 Joule heat source (W/m3) (Li-on battery cell – ECM)

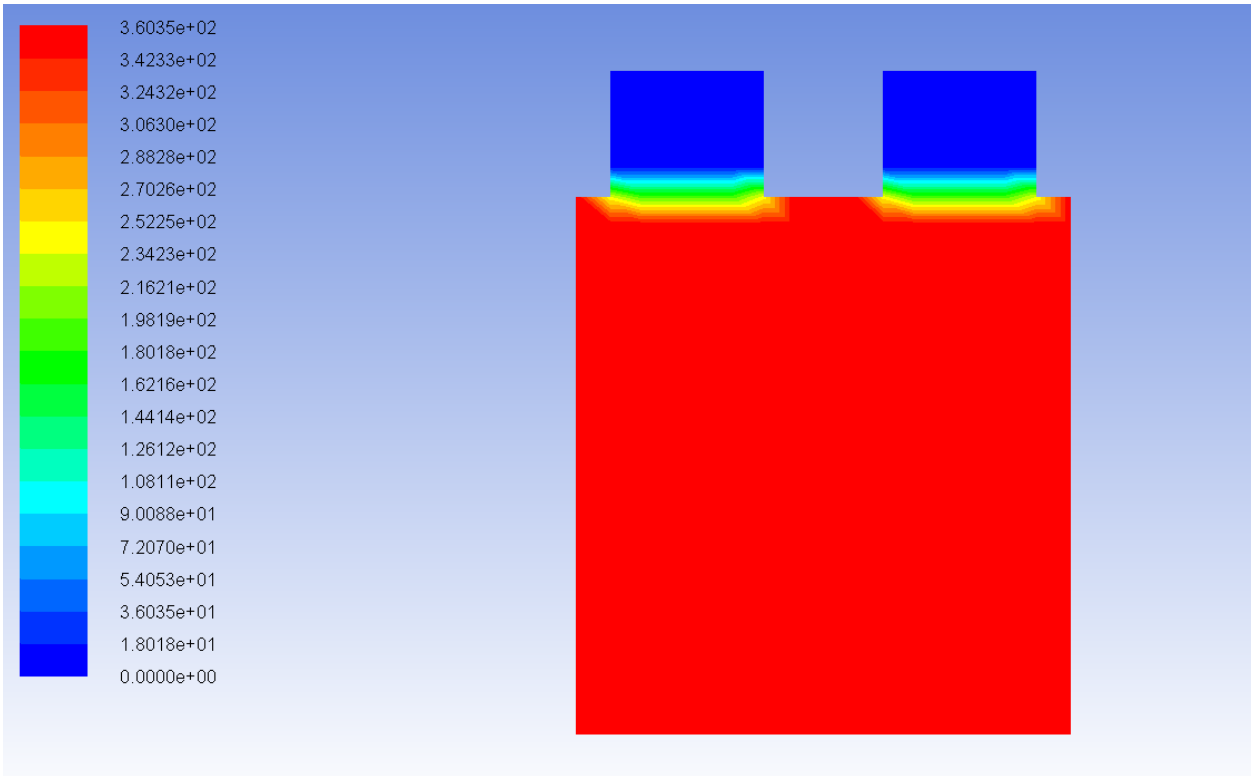

Figure 67 Electrochemical heat source (W/m3) (Li-on battery cell – ECM)

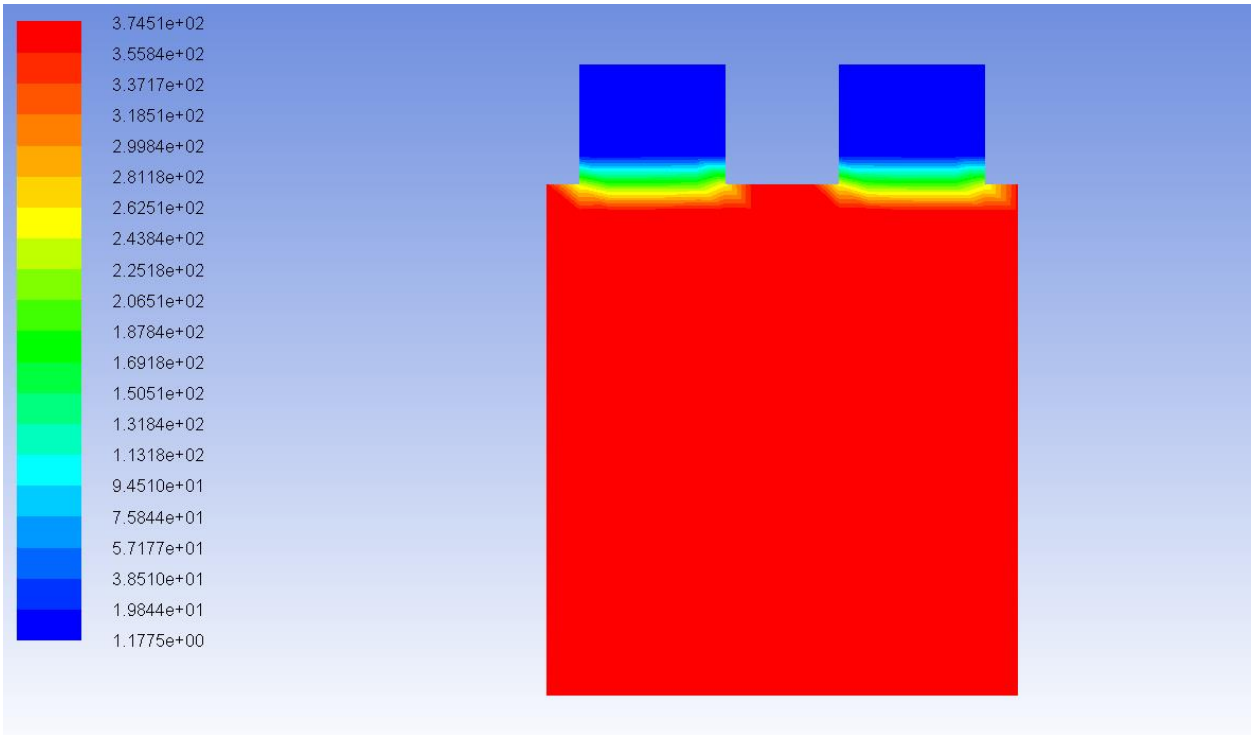

Figure 68 Total heat generation (W/m3) (Li-on battery cell – ECM)

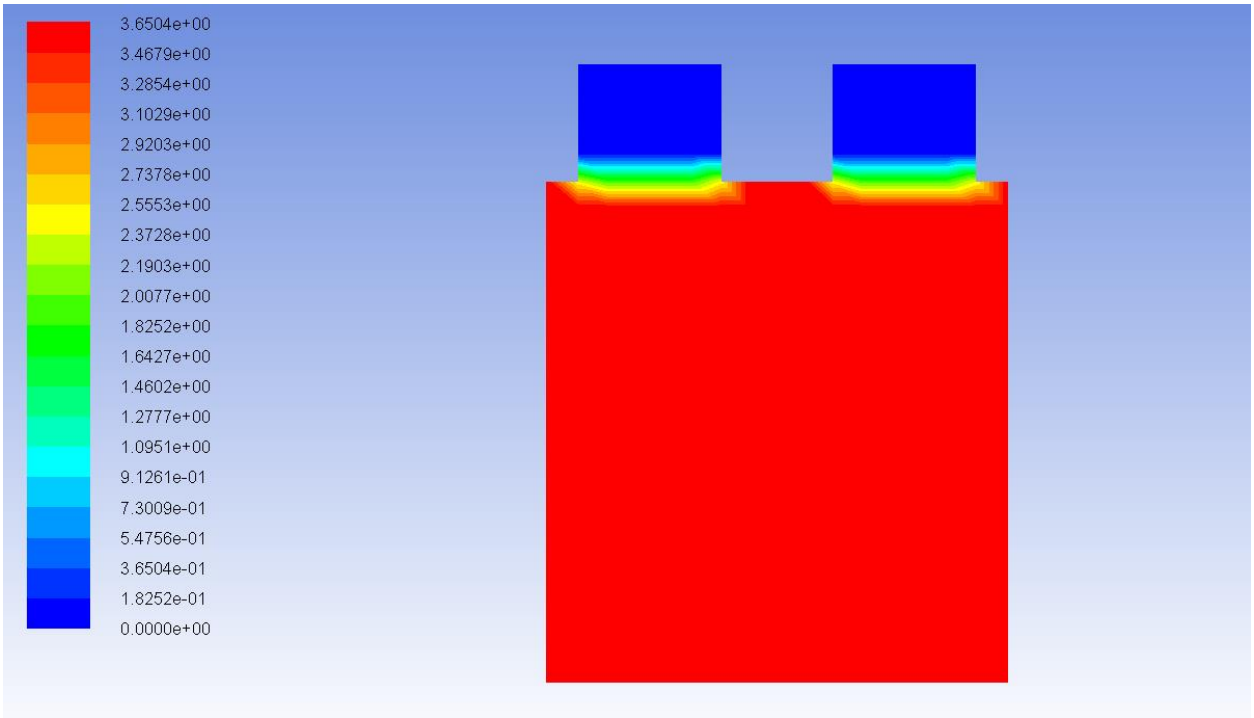

Figure 69 Battery cell voltage (V) (Li-on battery cell – ECM)

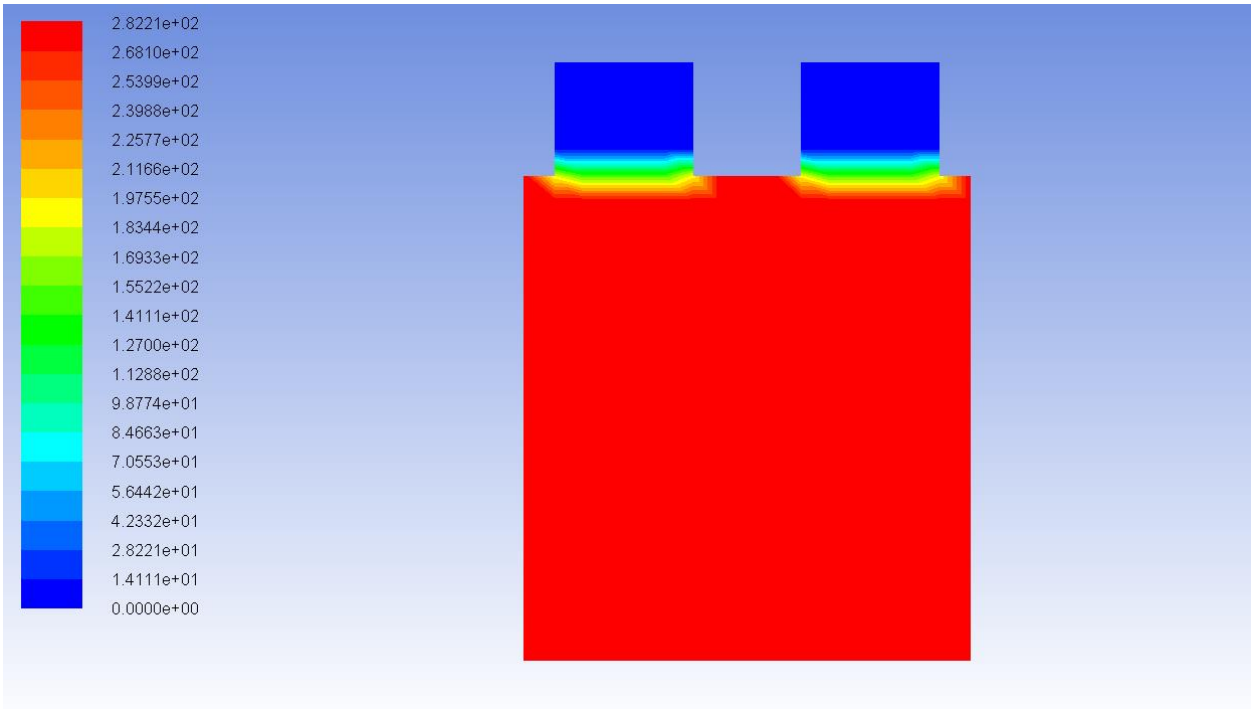

Figure 70 Activation overpotential (V) (Li-on battery cell – ECM)

Case 1 – Simulink 1 RC branch model

A lithium – ion cell rated at 31 Ah is simulated in Matlab/Simulink under 20 ^{o} C ambient temperature and a specified charge – discharge pattern using the 1 RC branch equivalent circuit model of the lithium - ion cell. Subsequently, the test data is changed such that the simulation is executed for -20 ^{o}C ambient temperature.

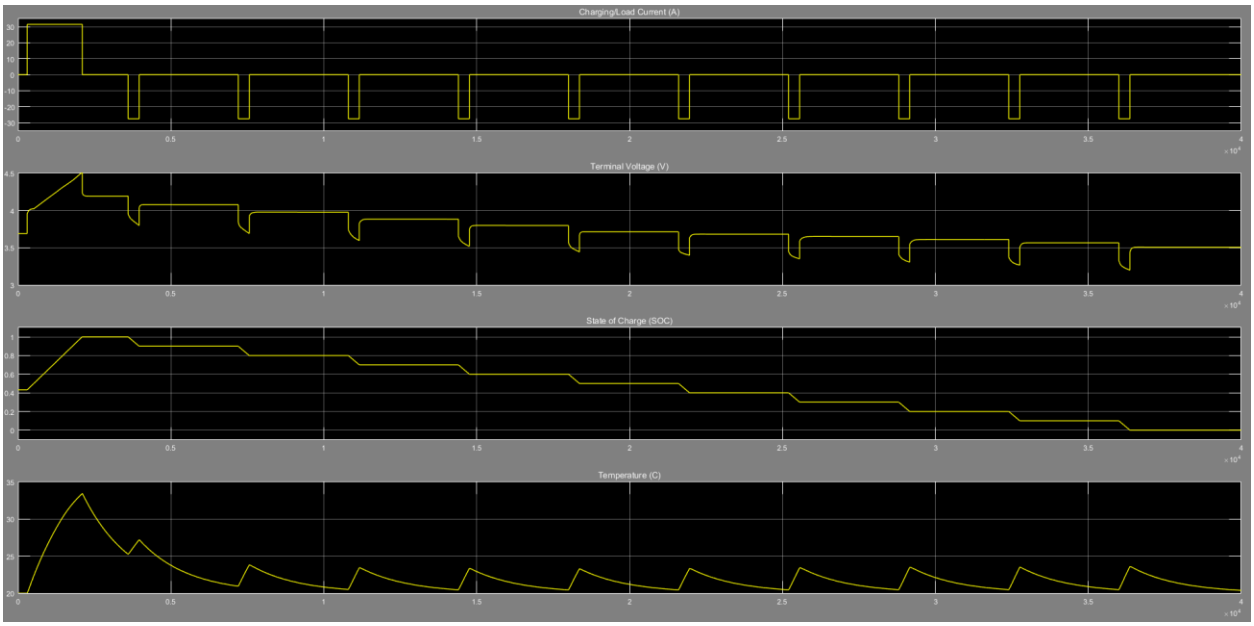

Figure 71 Lithium - ion cell simulation at 20 C ambient temperature (1 RC branch equivalent circuit model)

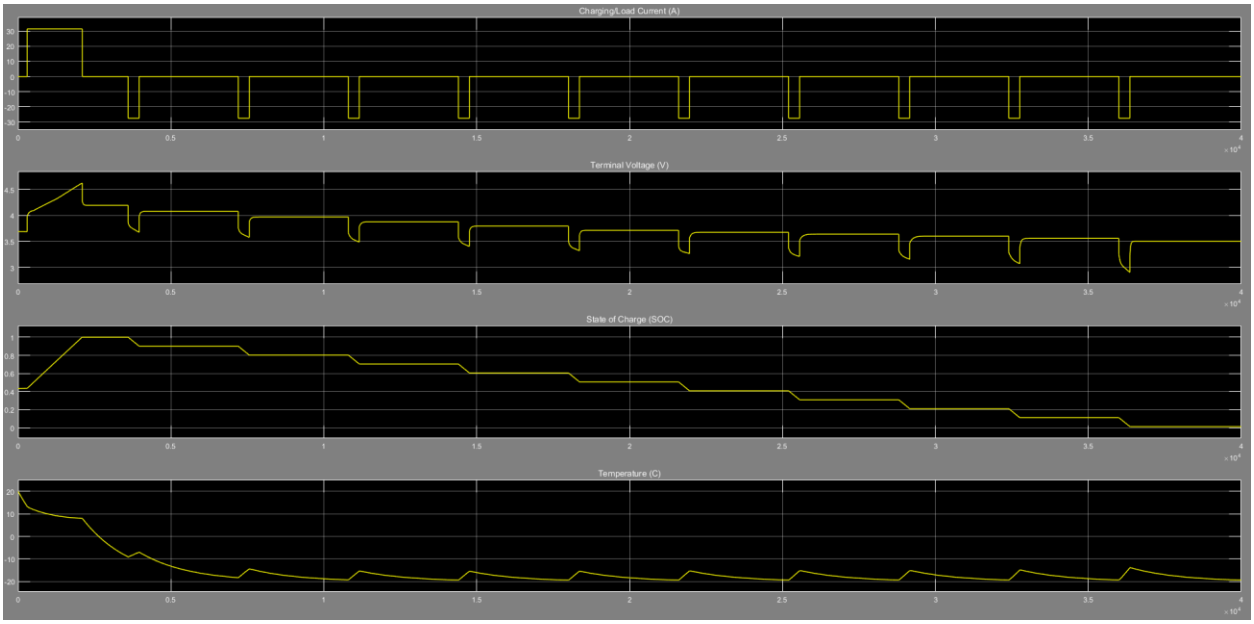

Figure 72 Lithium - ion cell simulation at -20 C ambient temperature (1 RC branch equivalent circuit model)

Under the assumption that the load is capable of being supplied with certain amount of current regardless of the battery SOC meaning that cell impedance remains constant, it is observed that the battery SOC and the terminal voltage do not depend on the ambient temperature. However, the battery model components strongly depend on both SOC and ambient temperature as shown in [50]. As suggested in [50], the investigation of the current magnitude effect as well as similar responses of battery packs are worth being studied for drawing conclusions. Thus, the effect discharge current on the lithium – ion cell parameters is examined. In all scenarios the values are taken from the capacitor (C1) output.

- **Scenario 1: Reference discharge current pulse (27.625 A)**

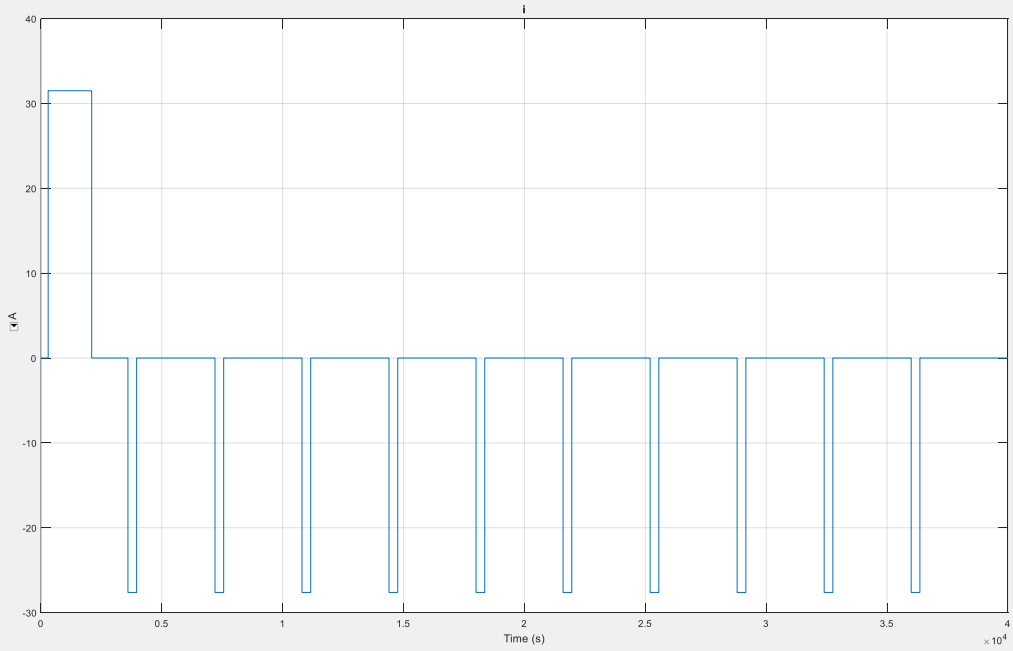

Figure 73 Scenario 1: Discharge current pulse of the lithium - ion cell (1 RC branch model)

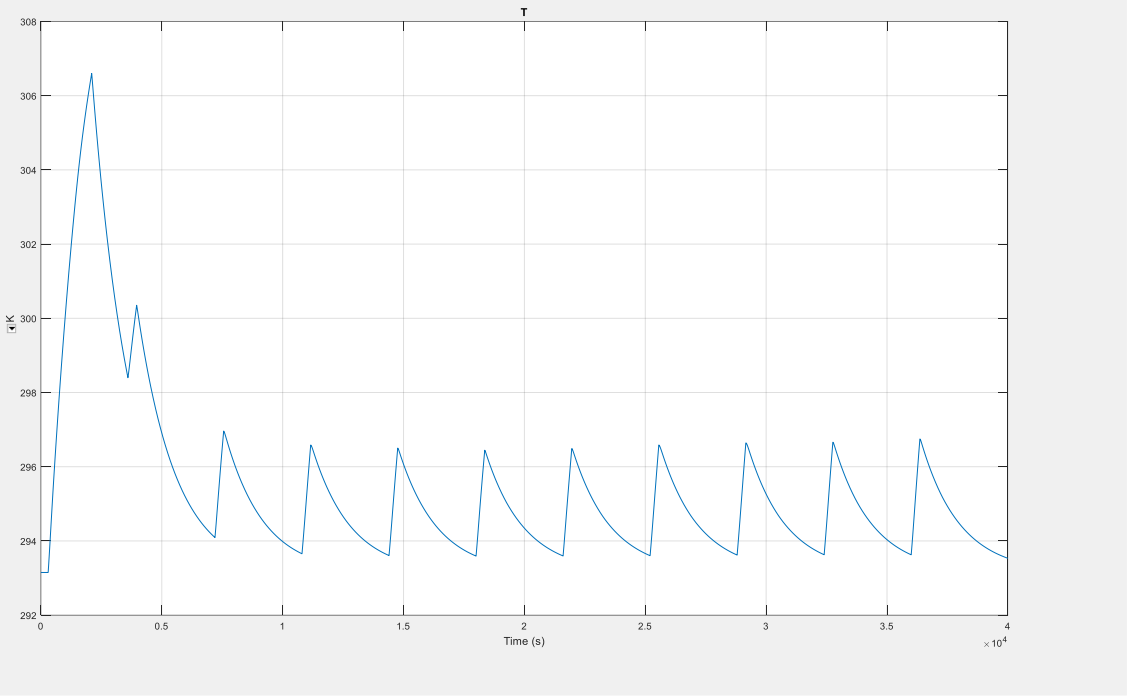

Figure 74 Scenario 1: Temperature of the lithium - ion cell (1 RC branch model)

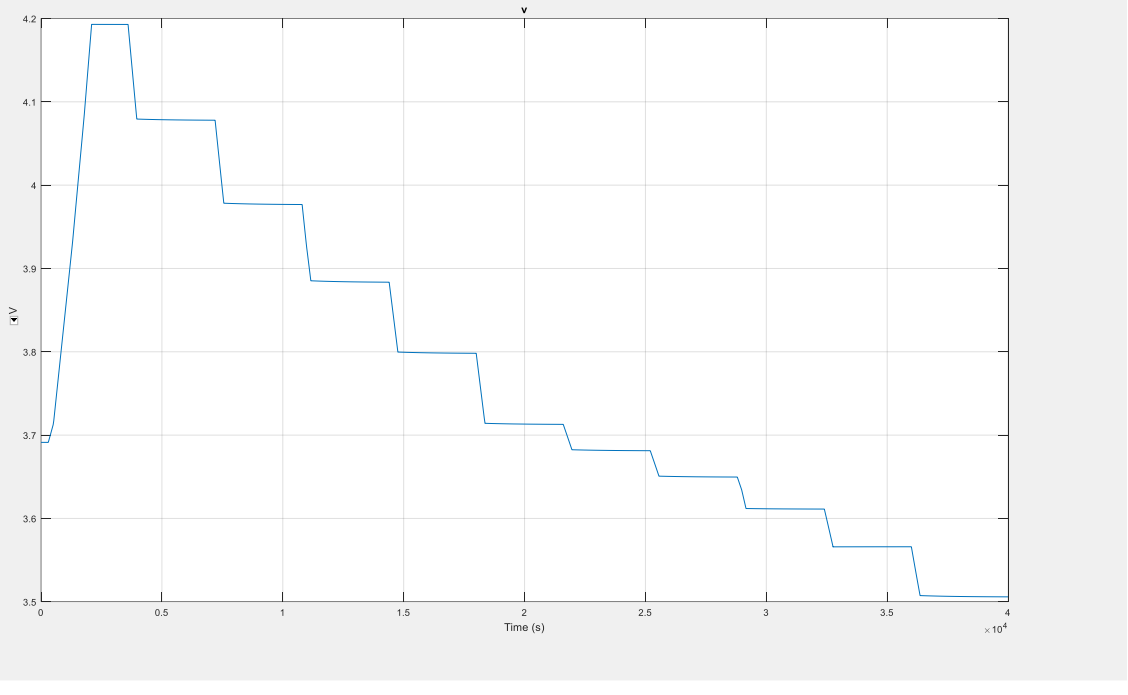

Figure 75 Scenario 1: Voltage of the lithium - ion cell (1 RC branch model)

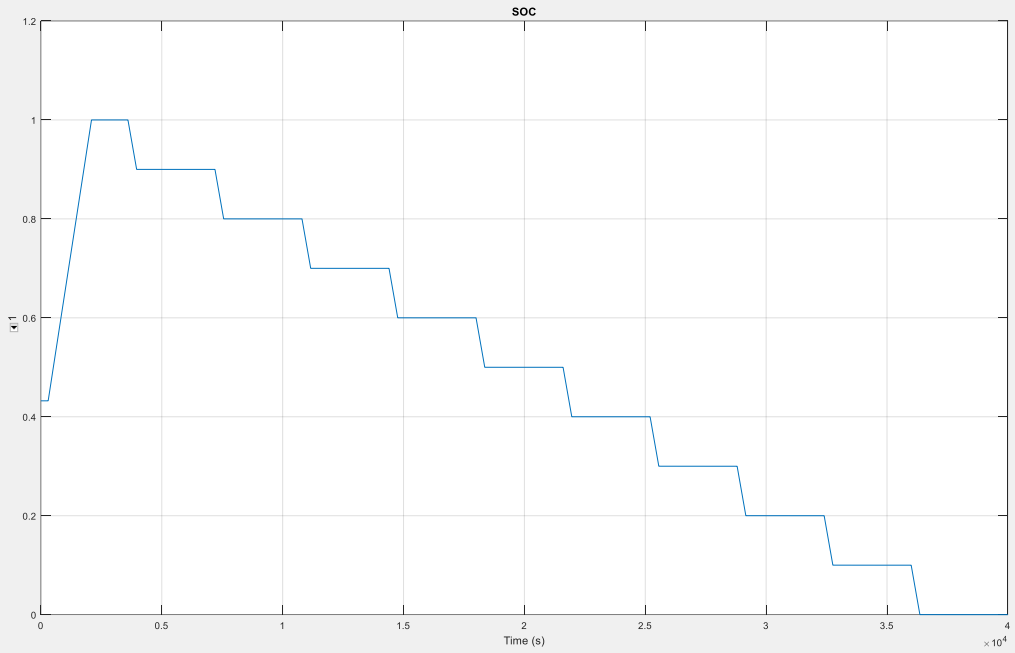

Figure 76 Scenario 1: SOC of the lithium - ion cell (1 RC branch model)

- **Scenario 2 : 40 A discharge current pulse**

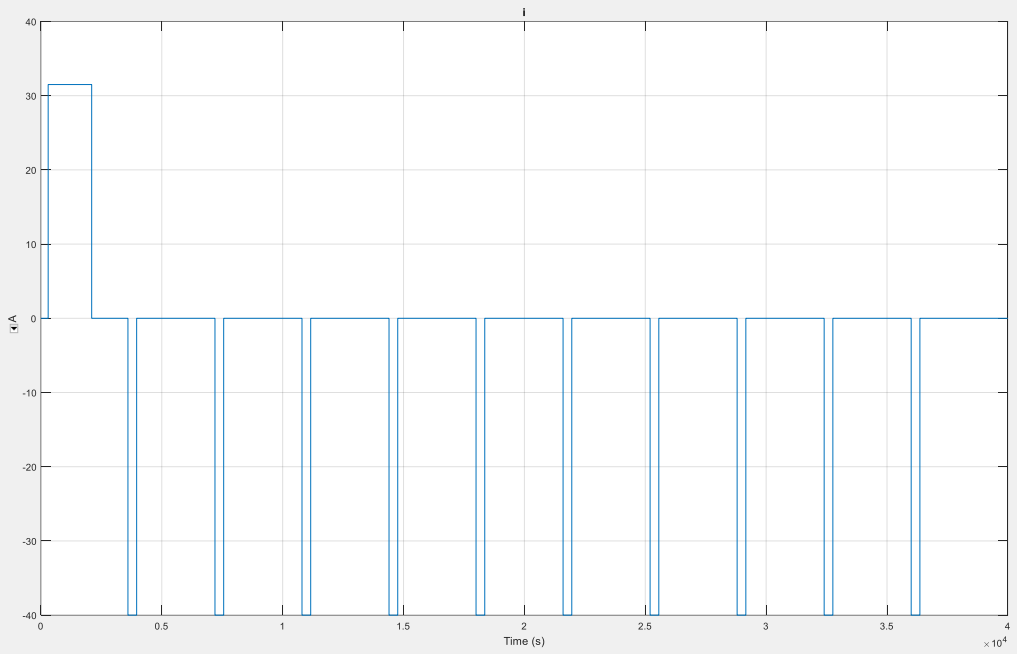

Figure 77 Scenario 2: Discharge current pulse of the lithium - ion cell (1 RC branch model)

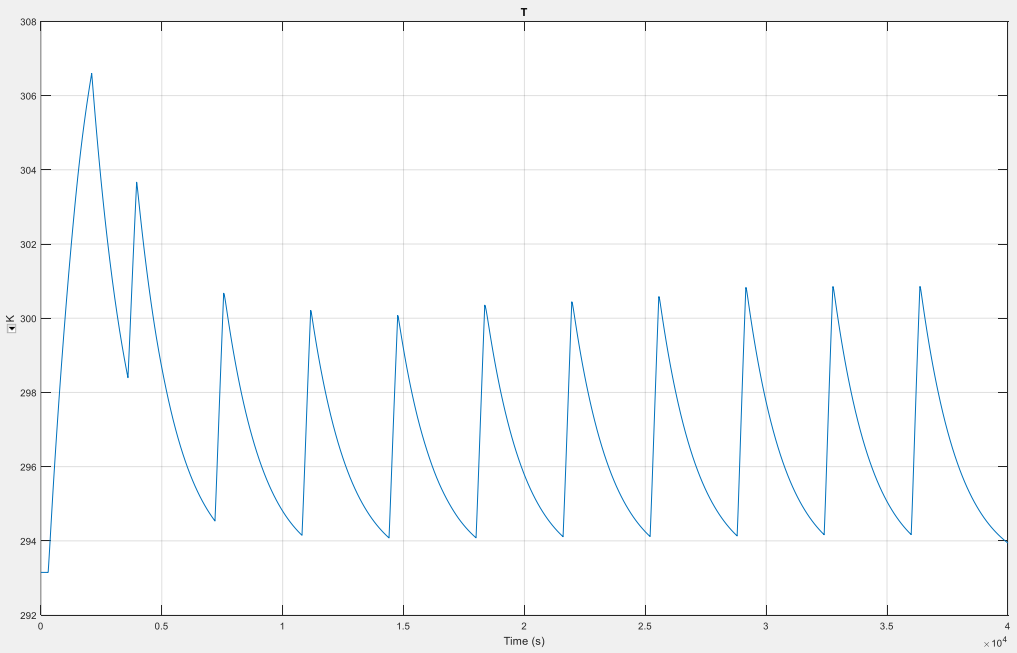

Figure 78 Scenario 2: Temperature of the lithium - ion cell (1 RC branch model)

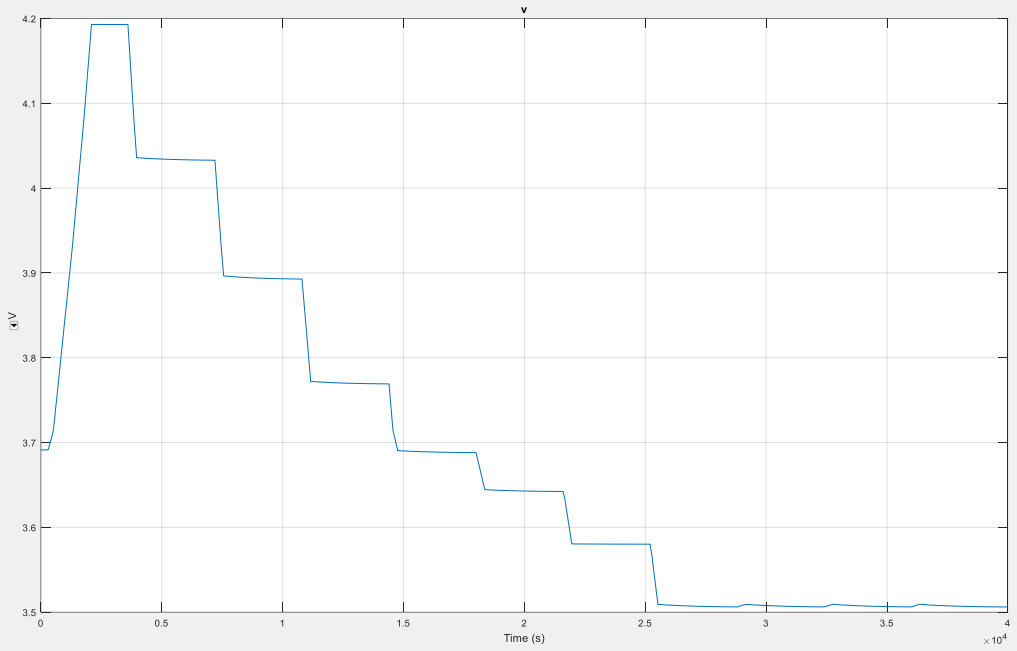

Figure 79 Scenario 2: Voltage of the lithium - ion cell (1 RC branch model)

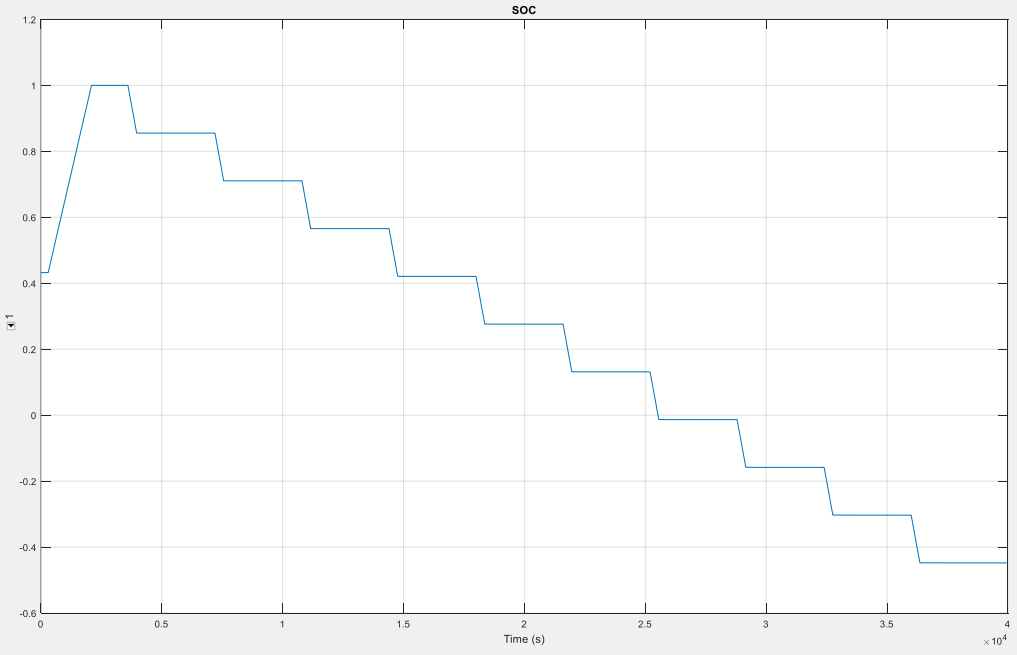

Figure 80 Scenario 2: SOC of the lithium - ion cell (1 RC branch model)

- **Scenario 3: 13.5 A discharge current pulse**

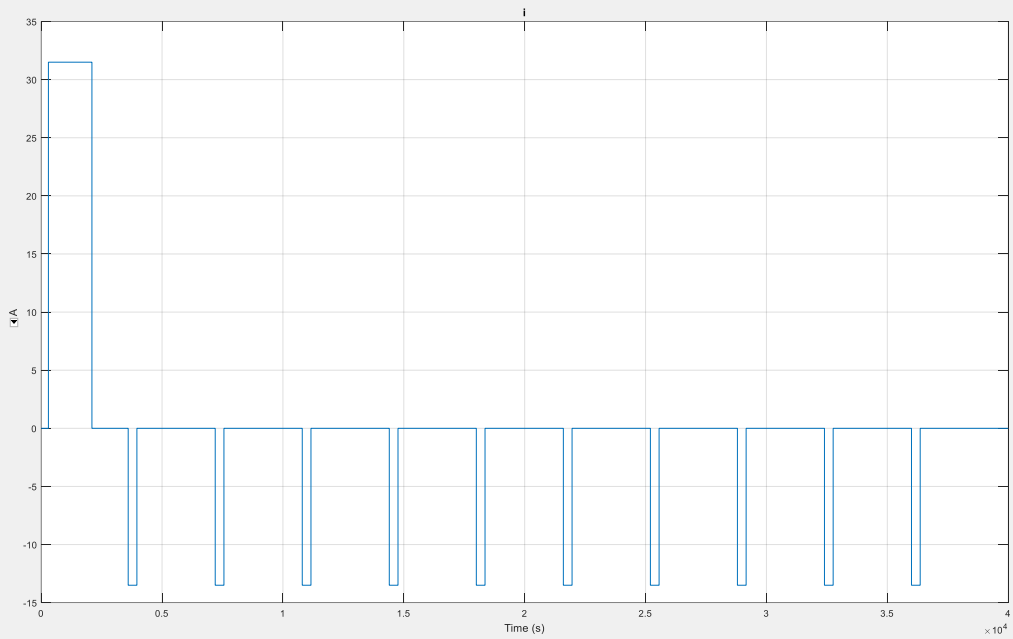

Figure 81 Scenario 3: Discharge current pulse of the lithium - ion cell (1 RC branch model)

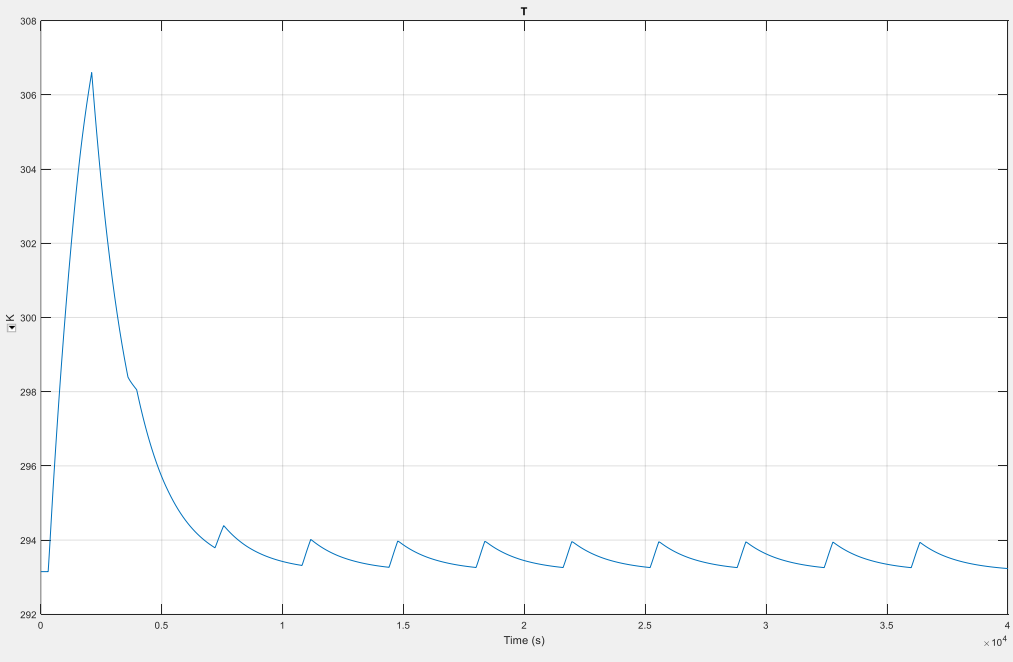

Figure 82 Scenario 3: Temperature of the lithium - ion cell (1 RC branch model)

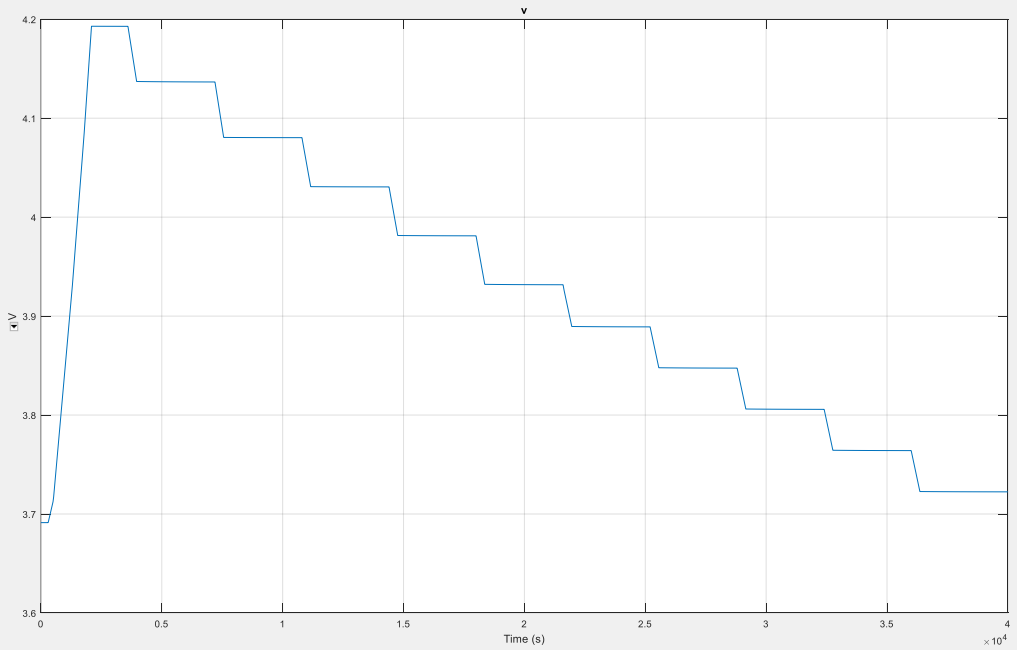

Figure 83 Scenario 3: Voltage of the lithium - ion cell (1 RC branch model)

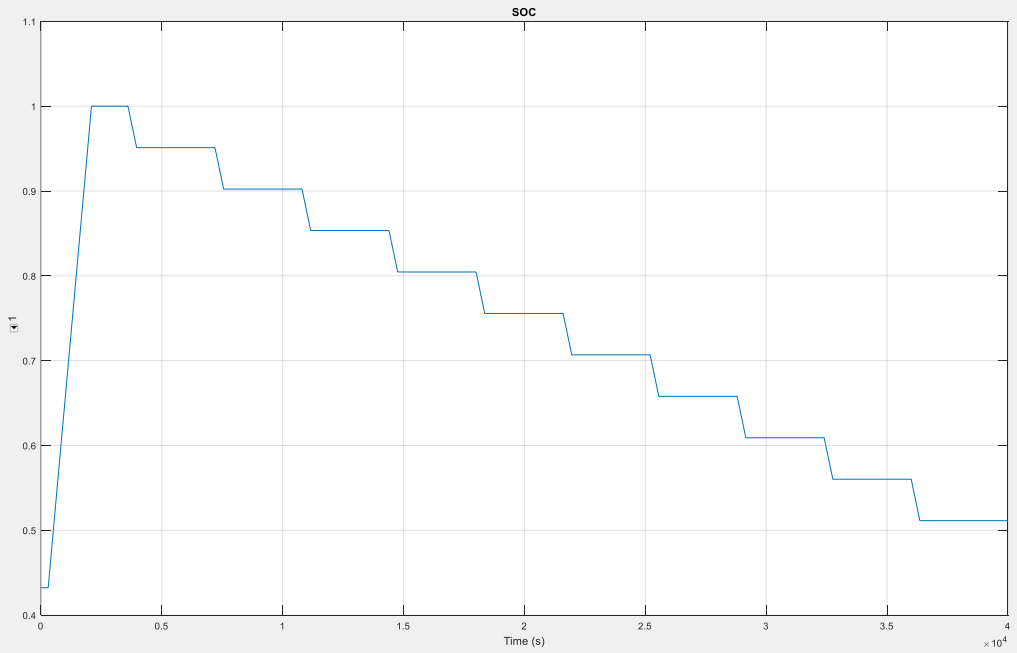

Figure 84 Scenario 3: SOC of the lithium - ion cell (1 RC branch model)

- **Scenario 4: Variable discharge current pulse between 13.5 A and 40 A**

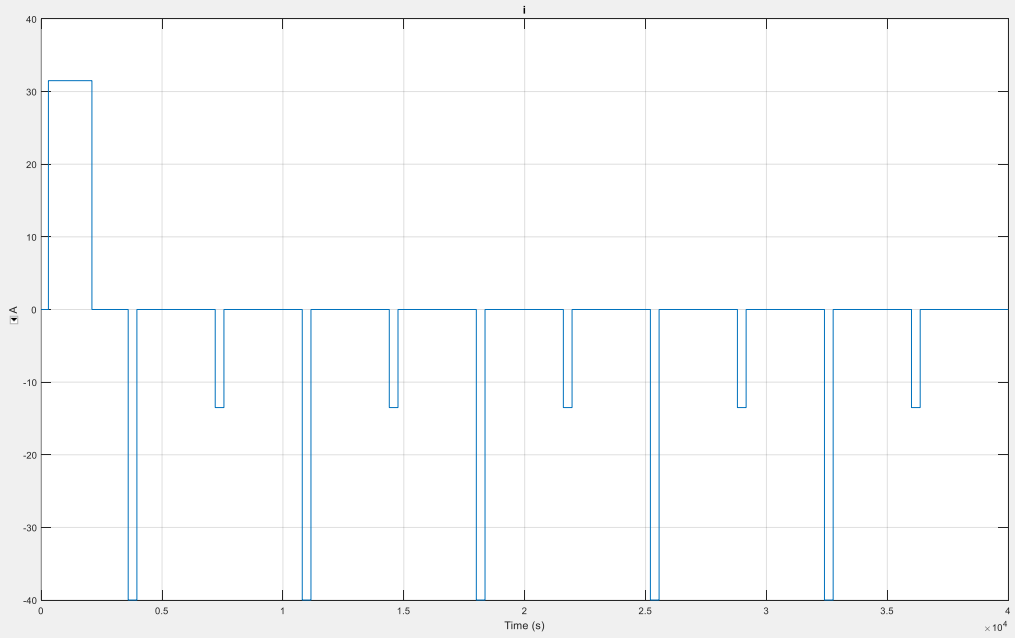

Figure 85 Scenario 4: Discharge current pulse of the lithium - ion cell (1 RC branch model)

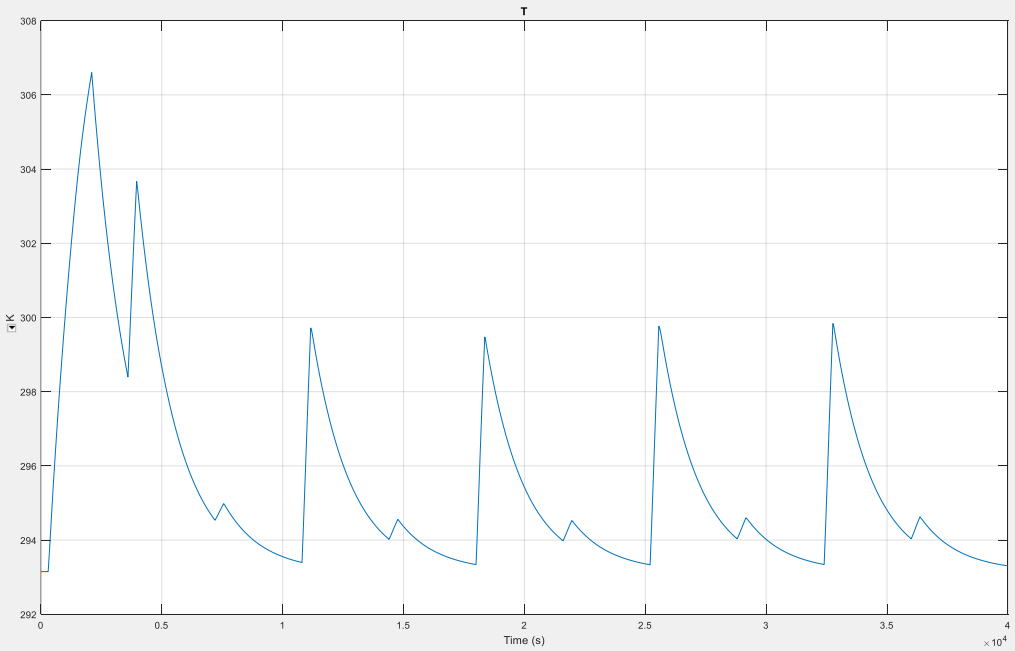

Figure 86 Scenario 4: Temperature of the lithium - ion cell (1 RC branch model)

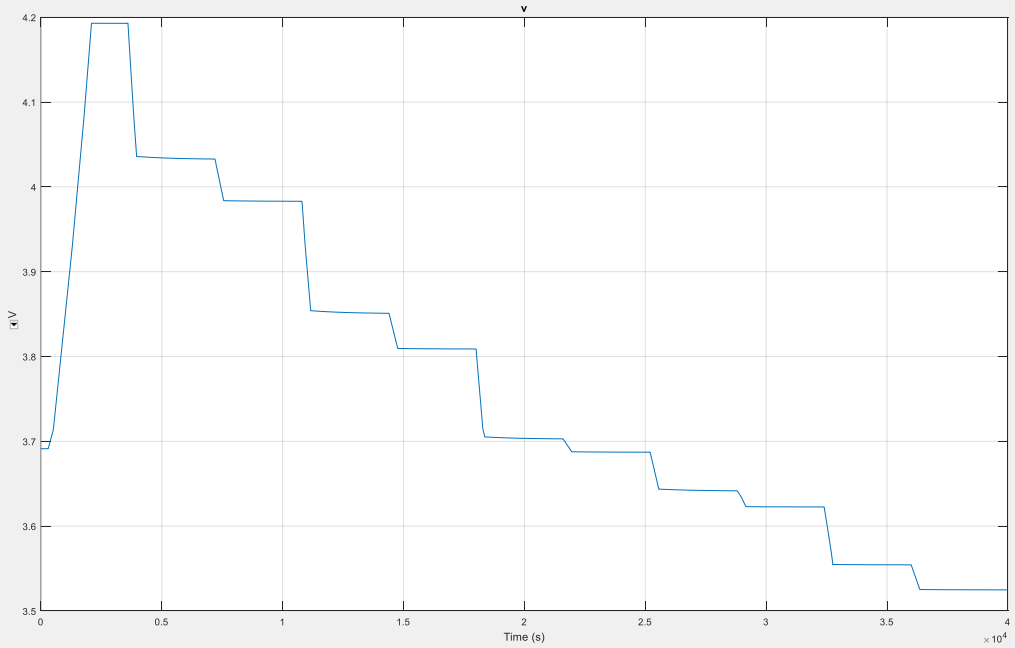

Figure 87 Scenario 3: Voltage of the lithium - ion cell (1 RC branch model)

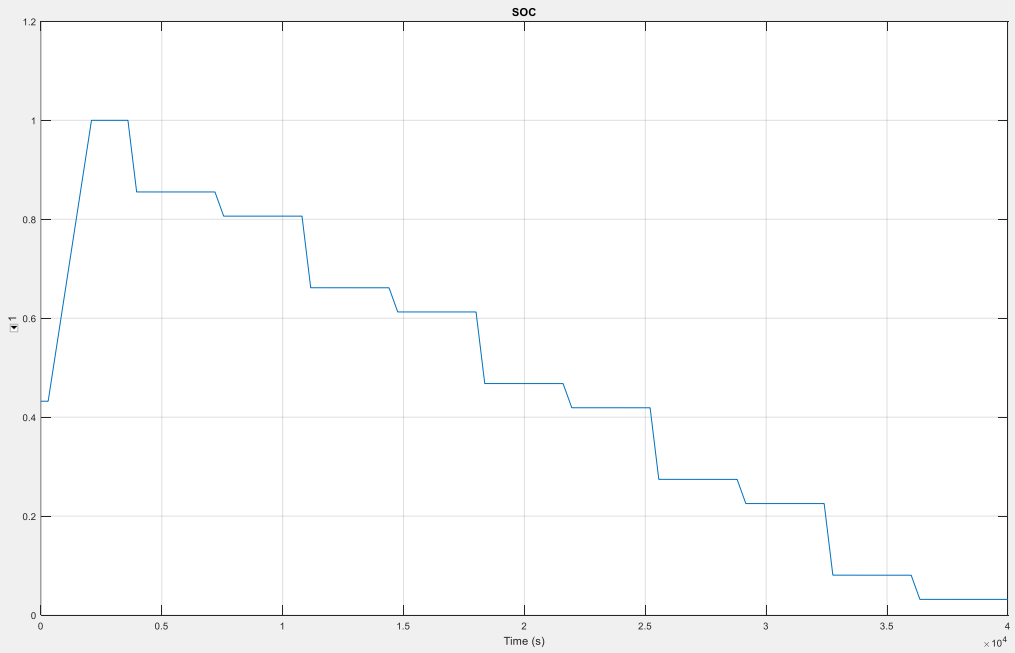

Figure 88 Scenario 4: SOC of the lithium - ion cell (1 RC branch model)

Scenarios 1, 2 and 3 include changes in the discharge current pulse of approximately 50%. The temperature change equals 3 K,7 K and less than 1 K in scenarios 1 ,2 and 3 respectively, whereas the SOC drops to zero after 3600 s in scenario 1 and after 2600 s in scenario 2. The SOC of scenario 3 becomes the half after 3600 s and the corresponding voltage drops to 3.7 V, which is 0.2 V higher than the voltage of the other two scenarios. As to scenario 4, SOC becomes almost 5% after 3600 s. Hence, the discharge current has an approximately linear effect on the temperature deviation, while the its effect on the SOC of the lithium – ion cell ion cell become less significant in changes of discharge current of high value.

Case 1 – Simulink 2 RC branches model

The same simulations are executed with the 2 RC branches equivalent circuit model.

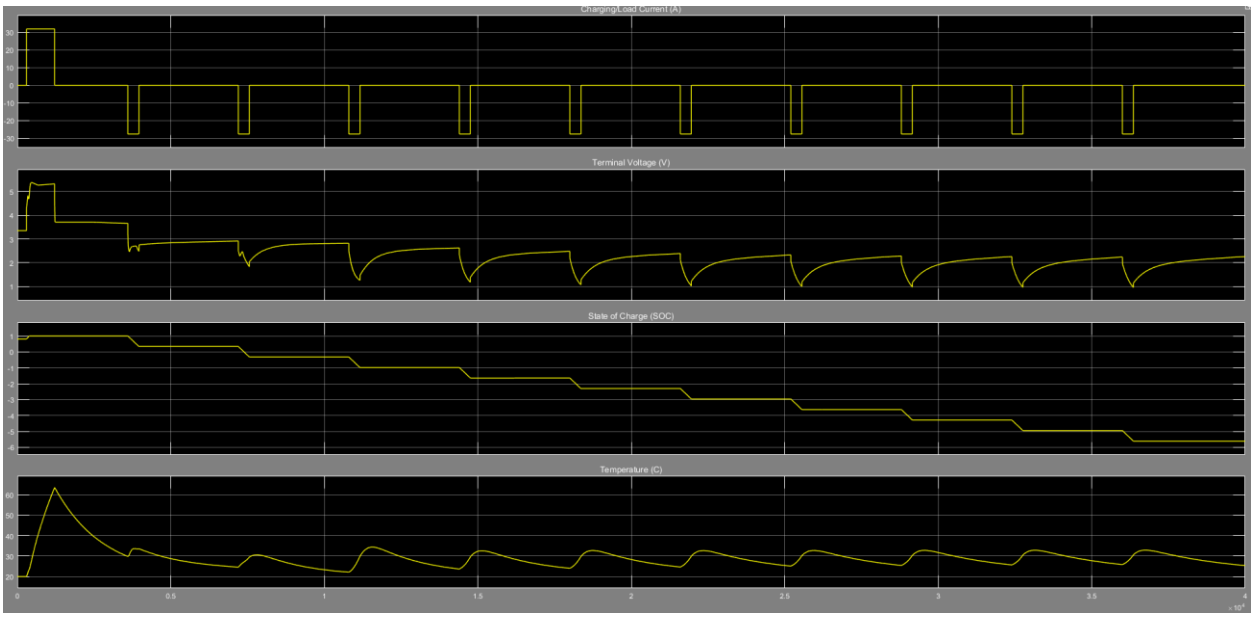

Figure 89 Lithium - ion cell simulation at 20 C ambient temperature (2 RC branch equivalent circuit model)

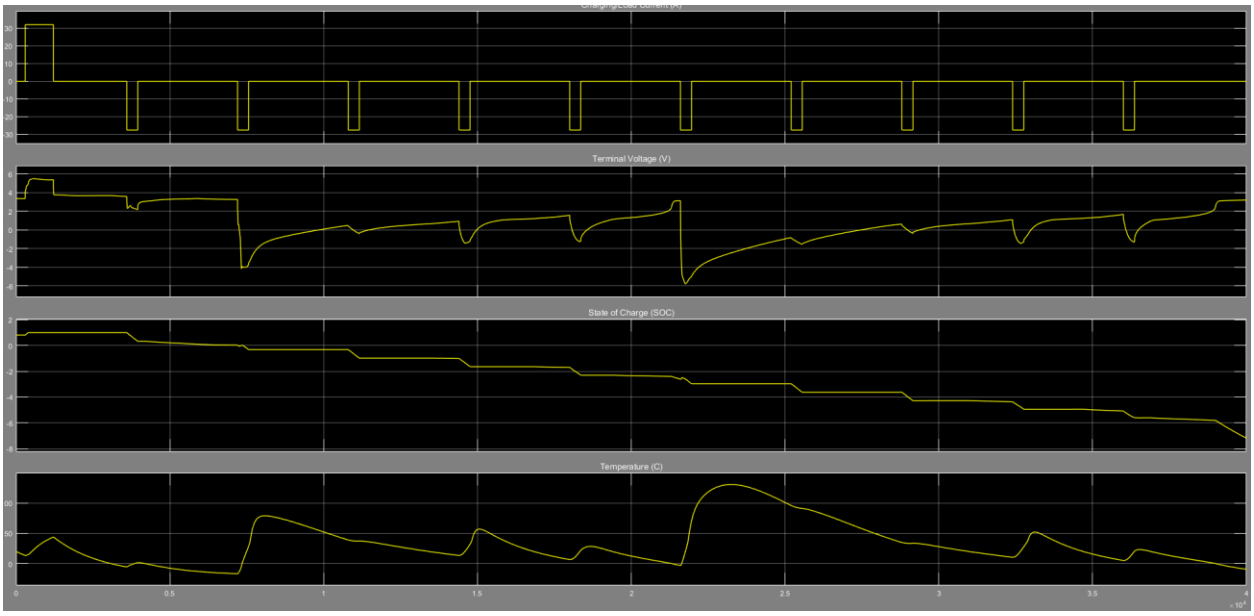

Figure 90 Lithium - ion cell simulation at -20 C ambient temperature (2 RC branch equivalent circuit model)

- **Scenario 1: Reference discharge current pulse (27.625 A)**

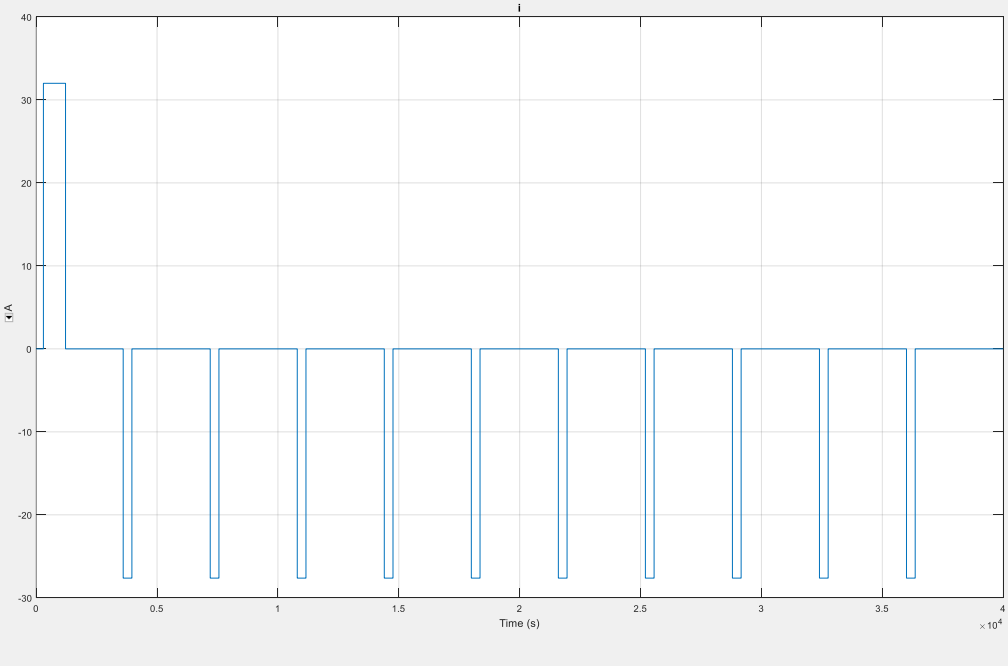

Figure 91 Scenario 1: Discharge current pulse of the lithium - ion cell (2 RC branches model)

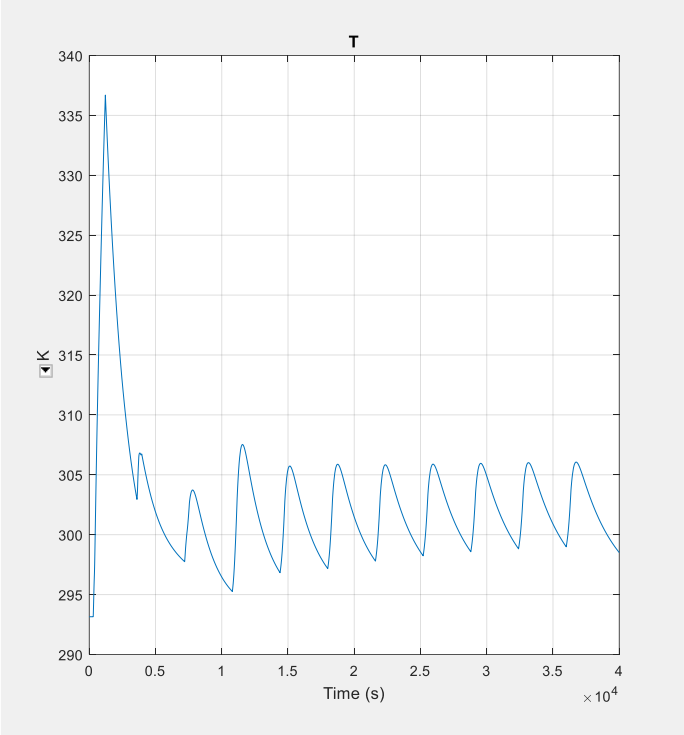

Figure 92 Scenario 1: Temperature of the lithium - ion cell (2 RC branches model)

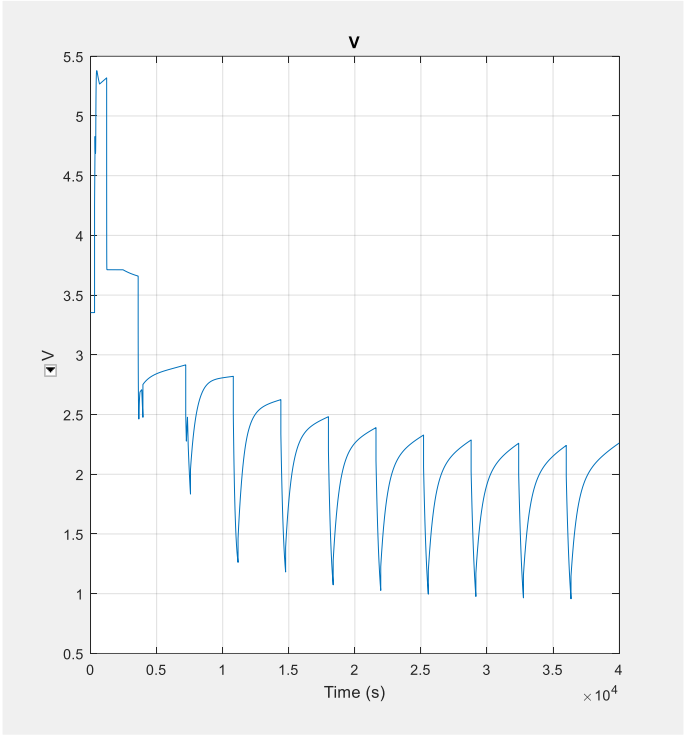

Figure 93 Scenario 1: Terminal voltage of the lithium - ion cell (2 RC branches model)

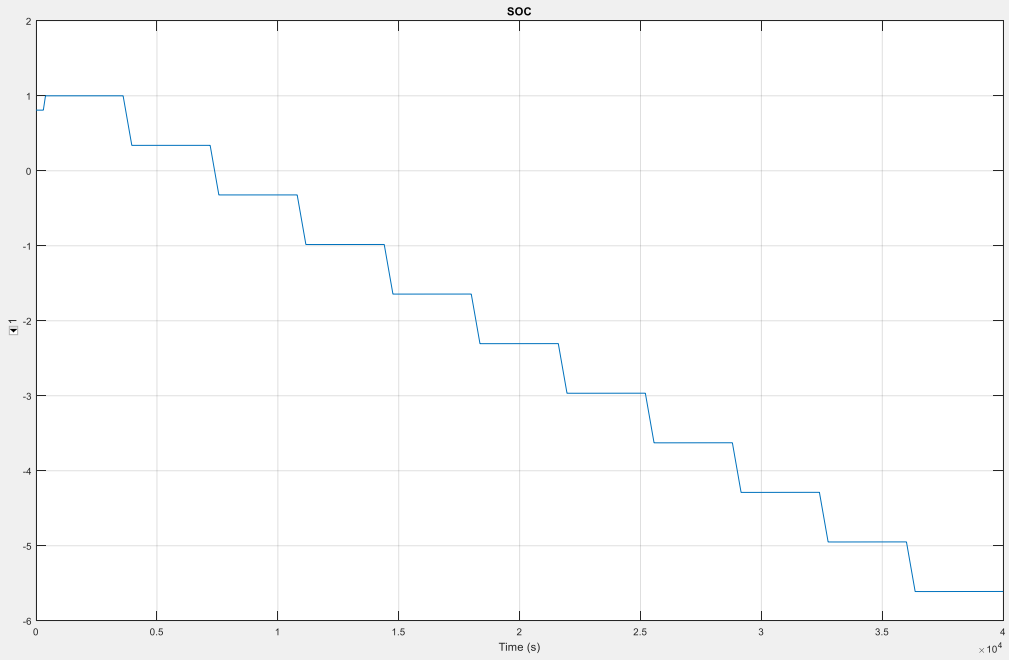

Figure 94 Scenario 1: SOC of the lithium - ion cell (2 RC branches model)

- **Scenario 2 : 40 A discharge current pulse**

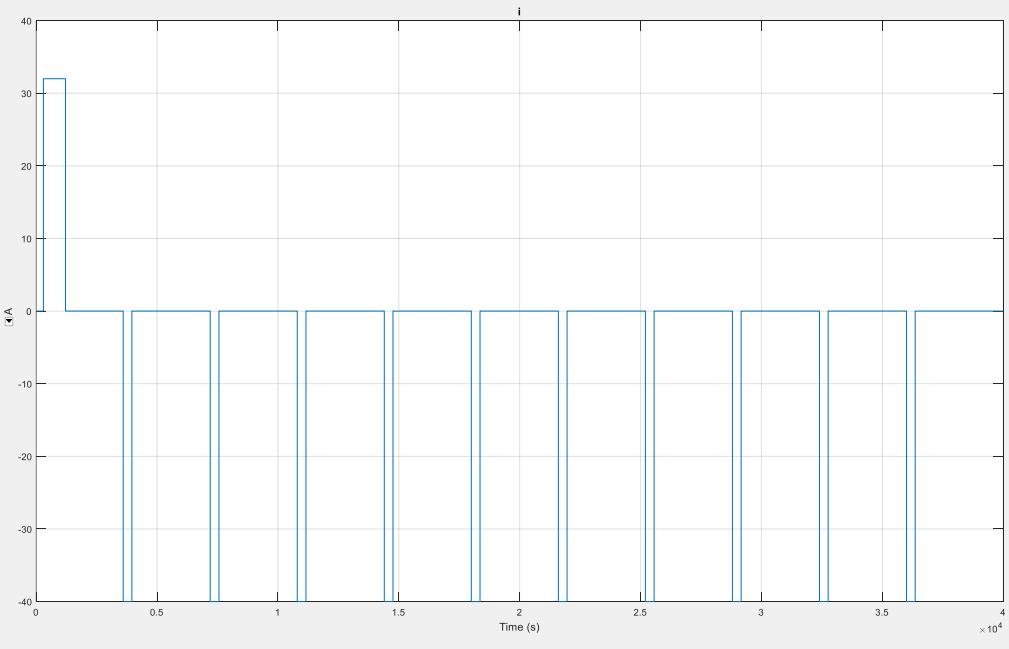

Figure 95 Scenario 2: Discharge current pulse of the lithium - ion cell (2 RC branches model)

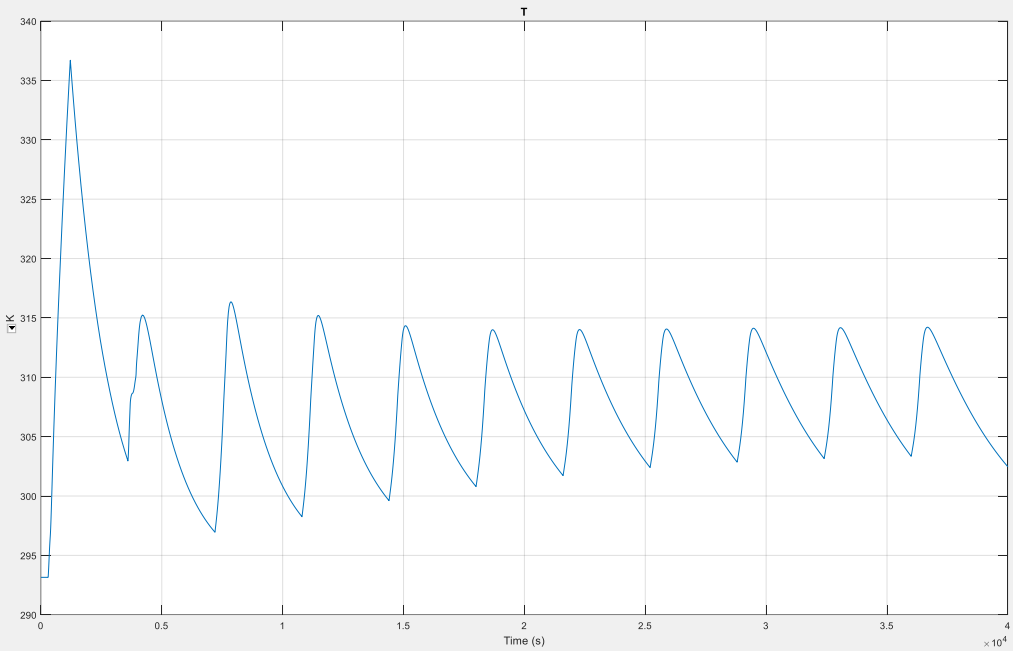

Figure 96 Scenario 2: Temperature of the lithium - ion cell (2 RC branches model)

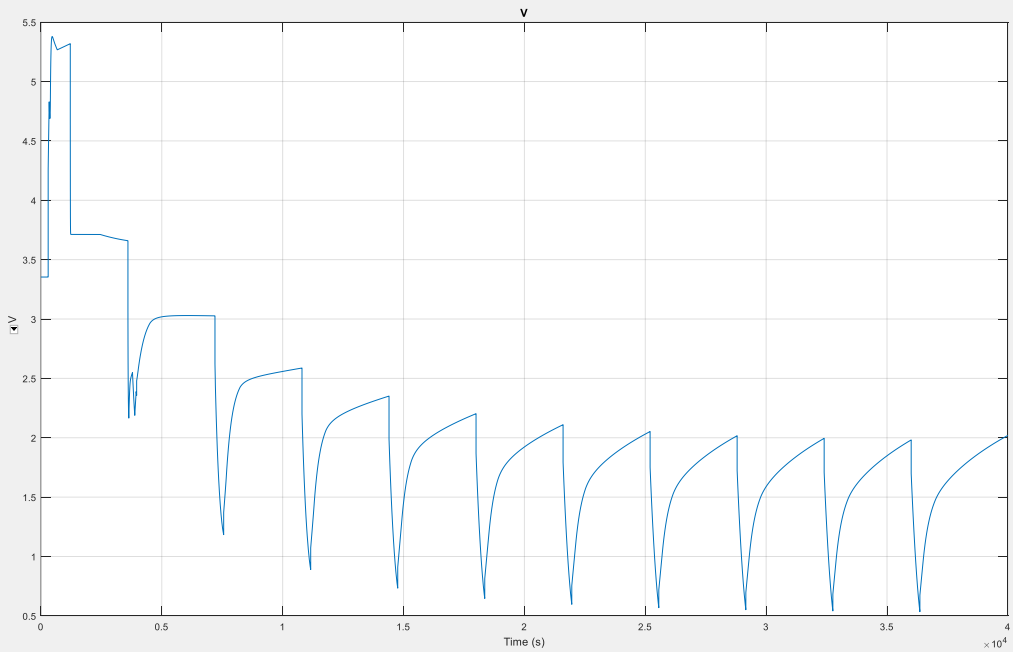

Figure 97 Scenario 2: Terminal voltage of the lithium - ion cell (2 RC branches model)

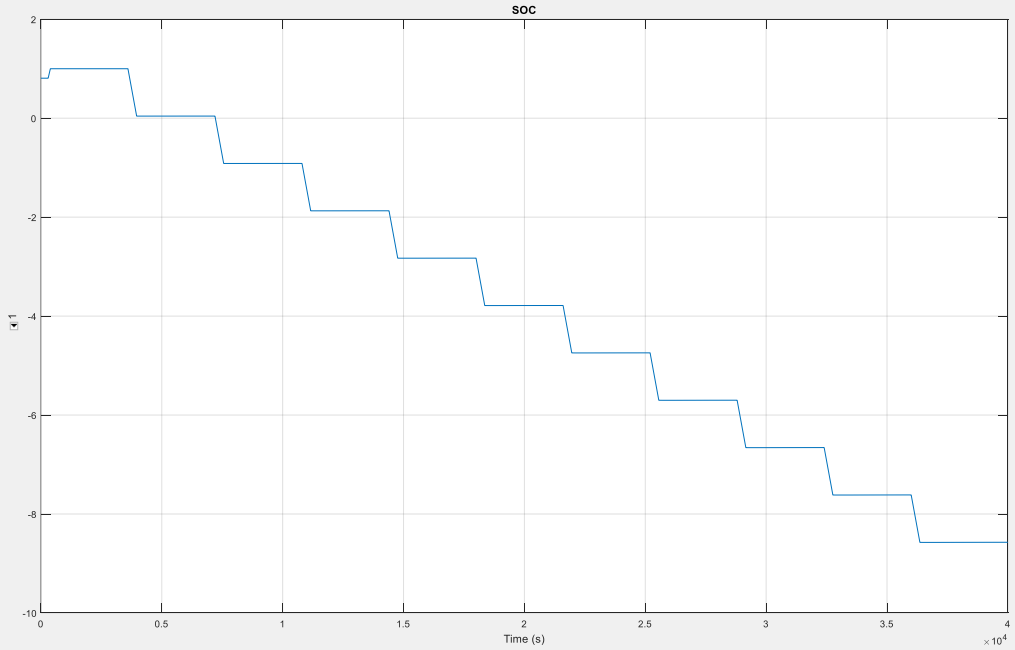

Figure 98 Scenario 2: SOC of the lithium - ion cell (2 RC branches model)

- **Scenario 3: 13.5 A discharge current pulse**

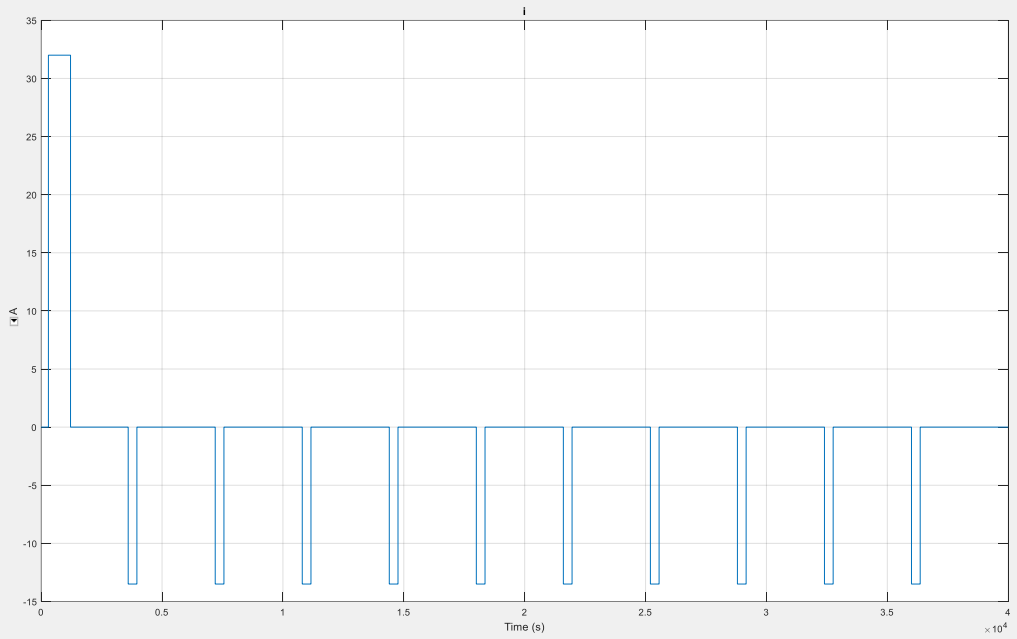

Figure 99 Scenario 3: Discharge current pulse of the lithium - ion cell (2 RC branches model)

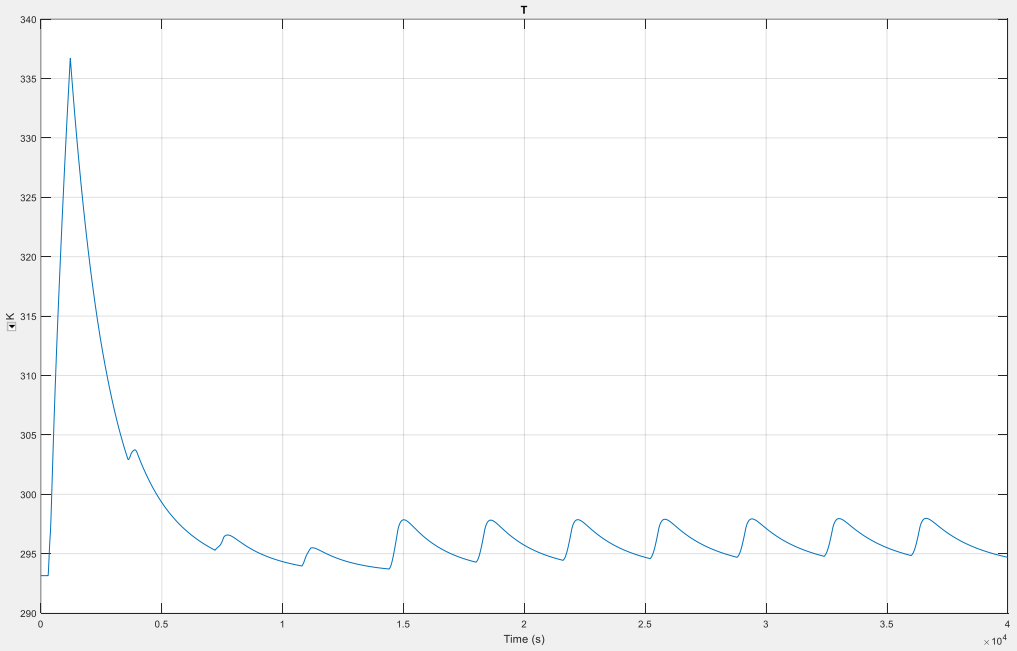

Figure 100 Scenario 3: Temperature of the lithium - ion cell (2 RC branches model)

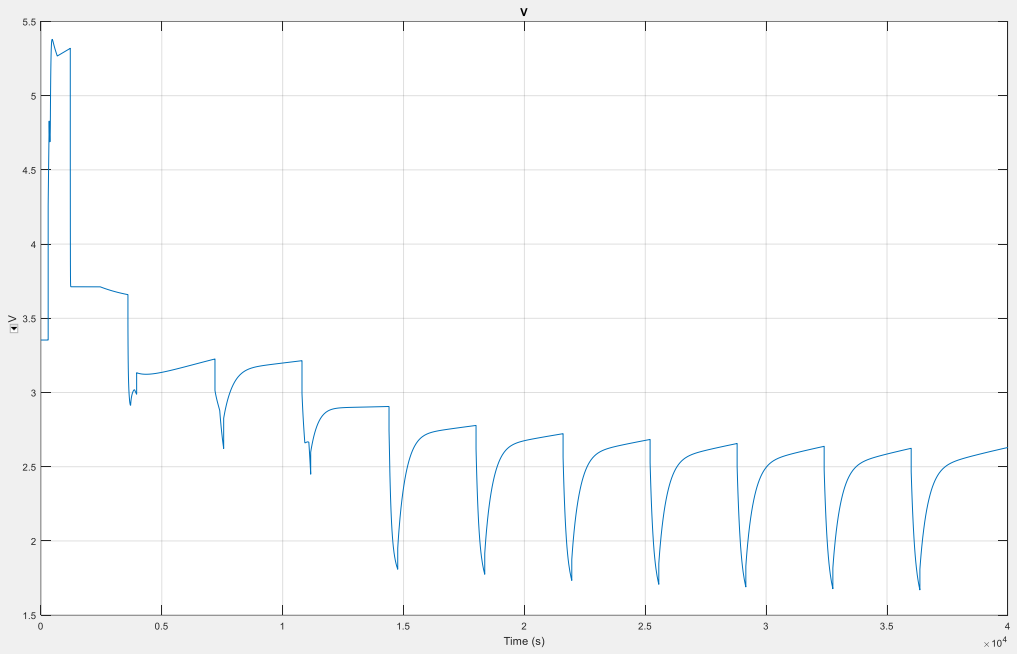

Figure 101 Scenario 3: Terminal voltage of the lithium - ion cell (2 RC branches model)

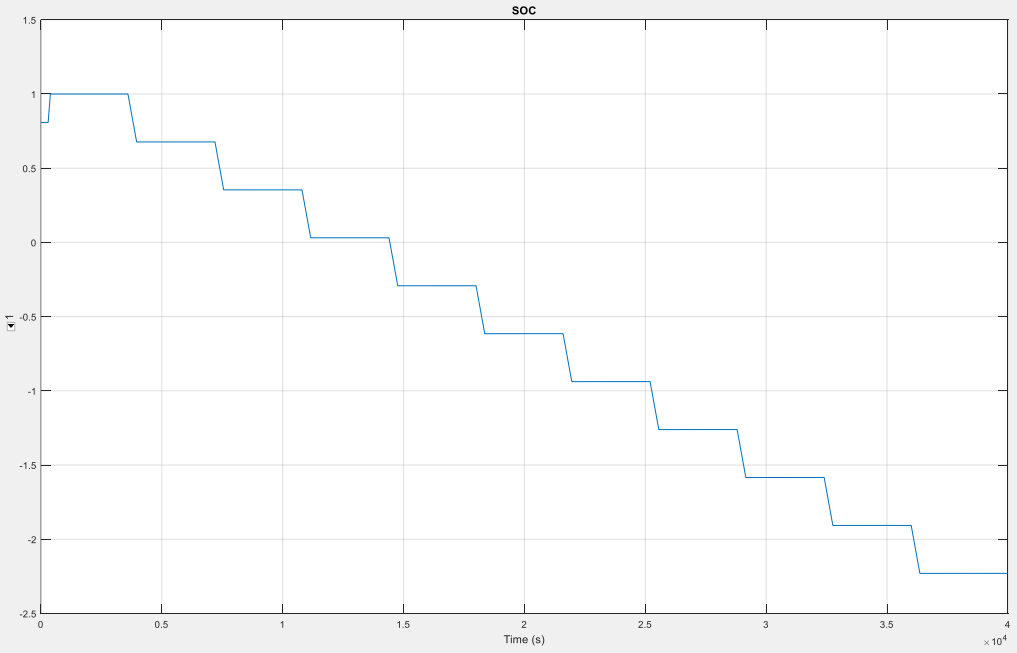

Figure 102 Scenario 3: SOC of the lithium - ion cell (2 RC branches model)

- **Scenario 4: Variable discharge current pulse between 13.5 A and 40 A**

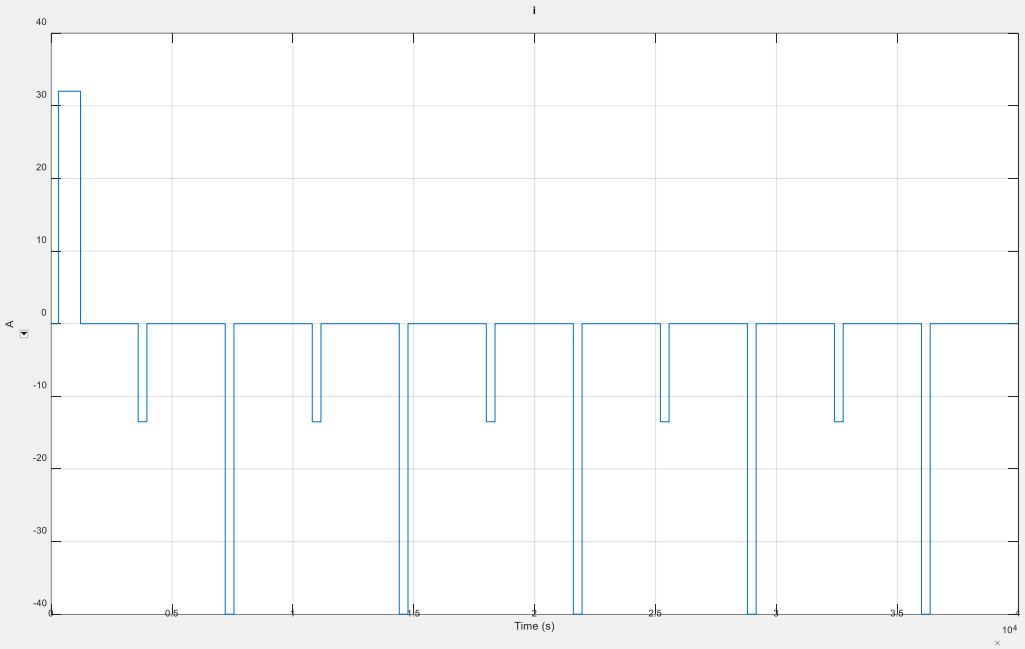

Figure 103 Scenario 4: Discharge current pulse of the lithium - ion cell (2 RC branches model)

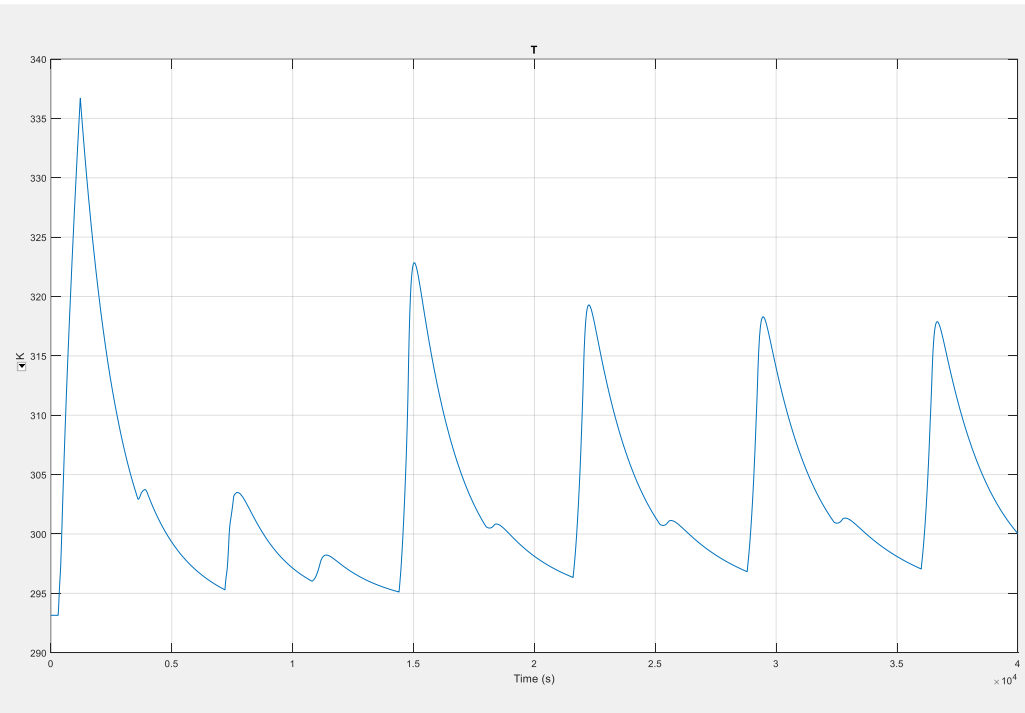

Figure 104 Scenario 4: Temperature of the lithium - ion cell (2 RC branches model)

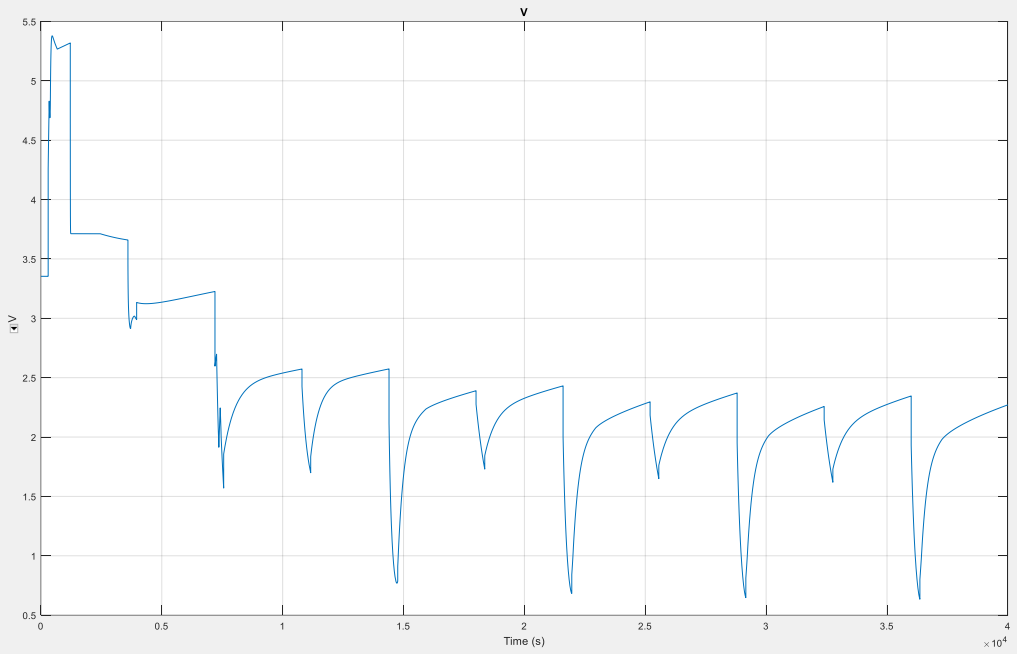

Figure 105 Scenario 4: Terminal voltage of the lithium - ion cell (2 RC branches model)

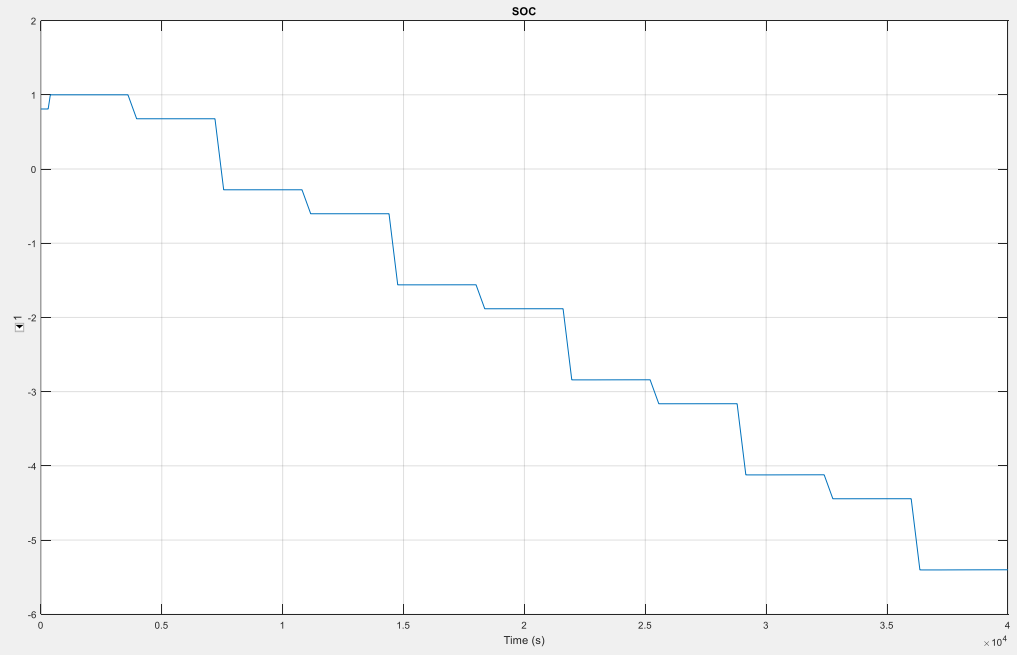

Figure 106 Scenario 4: SOC of the lithium - ion cell (2 RC branches model)

Case 1 – Comparison of results 1RC and 2 RC branches model

Comparing the simulation results of the 2 RC branches to the 1 RC branch model, it is observed that the 2 RC branches circuit model results in higher temperature changes (e.g. 11 K in scenario 2). As to the SOC of the lithium – ion significantly differs from the estimated SOC of the 1 RC branch model. In particular, in scenario 2 SOC becomes zero approximately after 700, while in other scenarios it becomes zero after 350 s. The terminal voltage of the lithium – ion cell also decreases as the discharge current increases.

Case 1 – Comsol Multiphysics

Subsequently, the lithium – ion battery cell model in Comsol Multiphysics is simulated so as to examine the DoD distribution as a function of discharge time in the positive electrode [55]. The DoD distribution is affected by various factors, such as the positive electrode's thickness, the current collector's position, the electrode reaction kinetics and mass transport phenomena [55].

The electrolyte is selected to be a polymer electrolyte ("1:2 EC:DMC and p(VdF-HFP)") and LiFePO4 is selected as the positive electrode material instead of LMO as in the tutorial in [55], since it provides acceptable properties in terms of safety, power density, SOC and it has a relatively low cost. The rest of the parameters are set to be the same.

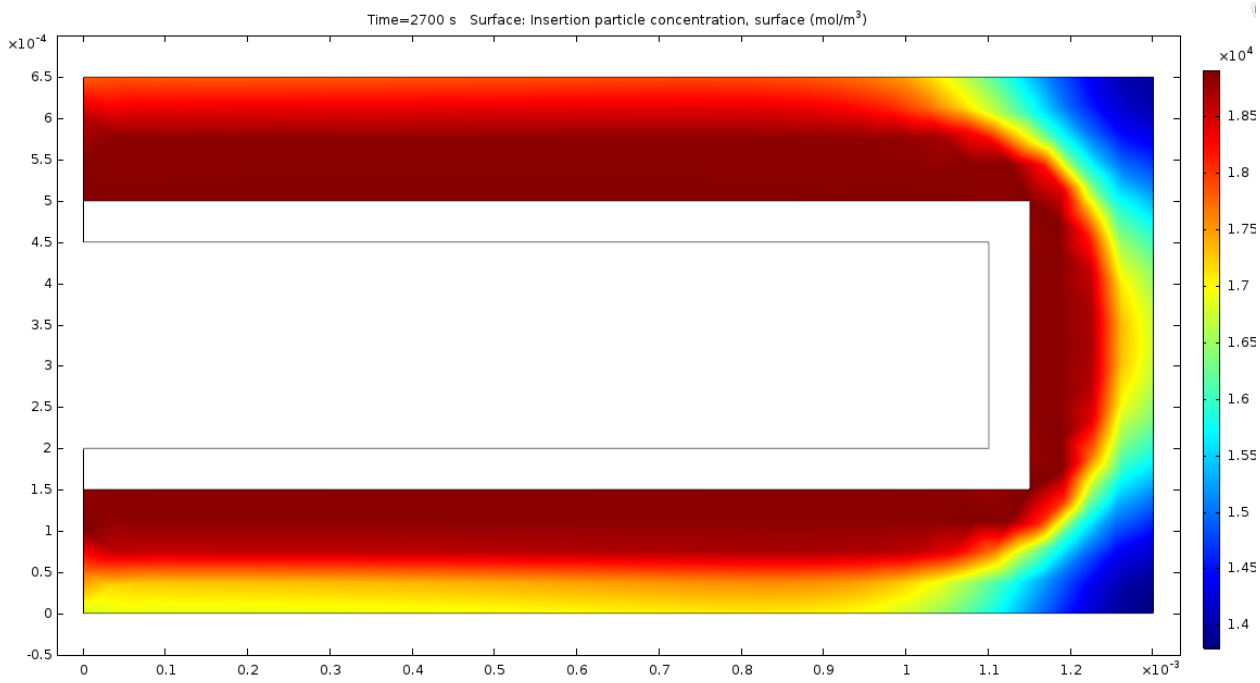

Figure 107 Lithium concentration at the surface of the lithium - ion cell electrode particles after 2700 s (Comsol)

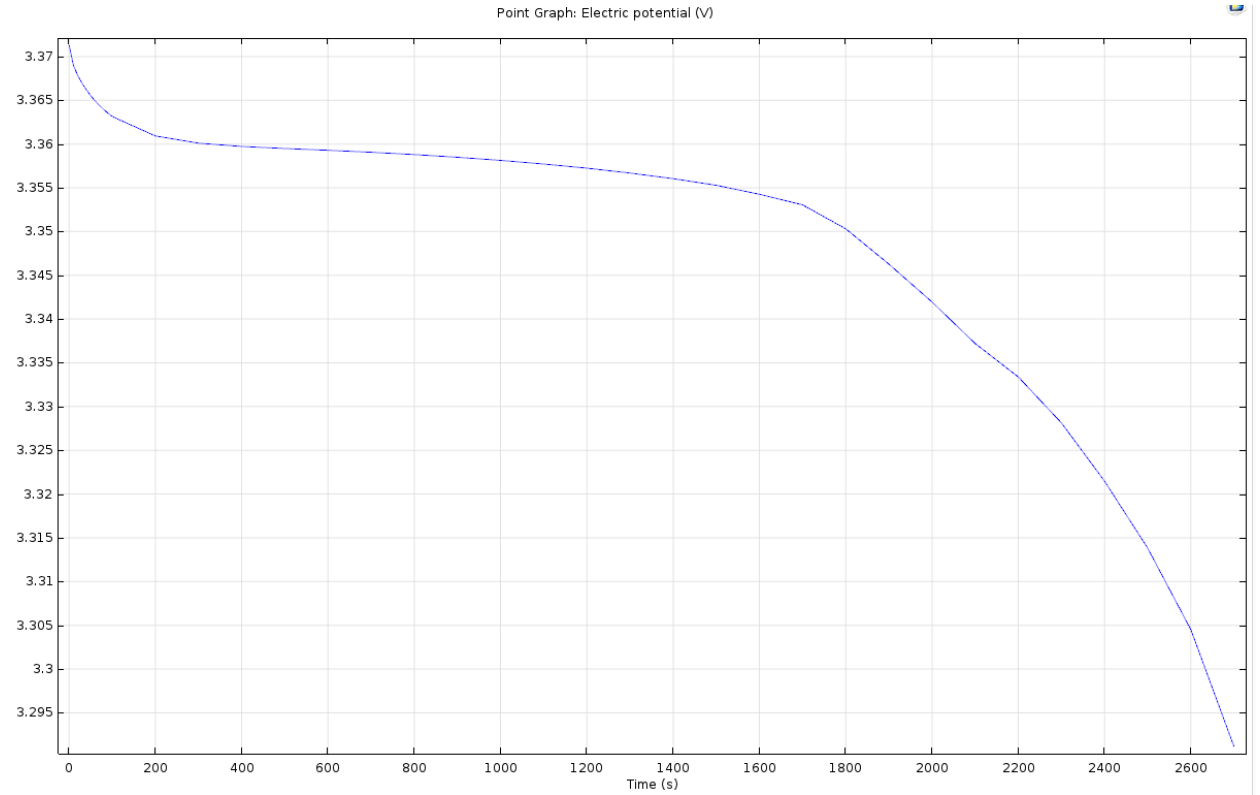

Figure 108 Cell voltage variation during discharge (Lithium ion cell model in Comsol)

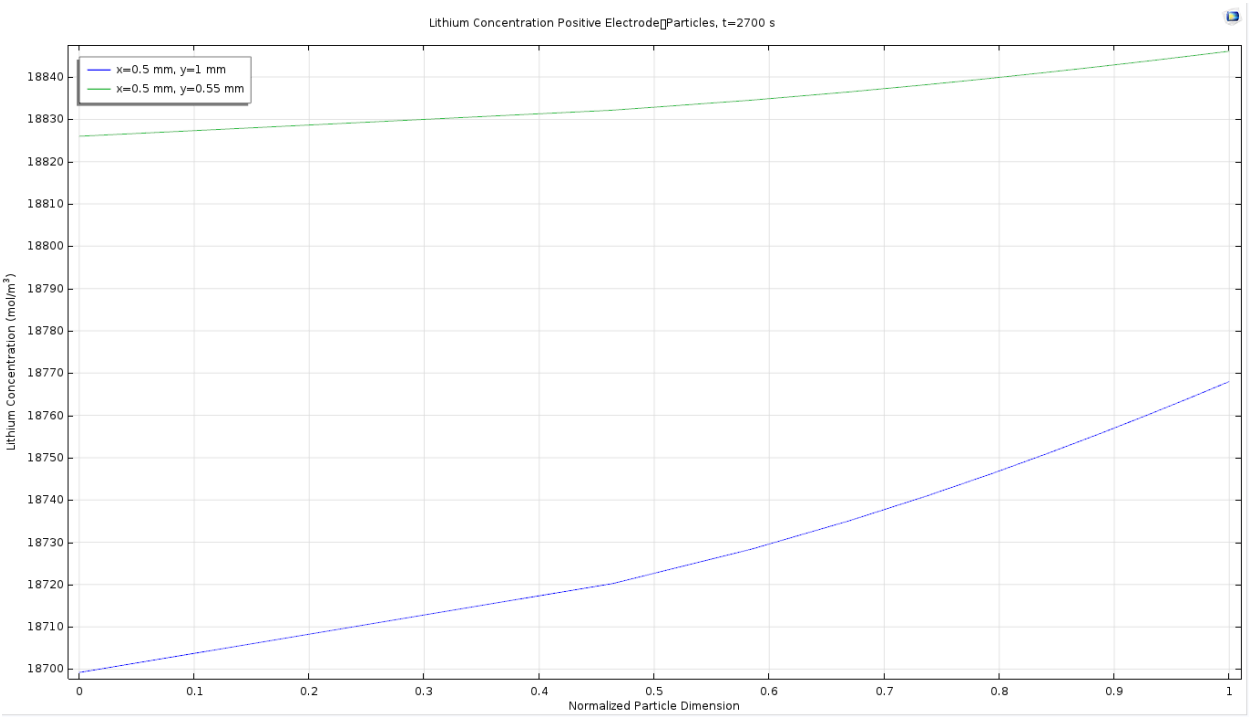

Figure 109 Lithium concentration in the positive electrode particles at (x=0.5 mm, y=0.1 mm) and (x=0.5 mm, y=0.55 mm) of the lithium ion cell model in Comsol

During discharging the concentration of lithium in the positive electrode increases [55]. The blue line in the lithium concentration in the positive electrode particles signifies that the discharge is less intense at points located at longer distance from the current collector [55].

Comparing the results to those of [55], LFP as a positive electrode material decreased the lithium concentration at the surface of the electrode particles and resulted in less voltage during discharge, whereas LFP appears to have a more uniform lithium concentration distribution than LMO.

3.2.2 Case 2 : Temperature effect on lithium – ion battery

The "lithium – ion temperature dependent battery model" is utilized for studying the temperature effects on the lithium – ion battery. Battery A lithium – ion battery ($LiFeMgPO_4$) simulating temperature effects is rated at 12.8 V with a rated capacity of 40 Ah. The battery also has an initial SOC of 100% and a battery response time of 30 s. Battery B not simulating temperature effects is rated at 7 V with a rated capacity of 5.4 Ah. The batteries' discharge curves, as well as the ambient temperature step function plot along with the simulation results (Scenario 1) are given below.

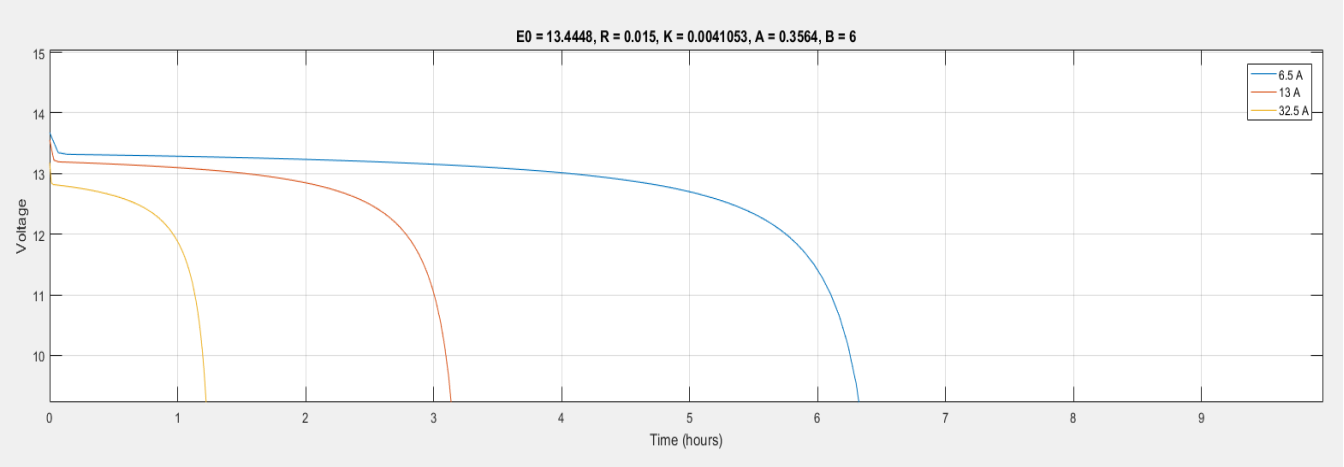

Figure 110 Battery A discharge curve ("lithium – ion temperature dependent battery model")

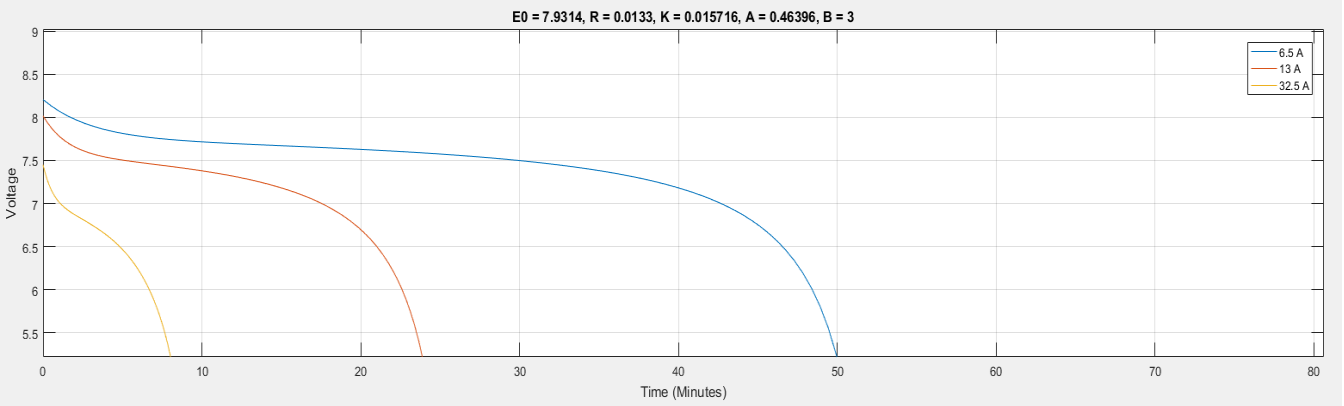

Figure 111 Battery B discharge curve ("lithium – ion temperature dependent battery model")

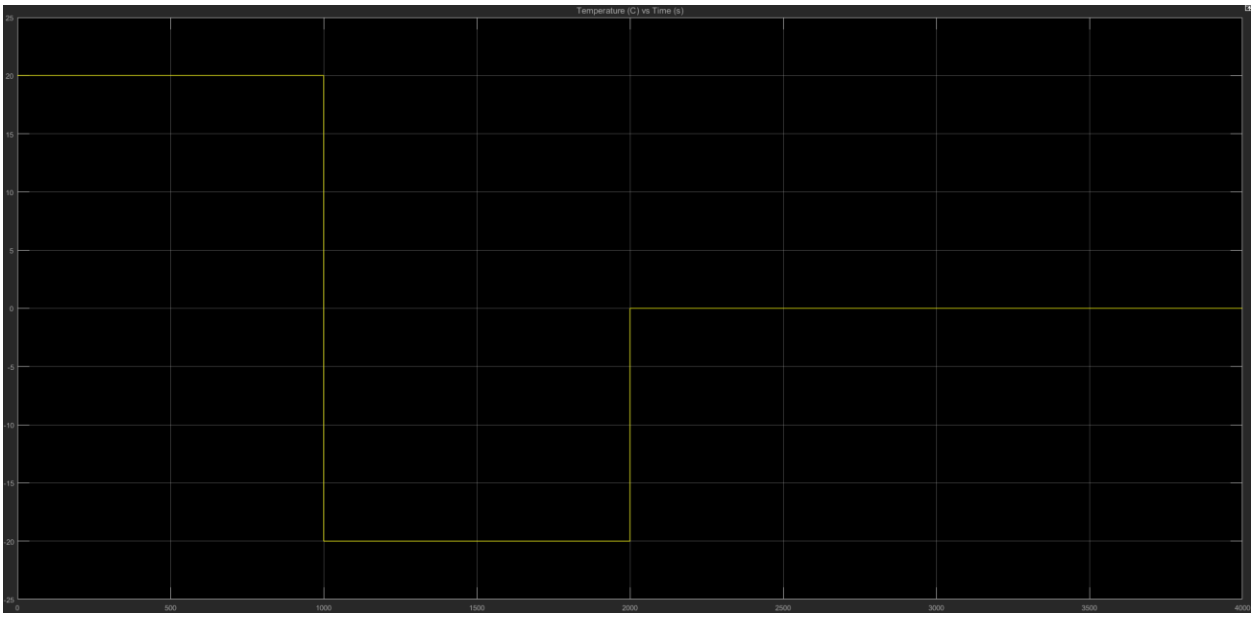

Figure 112 Ambient temperature step function ("lithium – ion temperature dependent battery model")

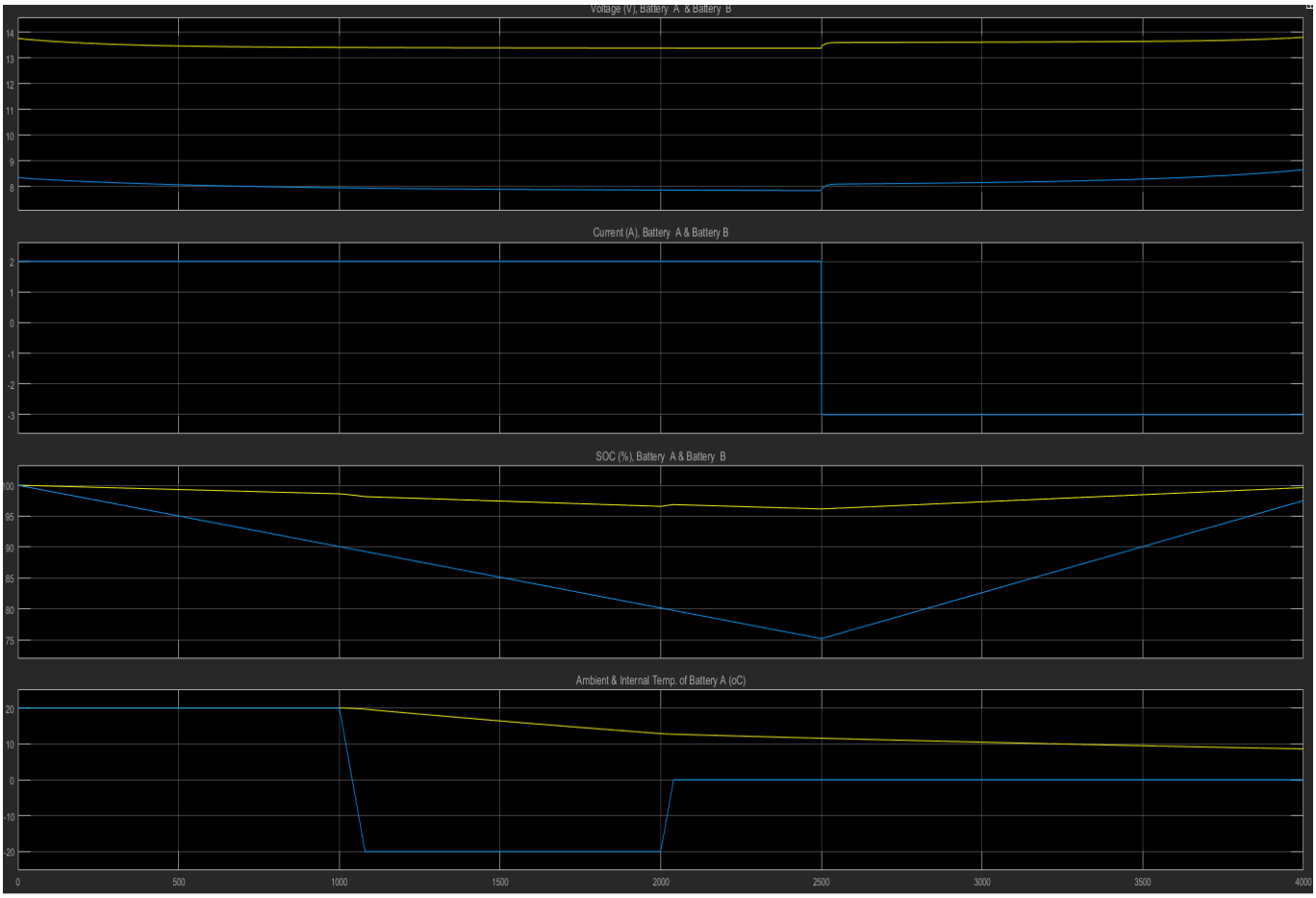

Figure 113 Simulation results ("lithium – ion temperature dependent battery model")

During the discharging of the batteries with 2A and during the temperature drop, a slight decrease in both batteries' voltage is observed until a steady state value is reached. The decrease in the voltage and in the SOC of battery B is attributed to the decrease in the battery capacity, whereas the decrease in the voltage and in the SOC of battery A is attributed to both the capacity reduction and to the temperature drop, which is followed by a reduction of the battery internal temperature. Due to temperature increase from -20 to 0 ^{o}C, the SOC of battery B seems to be stabilized, whereas the SOC of battery A keeps rapidly decreasing. During the charging of the batteries with -3 A, both batteries' voltages increase, as well as their SOCS, while the SOC of battery B increases more rapidly. Thus, in this case the temperature seems to have a positive effect on the battery response at odds with the simulation results of [49], where battery A is a 7.4 V 5.4 Ah $LiCoO_2$.

3.2.3 Case 3 : Lithium – ion battery internal fault

An internal short circuit of a lithium – ion battery cell generally leads to the bridging of anode and cathode. As a result, uncontrolled charge flow produces overheating due to the internal resistance and destabilizes the active materials within the battery, which means that the battery structure is at risk due to the produced heat and pressure, while there is the likelihood of a combustion event taking place [54]. The battery management system is responsible for protecting the battery under overcurrent conditions [54]. A method for testing the behavior of lithium – ion battery during internal short circuit is subjecting cells to localized indentations and the cell temperature along with the open circuit voltage and the indenter's position are measured [54].

A lithium – ion battery model consisting of 20 cells in series with a fault at 10^{th} cell is simulated in Simulink. The fault is represented by reducing the nominal open circuit voltage and the nominal capacity of the 10^{th} cell, whereas the cell resistance increases. The charging and discharging cycles are represented by an ideal current source being equal to 20sin(0.01047t) A. The cells have a thickness of 0.1 m and an area of 0.001 m^2, while their thermal conductivity equals 200 W/mK. Five fault scenarios are executed changing the parameters of the cell under short circuit.

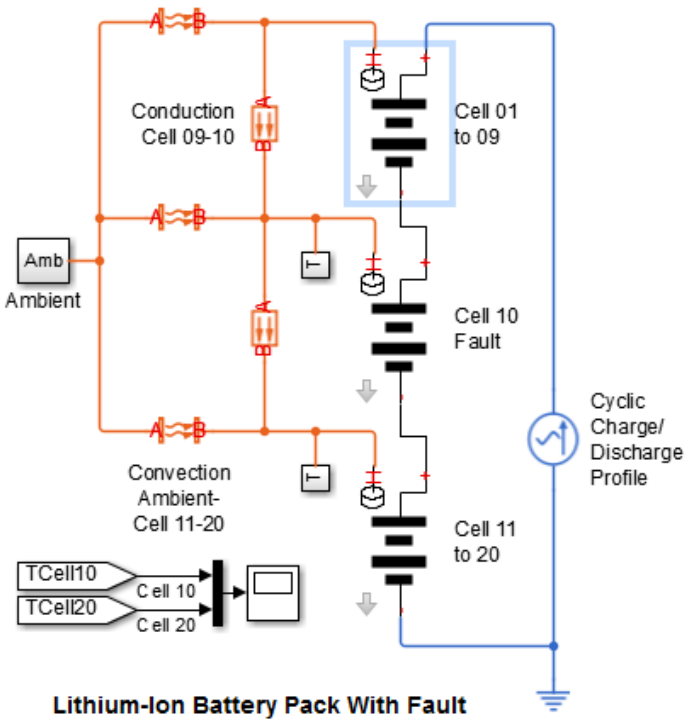

Figure 114 Simulink lithium - ion battery model with fault [49]

- **Scenario 1: Capacity = 0.9*NV, Open circuit voltage = 0.5*NV, Cell resistance = 3*NV**

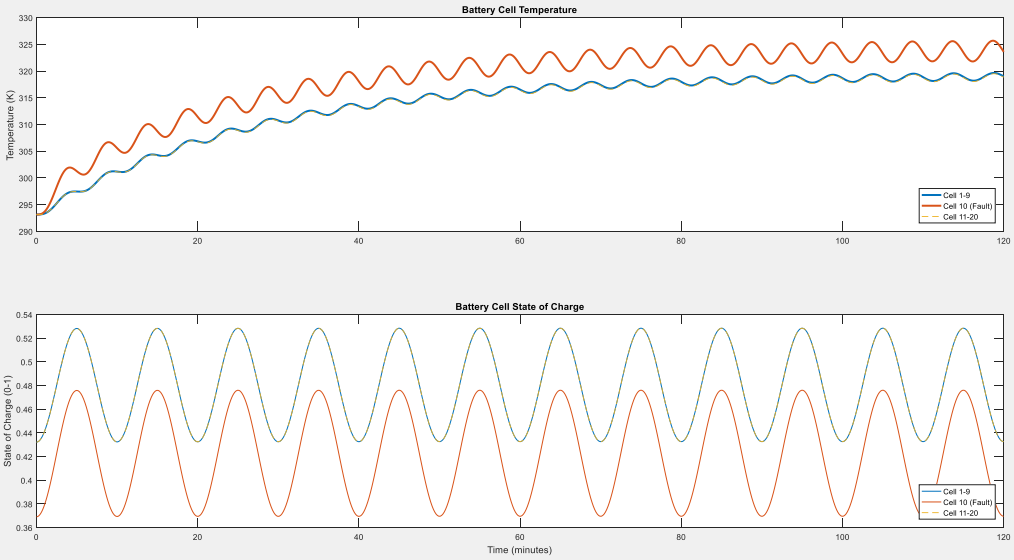

Figure 115 Scenario 1: SOC and temperature of lithium - ion battery under internal fault

- **Scenario 2: Capacity = 0.2*NV, Open circuit voltage = 0.5*NV, Cell resistance = 3*NV**

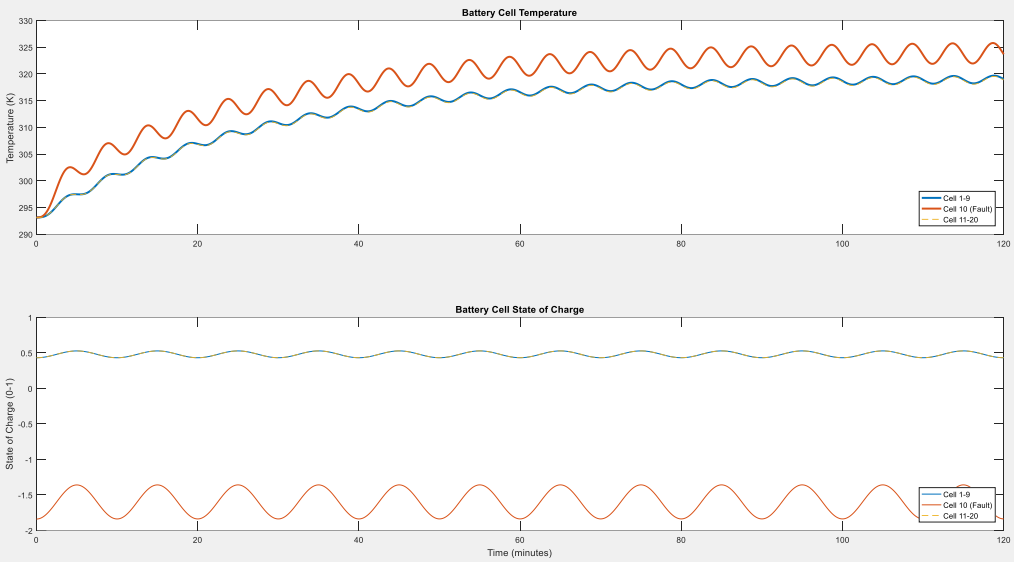

Figure 116 Scenario 2: SOC and temperature of lithium - ion battery under internal fault

- **Scenario 3: Capacity = 0.2*NV, Open circuit voltage = 0.1*NV, Cell resistance = 3*NV**

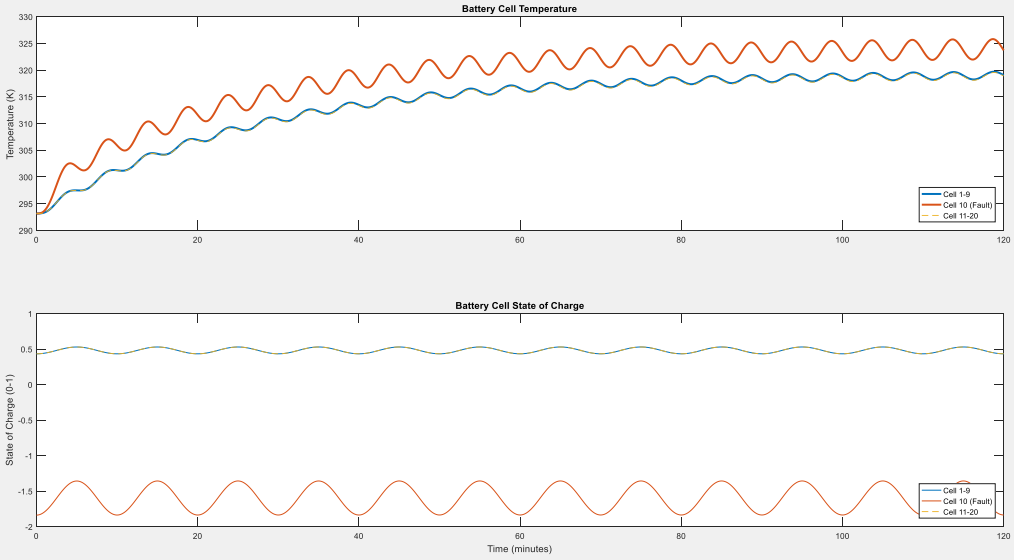

Figure 117 Scenario 3: SOC and temperature of lithium - ion battery under internal fault

- **Scenario 4: Capacity = 0.2*NV, Open circuit voltage = 0.1*NV, Cell resistance = 7*NV**

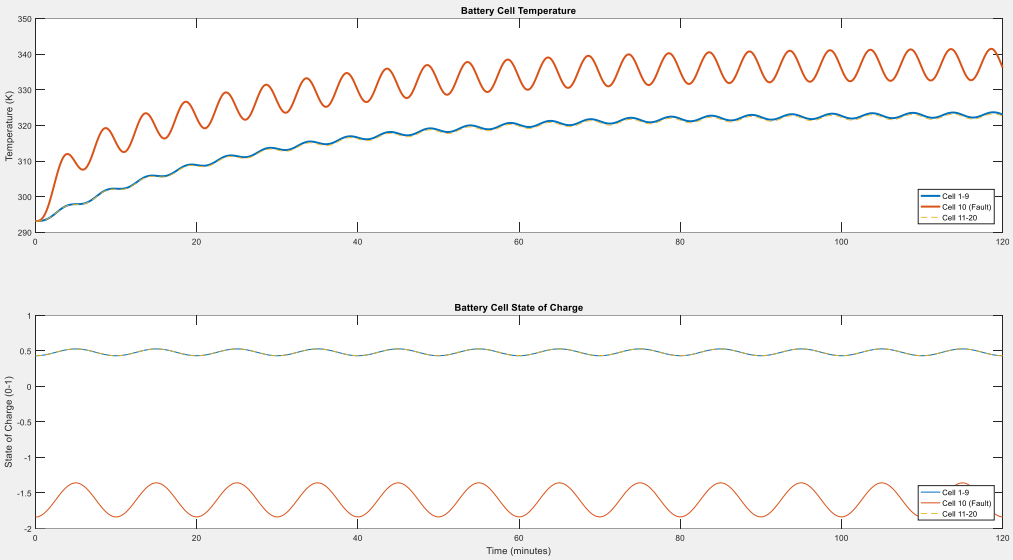

Figure 118 Scenario 4: SOC and temperature of lithium - ion battery under internal fault

It is observed that the capacity reduction of the cell under fault decreases the SOC ripple of the healthy cells and drops the SOC of the 10th cell to zero, while the decrease in the open circuit voltage of the cell under fault has no effect on the temperature and SOC curves of all the cells. However, the increase in the cell resistance of the 10th cell increases its temperature by 10 K and the other cells' temperature by approximately 5 K.

3.2.4 Case 4 : Air – cooling, C-factor, battery radius and reaction rate coefficient effects on the lithium -ion battery

The lithium - ion battery 3d thermal model is employed in Comsol Multiphysics for studying the effect of air - cooling on a lithium – ion battery. It is assumed that the battery is installed in a battery pack being composed of battery matrices. The cell potential versus the current load, the temperature changes (minimum, maximum and average temperatures) and the surface temperature of the battery are examined. The differences observed between charging and discharging are attributed to the entropy changes caused by the corresponding reactions [55].

The problem solving method consists of the consecutive steps: Initially, a steady state solution at 298 K is provided. Subsequently, solutions for the battery potentials are calculated at the time step being equal to 0. Finally, the solutions of the first and second step are utilized on a time-dependent study of the problem for initializing the velocity, the potentials and the pressure.

In [55] the inlet velocity equals 0.1 m/s, while the outlet pressure equals 1 atm. Other things being equal, the inlet air velocity is changed and three scenarios are examined.

- **Scenario 1: Inlet air velocity = 0.2 m/s**

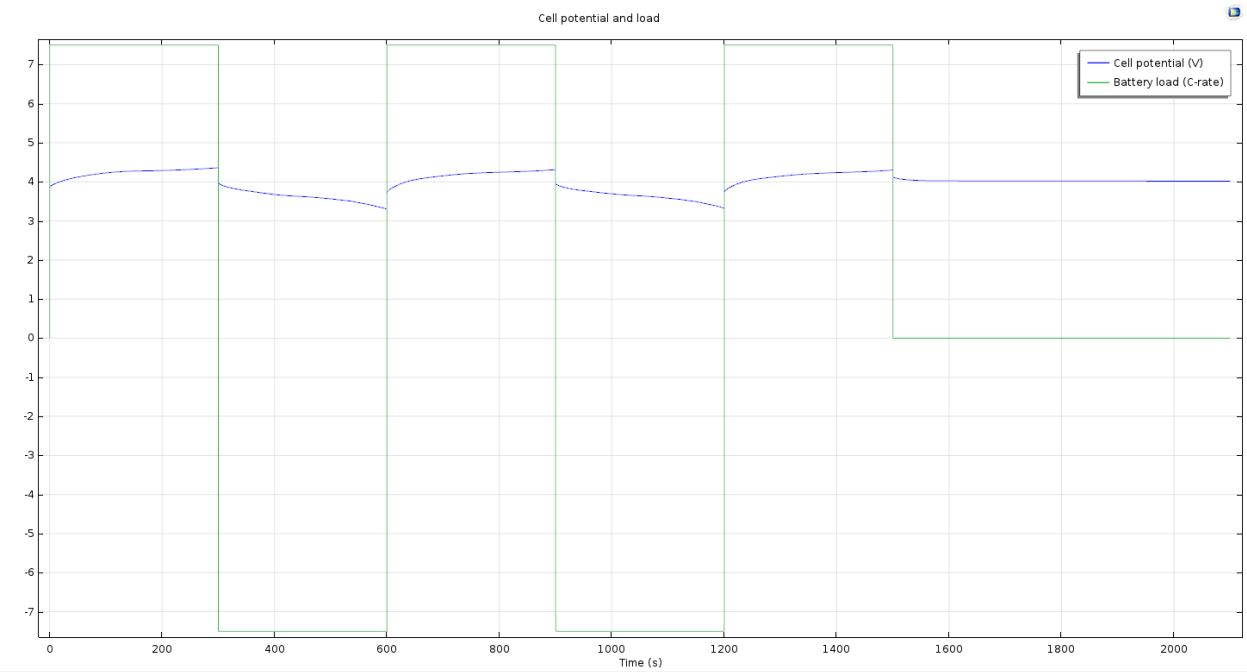

Figure 119 Scenario 1: Cell potential vs load current of lithium - ion battery 3d thermal model (Comsol Multiphysics)

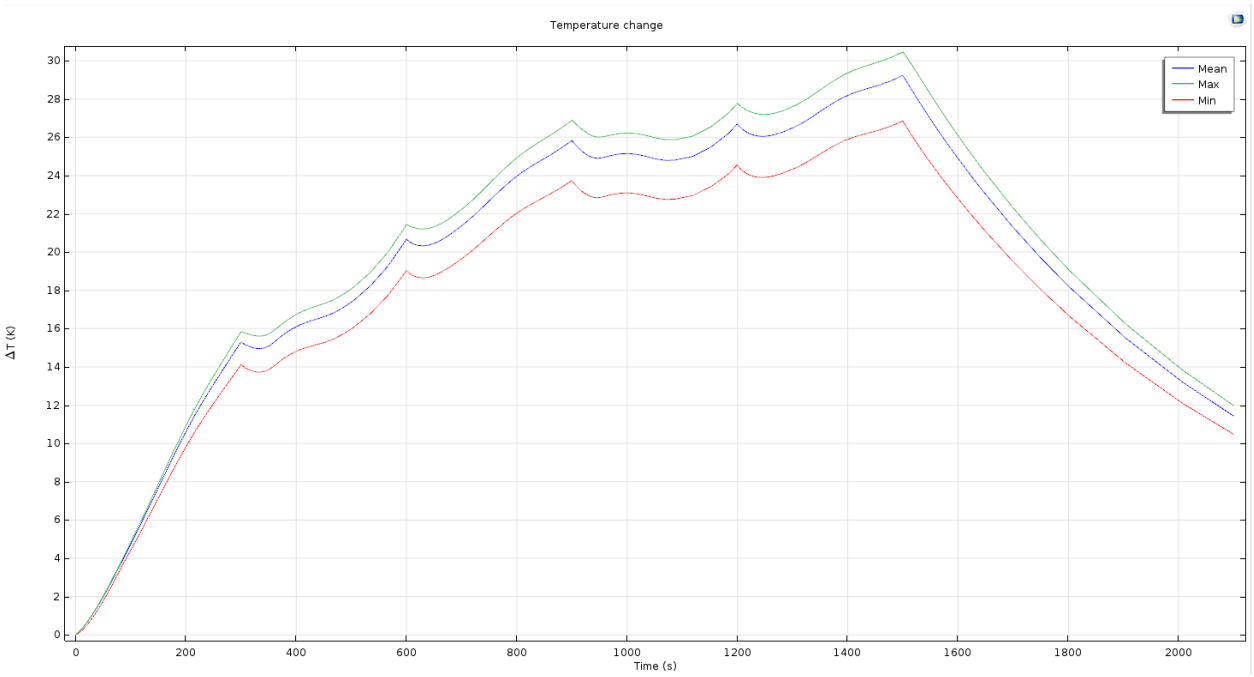

Figure 120 Scenario 1: Temperature changes of lithium - ion battery 3d thermal model (Comsol Multiphysics)

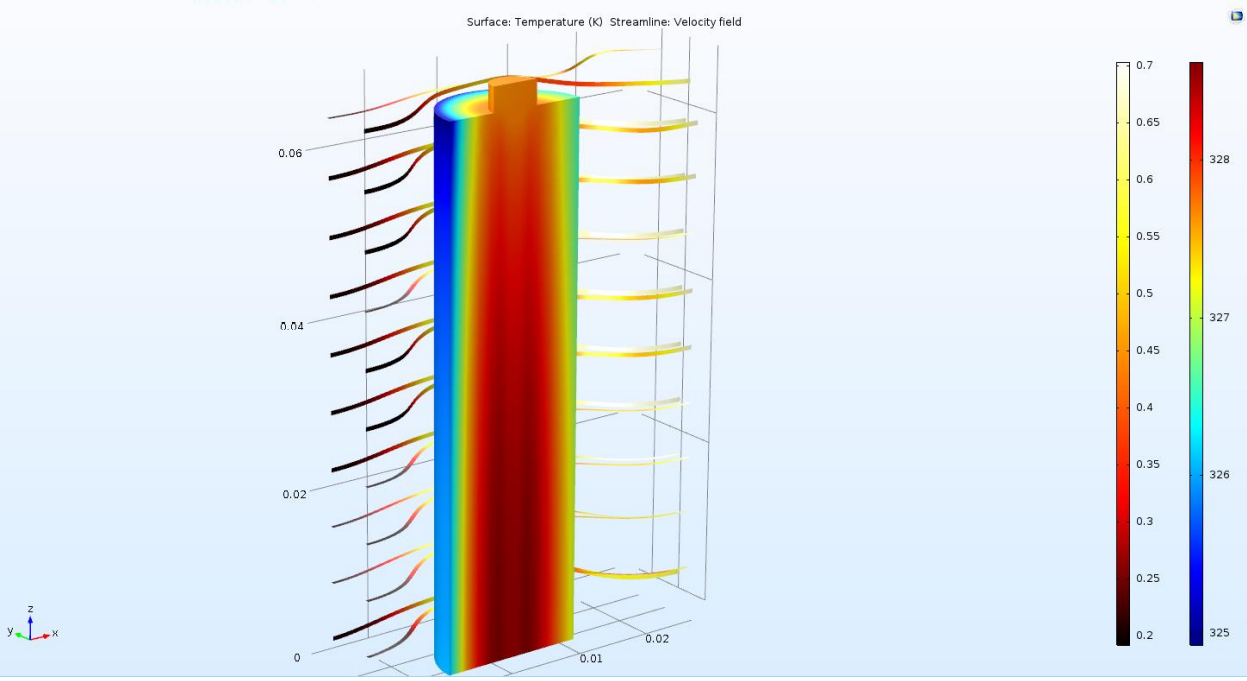

Figure 121 Scenario 1: Surface temperature of lithium - ion battery 3d thermal model (Comsol Multiphysics)

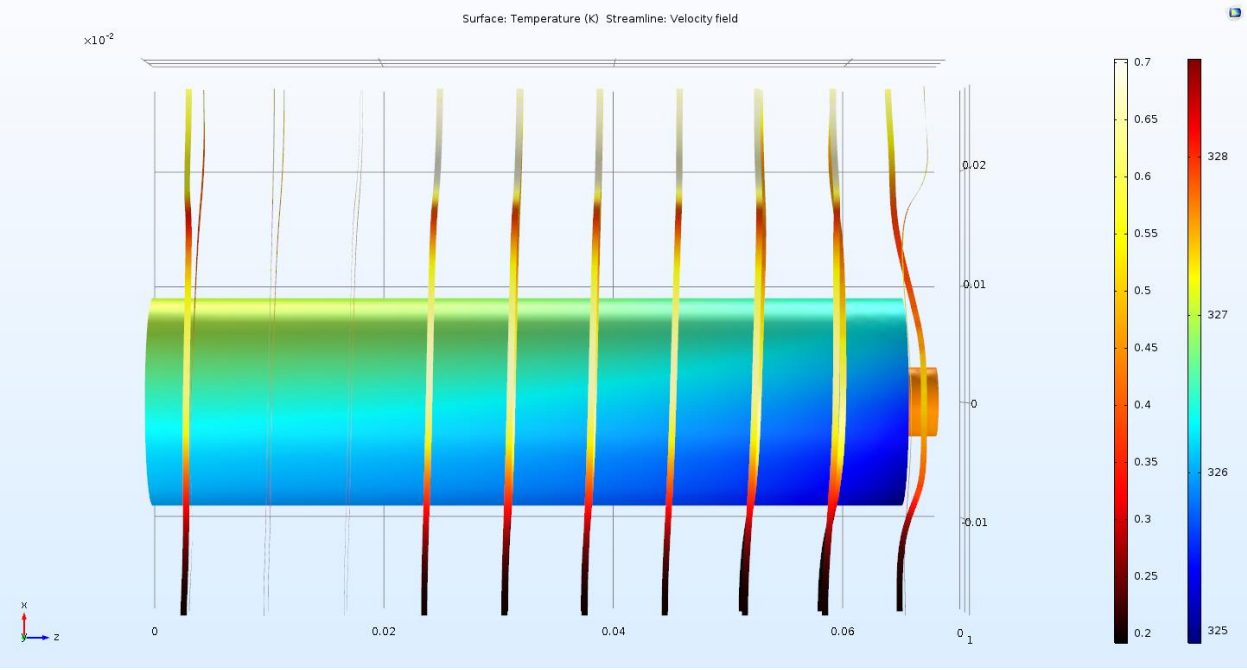

Figure 122 Scenario 1: Top view of surface temperature of lithium - ion battery 3d thermal model (Comsol Multiphysics)

- **Scenario 2: Inlet air velocity = 0.5 m/s**

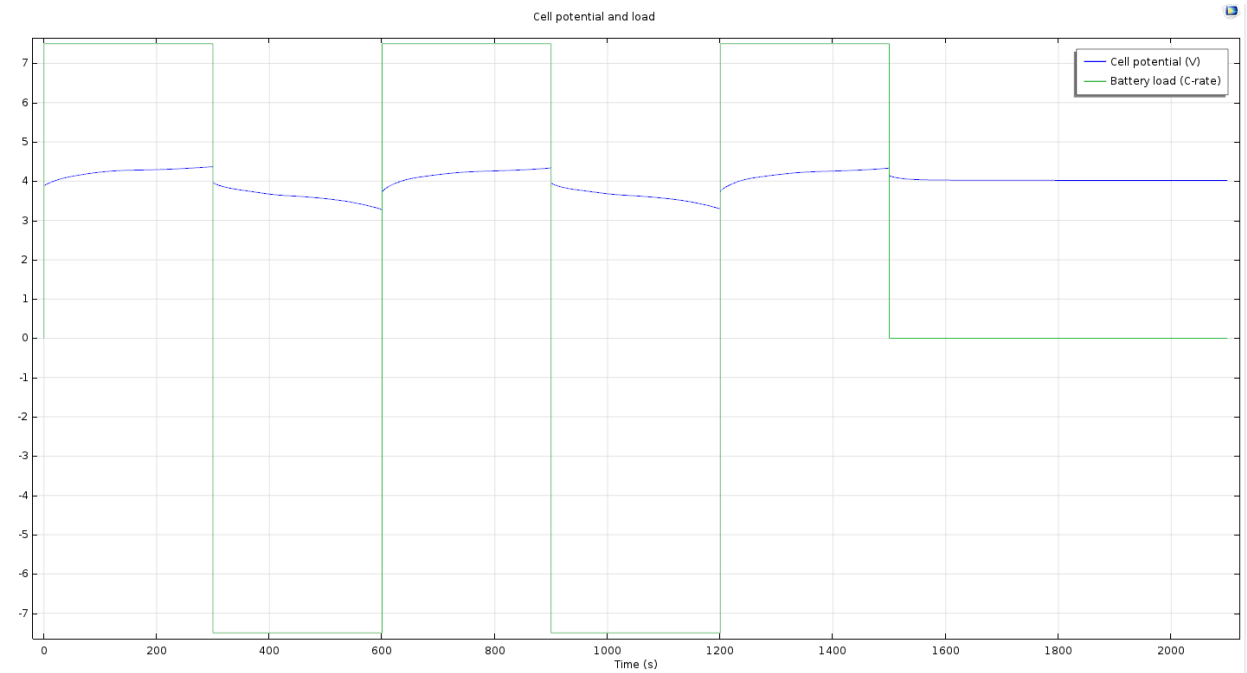

Figure 123 Scenario 2: Cell potential vs load current of lithium - ion battery 3d thermal model (Comsol Multiphysics)

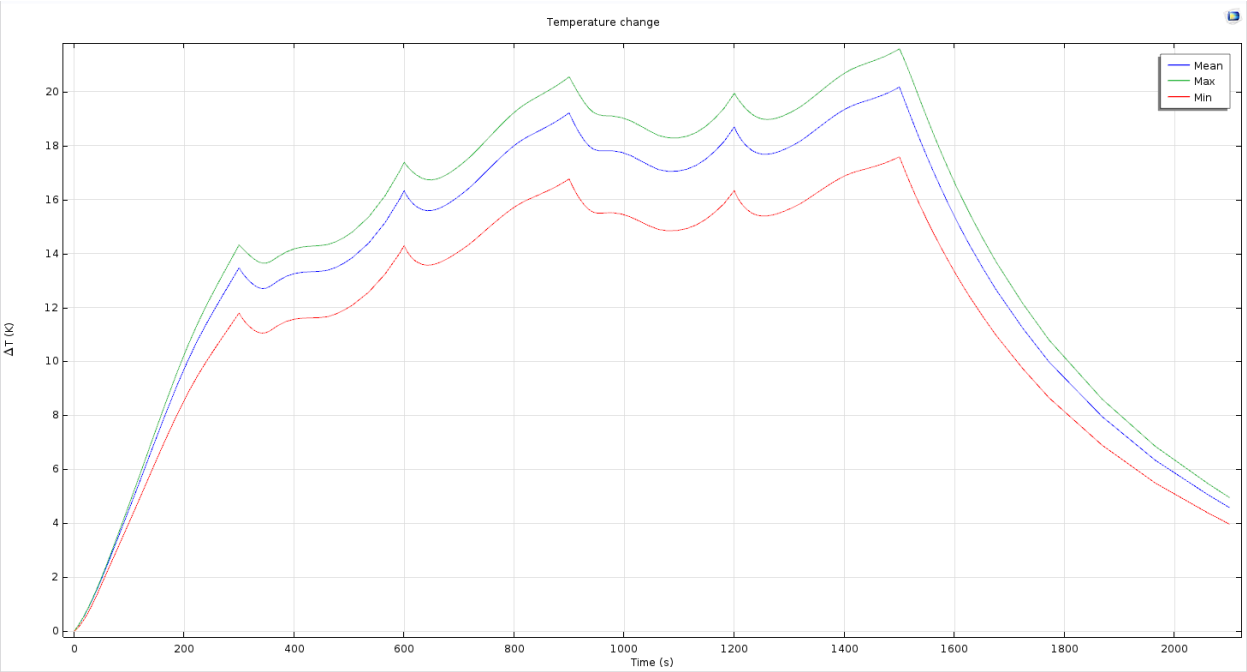

Figure 124 Scenario 2: Temperature changes of lithium - ion battery 3d thermal model (Comsol Multiphysics)

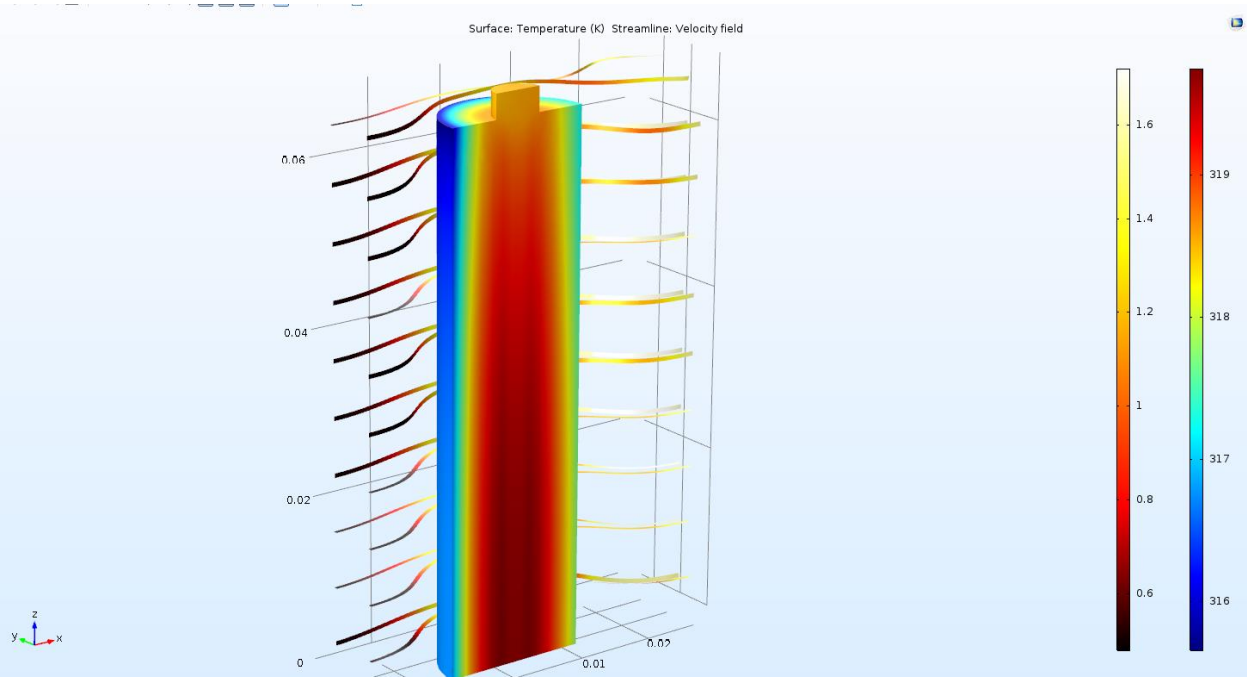

Figure 125 Scenario 2: Surface temperature of lithium - ion battery 3d thermal model (Comsol Multiphysics)

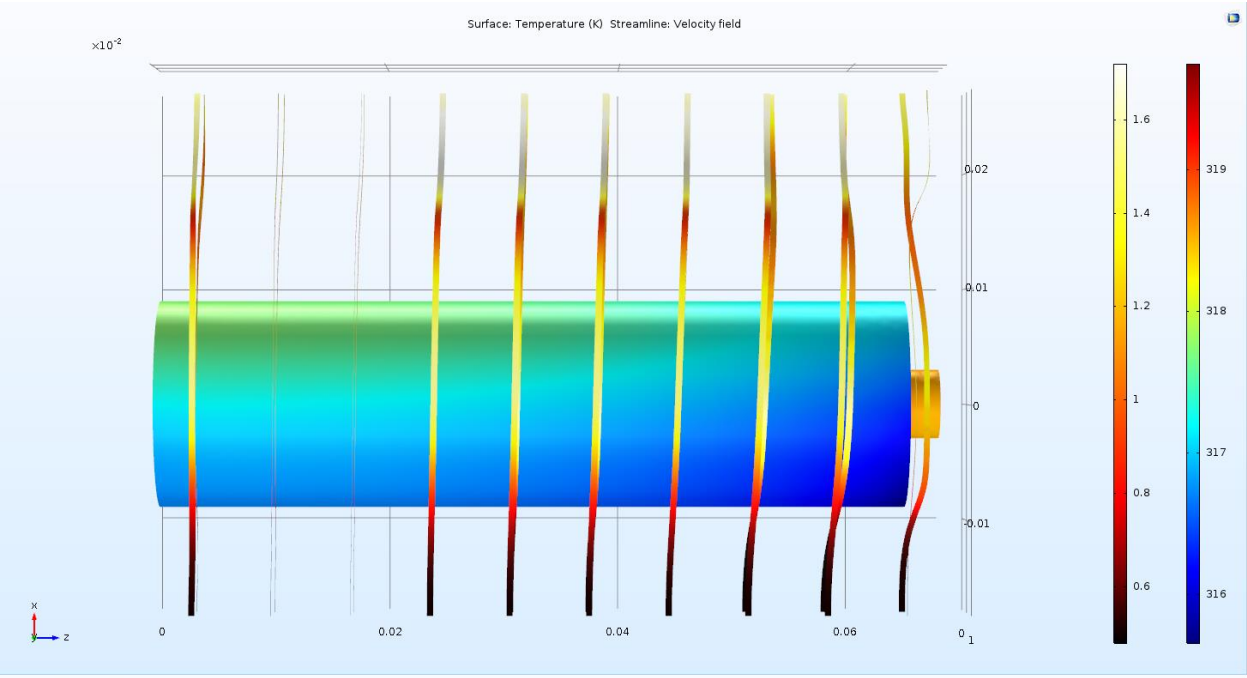

Figure 126 Scenario 2: Top view of surface temperature of lithium - ion battery 3d thermal model (Comsol Multiphysics)

- **Scenario 3: Inlet air velocity = 1 m/s**

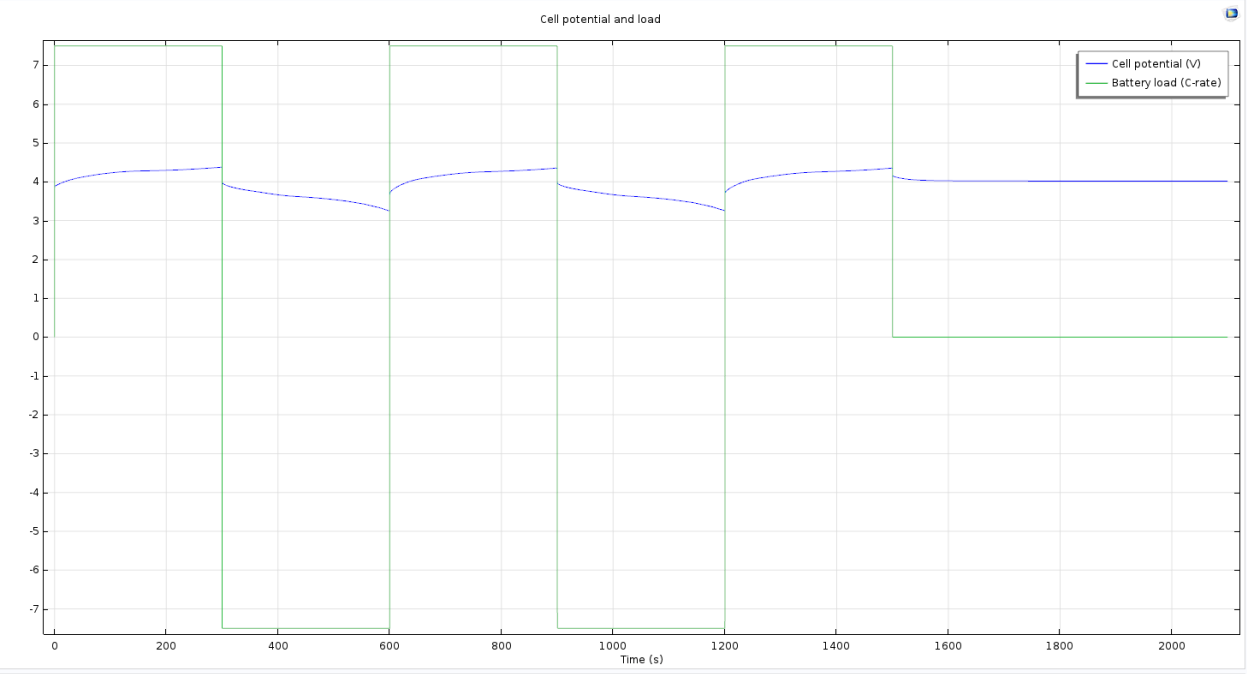

Figure 127 Scenario 3: Cell potential vs load current of lithium - ion battery 3d thermal model (Comsol Multiphysics)

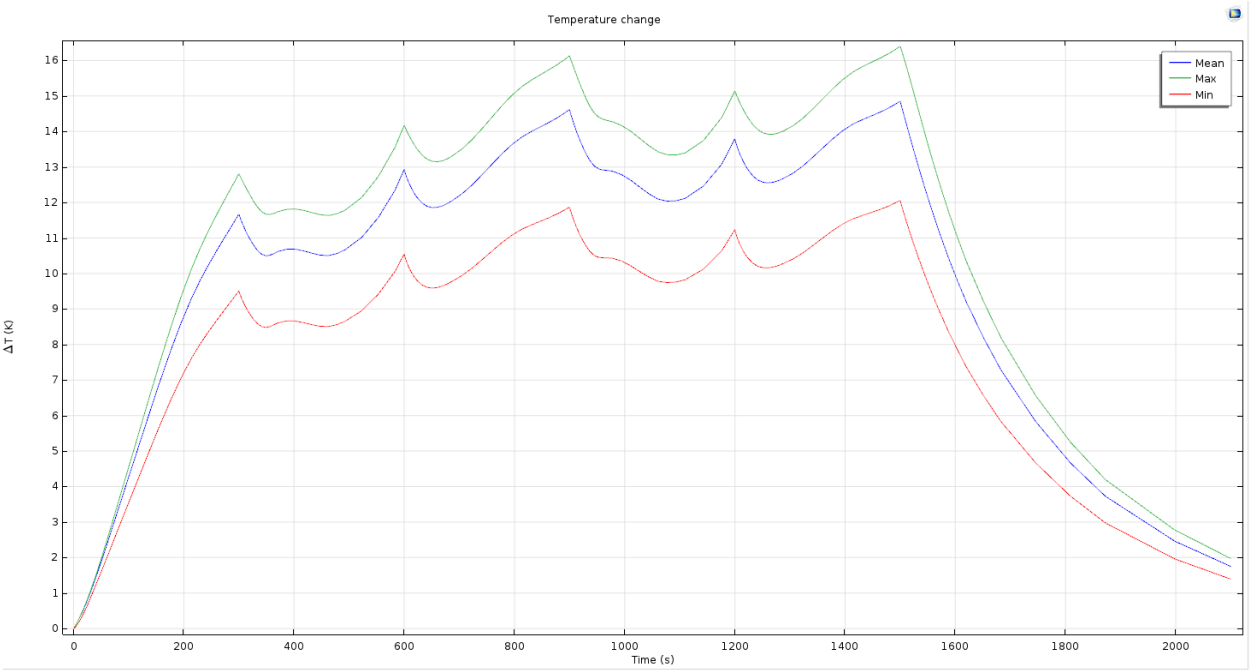

Figure 128 Scenario 3: Temperature changes of lithium - ion battery 3d thermal model (Comsol Multiphysics)

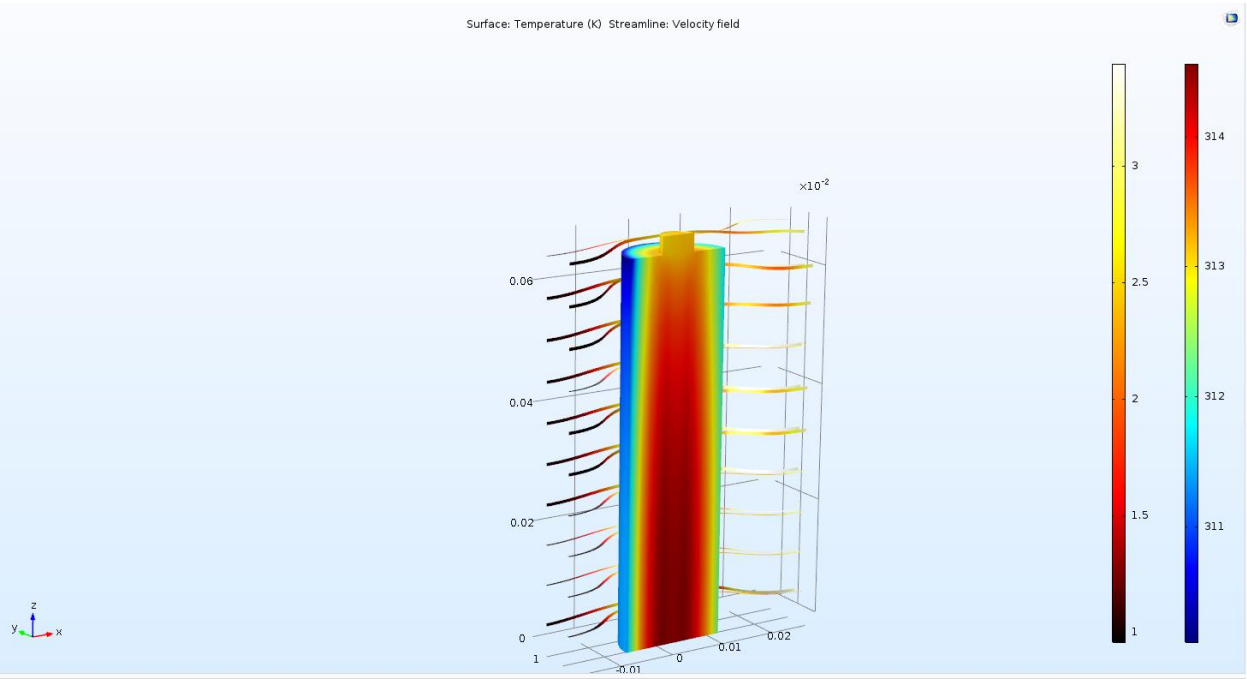

Figure 129 Scenario 3: Surface temperature of lithium - ion battery 3d thermal model (Comsol Multiphysics)

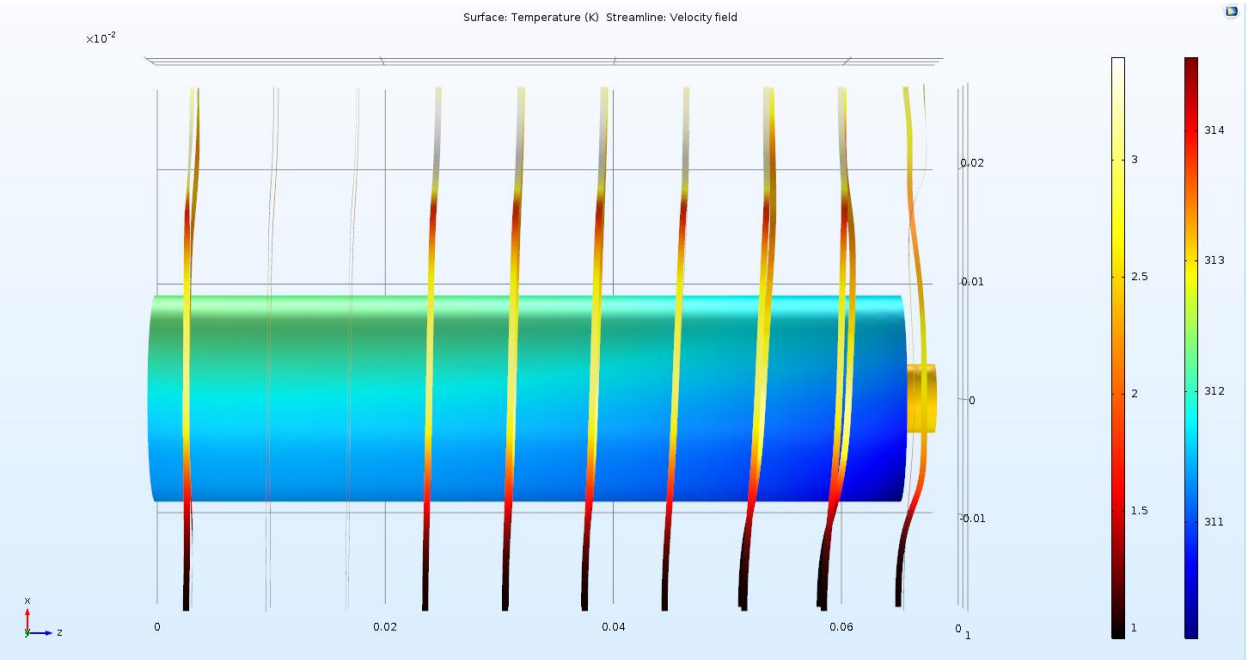

Figure 130 Scenario 3: Top view of surface temperature of lithium - ion battery 3d thermal model (Comsol Multiphysics)

Other things being equal and keeping the inlet air velocity at 1 m/s, three more scenarios are defined changing the battery's C-factor being initially equal to 7.5.

- **Scenario 4: C-factor = 1**

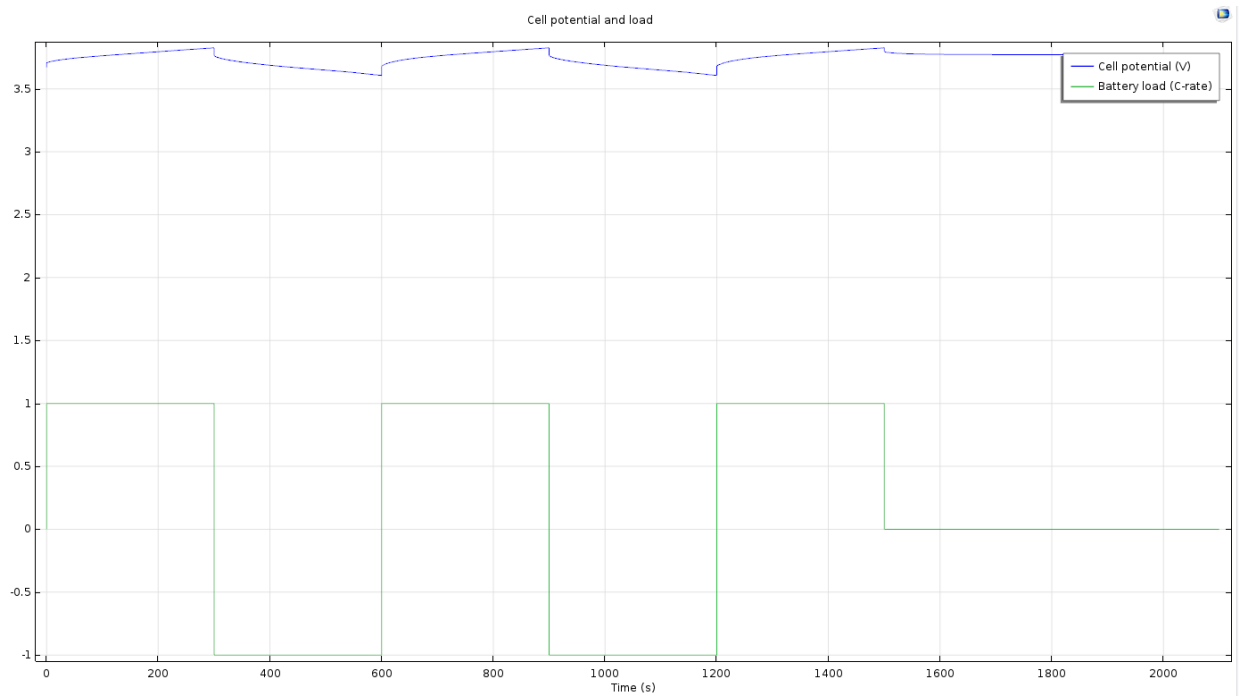

Figure 131 Scenario 4: Cell potential vs load current of lithium - ion battery 3d thermal model (Comsol Multiphysics)

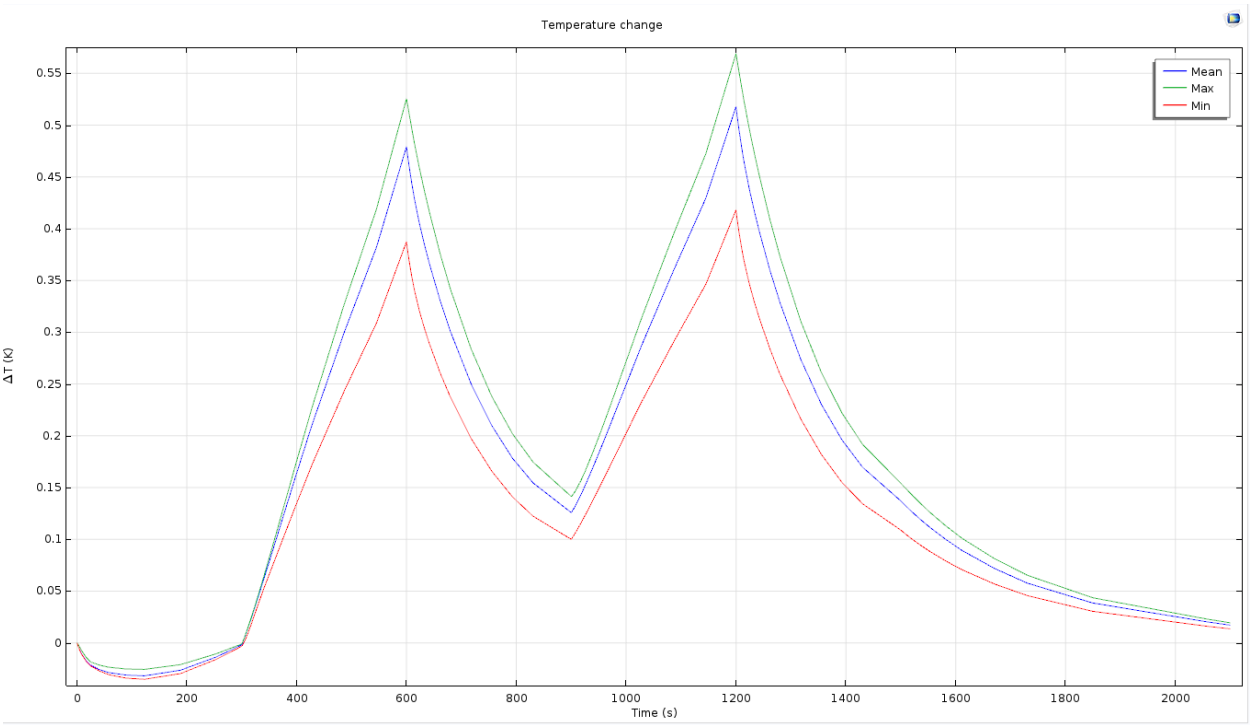

Figure 132 Scenario 4: Temperature changes of lithium - ion battery 3d thermal model (Comsol Multiphysics)

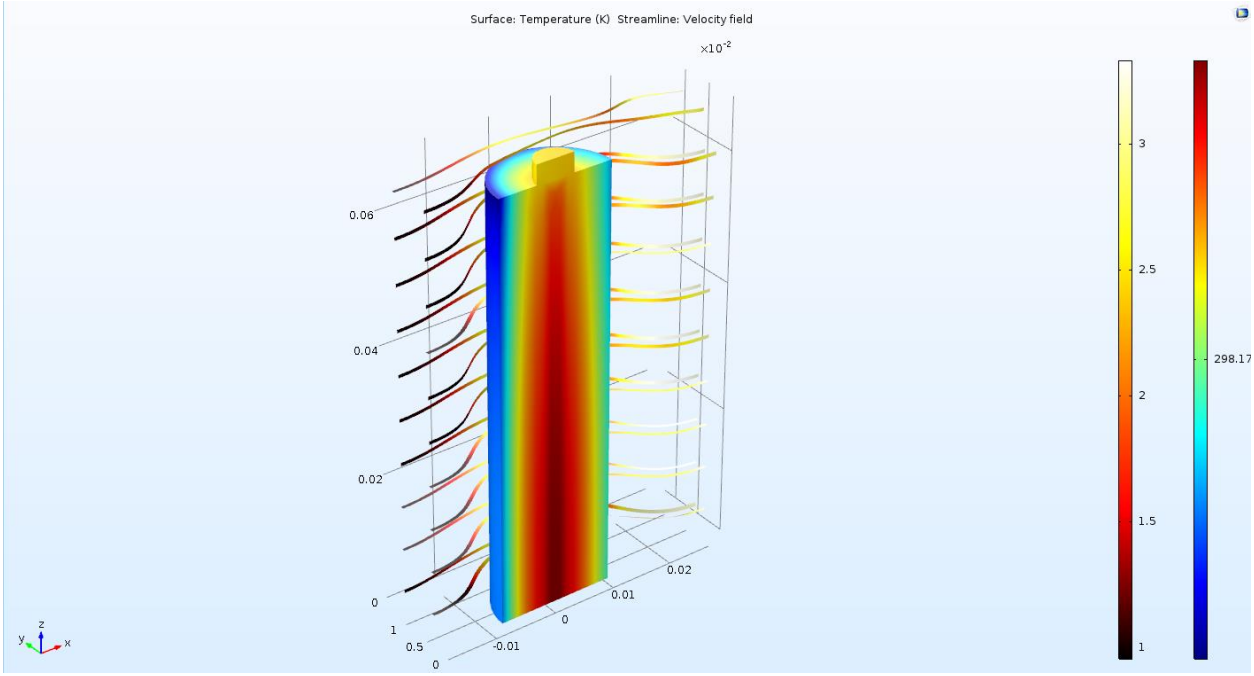

Figure 133 Scenario 4: Surface temperature of lithium - ion battery 3d thermal model (Comsol Multiphysics)

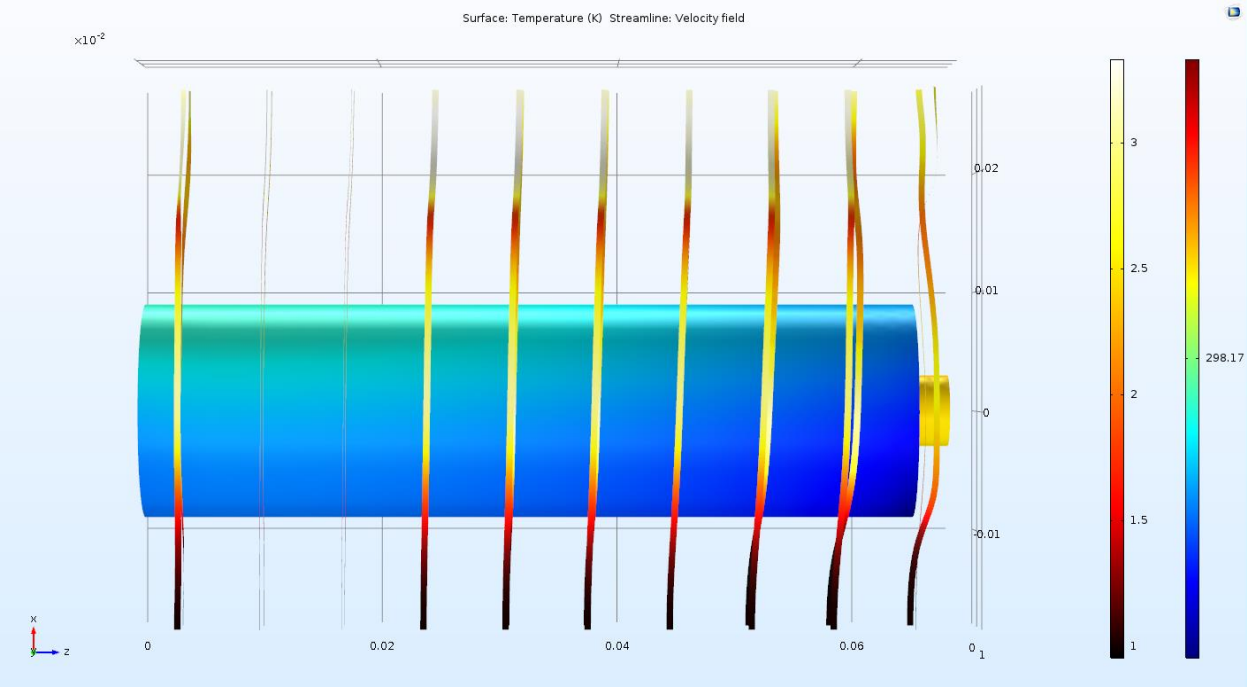

Figure 134 Scenario 4: Top view of surface temperature of lithium - ion battery 3d thermal model (Comsol Multiphysics)

- **Scenario 5: C-factor = 5**

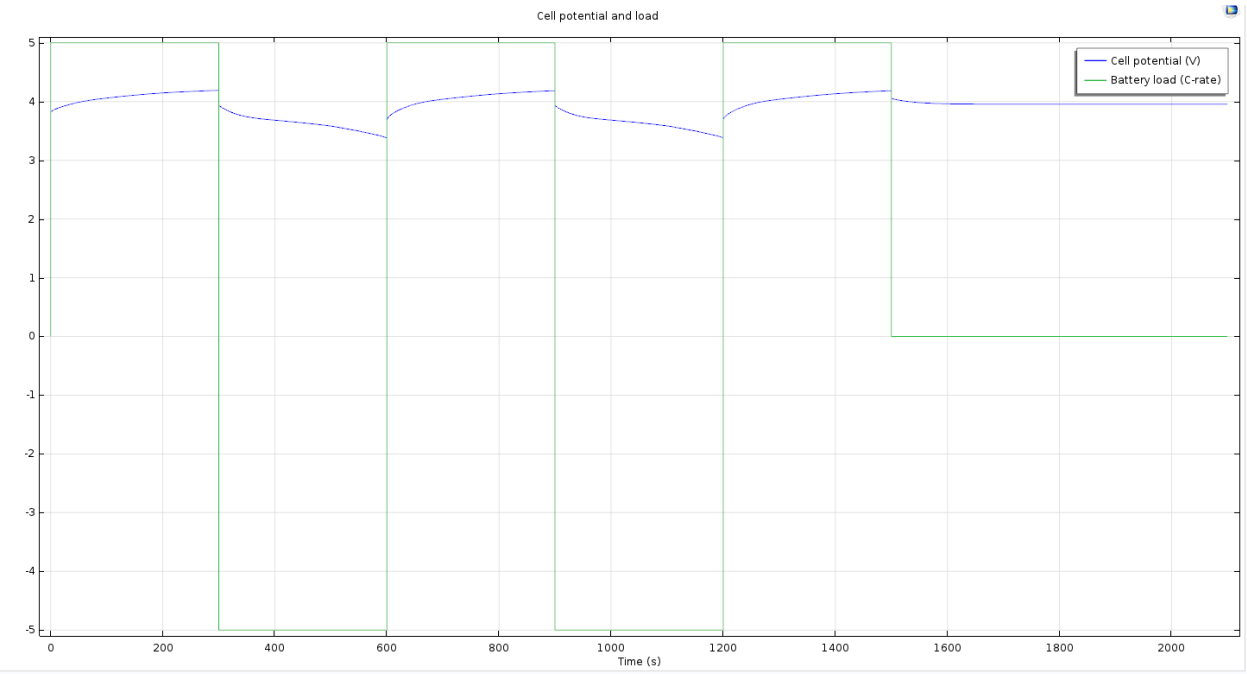

Figure 135 Scenario 5: Cell potential vs load current of lithium - ion battery 3d thermal model (Comsol Multiphysics)

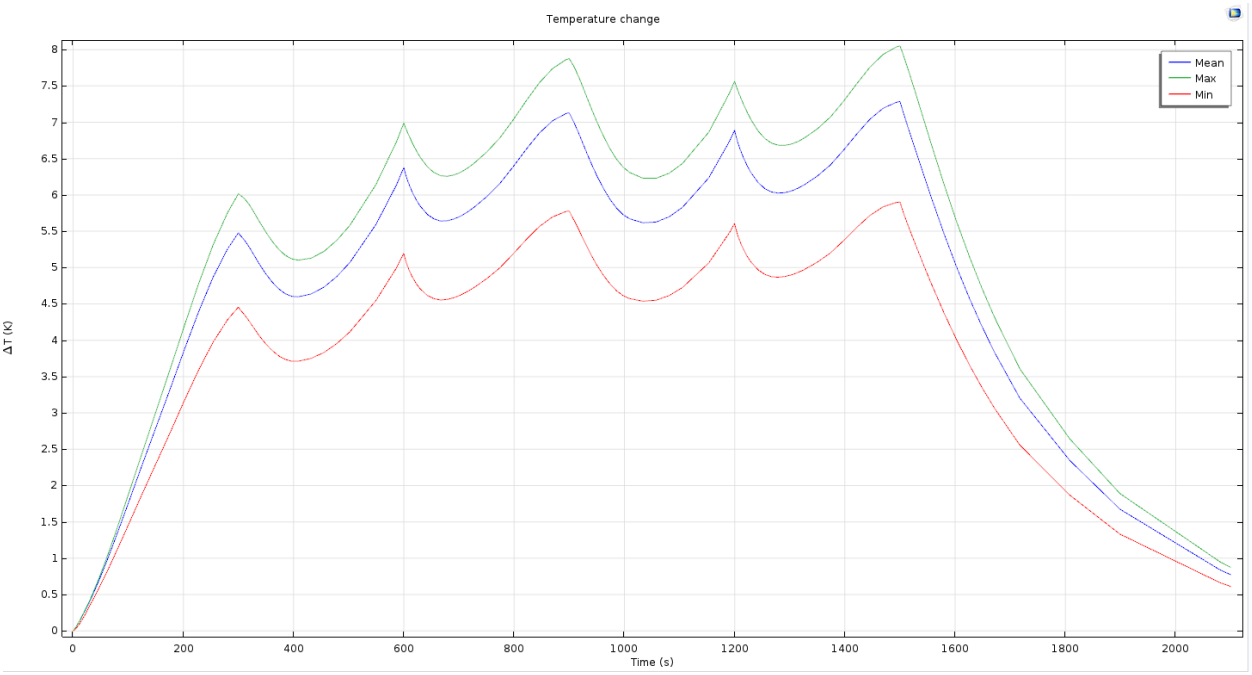

Figure 136 Scenario 5: Temperature changes of lithium - ion battery 3d thermal model (Comsol Multiphysics)

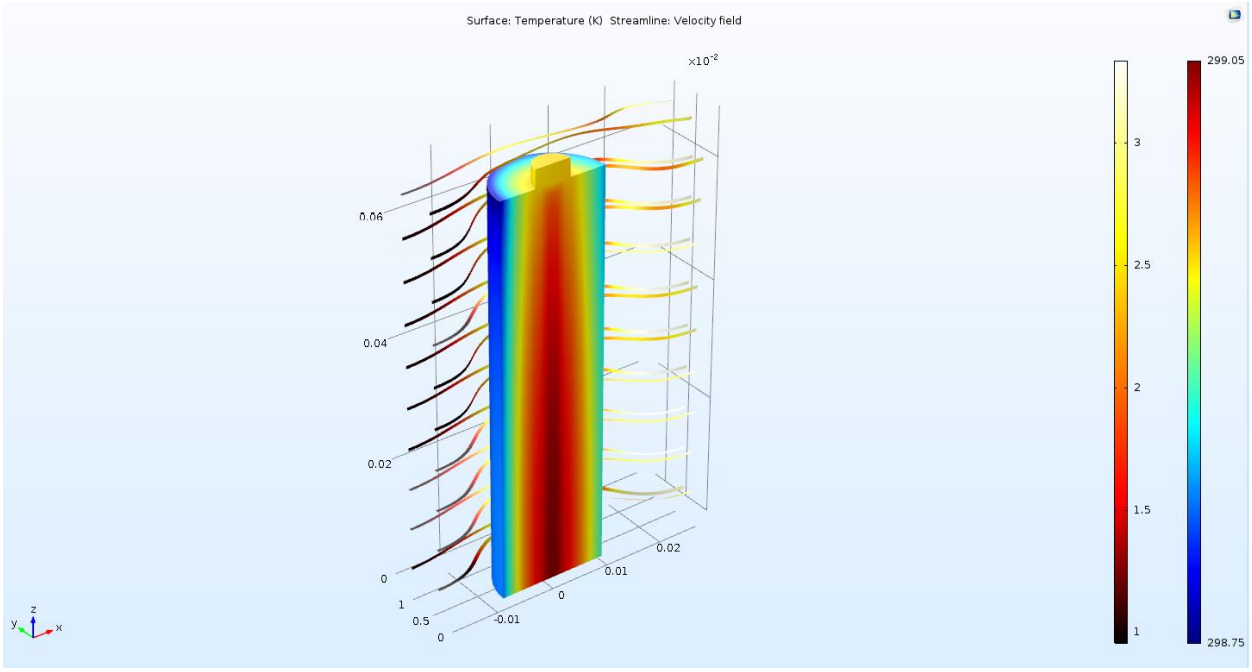

Figure 137 Scenario 5: Surface temperature of lithium - ion battery 3d thermal model (Comsol Multiphysics)

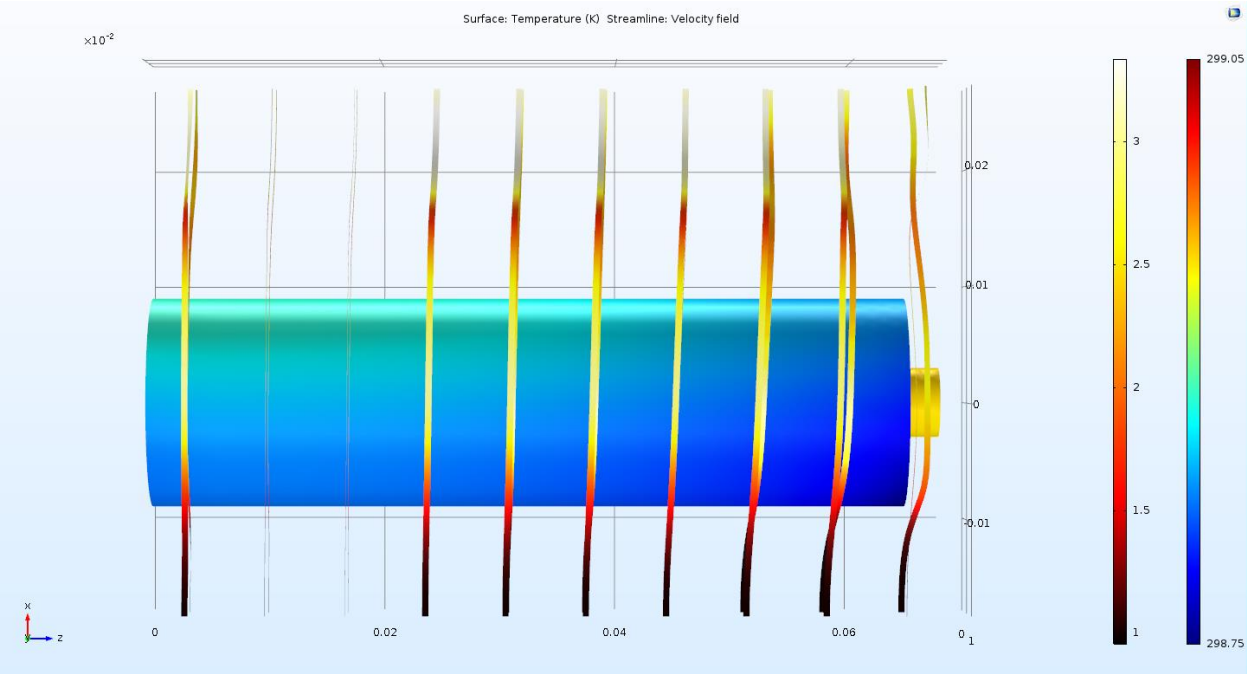

Figure 138 Scenario 5: Top view of surface temperature of lithium - ion battery 3d thermal model (Comsol Multiphysics)

- **Scenario 6: C-factor = 10**

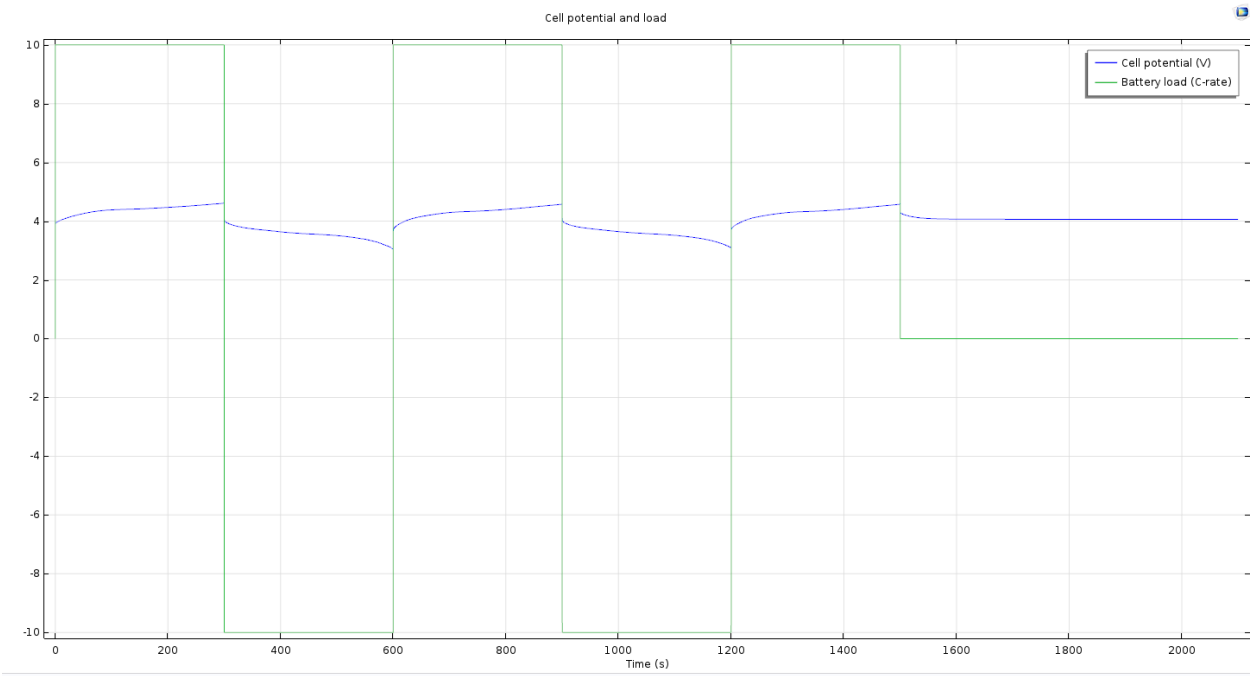

Figure 139 Scenario 6: Cell potential vs load current of lithium - ion battery 3d thermal model (Comsol Multiphysics)

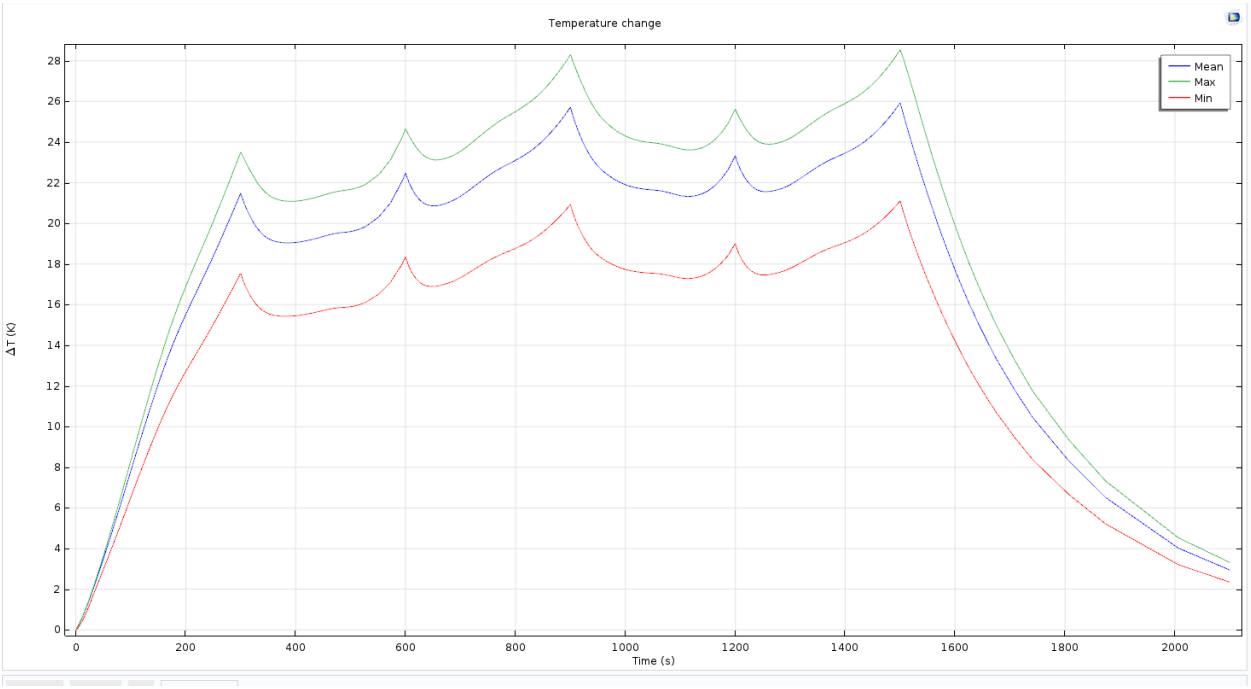

Figure 140 Scenario 6: Temperature changes of lithium - ion battery 3d thermal model (Comsol Multiphysics)

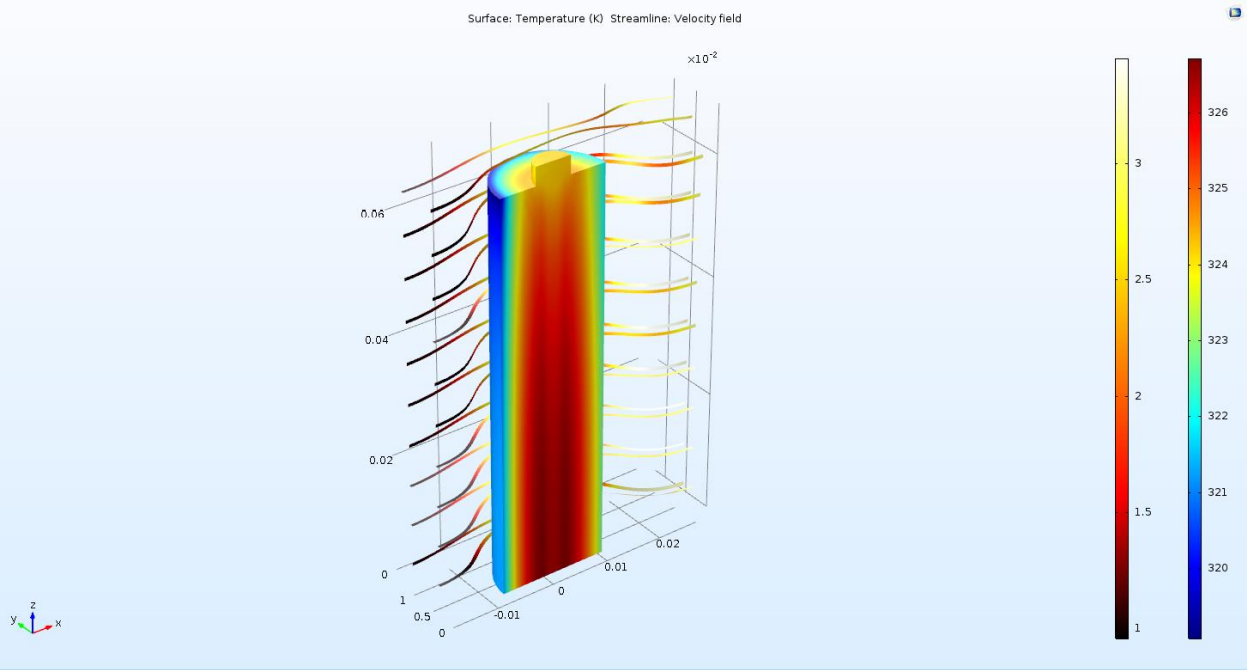

Figure 141 Scenario 6: Surface temperature of lithium - ion battery 3d thermal model (Comsol Multiphysics)

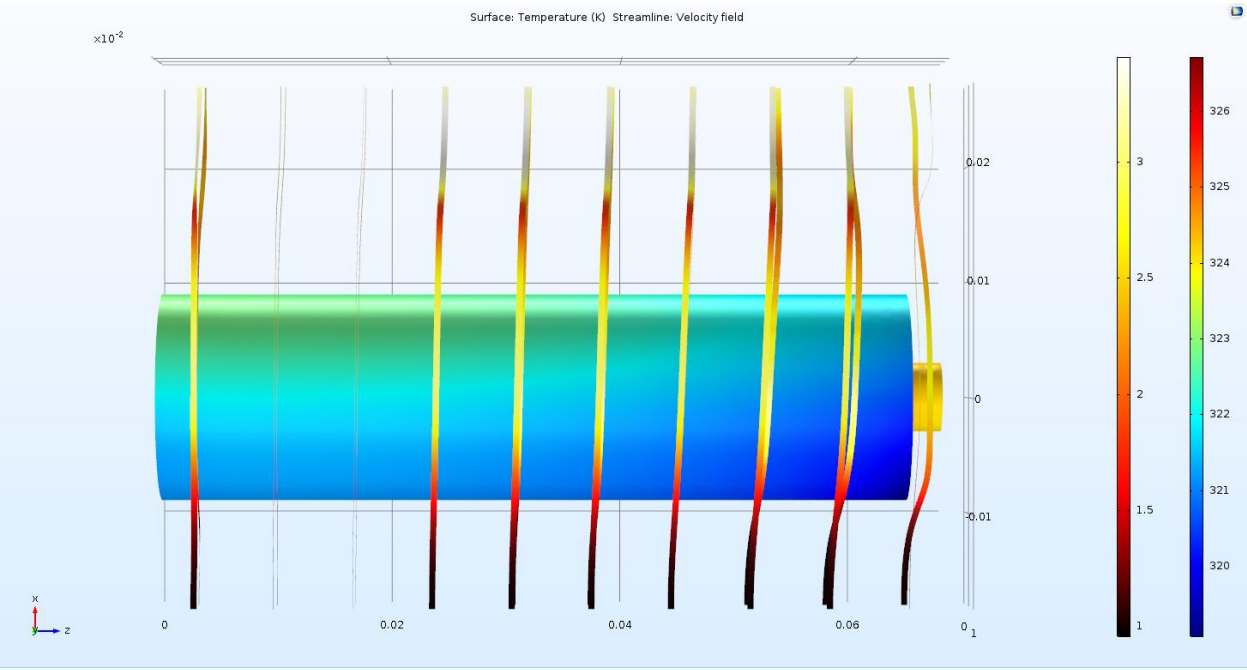

Figure 142 Scenario 4: Top view of surface temperature of lithium - ion battery 3d thermal model (Comsol Multiphysics)

Other things being equal and keeping the C-factor equal to 10 and the battery heat capacity equal to 1399.1 J/kgK, the initial battery radius (0.009 m) is changed and two more scenarios are defined. The battery radius change directly affects the length of the inlet flow region and the battery – battery distance in matrix.

- **Scenario 7: Battery radius = 0.015 m**

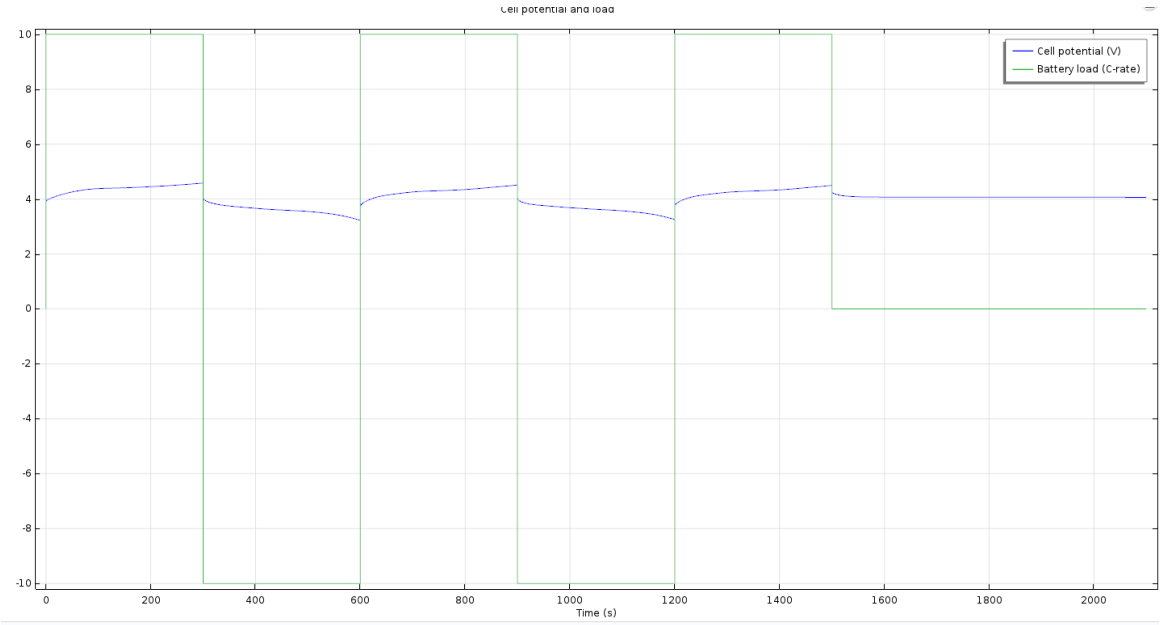

Figure 143 Scenario 7: Cell potential vs load current of lithium - ion battery 3d thermal model (Comsol Multiphysics)

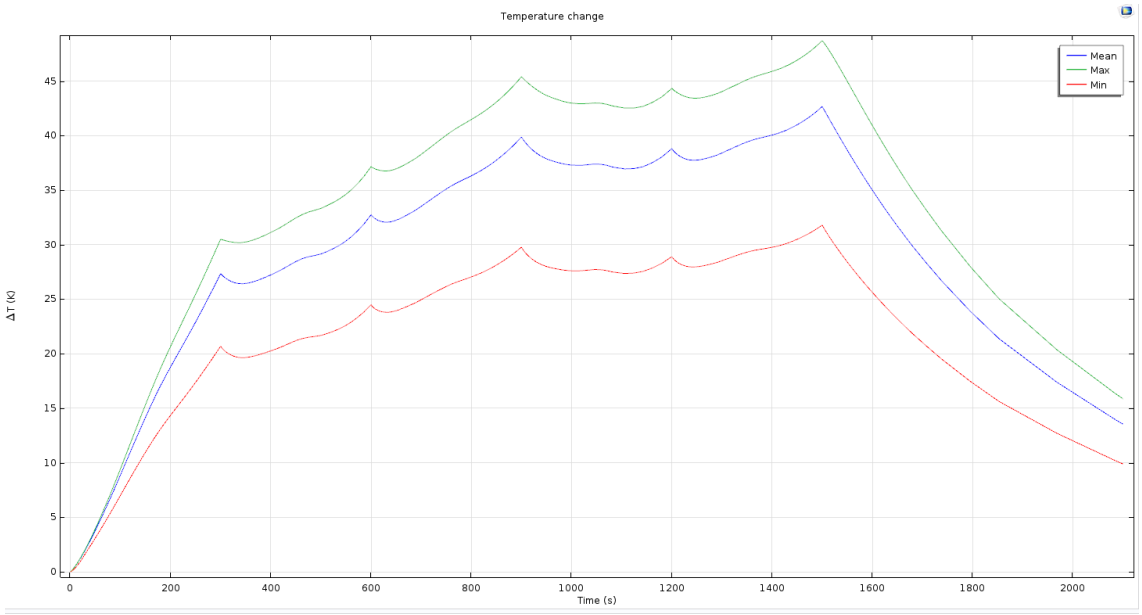

Figure 144 Scenario 7: Temperature changes of lithium - ion battery 3d thermal model (Comsol Multiphysics)

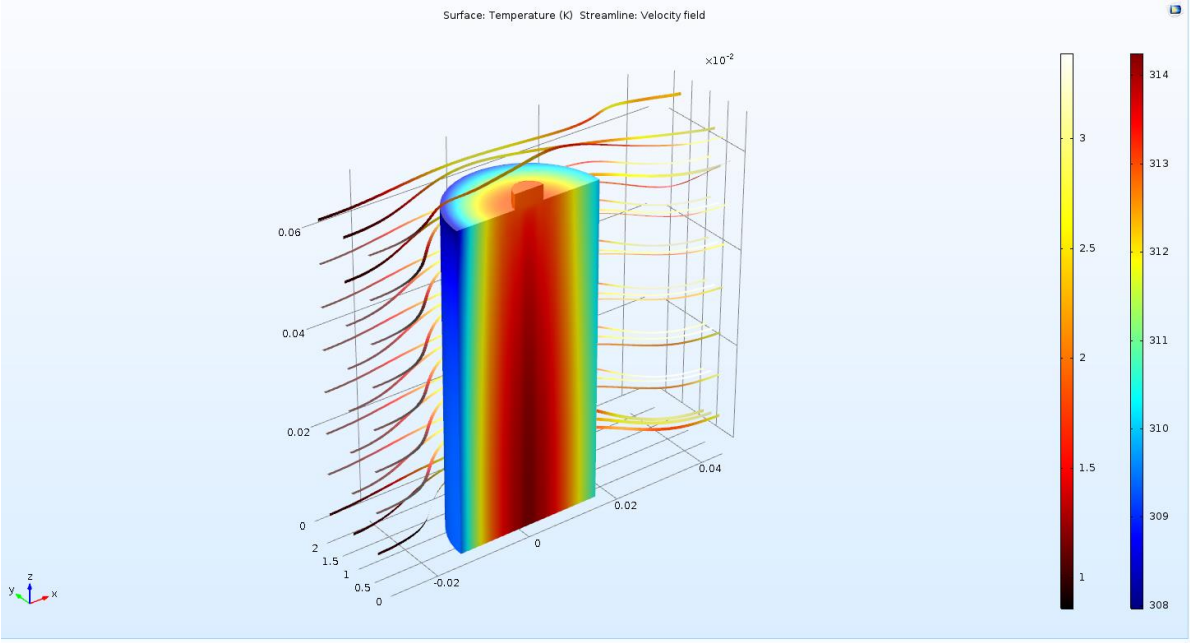

Figure 145 Scenario 7: Surface temperature of lithium - ion battery 3d thermal model (Comsol Multiphysics)

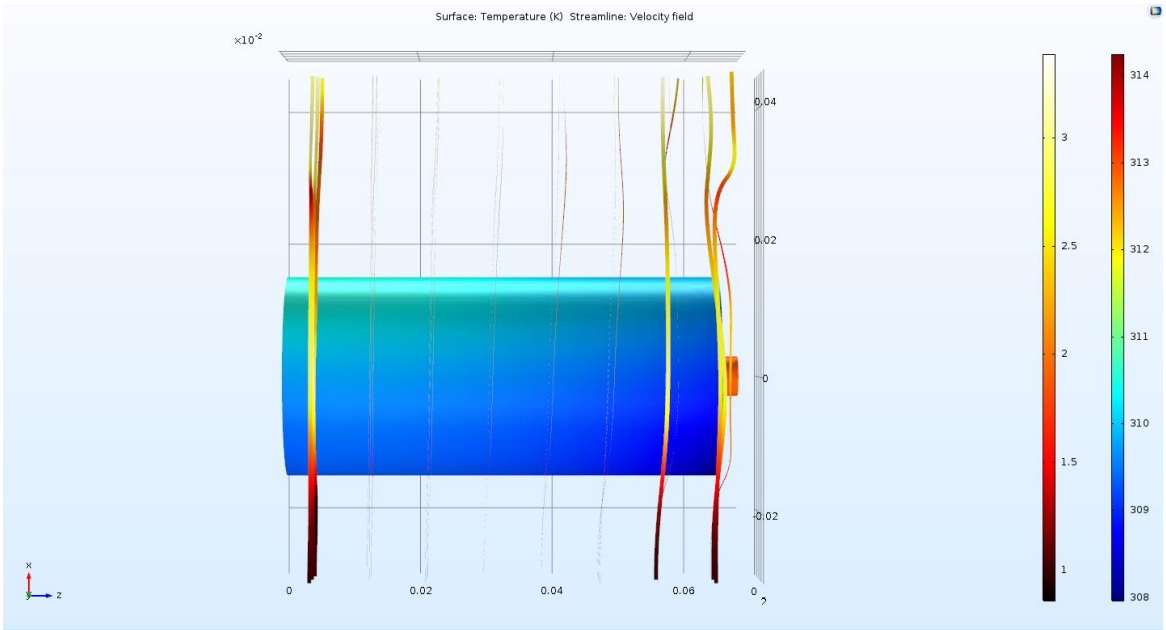

Figure 146 Scenario 7: Top view of surface temperature of lithium - ion battery 3d thermal model (Comsol Multiphysics)

- **Scenario 8: Battery radius = 0.025 m**

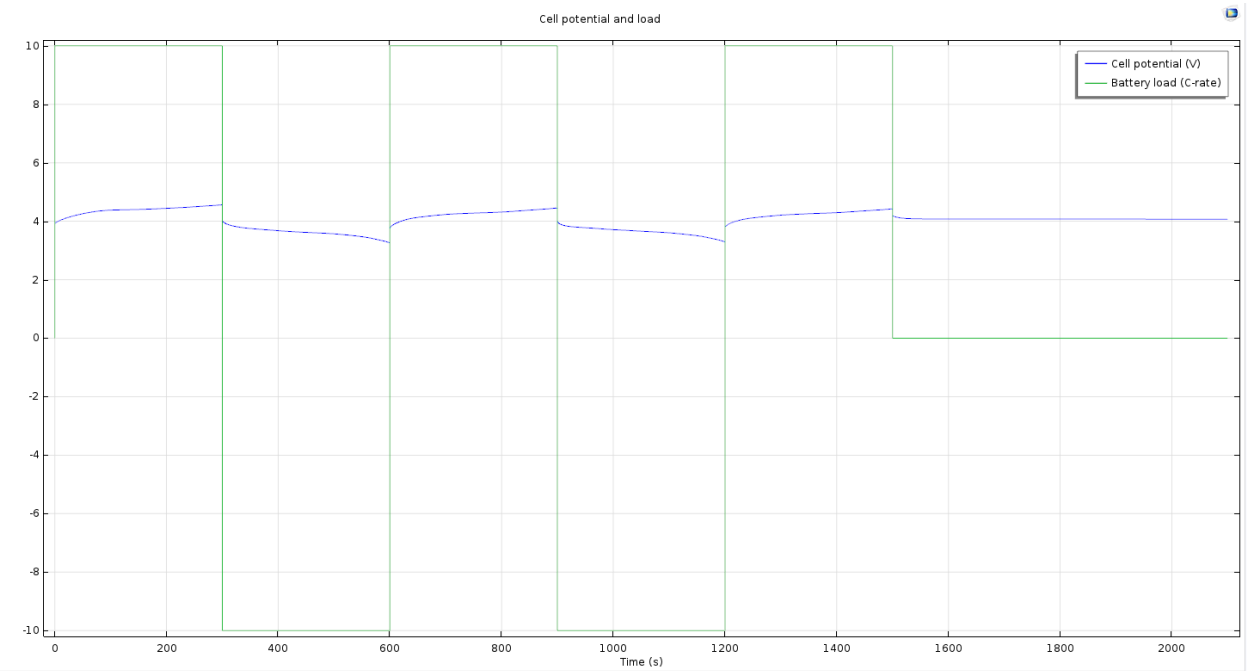

Figure 147 Scenario 8: Cell potential vs load current of lithium - ion battery 3d thermal model (Comsol Multiphysics)

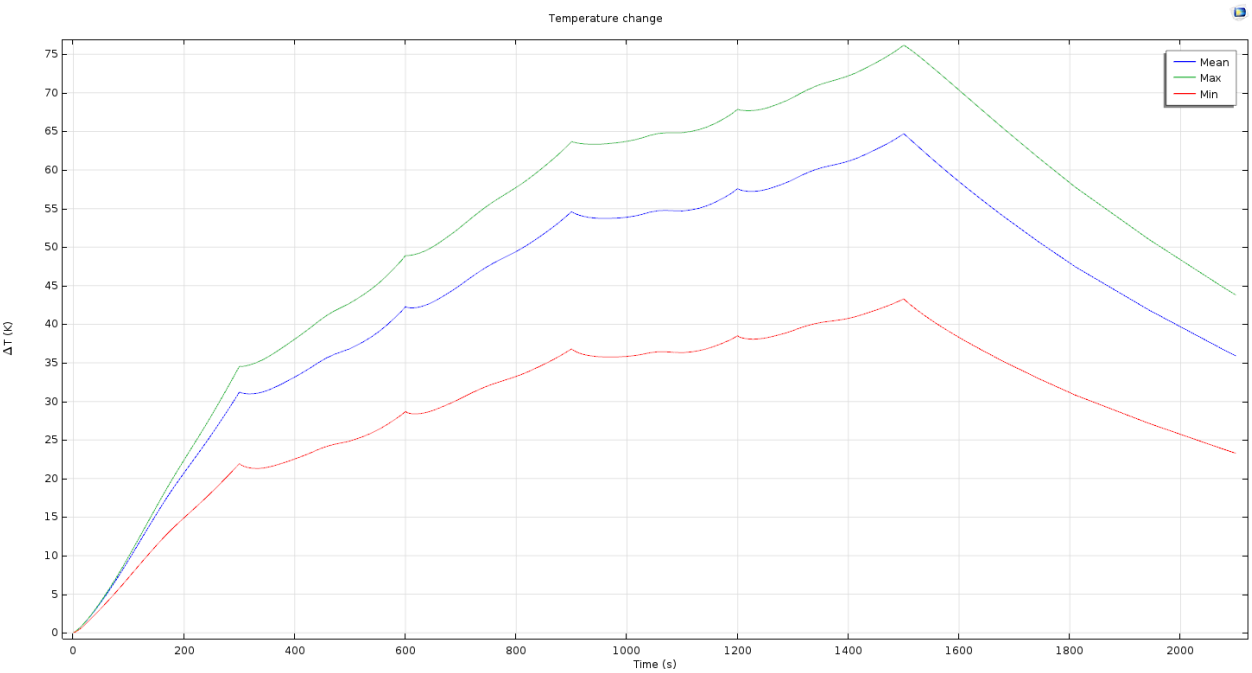

Figure 148 Scenario 8: Temperature changes of lithium - ion battery 3d thermal model (Comsol Multiphysics)

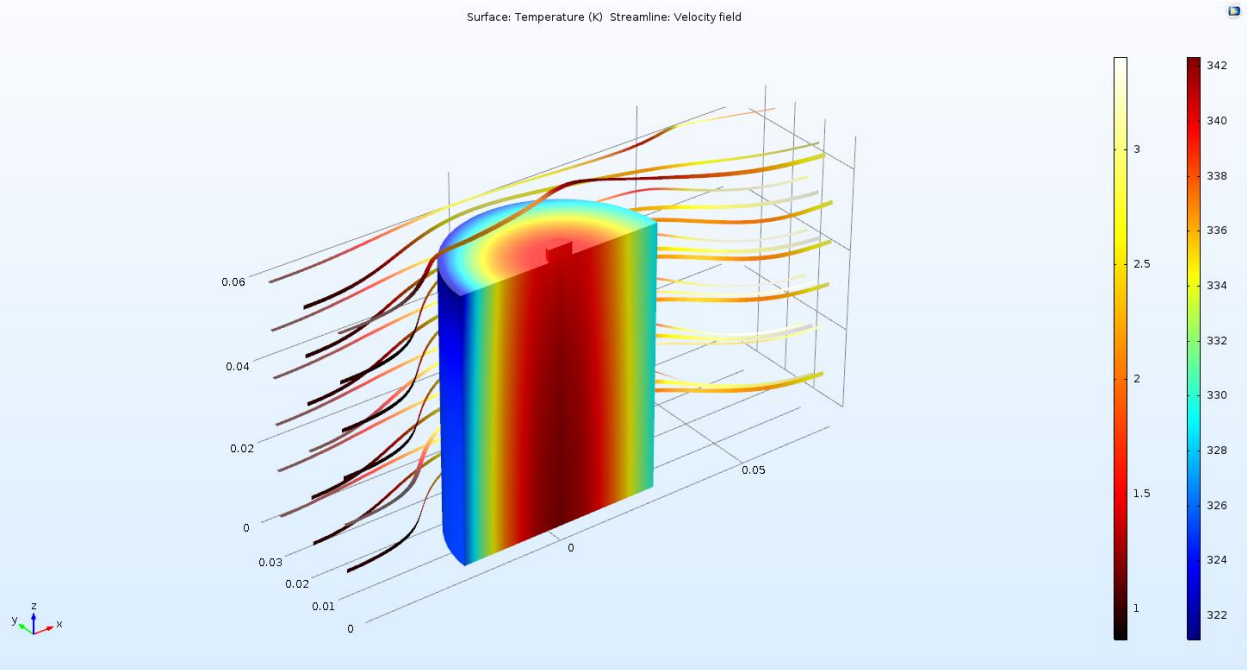

Figure 149 Scenario 8: Surface temperature of lithium - ion battery 3d thermal model (Comsol Multiphysics)

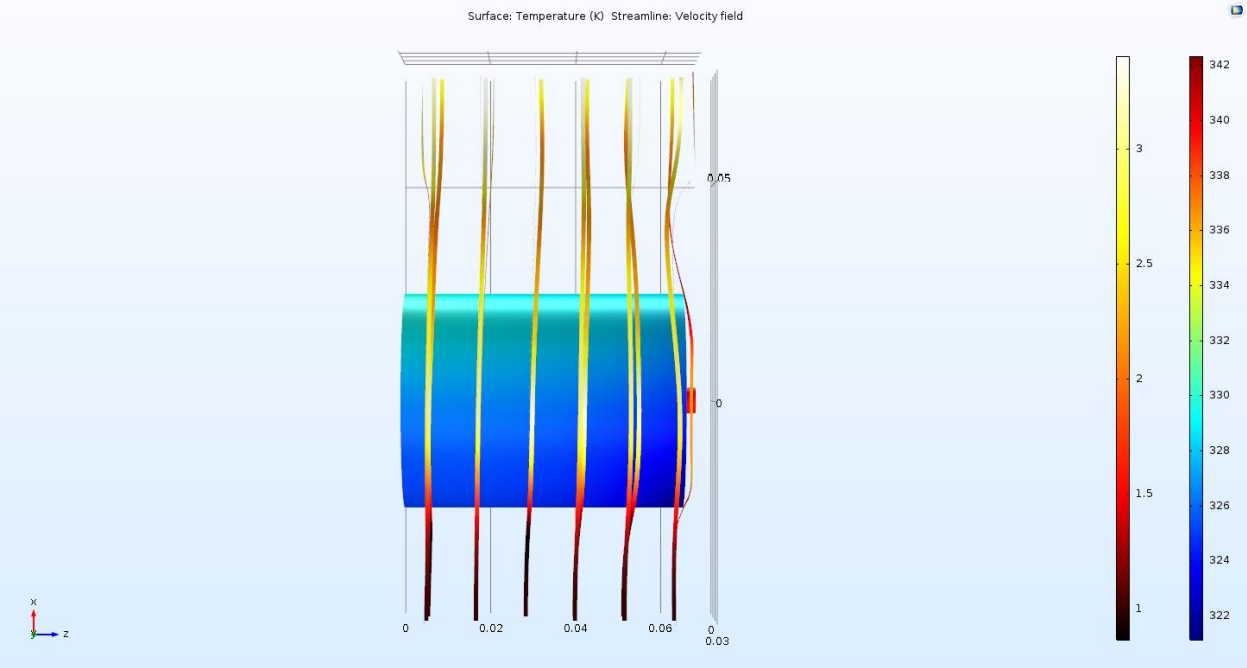

Figure 150 Scenario 8: Top view of surface temperature of lithium - ion battery 3d thermal model (Comsol Multiphysics)

The battery heat capacity is defined as the heat required to increase or reduce the battery's temperature by 1 degree ^{o}C. The battery heat generation deriving from Joule losses and enthalpy changes owing to

electrochemical reactions during charging and discharging is essential to the thermal management system design [60]. Thus, other things being equal, scenario 9 with battery radius equal to 9 mm and having the reaction rate coefficient in the positive electrode from $5*10^{-10}$ to $10*10^{-10}$ m/s changed and the reaction rate coefficient in the positive electrode from $2*10^{-11}$ to $4*10^{-11}$ m/s, is simulated.

- **Scenario 9: Reaction rate coefficient in the positive electrode = $10*10^{-10}$ m/s, Reaction rate coefficient in the negative electrode = $4*10^{-11}$ m/s**

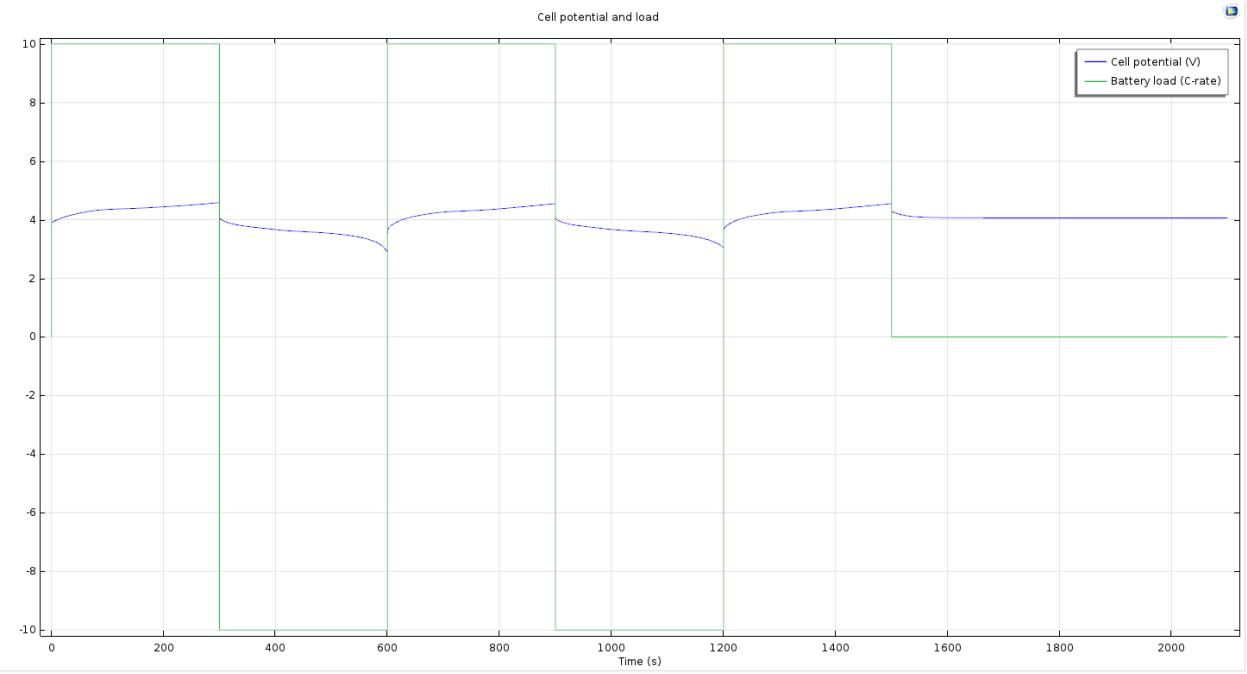

Figure 151 Scenario 9: Cell potential vs load current of lithium - ion battery 3d thermal model (Comsol Multiphysics)

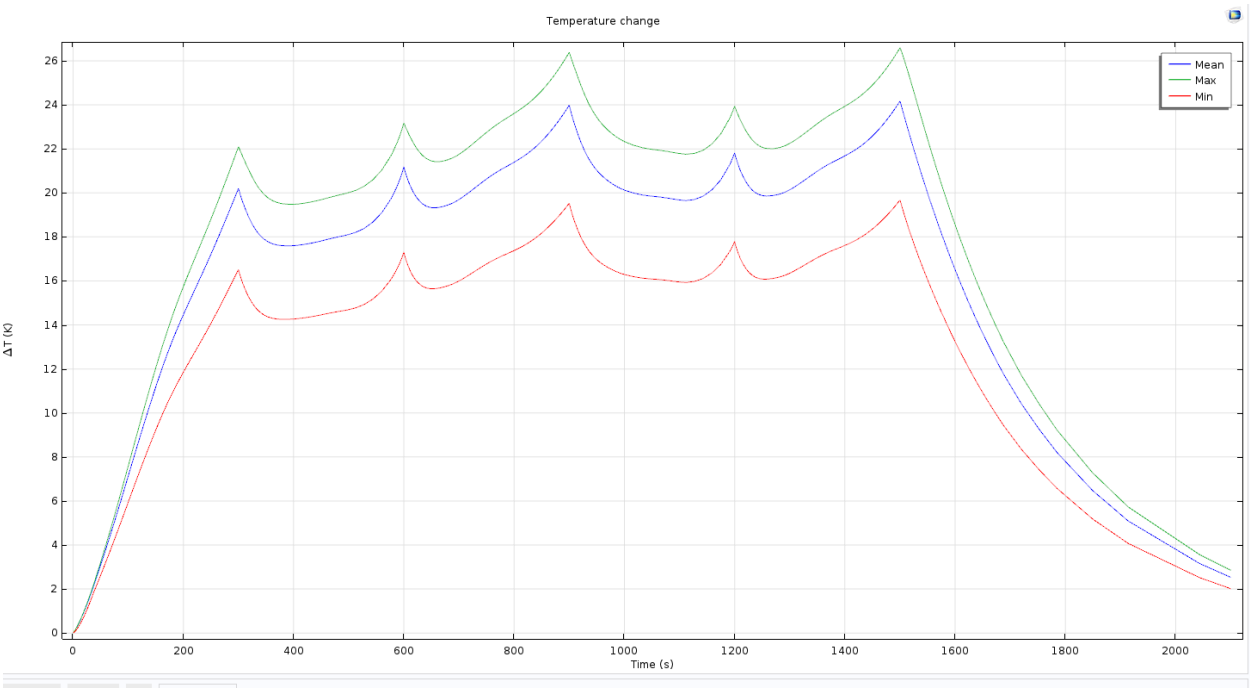

Figure 152 Scenario 9: Temperature changes of lithium - ion battery 3d thermal model (Comsol Multiphysics)

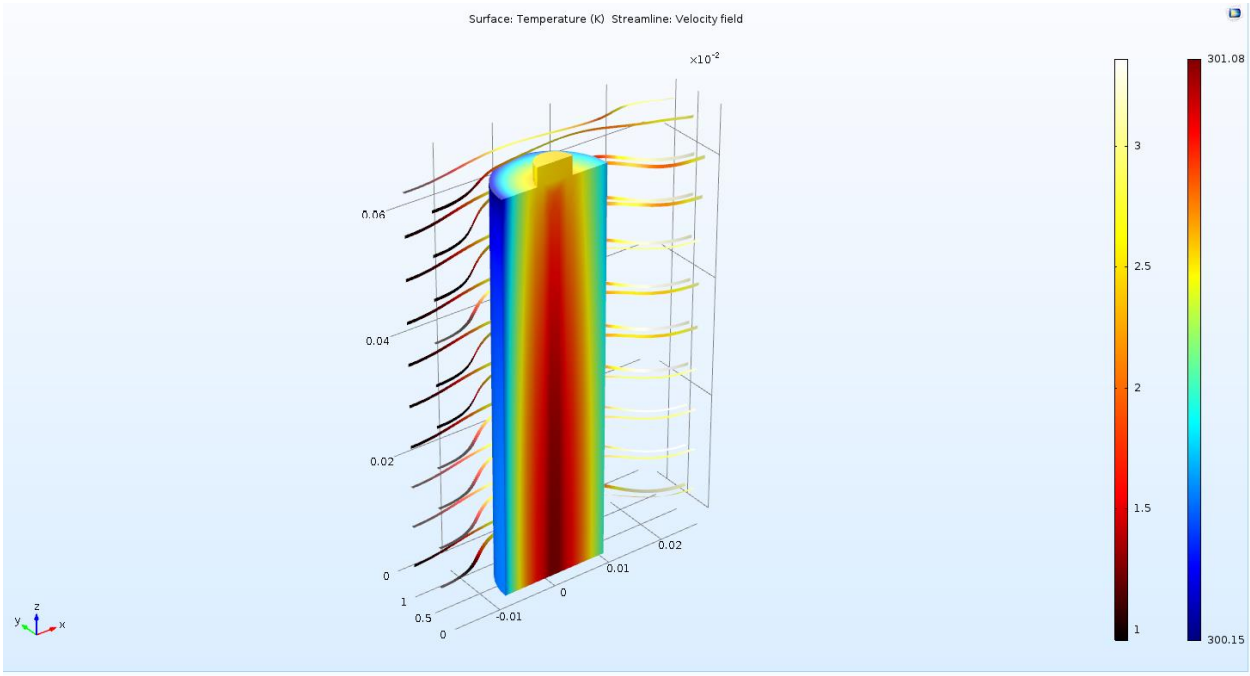

Figure 153 Scenario 9: Surface temperature of lithium - ion battery 3d thermal model (Comsol Multiphysics)

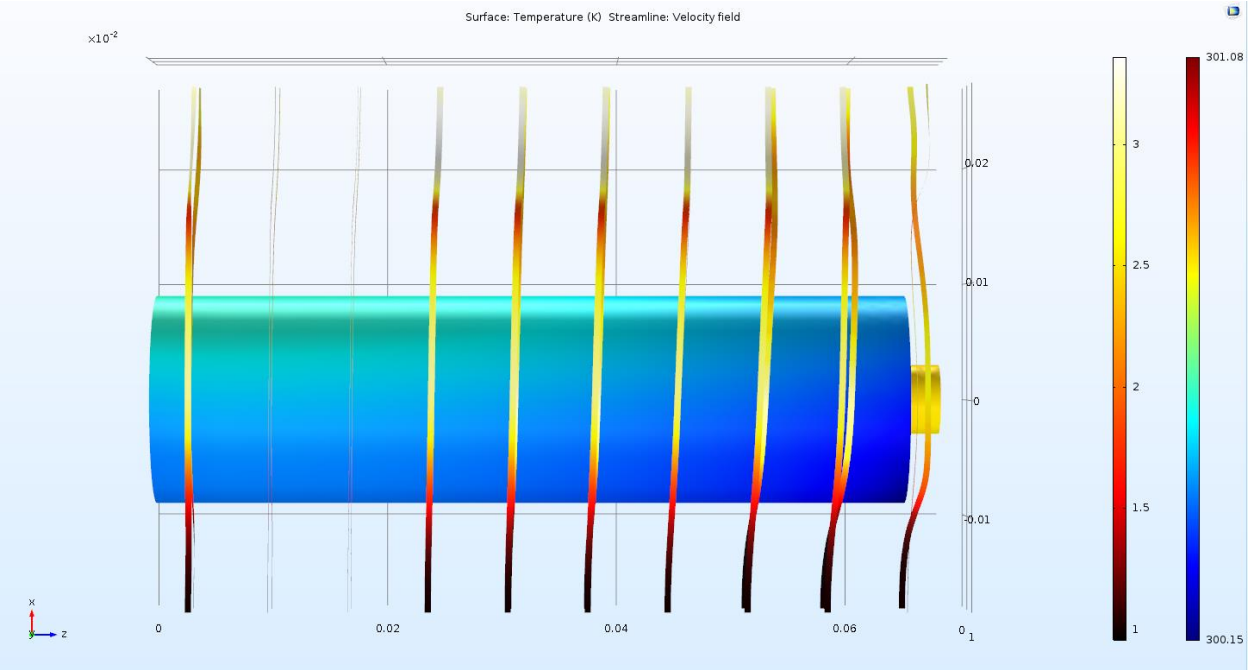

Figure 154 Scenario 9: Top view of surface temperature of lithium - ion battery 3d thermal model (Comsol Multiphysics)

The increase in the inlet air velocity decreased the surface temperature of the battery and the average temperature change during simulation, whereas the voltage profile remained the same. In particular, the surface temperature decreased by 14 K due to the inlet air velocity increase from 0.2 to 1 m/s.

Comparing scenario 3 to scenario 4, the decrease in the C-factor from 7.5 to 1 resulted in the voltage reduction by approximately 0.4 V, while the surface temperature approximately reached the inlet temperature and the temperature changes during simulation became negligible, which means the less the C-factor the more thermally stable the battery. The results of scenarios 5 and 6 indicate that the increase in the C-ratio significantly increases the surface temperature and the temperature changes, does not force the voltage to exceed a maximum (nominal) value and results in the expansion of the area on the battery's active material having the maximum temperature.

On the other hand, the changes in the battery radius do not exhibit a specific trend. In particular, despite the fact that the increase in the battery radius from 9 to 15 mm resulted in lower surface temperature and significantly higher temperature changes during simulation, the increase in the battery radius from 15 to 25 mm resulted in surface temperature increase by approximately 28 K and a slightly different

temperature change profile, indicating that the both the acceptable surface temperature and the temperature changes should determine the battery radius and the inverse is not possible.

Comparing scenario 6 to scenario 9, the reaction rate coefficients' doubling did not affect the temperature change profile during the simulation. However, the surface temperature decreased by 25 K and the surface temperature on the whole surface of the battery, including the active material's region and the back side of the battery, became the same. Since both the surface temperature reduction and the surface temperature being uniform are desirable, a proper reaction rate could contribute to the thermal stability of the battery.

3.2.5 Case 5 : VCU parameters determining driver's experience in a EV during braking

Other things being equal, maximum braking torque for the vehicle and the electric motor rotary speed threshold to regenerate battery determines three scenarios. In the first scenario, the results are obtained from [62]. The simulations are carried out with the New European Driving Cycle for automatic transmission.

- **Scenario 1: Maximum braking torque = 1000 Nm, electric motor rotary speed threshold to regenerate battery = 70 rev/min**

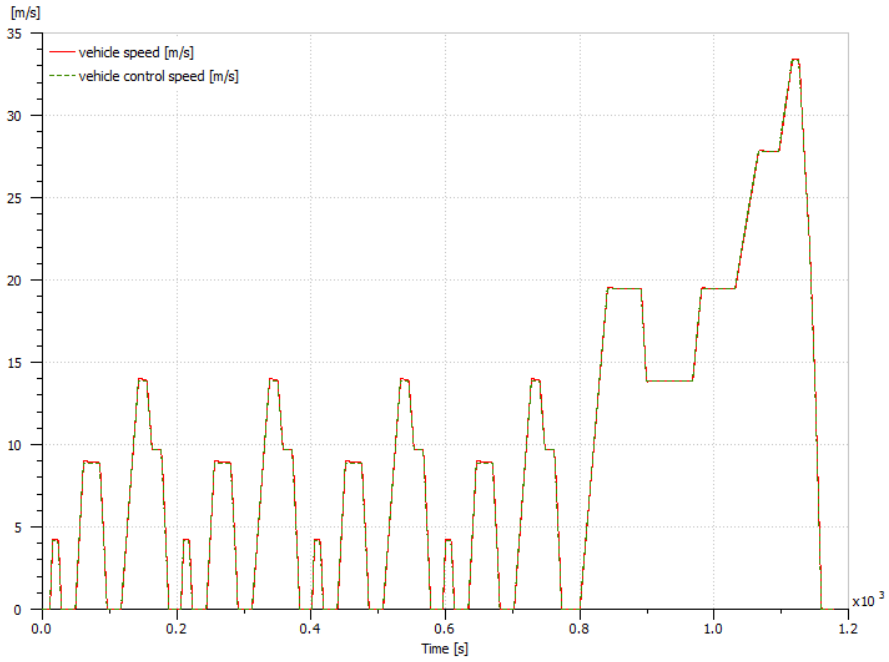

Figure 155 Scenario 1: Vehicle speed vs vehicle control speed (LMS ImagineLab – EV model with VCU) [62]

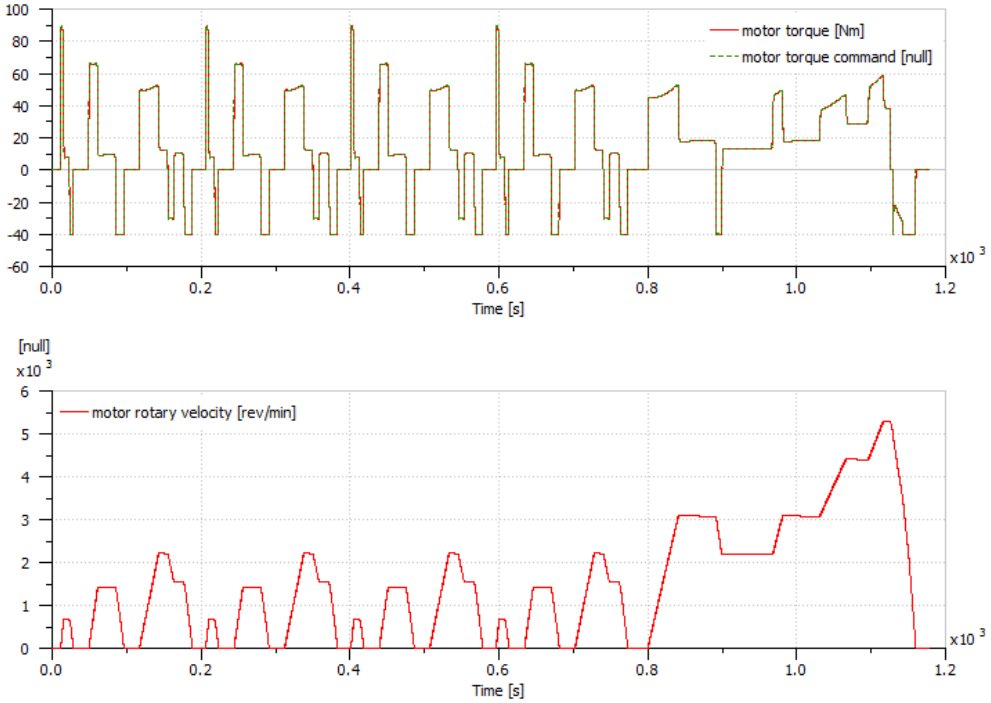

Figure 156 Scenario 1: Motor torque vs motor control torque, motor rotary velocity (LMS ImagineLab – EV model with VCU) [62]

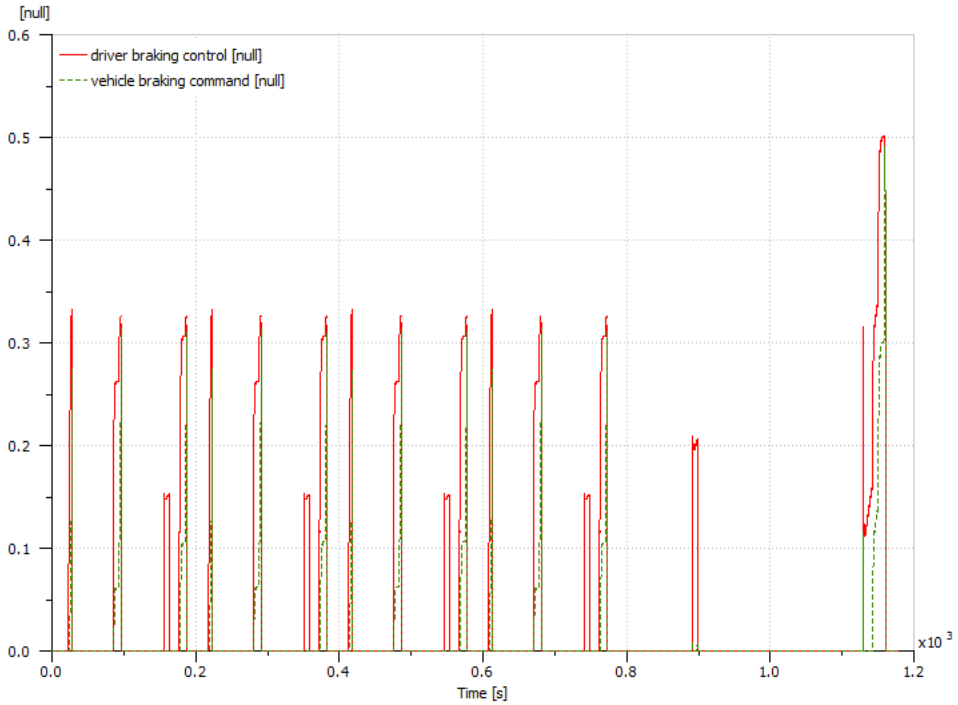

Figure 157 Scenario 1: Driver braking control vs vehicle braking command (LMS ImagineLab – EV model with VCU) [62]

- **Scenario 2: Maximum braking torque = 100 Nm, electric motor rotary speed threshold to regenerate battery = 70 rev/min**

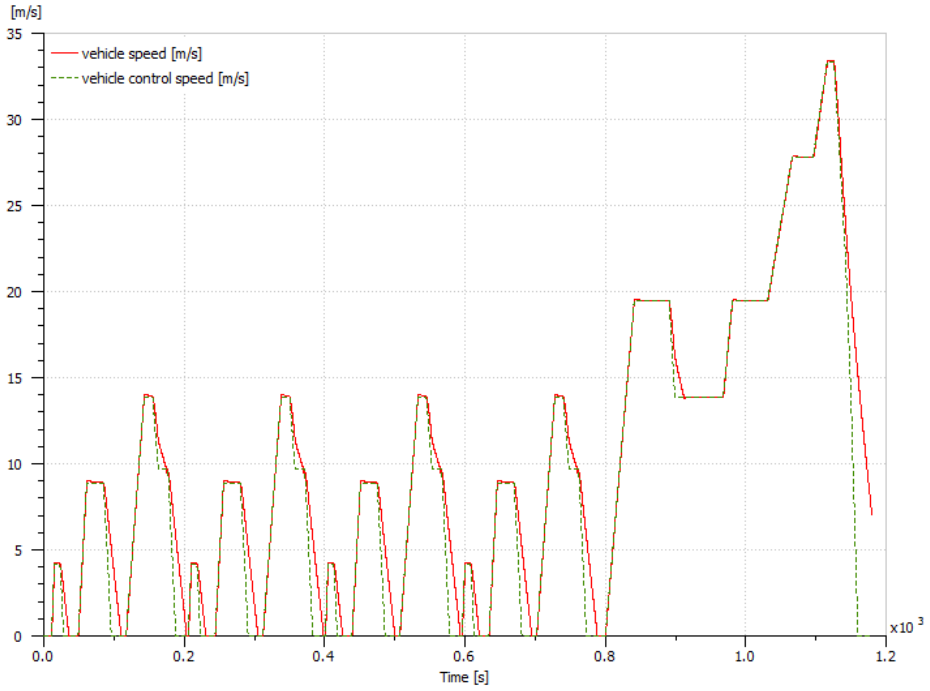

Figure 158 Scenario 2: Vehicle speed vs vehicle control speed (LMS ImagineLab – EV model with VCU)

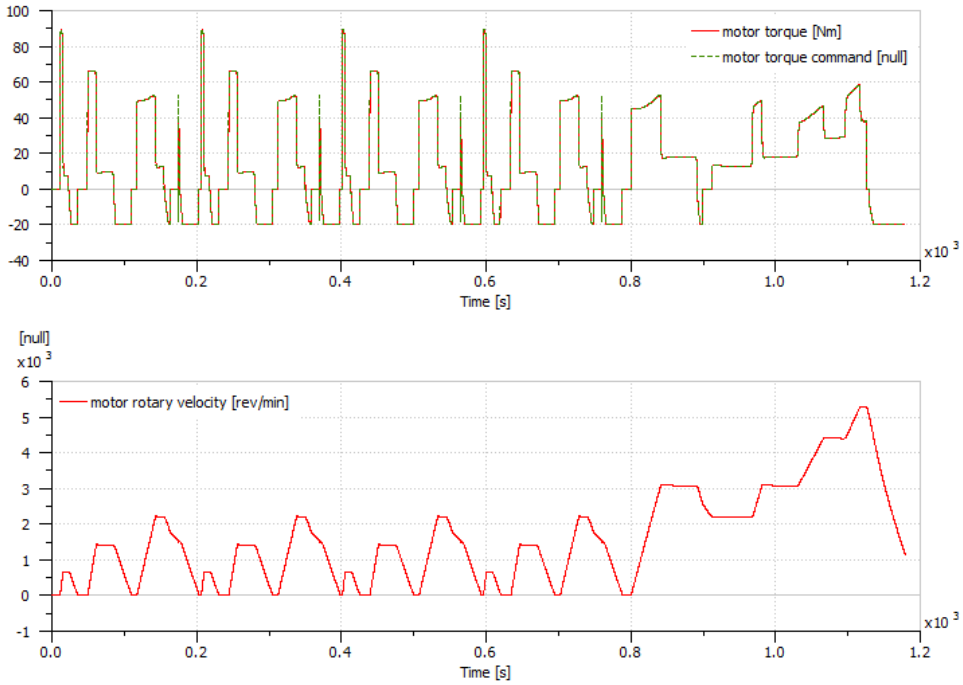

Figure 159 Scenario 2: Motor torque vs motor control torque, motor rotary velocity (LMS ImagineLab – EV model with VCU)

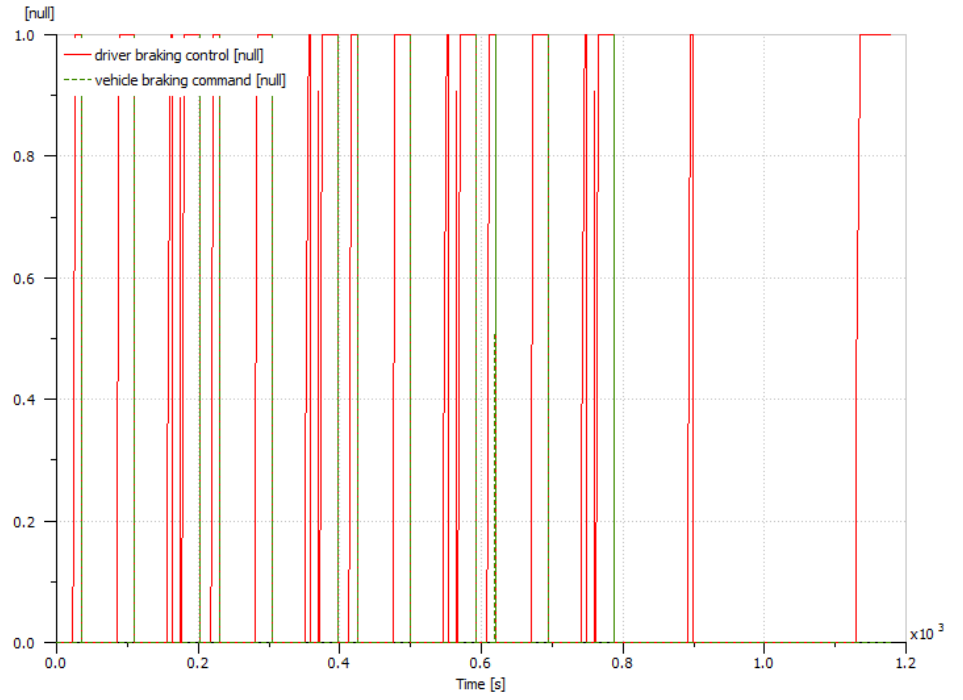

Figure 160 Scenario 2: Driver braking control vs vehicle braking command (LMS ImagineLab – EV model with VCU)

- **Scenario 3: Maximum braking torque = 100 Nm, electric motor rotary speed threshold to regenerate battery = 1600 rev/min**

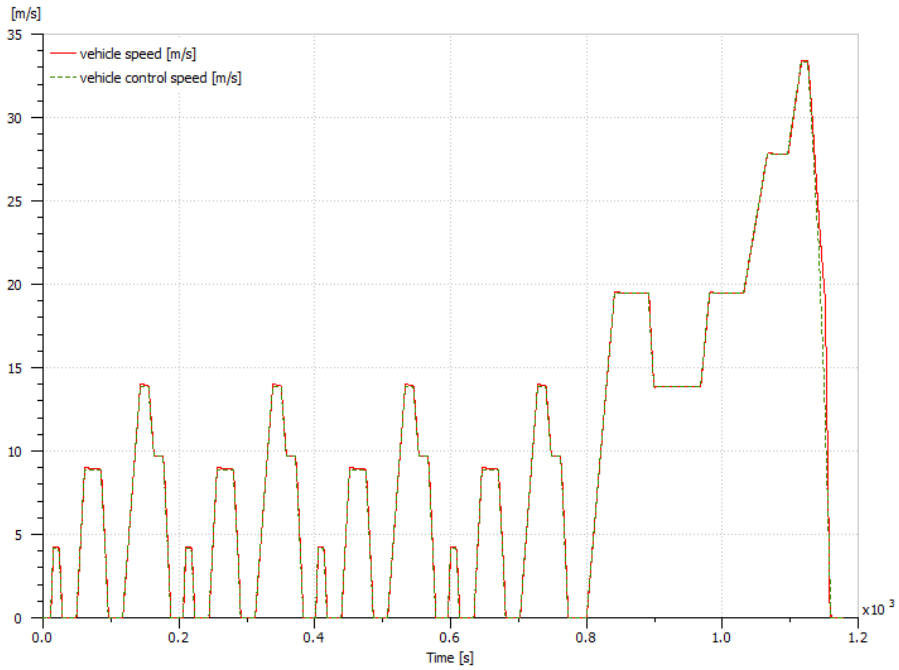

Figure 161 Scenario 3: Vehicle speed vs vehicle control speed (LMS ImagineLab – EV model with VCU)

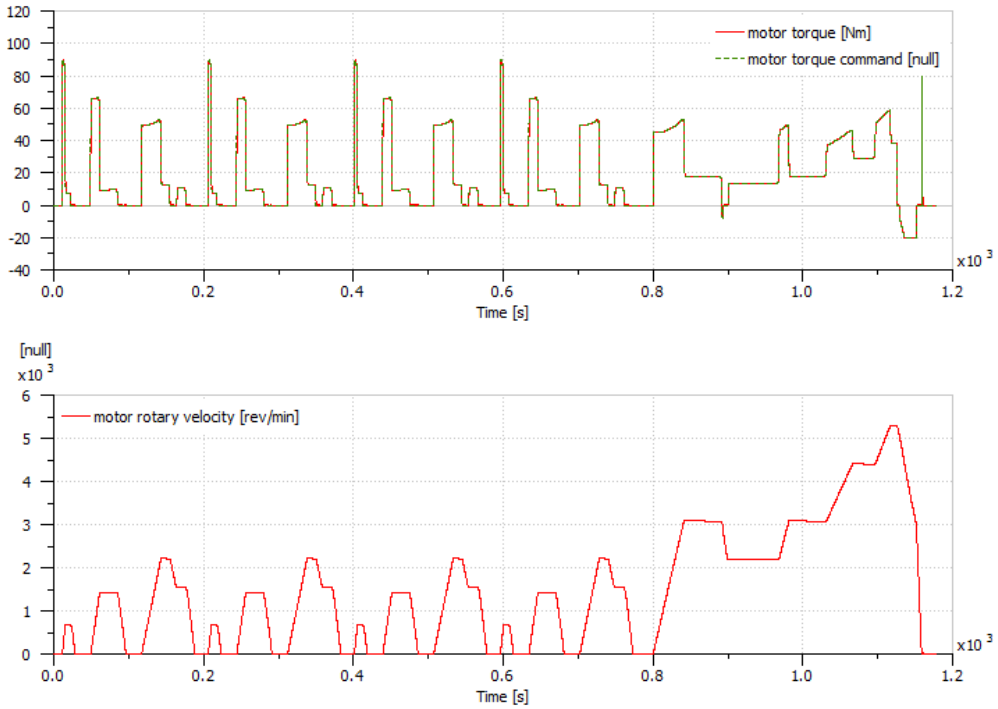

Figure 162 Scenario 3: Motor torque vs motor control torque, motor rotary velocity (LMS ImagineLab – EV model with VCU)

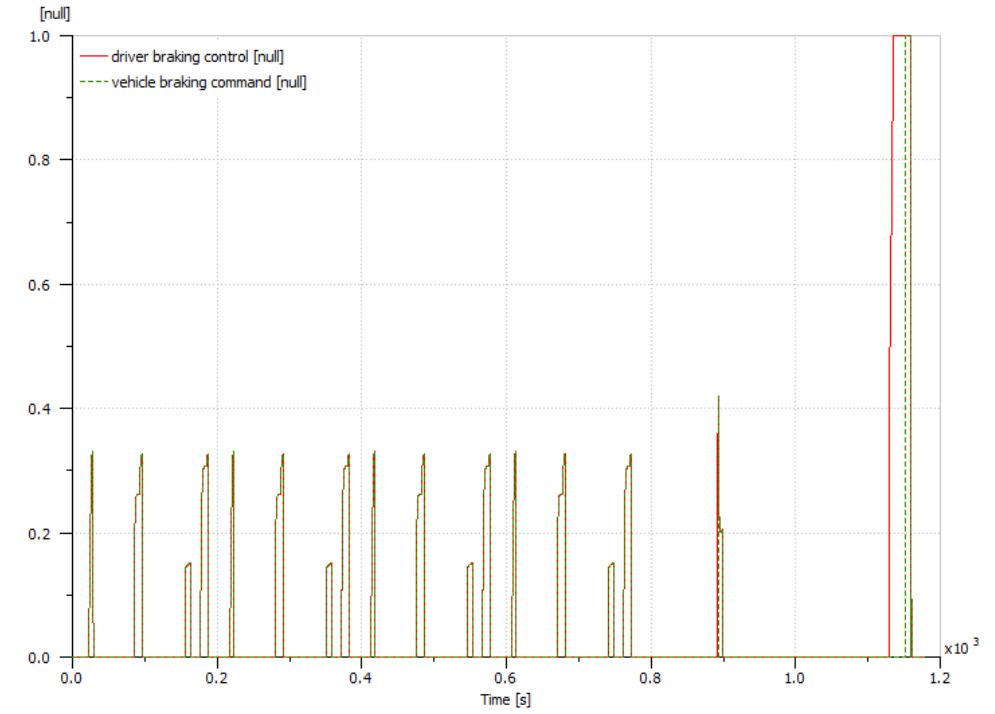

Figure 163 Scenario 3: Driver braking control vs vehicle braking command (LMS ImagineLab – EV model with VCU)

It is observed that the reduction in the maximum braking torque for the vehicle results in the deviation of the vehicle speed and the braking command from the corresponding reference values. This is due to the fact that during braking at high vehicle speeds the electric motor charges the battery for a longer time period and no hydraulic braking system is involved. Thus, in scenario 3 the increase in the electric motor rotary speed threshold to regenerate battery results in the curves' fitting. All in all, effective regenerative braking requires the maximum possible braking torque.

3.2.6 Case 6 : SCU limits and battery capacity effects on the EV behavior in cold environment

Since the battery's internal resistance and overpotential significantly increase at low temperatures, the battery's power capability decreases and the VCU may not be able to respond to the driver's needs [62]. In the first scenario, the external temperature is set to -20 ^{o}C, the SOC is set to 90%, the element maximum continuous charge current is set to 20 A, the element maximum pulse charge current is set to 30 A, the

element maximum continuous discharge current is set to 20 A and the element maximum pulse discharge current is set to 30 A. The results of the first scenario are obtained from [62]. Since reducing the discharge current limits in the SCU does not have an effect on the vehicle behavior, as it is a overdischarge prevention issue, three more scenarios changing the element nominal capacity (branches) of the lithium – ion battery from 2.3 Ah to 3.5 (Scenario 2), 10 (Scenario 3) and 19 Ah (Scenario 4), respectively. The driving cycle simulated is the NEDC.

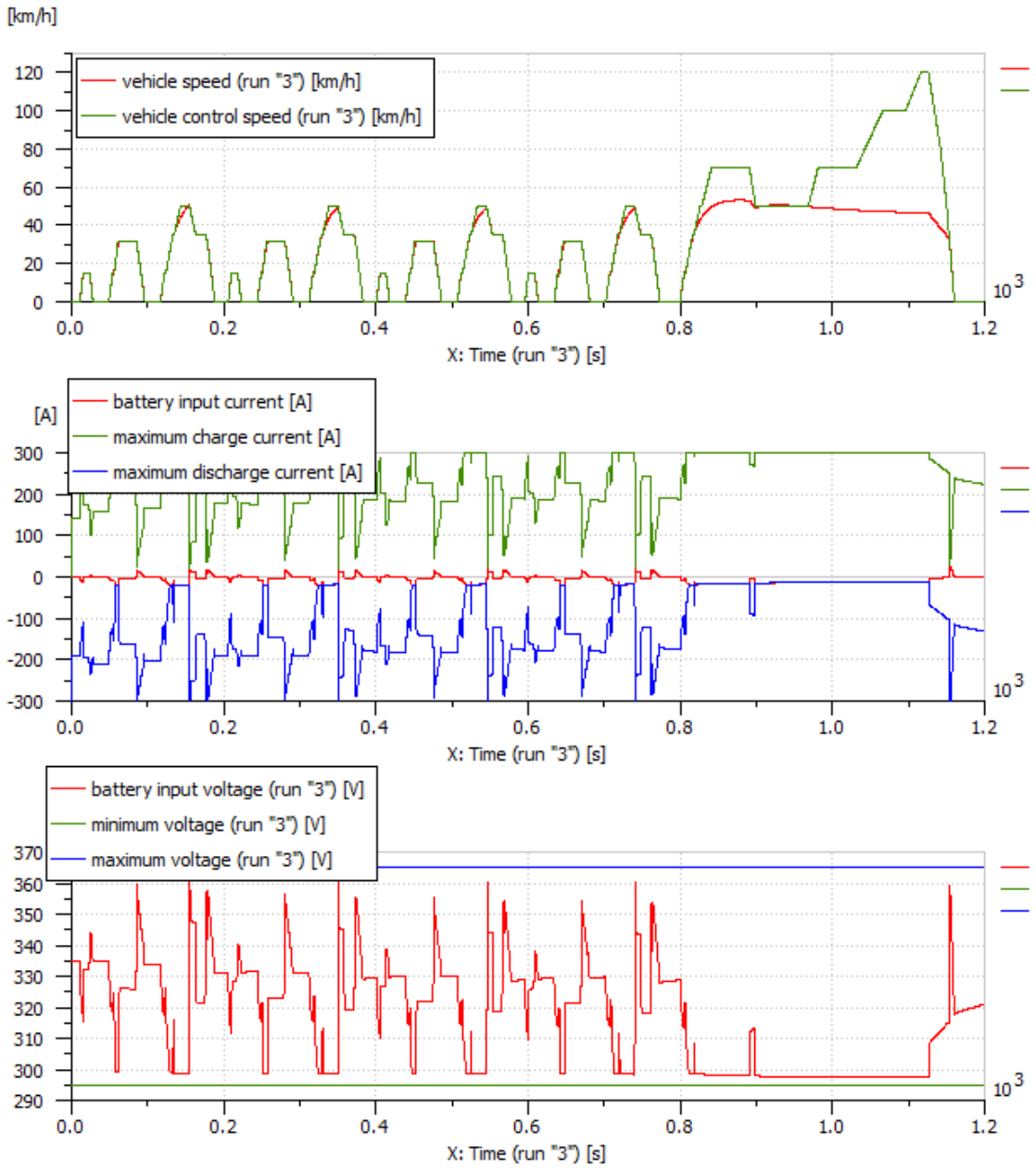

Figure 164 Simulations results of Scenario 1 (LMS ImagineLab – EV model with SCU in cold environment) [62]

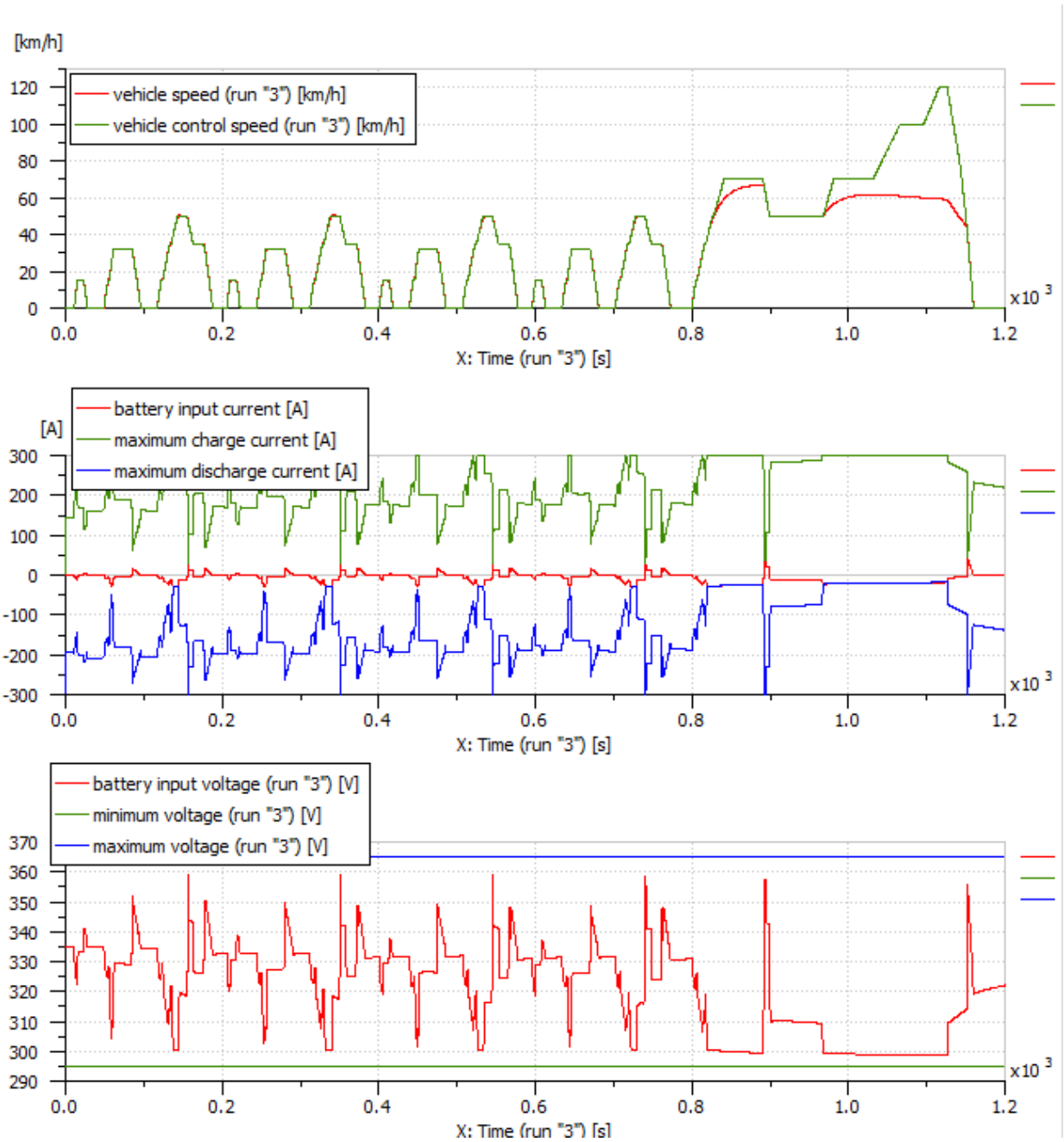

Figure 165 Simulations results of Scenario 2 (LMS ImagineLab – EV model with SCU in cold environment)

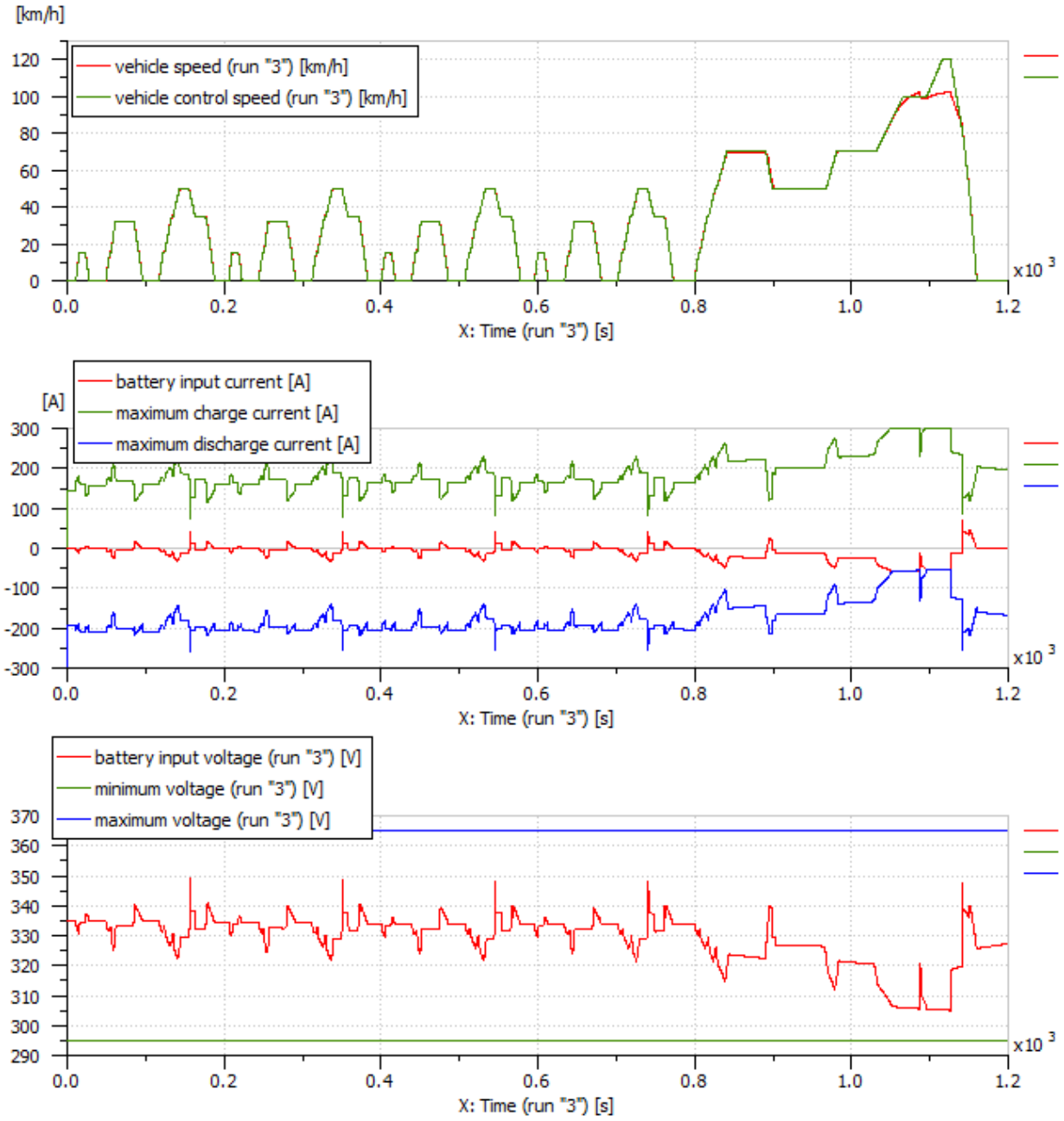

Figure 166 Simulations results of Scenario 3 (LMS ImagineLab – EV model with SCU in cold environment)

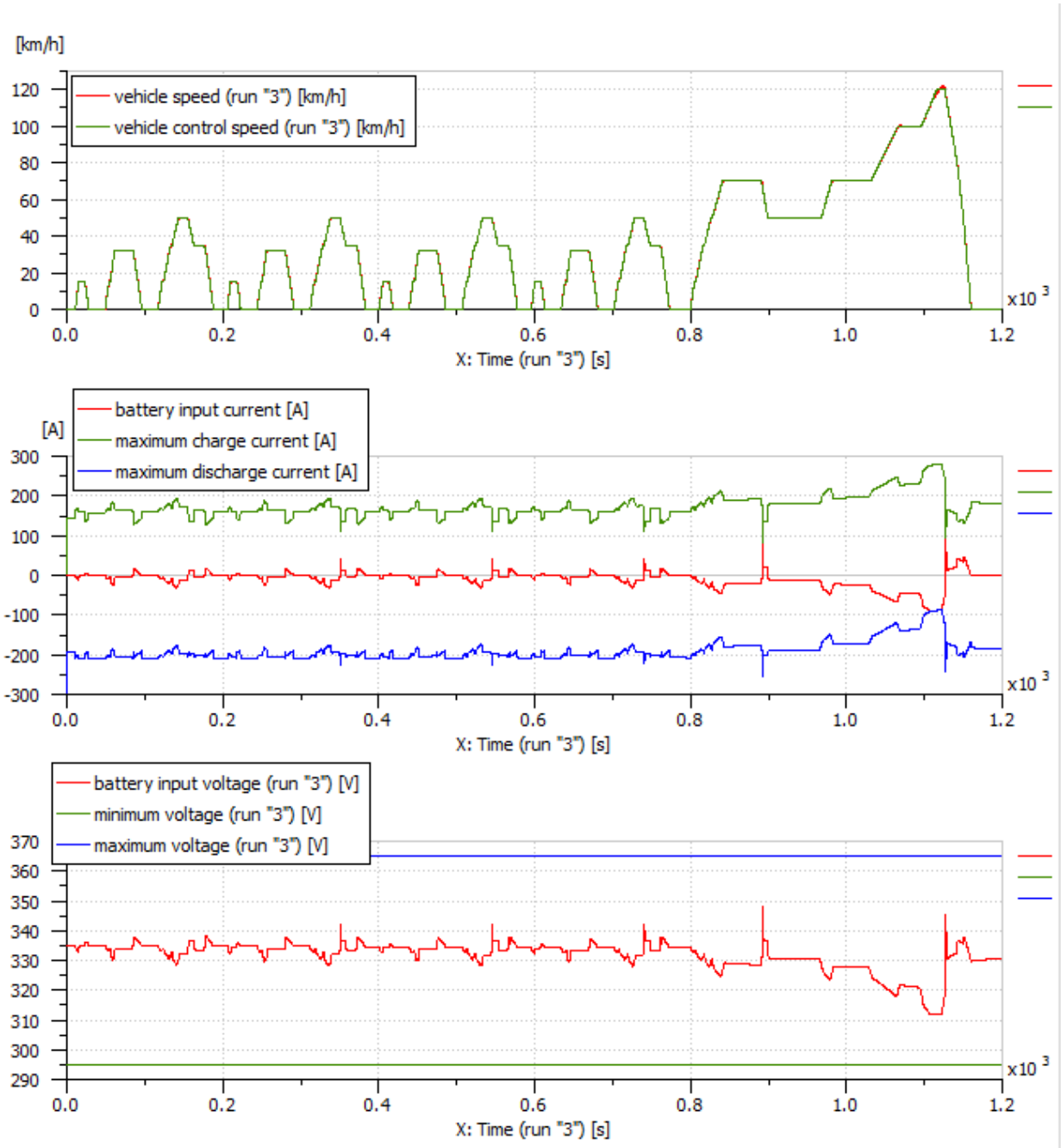

Figure 167 Simulations results of Scenario 4 (LMS ImagineLab – EV model with SCU in cold environment)

In scenario 1 at 8000 s the vehicle speed clearly cannot follow the control speed, which is also indicated by the comparison of the current and voltage limits to the real values. As described the reason is that the battery temperature is extremely low and in order for undervoltage to be averted, the SCU limits the available power for the vehicle and the discharge current reference value decreases to zero to avert the battery's overdischarge. In the following the battery capacity increases and as it is observed the vehicle speed gradually follows more accurately the control speed. With an element capacity of 19 Ah the VCU is able to meet the driver's demands.

3.2.7 Case 7 : Battery load, air flow rate, cell density, SOC effects on lithium – ion cell temperature

Several scenarios are simulated changing one parameter at a time in order to test the effects of different parameters of the lithium-ion battery on the cell temperature.

- **Scenario 1: Battery load = 12 kW**

The battery pack feeds the load and is fed with constant charge and discharge current steps, while it is exposed to 20 ^{o}C. In order for the battery pack's temperature to be kept between 35 and 45^{o}C, a fan is controlled by a thermostat which receives the temperature measurements. The lithium – ion cell and the battery case specifications are summarized in the table below.

Table 12

Lithium – ion Cell	**Battery case (Polypropylene)**
Specific heat = 2000 J/kgK	Thermal conductivity = 0.15 W/mK
Thermal conductivity = 23 W/mK	Specific heat = 1800 J/kgK
SOC = 60%	Material density = 900 kg / m^3

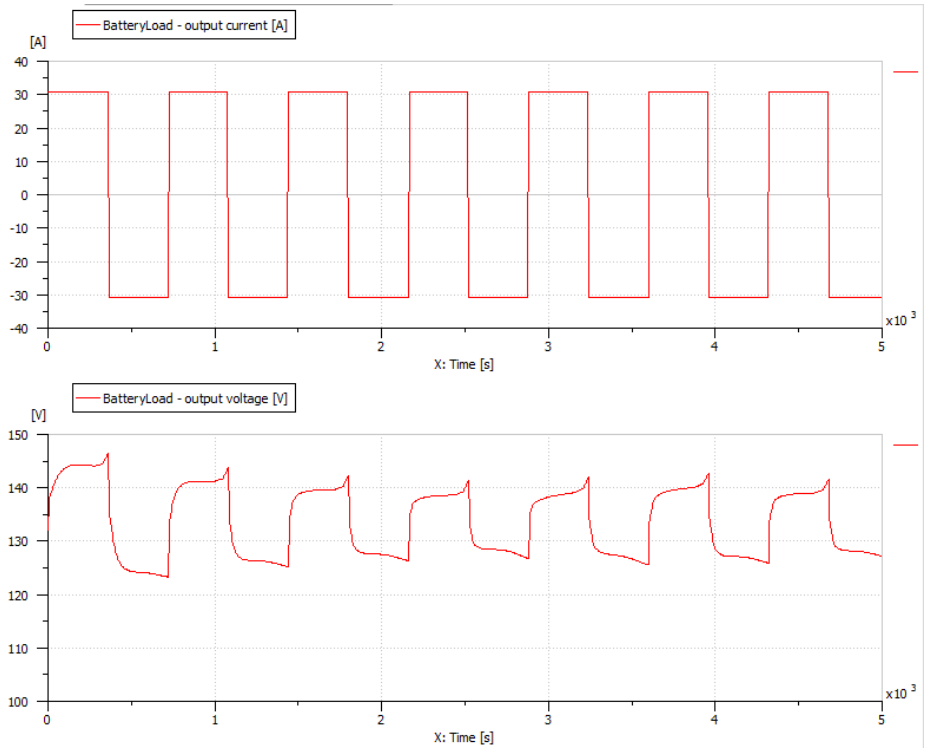

Figure 168 Scenario 1: Battery output current and voltage profile (LMS ImagineLab – Battery pack air – cooling model) [62]

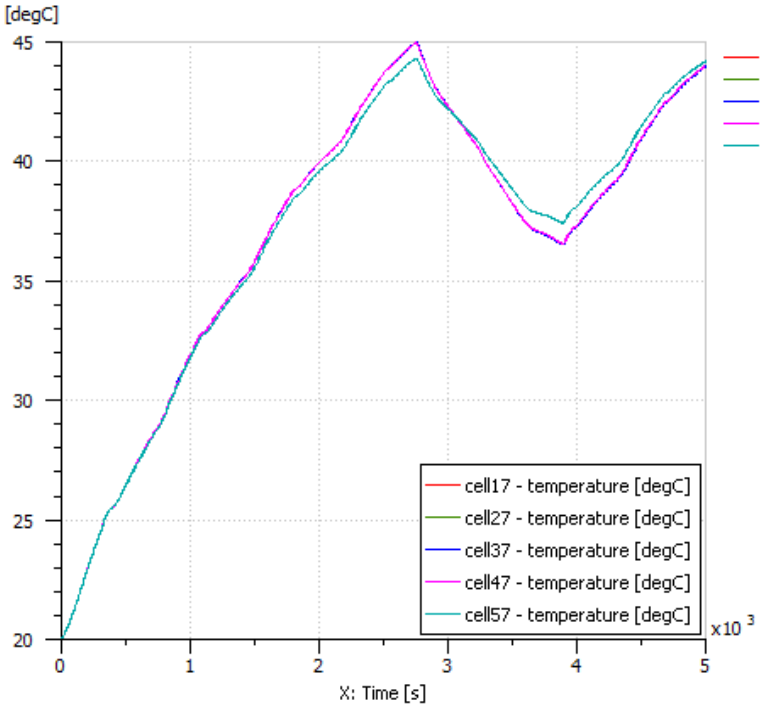

Figure 169 Scenario 1: Temperatures of cells of column 7 (LMS ImagineLab – Battery pack air – cooling model) [62]

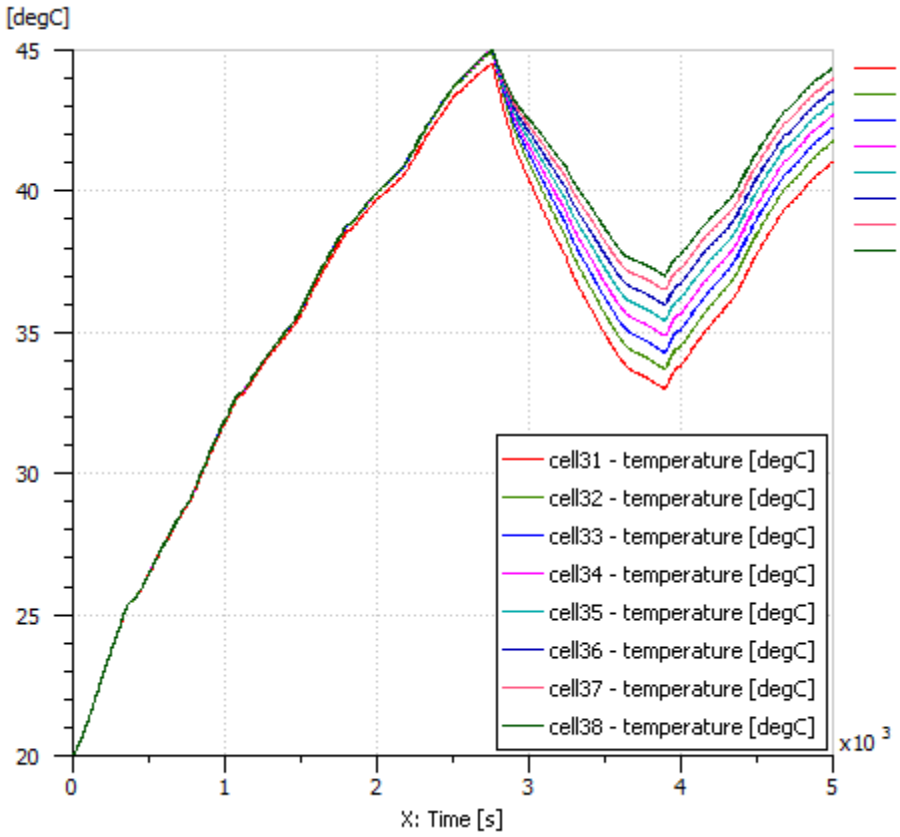

Figure 170 Scenario 1: Temperatures of cells of row 3 (LMS ImagineLab – Battery pack air – cooling model) [62]

- **Scenario 2: Battery load = 20 kW**

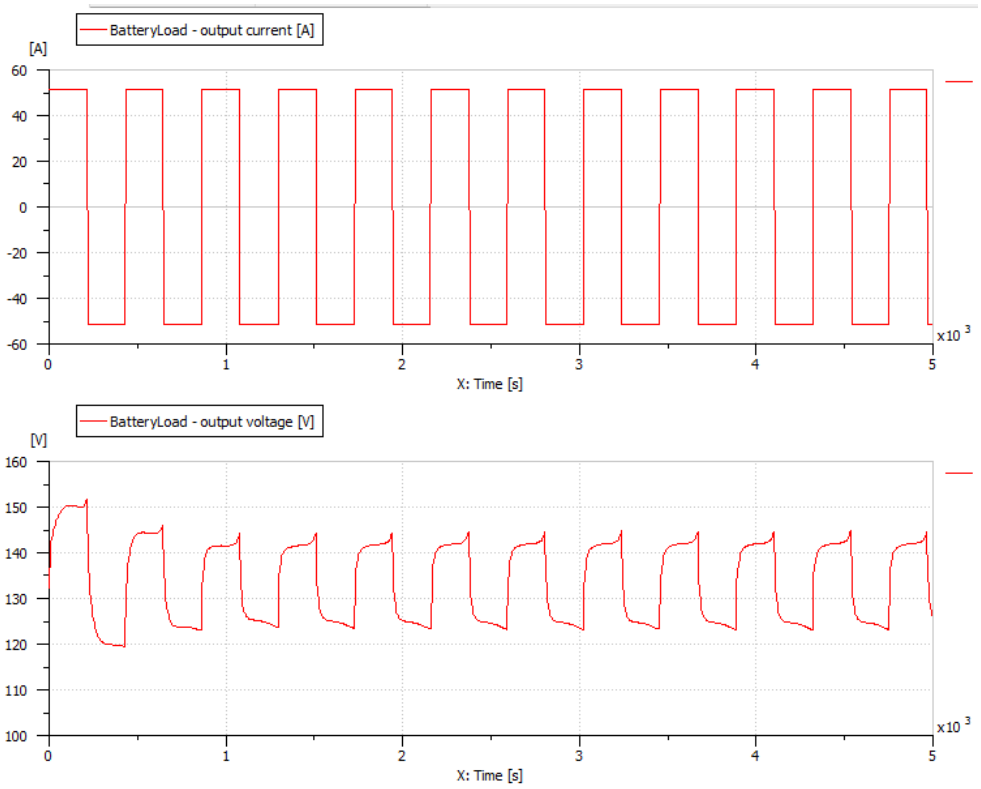

Figure 171 Scenario 2: Battery output current and voltage profile (LMS ImagineLab – Battery pack air – cooling model)

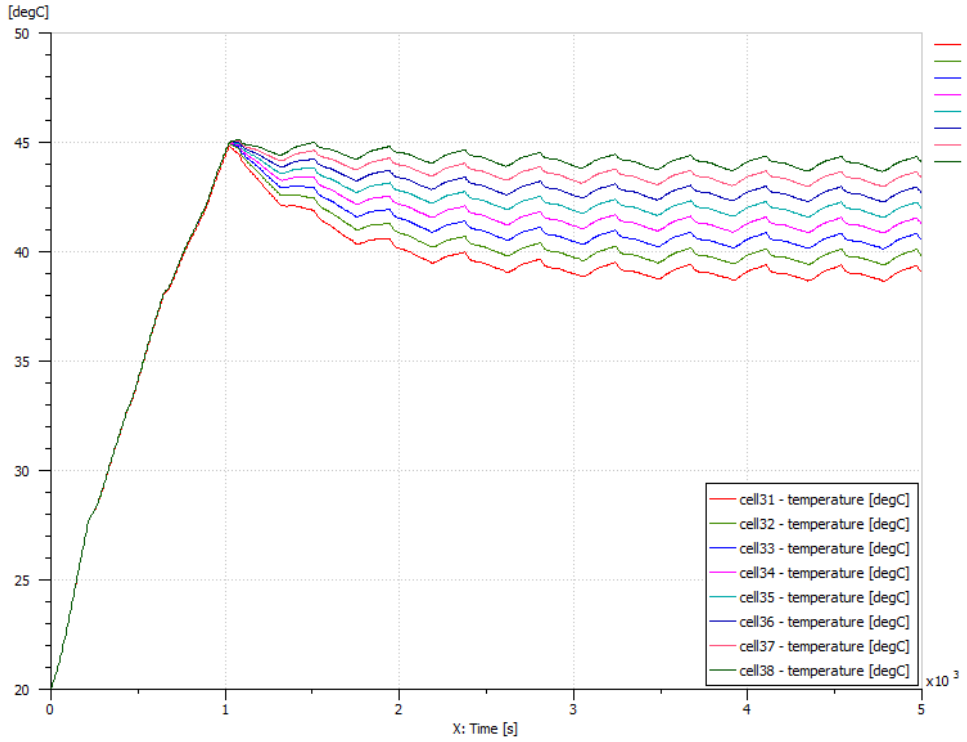

Figure 172 Scenario 2: Temperatures of cells of column 7 (LMS ImagineLab – Battery pack air – cooling model)

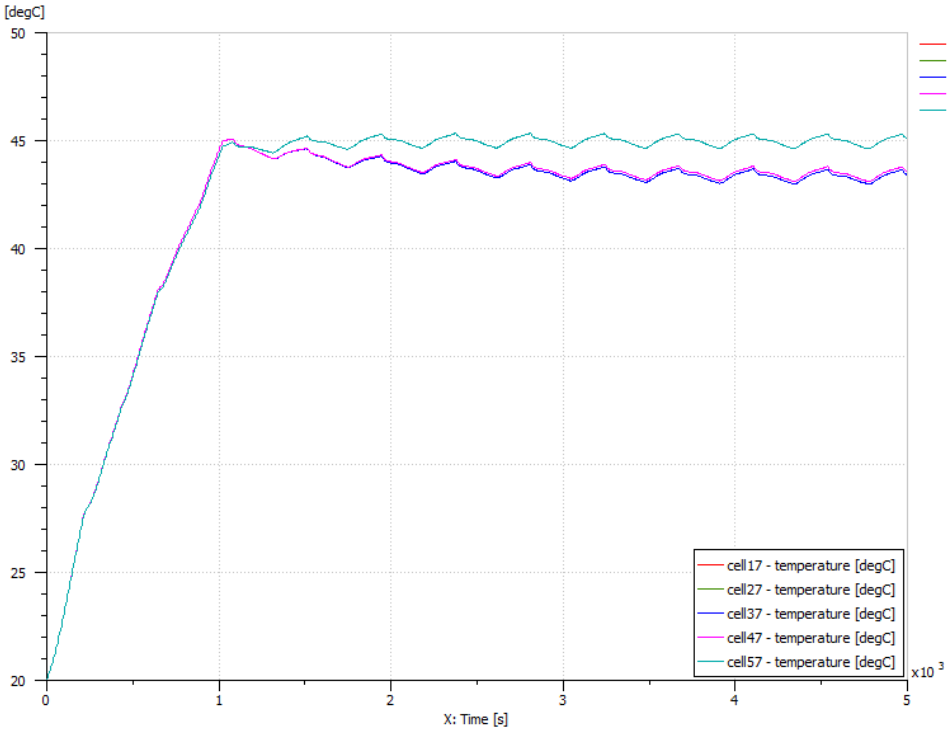

Figure 173 Scenario 2: Temperatures of cells of row 3 (LMS ImagineLab – Battery pack air – cooling model)

- **Scenario 3: Air flow rate = 120 g/s**

The nominal cell voltage is changed from 60 to 120 g/s.

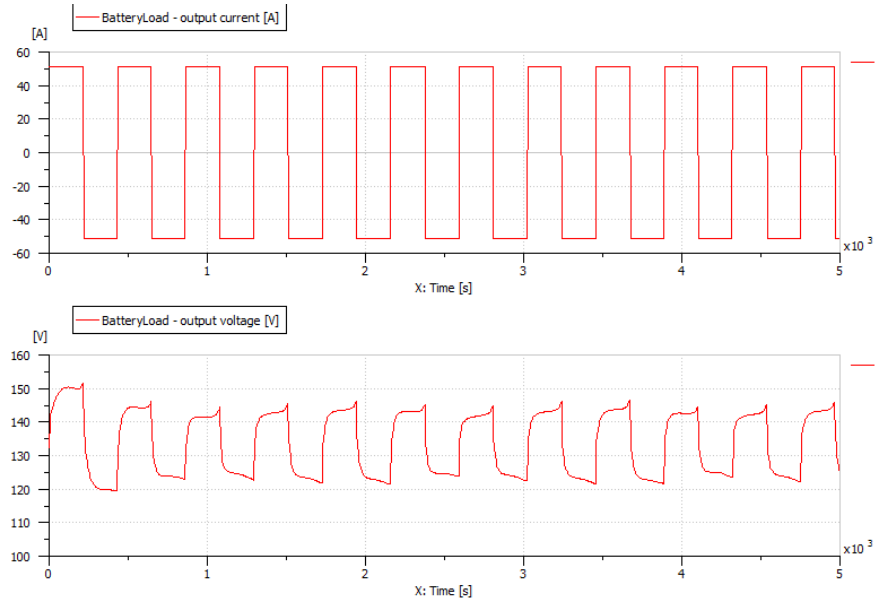

Figure 174 Scenario 3: Battery output current and voltage profile (LMS ImagineLab – Battery pack air – cooling model)

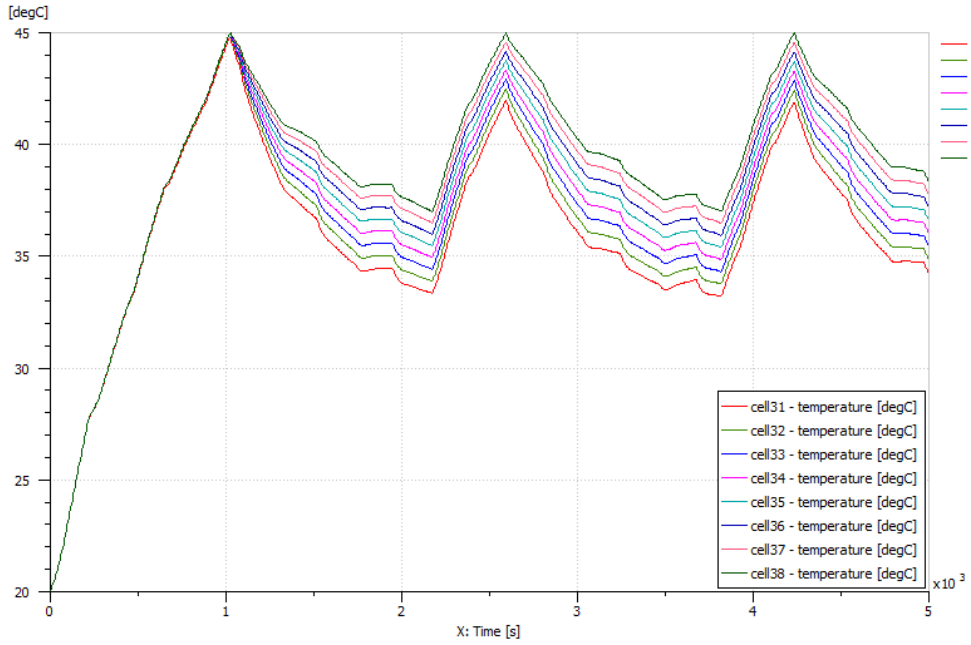

Figure 175 Scenario 3: Temperatures of cells of column 7 (LMS ImagineLab – Battery pack air – cooling model)

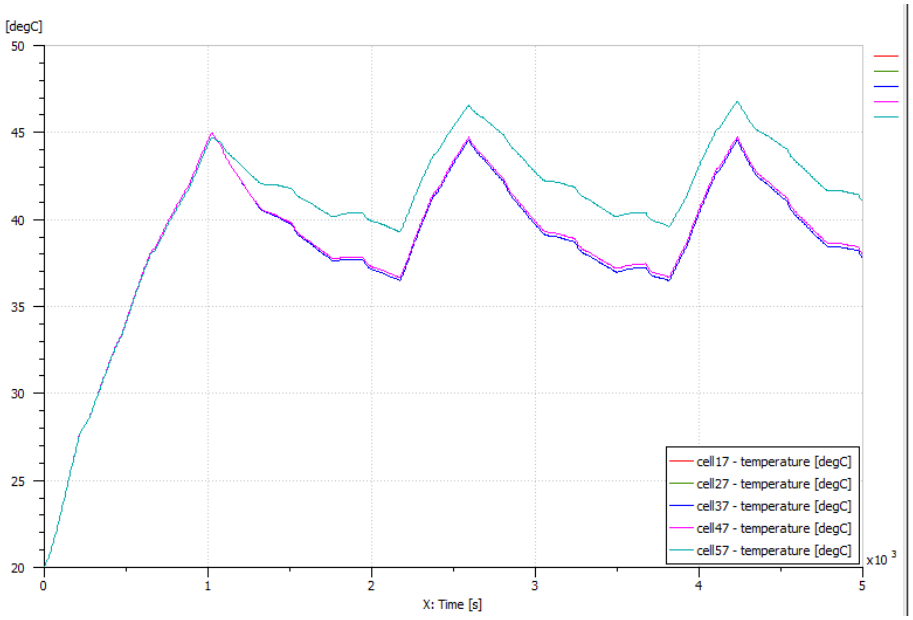

Figure 176 Scenario 3: Temperatures of cells of row 3 (LMS ImagineLab – Battery pack air – cooling model)

- **Scenario 4: Cell density = 0.000004 kg/mm³**

The cell density is changed from 0.000002 to 0.000004 kg/mm³.

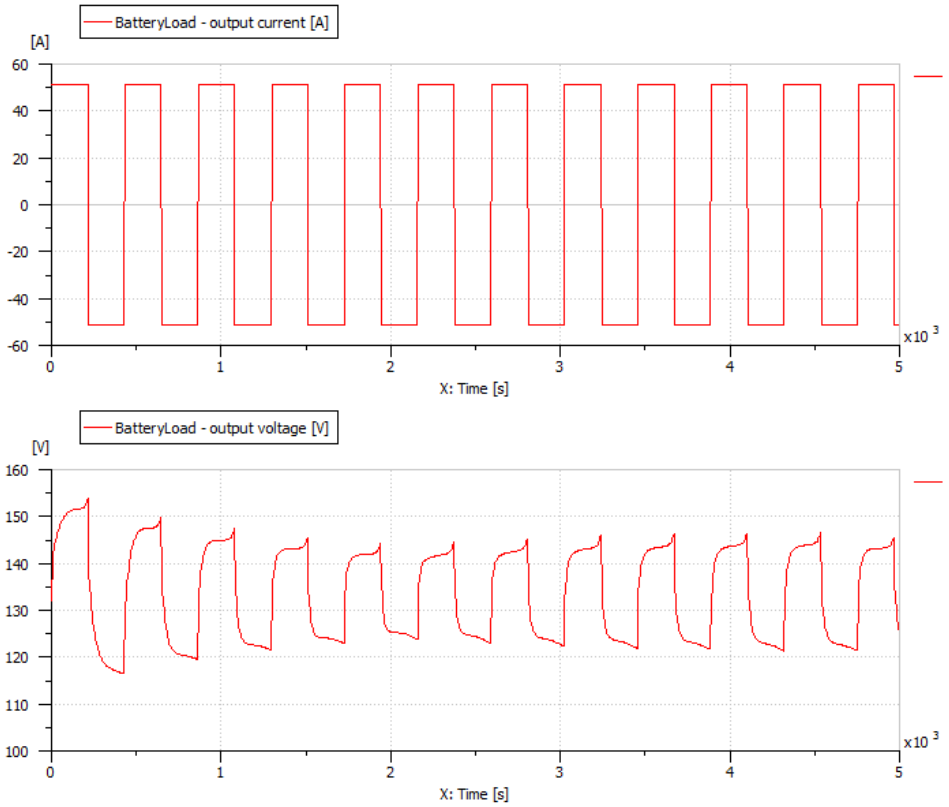

Figure 177 Scenario 4: Battery output current and voltage profile (LMS ImagineLab – Battery pack air – cooling model)

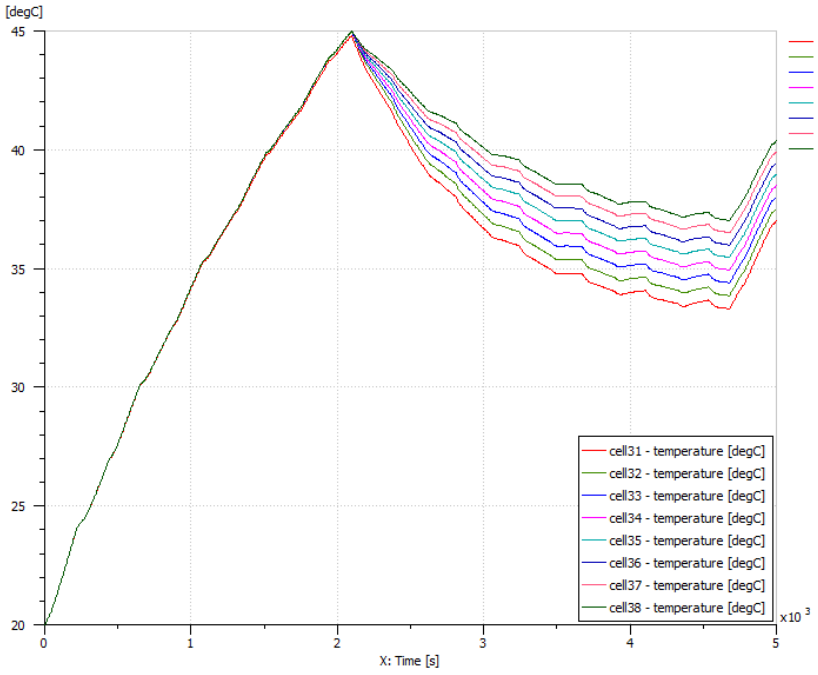

Figure 178 Scenario 4: Temperatures of cells of column 7 (LMS ImagineLab – Battery pack air – cooling model)

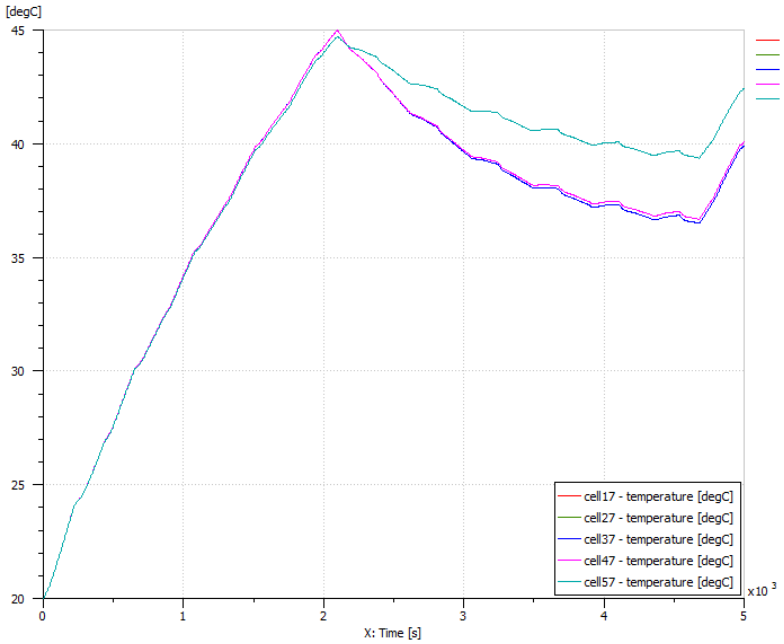

Figure 179 Scenario 4: Temperatures of cells of row 3 (LMS ImagineLab – Battery pack air – cooling model)

- **Scenario 5: Cells' SOC = 100%**

The cells' initial SOC is changed from 60 to 100%.

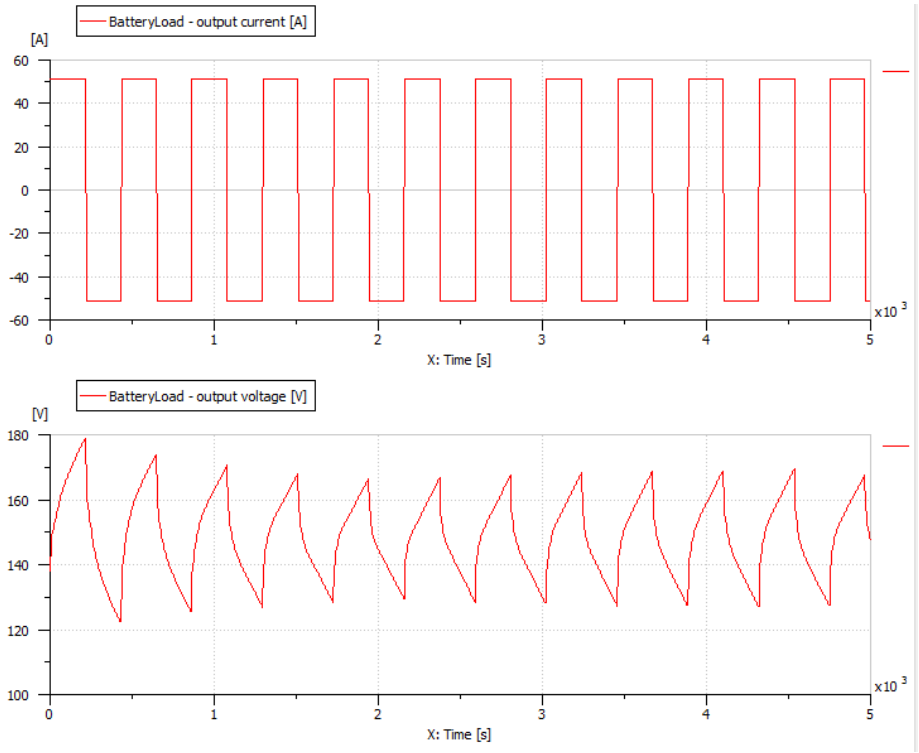

Figure 180 Scenario 5: Battery output current and voltage profile (LMS ImagineLab – Battery pack air – cooling model)

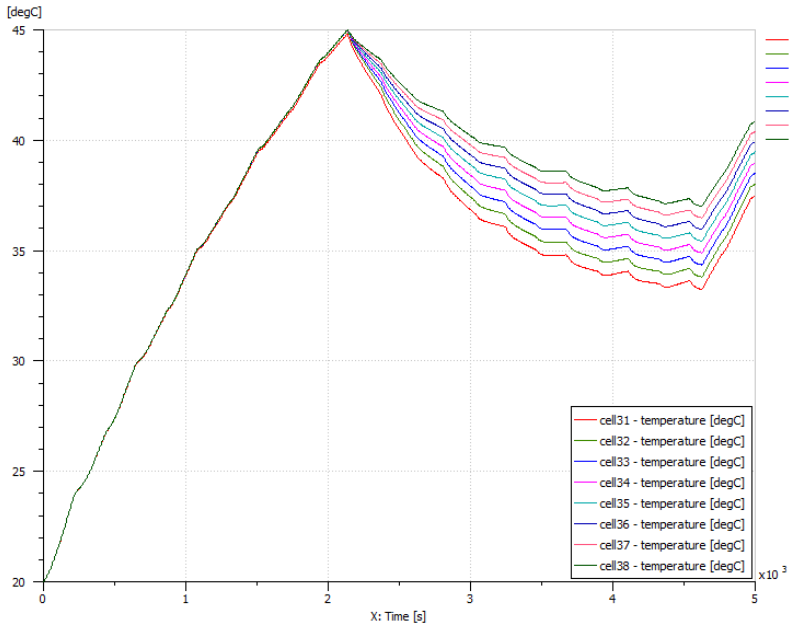

Figure 181 Scenario 5: Temperatures of cells of column 7 (LMS ImagineLab – Battery pack air – cooling model)

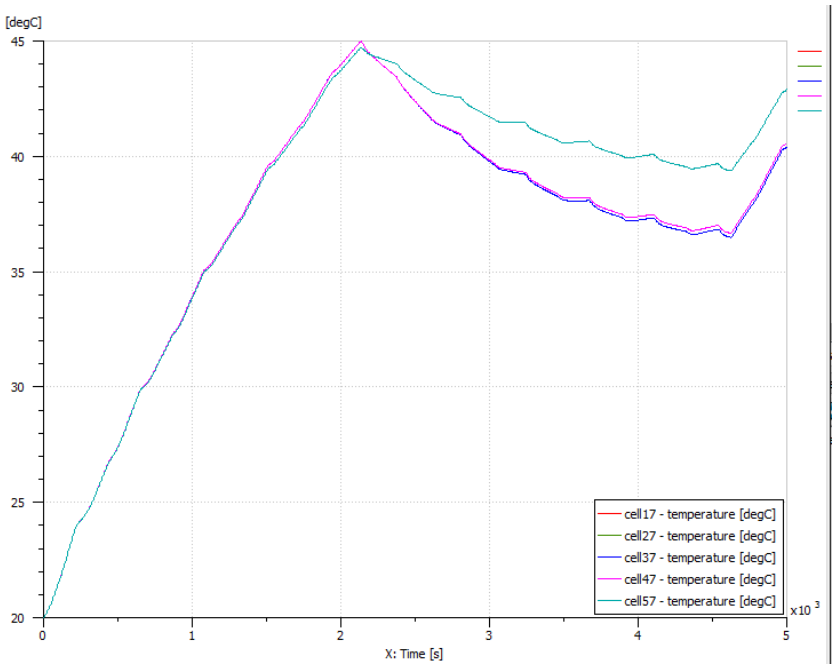

Figure 182 Scenario 5: Temperatures of cells of row 3 (LMS ImagineLab – Battery pack air – cooling model)

Due to the current flowing in each branch, the battery heats up. In order for the temperature not to exceed the acceptable limits, the fan begins functioning at intervals, while its being turned off results in the increase in the cells' temperatures [62]. From the slopes of the temperature profiles of the cells it is observed that during charging temperature changes faster, while during discharging temperature changes slower. From the temperature of cells of column 7 graph it can be verified that the farther the cell from the air inlet the higher its temperature. As expected, in scenario 2 the increase in the battery load resulted in both the output current and voltage profile change. The temperatures of the cells reached the upper limit faster (in 1000 s), while the fan is not able to reduce the temperature as low as in scenario 1 until the end of the simulation interval (5000 s) due to the higher load. In scenario 3 the doubling of the air flow rate slightly changes the voltage profile and renders heat dissipation more efficient as illustrated by the temperature profiles of the cells. Due to the doubling of the cell density in scenario 4, temperature decreases slower and the fan functions for a longer time period, whereas due to the increase in the SOC

of cells in scenario 5, the voltage profile changes such that voltage changes faster from charging to discharging condition and it does not follow the curve trend of the output current pulses.

3.2.8 Case 8 : Comparison of old and new lithium – ion battery under the HWFET driving cycle

The EV battery aging model is utilized for comparing the performance of an old and a new lithium – ion battery under the HWFET driving cycle, which is employed to assess the highway fuel economy, whereas NEDC and FTP driving cycles represent driving conditions in urban areas [63][64].

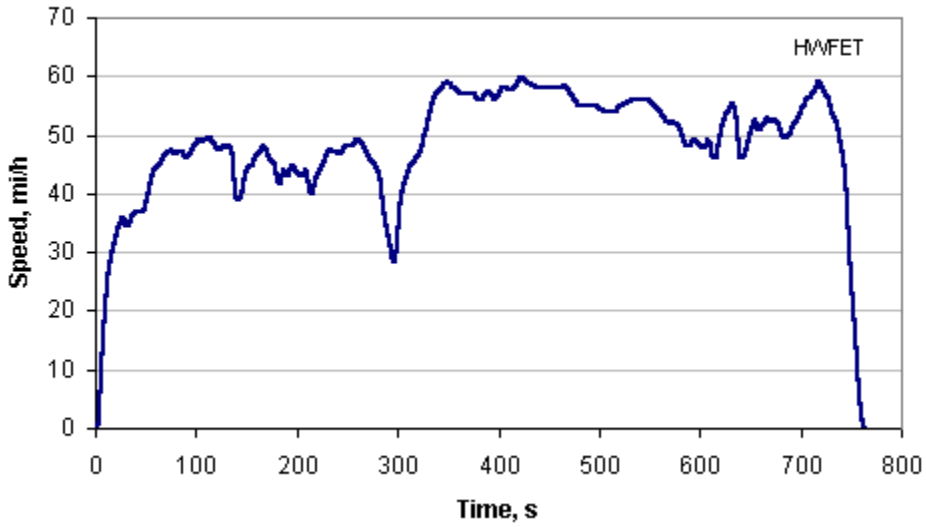

Figure 183 HWFET driving cycle [63]

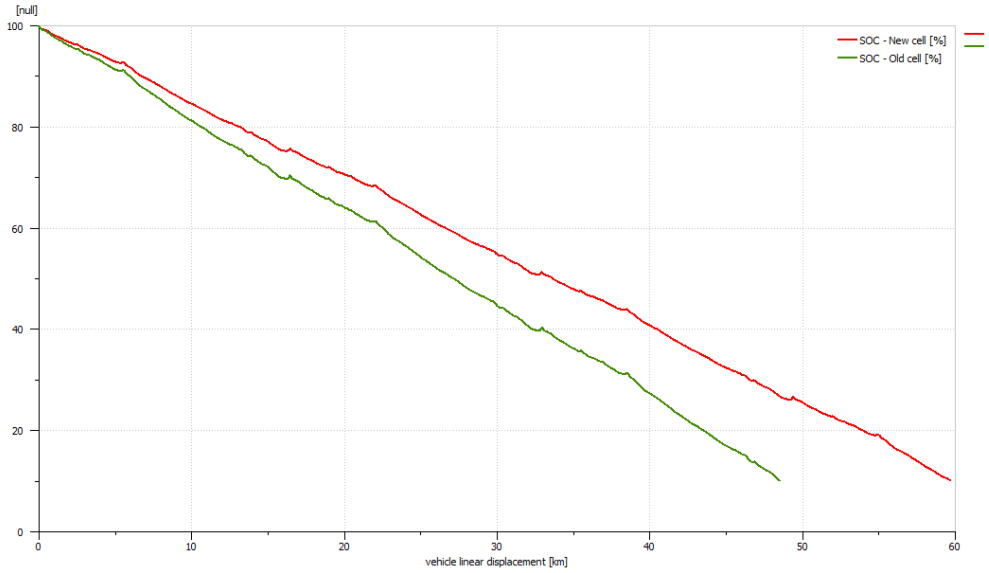

Figure 184 Vehicle's autonomy (EV battery aging model - ImagineLab)

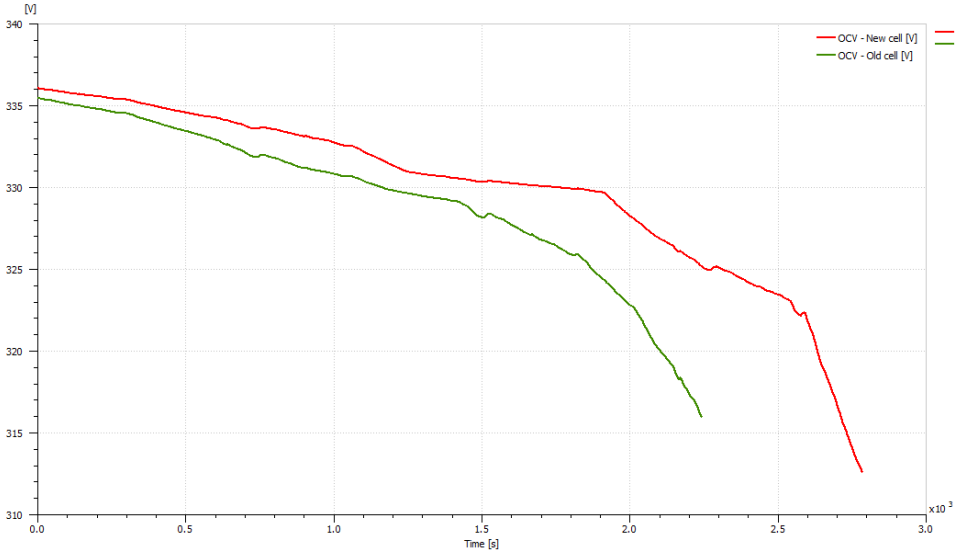

Figure 185 Evolution of battery's OCV Vehicle's autonomy (EV battery aging model - ImagineLab)

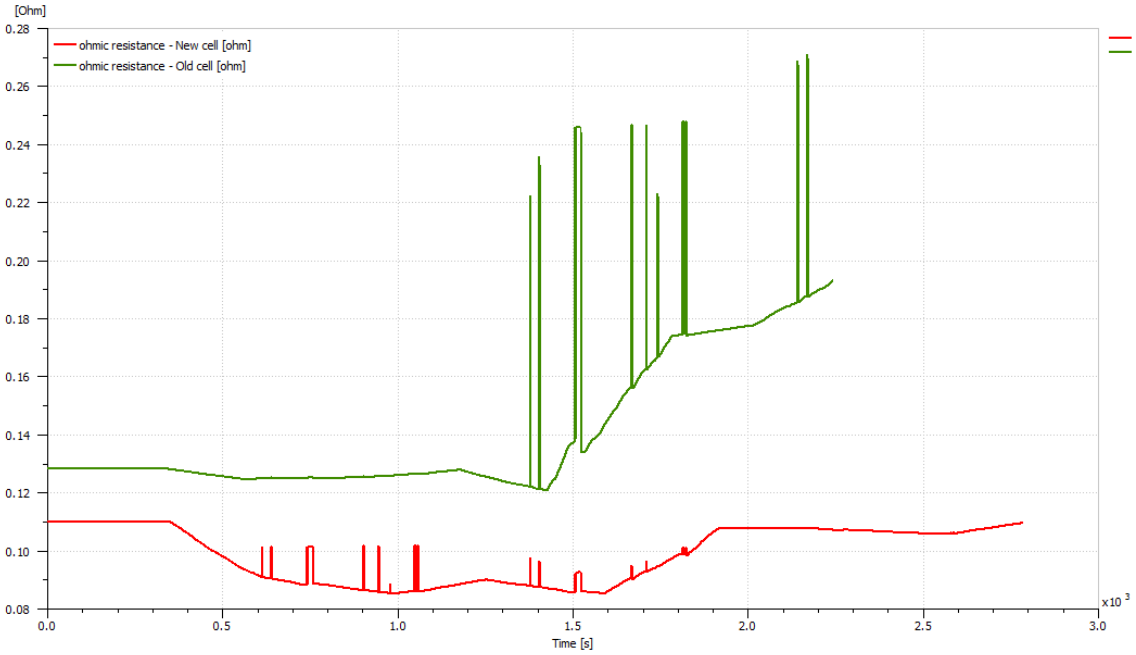

Figure 186 Evolution of battery's Ohmic resistance (EV battery aging model - ImagineLab)

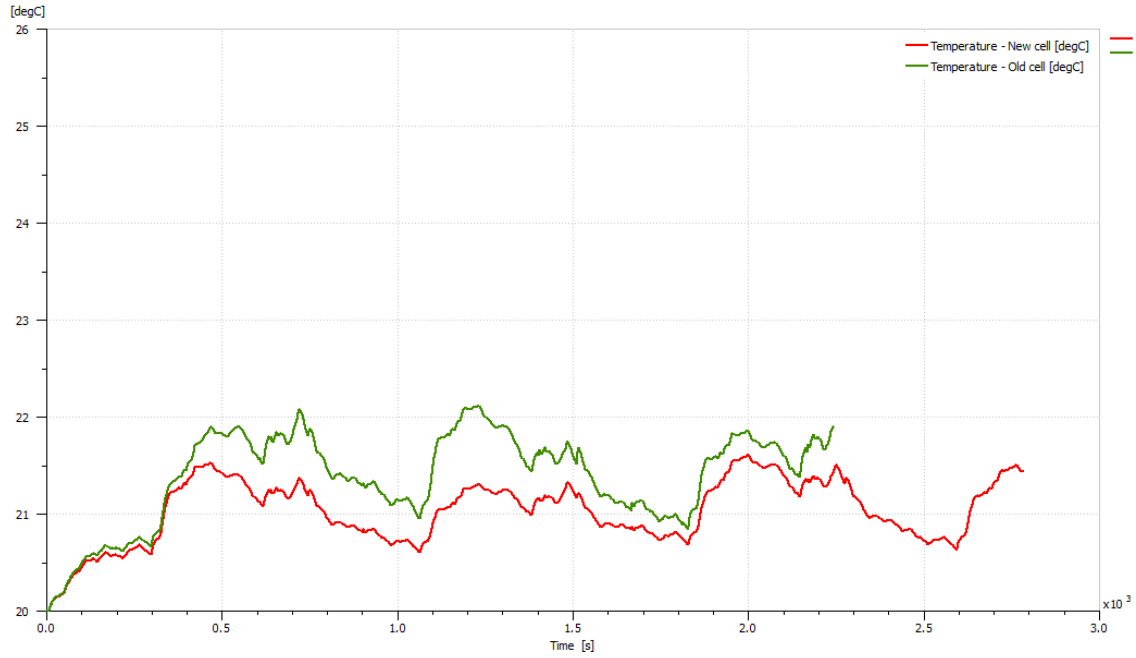

Figure 187 Evolution of battery's temperature (EV battery aging model - ImagineLab)

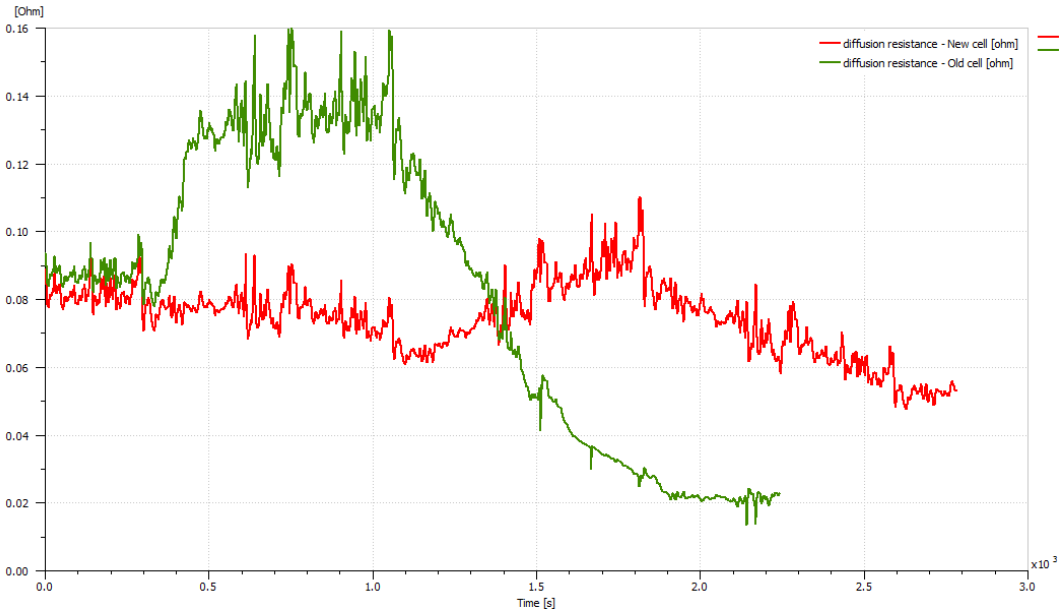

Figure 188 Evolution of battery's diffusion resistance (EV battery aging model - ImagineLab)

The vehicle's autonomy fades from 60 to 48 km due to battery aging, since the old battery has lower capacity and feeds the electric machine with higher currents due to its higher internal resistance. The higher internal resistance of the old battery also results in higher battery temperature due to the Joule effect (approximately 1 ^{o}C) deteriorating the aging effects, which thermal management strategies should be applied as functions of the battery's age. In addition, OCV decrease is faster in the old battery owing to the capacity fade and its Ohmic resistance rapidly increases as its SOC decreases to the lower limit. For low values of the SOC, the old battery exhibits lower diffusion resistance than the new battery.

Despite the fact that the HWFET has a higher average velocity than the NEDC driving cycle (77.7 instead of 33.6 km/h), the vehicle's autonomy is longer in case of the NEDC cycle, since the duration of the NEDC driving cycles equals 1180 s, while the duration of the HWFET driving cycle equals 765 s. Furthermore, the curves in the results above are smoother than those in [62], since the HWFET driving cycle curve is smoother than that of the NEDC driving cycle.

3.2.9 Case 9 : Selecting battery charging/discharging strategy depending on battery's chemistry and on the number of the cells

The model for evaluating charging strategies with respect to aging is employed to simulate the five charging scenarios under different lithium – ion battery chemistries and number of cells. In particular, the different lithium – ion batteries simulated are the high power LFP-C with 1000 cells with 2.3 Ah element nominal capacity, the high power NCA-C with 1000 cells and 2.3 Ah element nominal capacity, the high power LFP-C with 10000 cells and 0.23 Ah element nominal capacity and the high power NCA-C with 10000 cells and 0.23 Ah element nominal capacity.

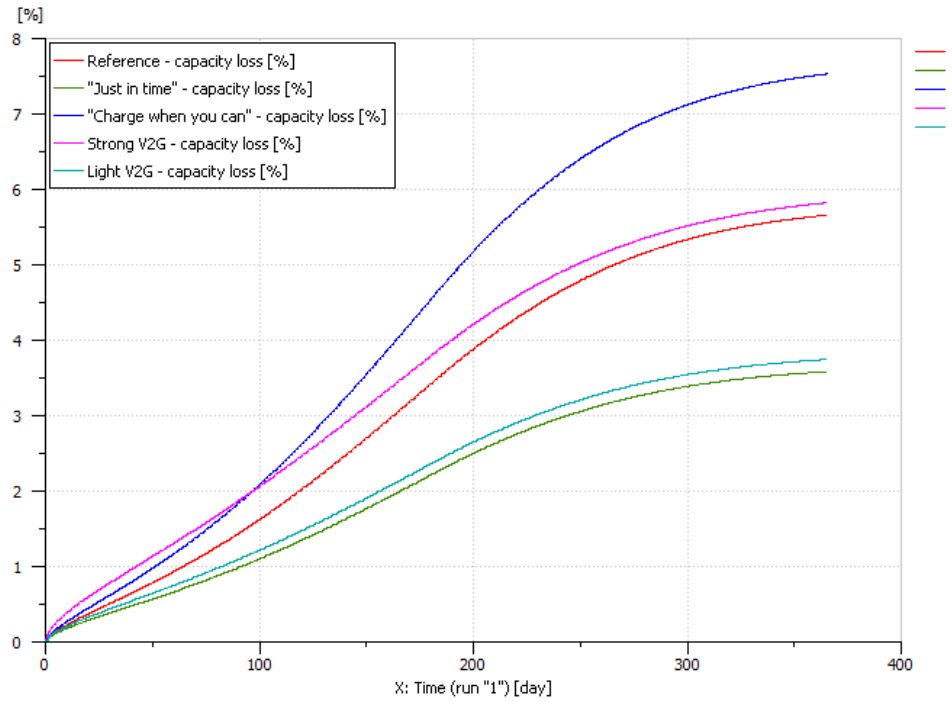

Figure 189 High power LFP-C with 1000 cells and 2.3 Ah element nominal capacity battery aging due to different charge/discharge strategies (Model for evaluating charging with respect to aging – ImagineLab) [62]

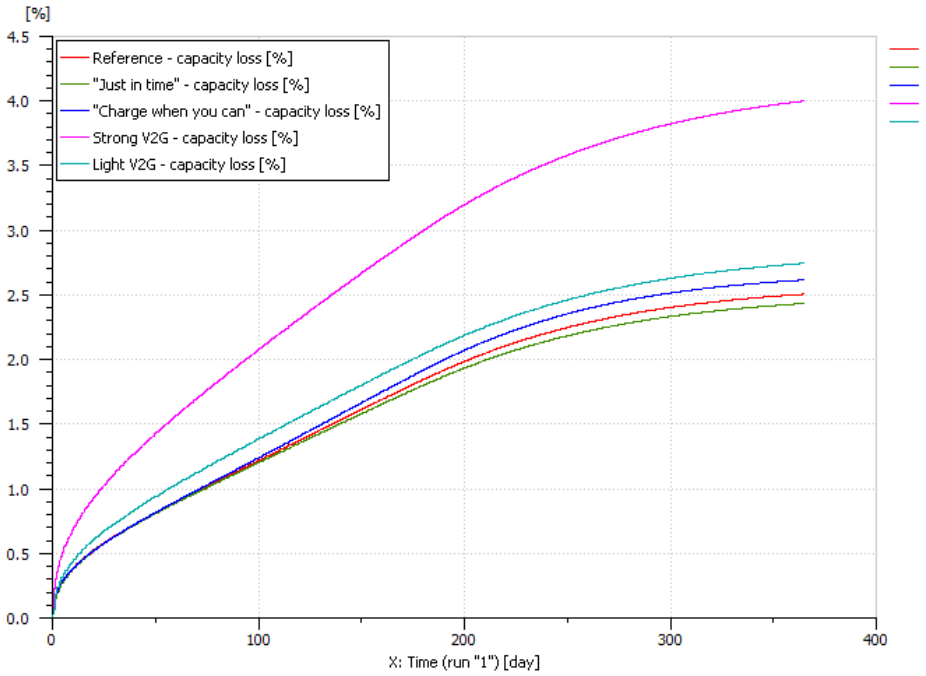

Figure 190 High power NCA-C with 1000 cells and 2.3 Ah element nominal capacity battery aging due to different charge/discharge strategies (Model for evaluating charging with respect to aging – ImagineLab) [62]

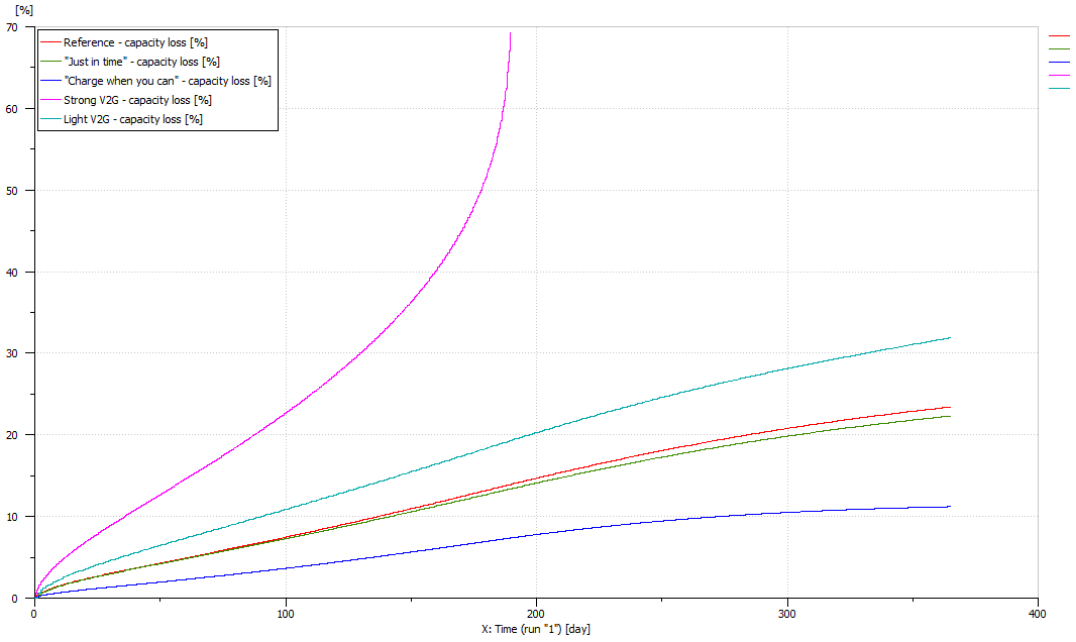

Figure 191 High power LFP-C with 10000 cells and 0.23 Ah element nominal capacity battery aging due to different charge/discharge strategies (Model for evaluating charging with respect to aging – ImagineLab) [62]

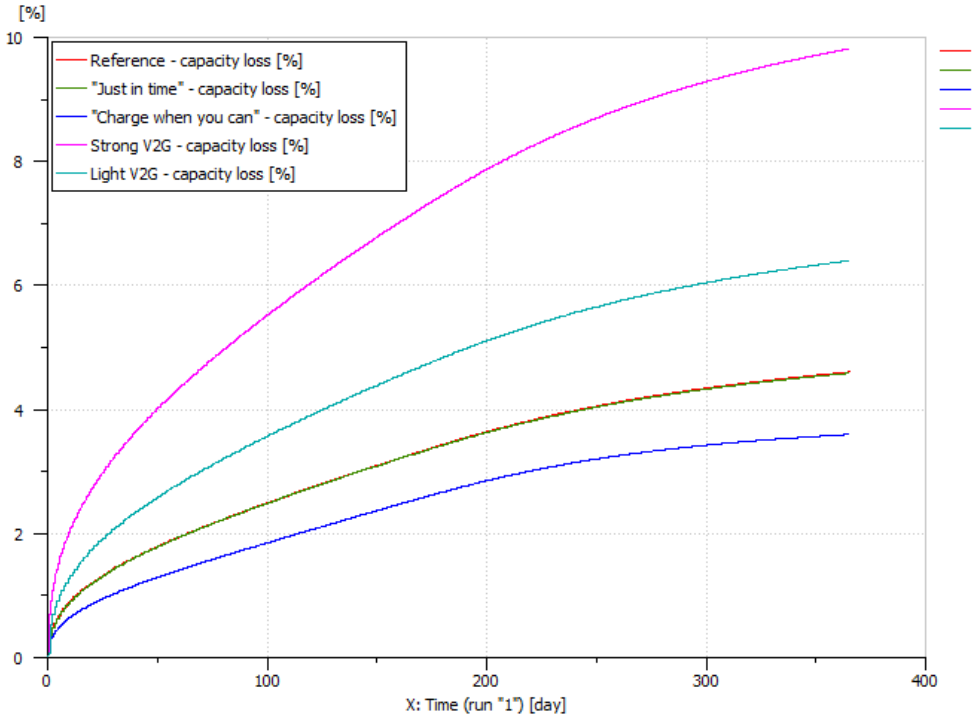

Figure 192 High power NCA-C with 10000 cells and 0.23 Ah element nominal capacity battery aging due to different charge/discharge strategies (Model for evaluating charging with respect to aging – ImagineLab) [62]

As to the battery arrangements with 1000 cells of nominal capacity of 2.3 Ah, the LFP – C battery exhibits the lowest capacity loss (3.6%) in the "Just in time" scenario according to which the battery is maintained at low SOC and is recharged just before the trip. In the light V2G scenario the LFP – C battery has a capacity loss of 3.7 % as its longer charging duration causes a higher degradation. The high capacity losses observed in the Strong V2G and in the reference scenarios are attributed to the increased number of recharges during a day and to the high SOC maintenance during night.

The NCA-C battery exhibits the lowest capacity loss (2.37%) in the "Just in time" scenario as well. However, in the two V2G scenarios the NCA-C battery has the highest capacity losses (2.73% and 3.98%) losses.

As to the battery arrangements with 10000 cells of nominal capacity of 0.23 Ah, the increase in the number of the cells resulted in the higher capacity losses and in the change of the order of the scenarios according to the corresponding capacity losses for both batteries. In particular, the "Charge when you can" scenario has the lowest capacities for both LFP-C and NCA-C batteries (11.2% and 3.6% respectively), while some scenarios, such as the strong V2G scenario in the case of LFP-C battery, become not viable due to extreme capacity losses.

All in all, LFP-C chemistry suffers less aging effects than the NCA-C chemistry, the increase in the number of the cells, other things being equal, deteriorates the aging phenomena and the optimal for minimizing the aging effects battery charging/discharging strategy depends on both the chemistry and the cell number of the battery.

3.2.10 Case 10 : Lithium – ion battery – supercapacitor system response to Formula – E load

The equivalent's circuit of the quasi – static supercapacitor includes the electrical leakage, the main capacitance and the internal resistance [62]. The leakage resistance is determined through discharge experiments on order of some hours (Δt>1) and is given by equation (3.2.10.1).

$$R_{leak} = U_{cell}(0)\frac{\Delta t}{C_{ACC} * \left(U_{cell}(\Delta t) - U_{cell}(0)\right)} = \frac{U_{cell}(0)}{I_{leak}} \quad (3.2.10.1)$$

Where I_{leak} is the discharge current.

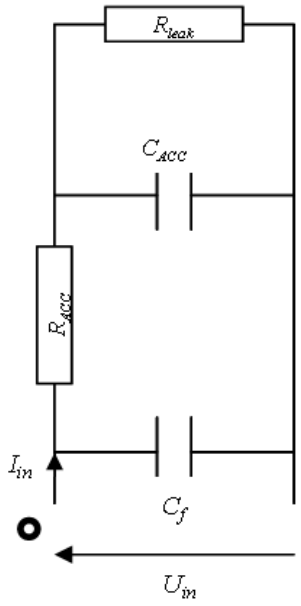

Figure 193 Equivalent circuit of quasi - state supercapacitor's model (ImagineLab) [62]

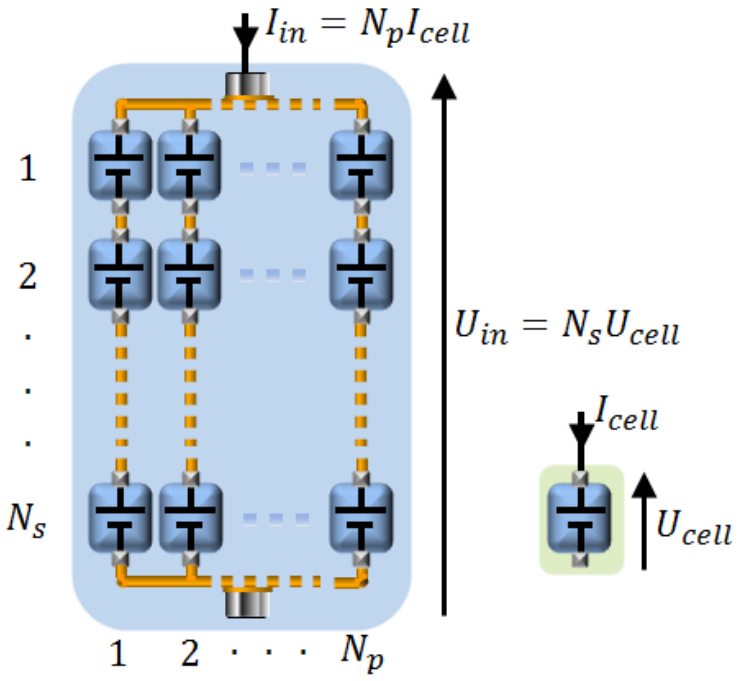

Figure 194 Supercapacitor pack consisting of Np branches and Ns cells in series (ImagineLab) [62]

The supercapacitor mainly suffers energy losses due to the Joule effect (internal resistance) and due to reversible heat losses, which are attributed to entropy variations and are expressed by means of an entropic coefficient. The internal resistance is set to 6 mΩ, while the entropic coefficient is set to zero.

The energy and power storage system model (ImagineLab) is utilized for simulating the response of a lithium – ion battery – supercapacitor system to a Formula – E load. The model parameters are summarized in the table below and are set according to the values in [37].

Table 13 Lithium - ion battery - supercapacitor hybrid system parameters

Battery rated voltage	1000 V
Battery rated energy	28 kWh
Battery cell rated capacity	20 Ah
Battery cell rated voltage	3.3 V
Supercapacitor maximum energy	0.5 kWh
Supercapacitor cell maximum voltage	2.7 V

Supercapacitor cell maximum capacity	15000 F
Load rated power	50 kW
Load peak power	80 kW

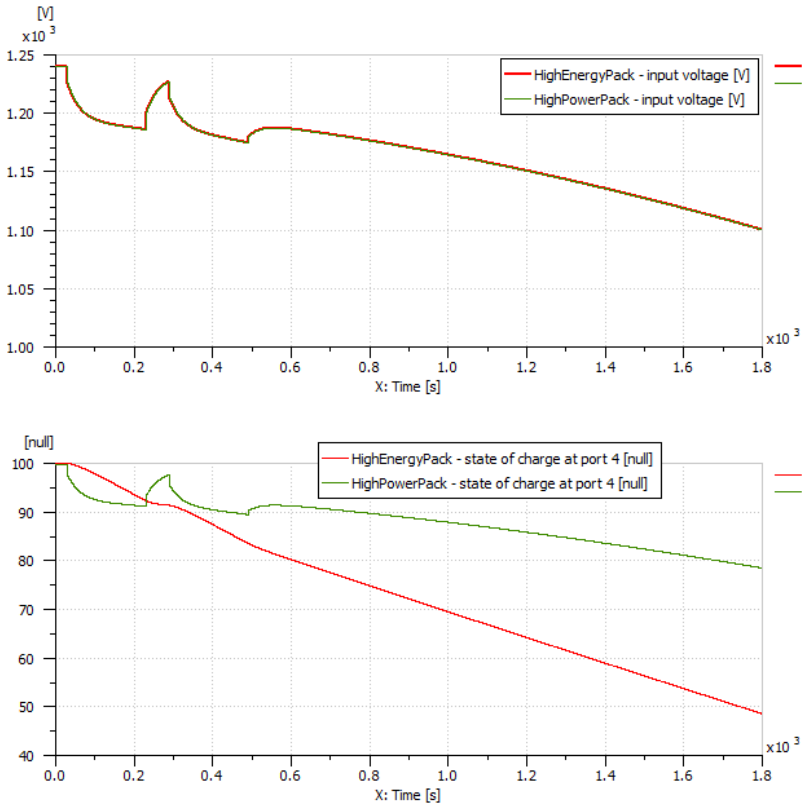

Figure 195 SOC of hybrid energy storage system components (The energy and power storage system model – Imaginelab)

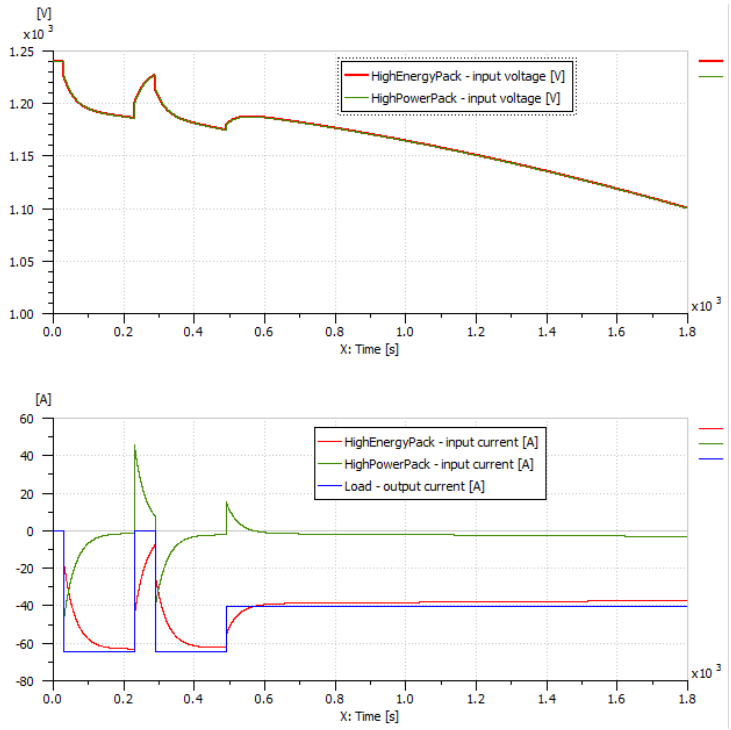

Figure 196 Load, battery and supercapacitor currents (The energy and power storage system model – Imaginelab)

The contribution of the supercapacitor is the battery's current remaining at reasonable levels. However, in the results of the simulation above the duration of the peak current period is quite long and as a result, the battery's current remains low only at the beginning of the peak current period. At the end of the simulation the battery's SOC equals 49%, while the supercapacitor's SOC equals 78%. During discharge current transitions, the current of the battery does not become zero instantaneously and a supercapacitor's current of opposite direction exists such that the Kirchoff's law is valid. Increase in the cell capacity or in the cell voltage capacity or in both of them entails the longer contribution of the supercapacitor to the load current.

A circuit breaker is added to the circuit such that the supercapacitor is connected only in peak demand cases.

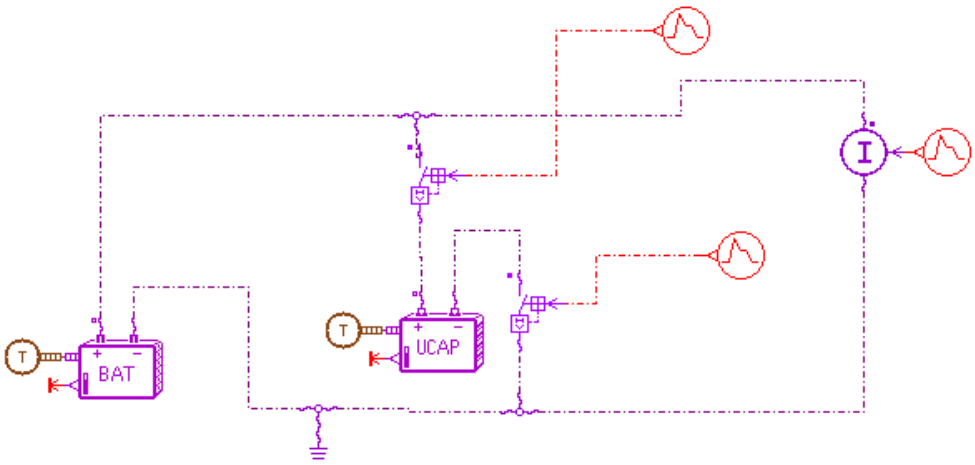

Figure 197 Hybrid energy storage system model with circuit breaker (The energy and power storage system model – Imaginelab)

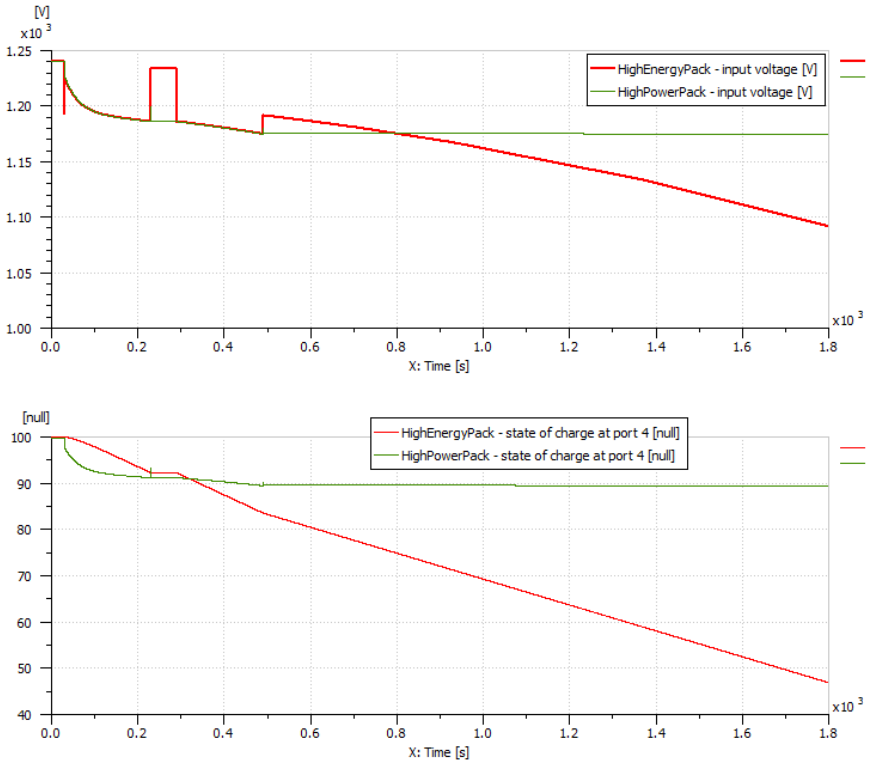

Figure 198 SOC of hybrid energy storage system components (The energy and power storage system model – Imaginelab)

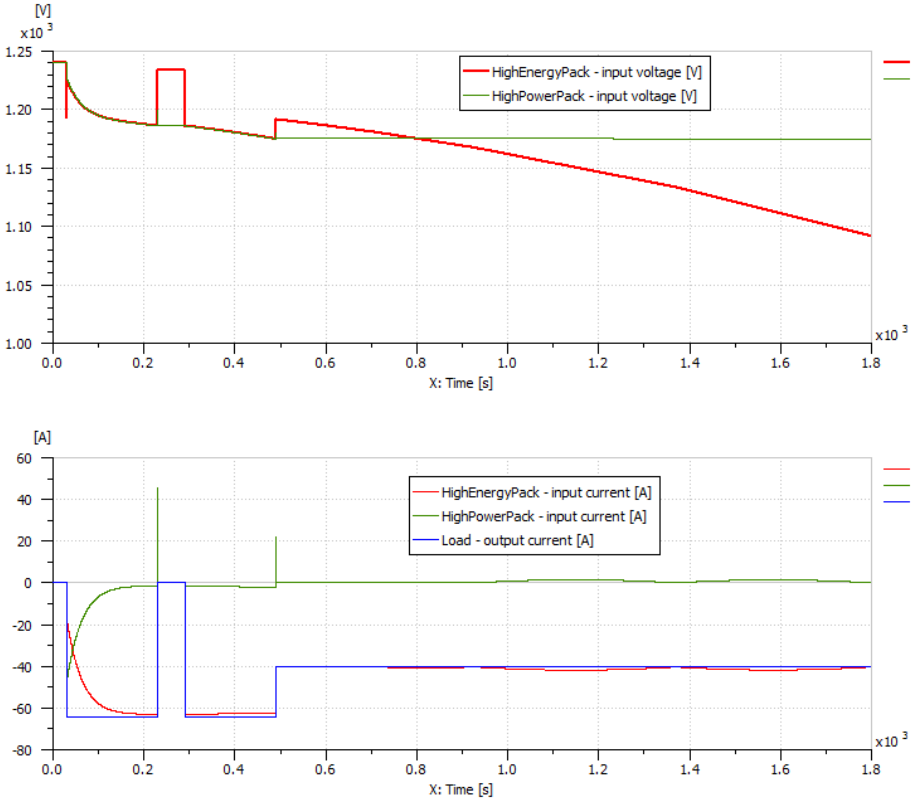

Figure 199 Load, battery and supercapacitor currents (The energy and power storage system model – Imaginelab)

The addition of the circuit breaker maintained the SOC of the supercapacitor at a higher level (89%), whereas the battery's SOC was slightly reduced. Furthermore, the transitional phenomena were reduced to the delay introduced by the circuit breaker.

3.2.11 Case 11 : Ambient temperature and initial SOC effects on battery cell load and voltage response

- **Scenario 1:**

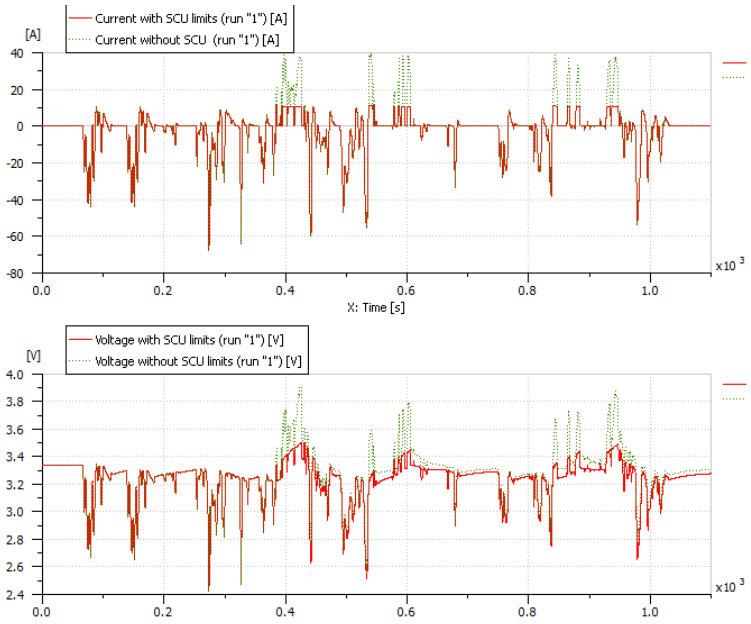

Figure 200 Scenario 2: Tamb = 20 oC, SOC = 80% (SCU based on look - up table model - ImagineLab) [62]

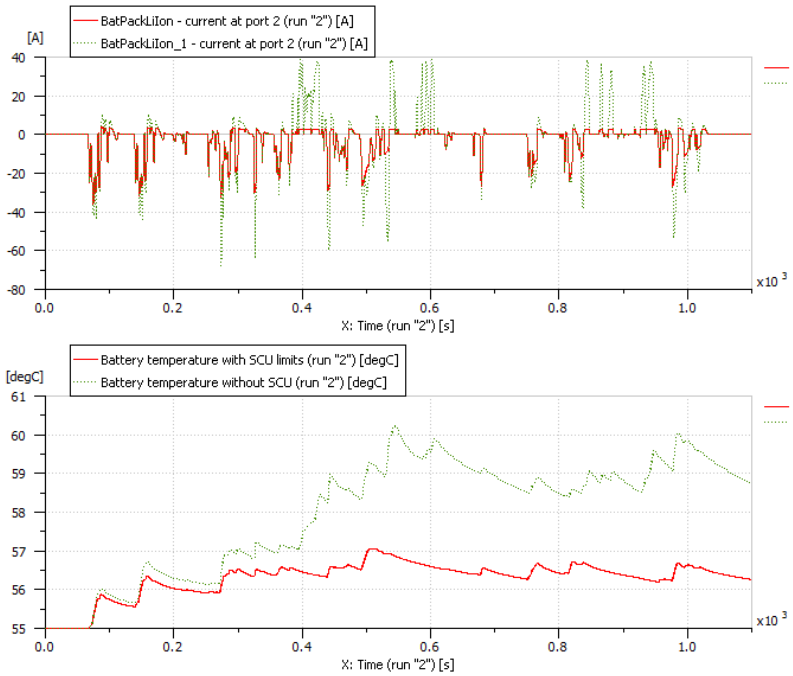

Figure 201 Scenario 2: Tamb = 55 oC, SOC = 40% (SCU based on look - up table model - ImagineLab) [62]

- **Scenario 2:**

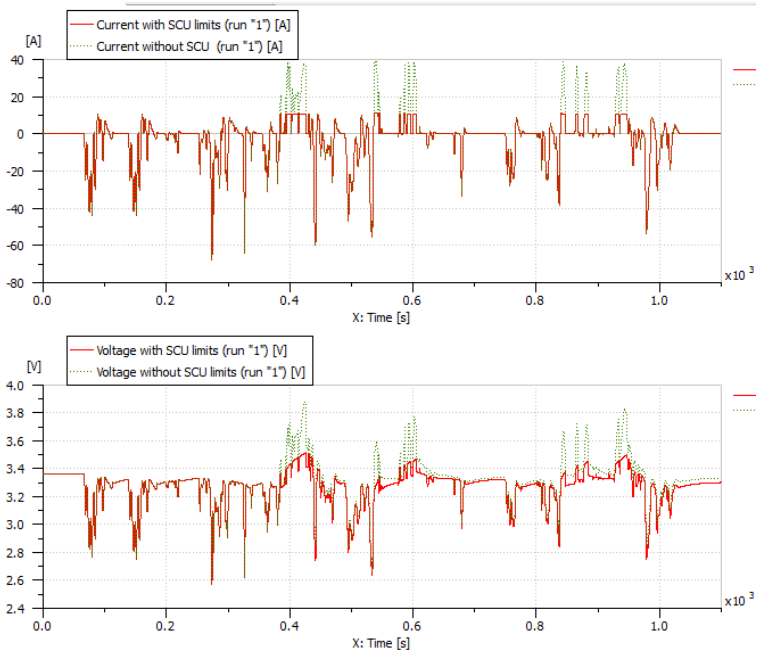

Figure 202 Scenario 2: Tamb = 25 oC, SOC = 90% (SCU based on look - up table model - ImagineLab)

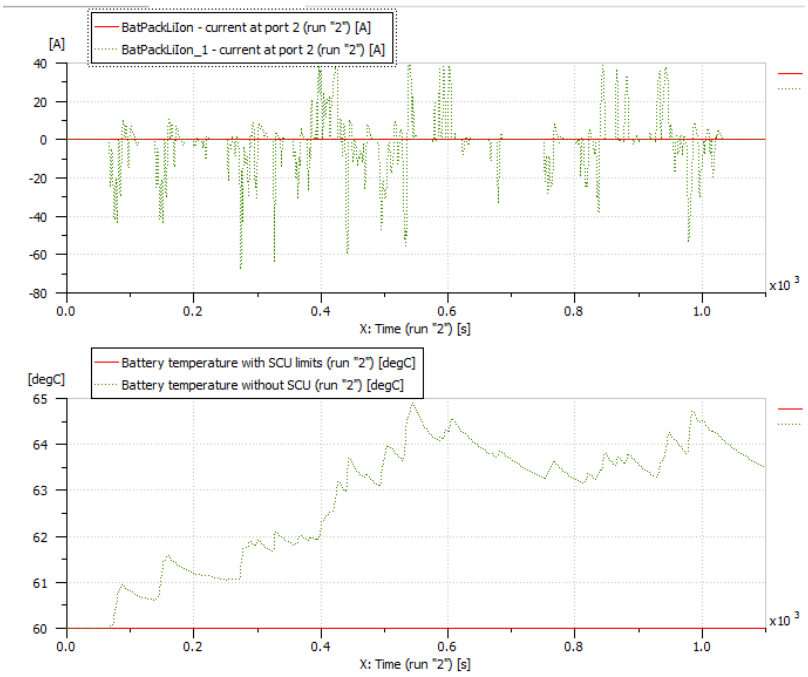

Figure 203 Scenario 2: Tamb = 60 oC, SOC = 50% (SCU based on look - up table model - ImagineLab)

SCU limits the battery cell current such that it always is lower than 30 A and as a result the cell remains below the safety limit of 3.6 V. In scenario 1 the temperature of the battery cell being not protected from the SCU reaches up to 60 ^{o}C (maximum temperature allowed by the manufacturer). On the other hand, the current of the battery cell under SCU decreases in order for overheating to be averted. In scenario 2 the increase in the SOC from 80% to 90% has no effect on the voltage and on the current response, whereas an ambient temperature of 60 ^{o}C results in the battery cell not protected from the SCU exceeding 60 ^{o}C during operation, whereas the battery cell under SCU is not allowed for operation.

3.2.12. Case 12 : Lithium – ion battery response to HEV driving cycles, heat capacity/battery density/thermal conductivity and initial cell voltage effects

- **Reference scenario:**

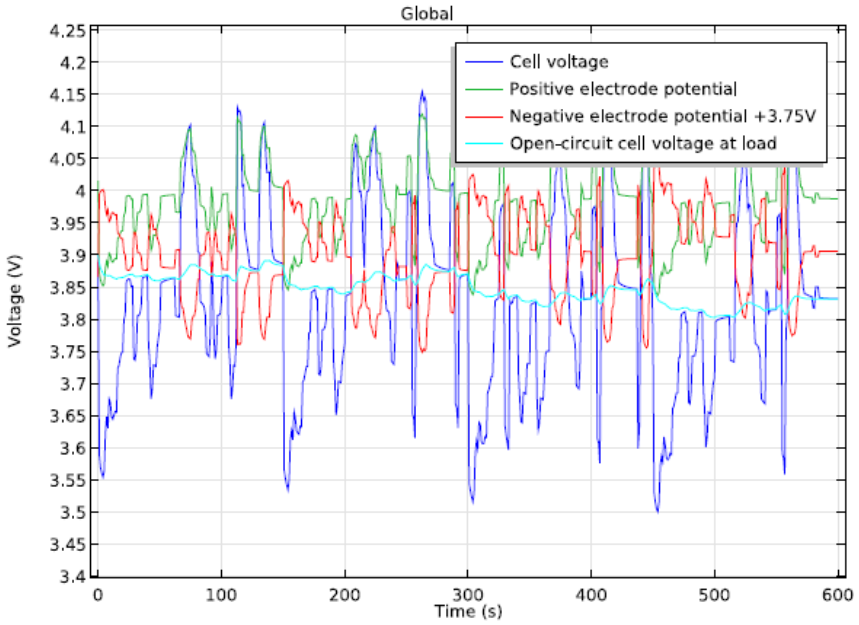

Figure 204 Reference scenario: Cell voltage, OCV, electrode potential (Lithium – ion battery response to HEV driving cycles - Comsol) [55]

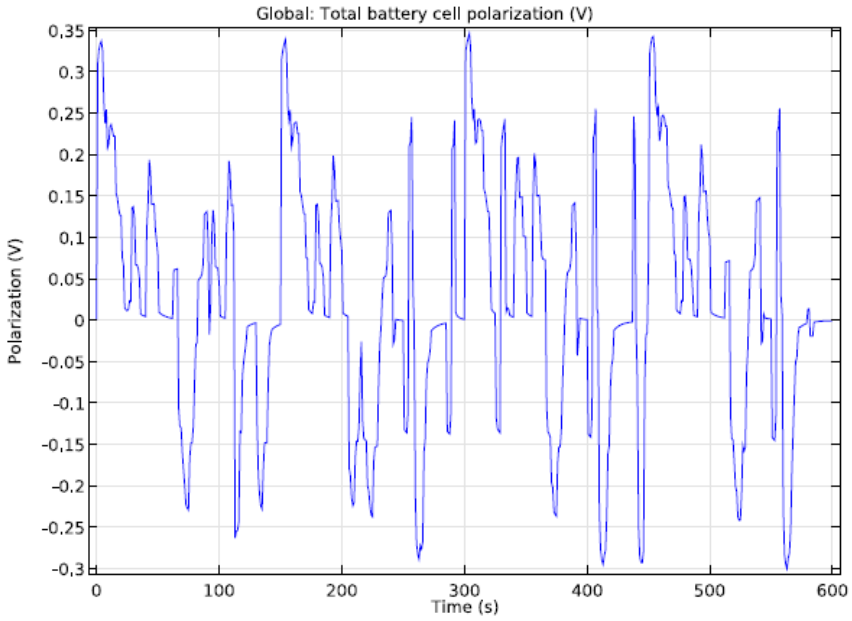

Figure 205 Reference scenario: Total polarization ((Lithium – ion battery response to HEV driving cycles - Comsol) [55]

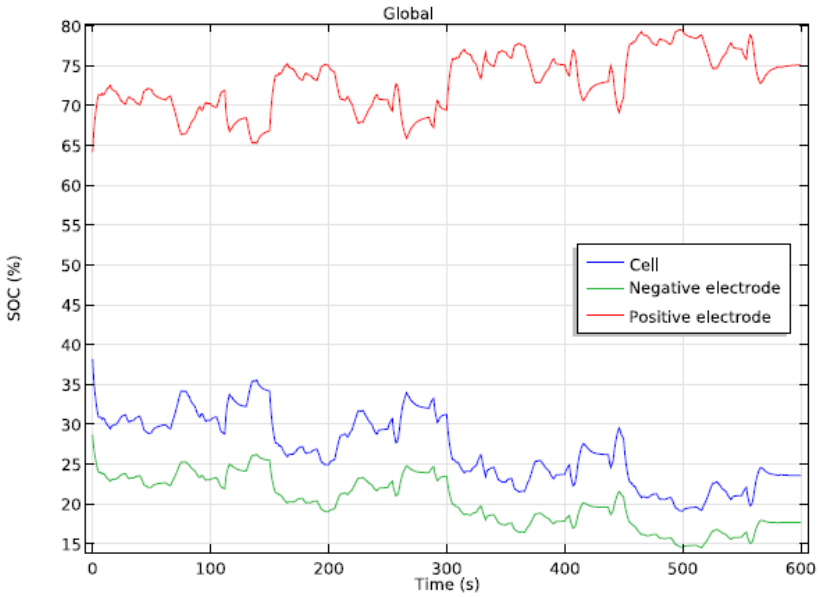

Figure 206 Reference scenario: Cell and electrodes SOC (Lithium – ion battery response to HEV driving cycles - Comsol) [55]

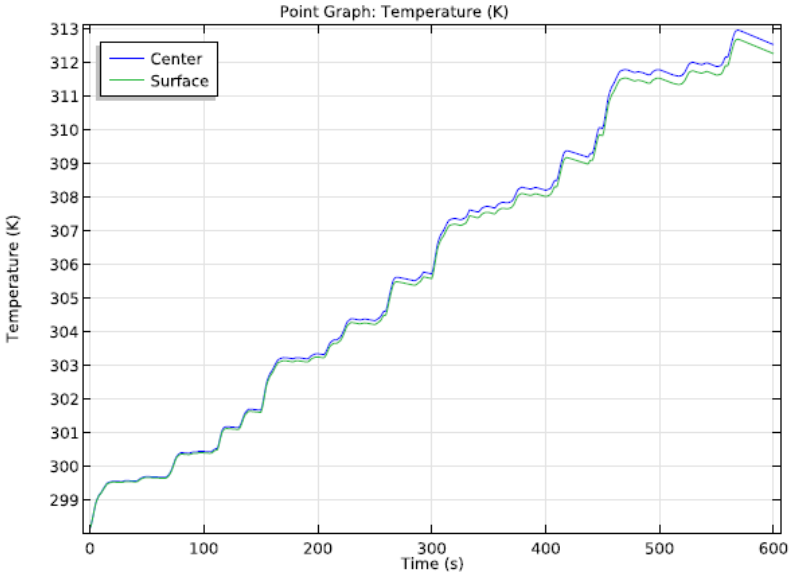

Figure 207 Reference scenario: Temperature at the current collector of the positive electrode (Lithium – ion battery response to HEV driving cycles - Comsol) [55]

- **Scenario 1:**

The positive electrode thickness is changed from $55*10^{-6}$ to $66*10^{-6}$ m (20% increase) and the positive electrode heat capacity is changed from 1269.2 to 1523.04 J/kgK.

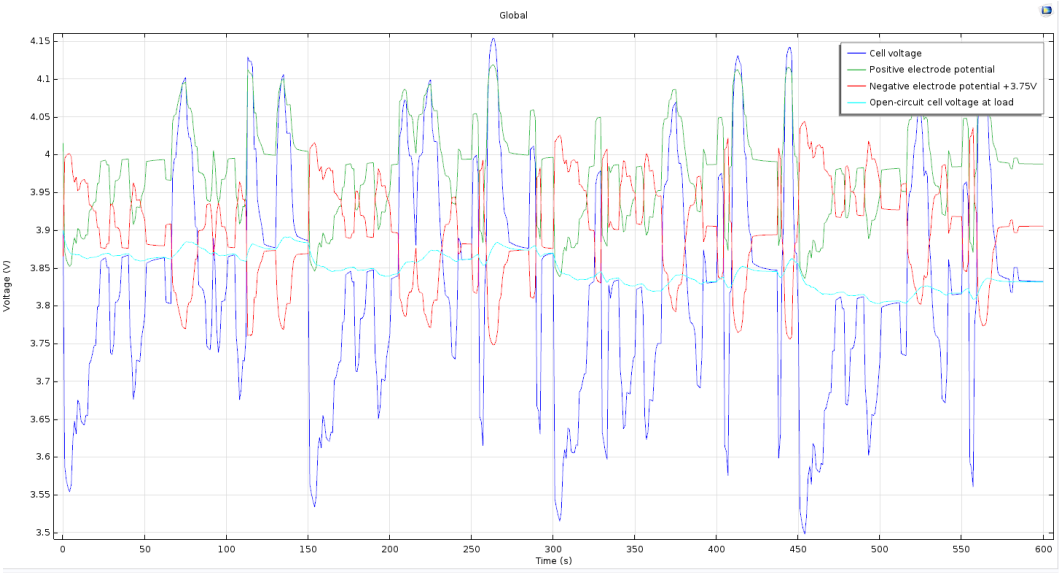

Figure 208 Scenario 1: Cell voltage, OCV, electrode potential (Lithium – ion battery response to HEV driving cycles - Comsol)

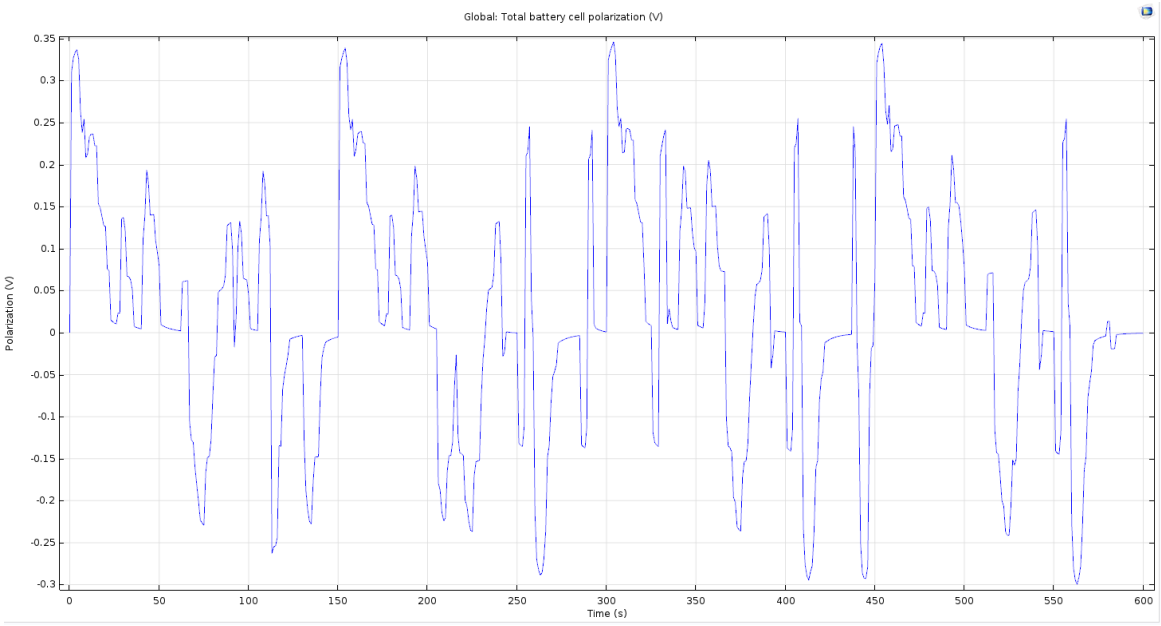

Figure 209 Scenario 1: Total polarization (Lithium – ion battery response to HEV driving cycles - Comsol)

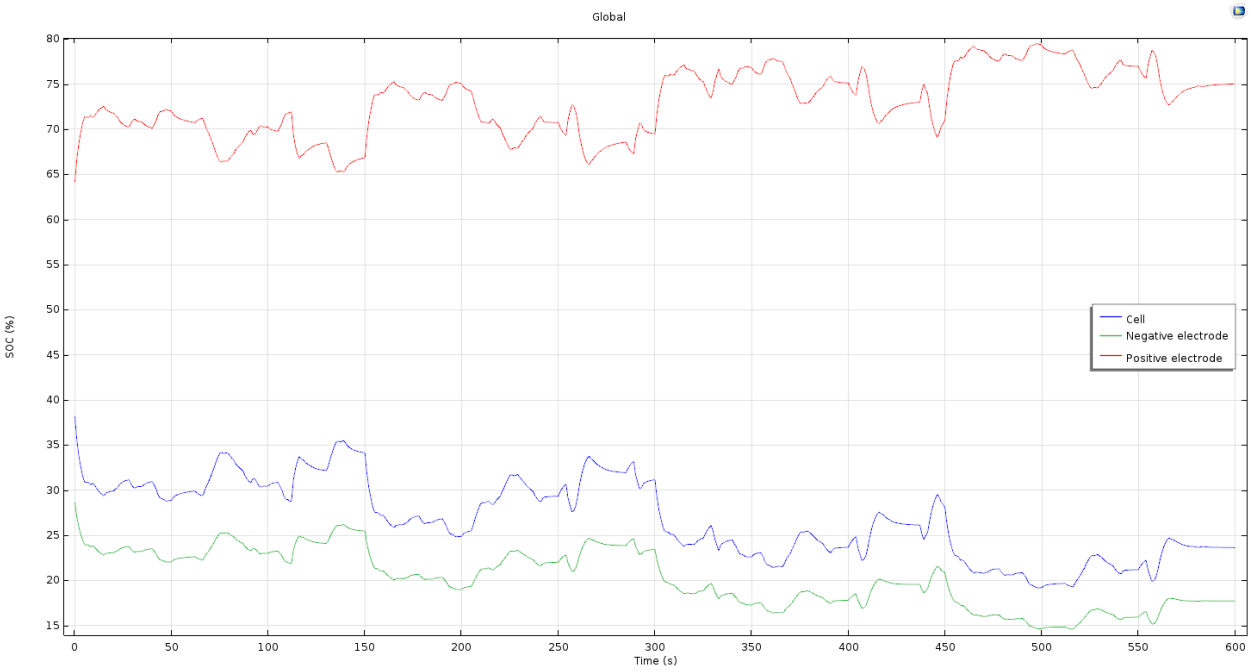

Figure 210 Scenario 1: Cell and electrodes SOC (Lithium – ion battery response to HEV driving cycles - Comsol)

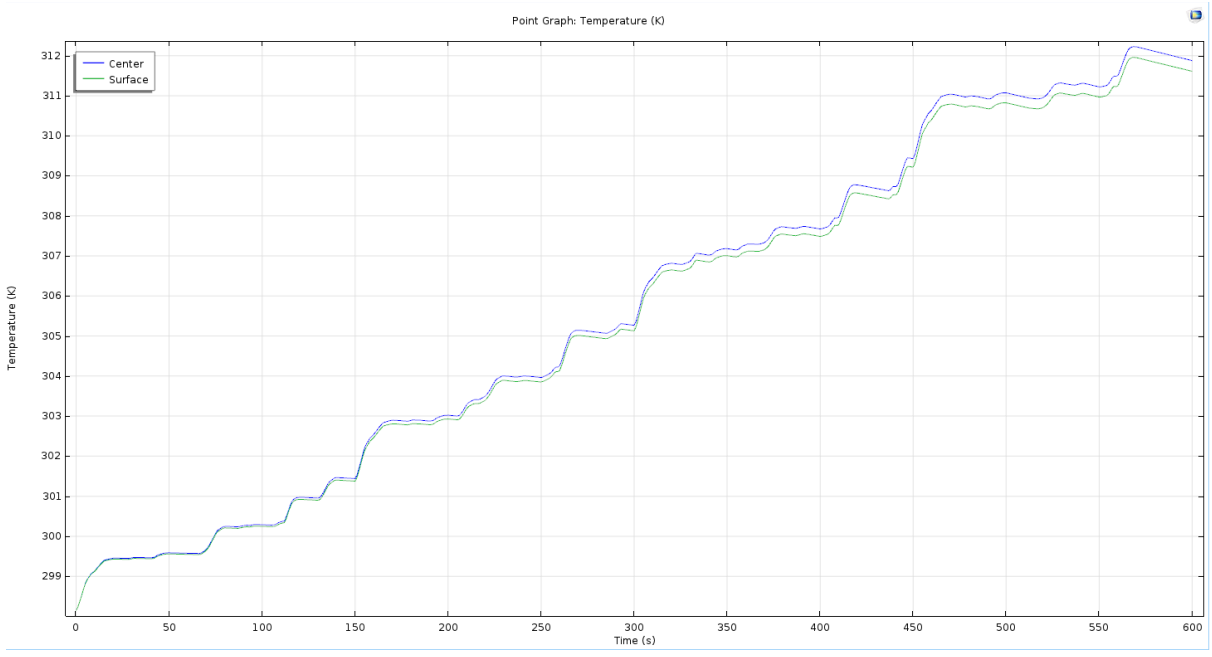

Figure 211 Scenario 1: Temperature at the current collector of the positive electrode (Lithium – ion battery response to HEV driving cycles - Comsol)

- **Scenario 2:**

The positive electrode density is changed from 2328.5 to 2794.2 kg/m^3 (20% increase).

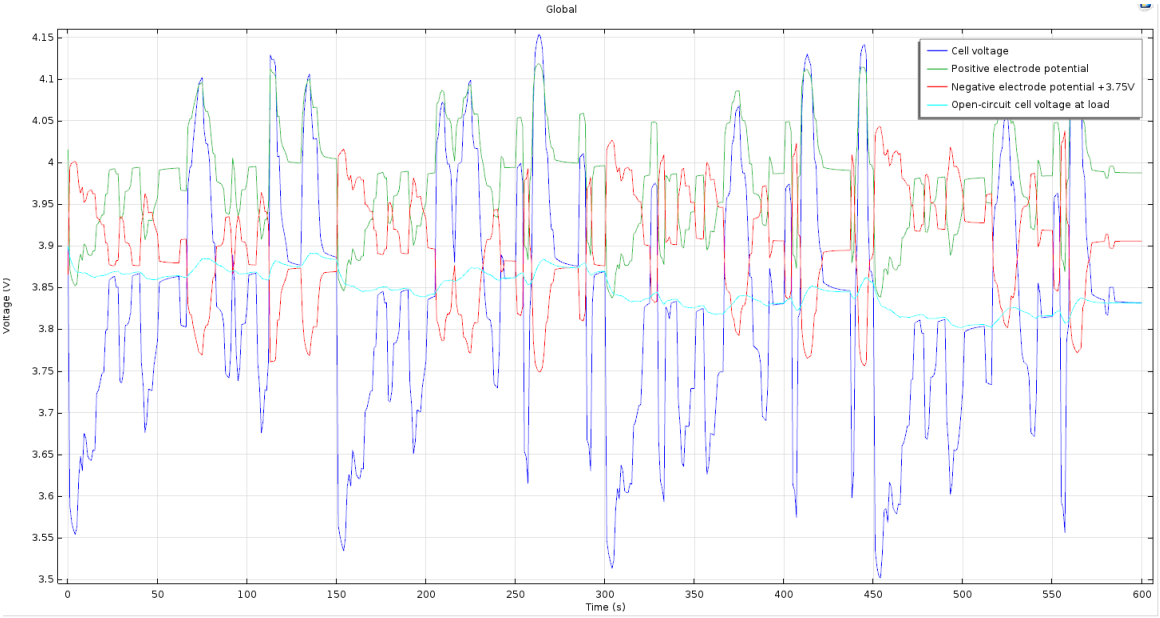

Figure 212 Scenario 2: Cell voltage, OCV, electrode potential (Lithium – ion battery response to HEV driving cycles - Comsol)

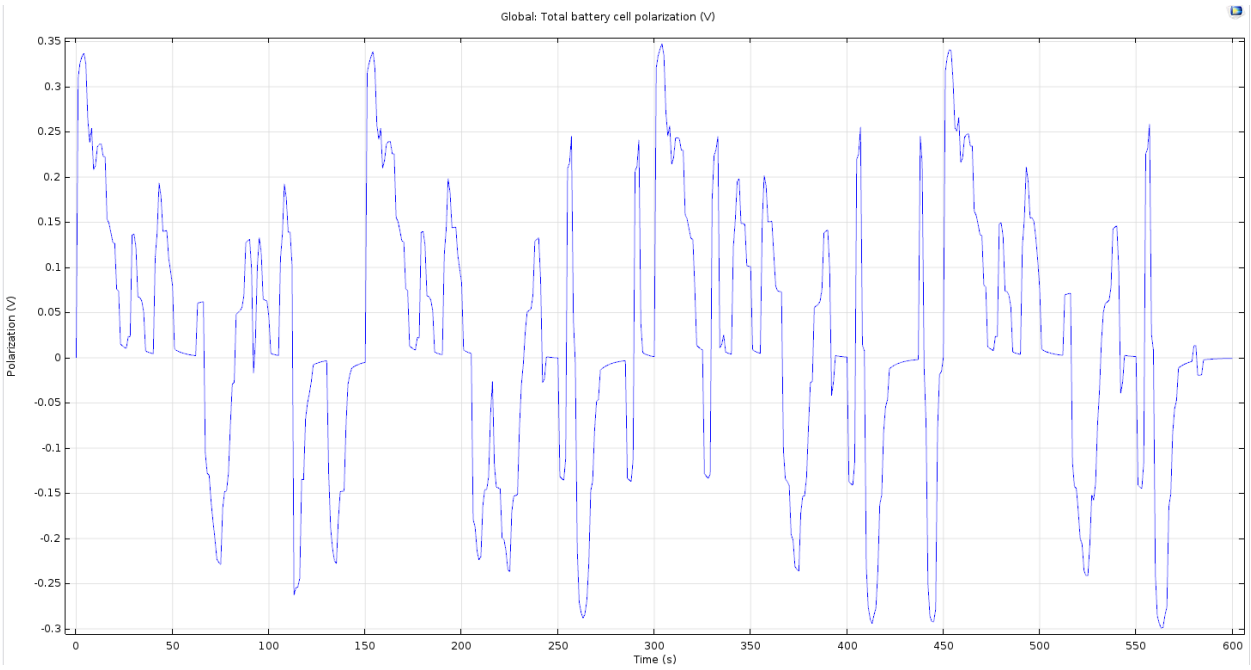

Figure 213 Scenario 2: Total polarization (Lithium – ion battery response to HEV driving cycles - Comsol)

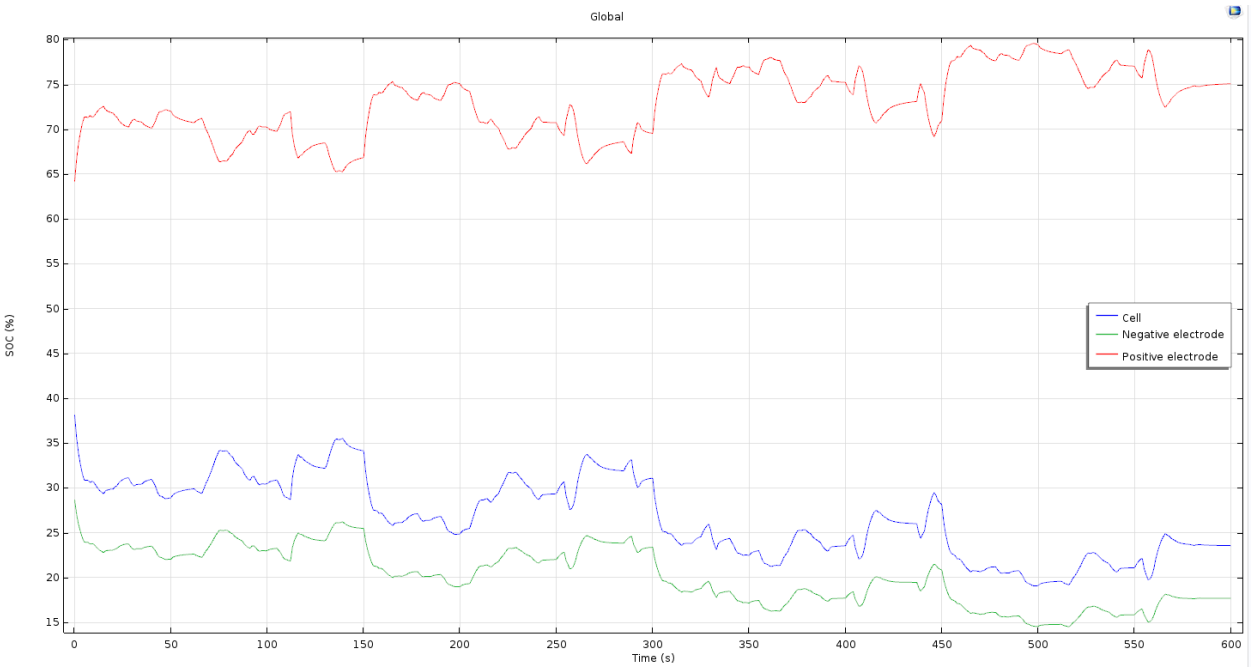

Figure 214 Scenario 2: Cell and electrodes SOC (Lithium – ion battery response to HEV driving cycles - Comsol)

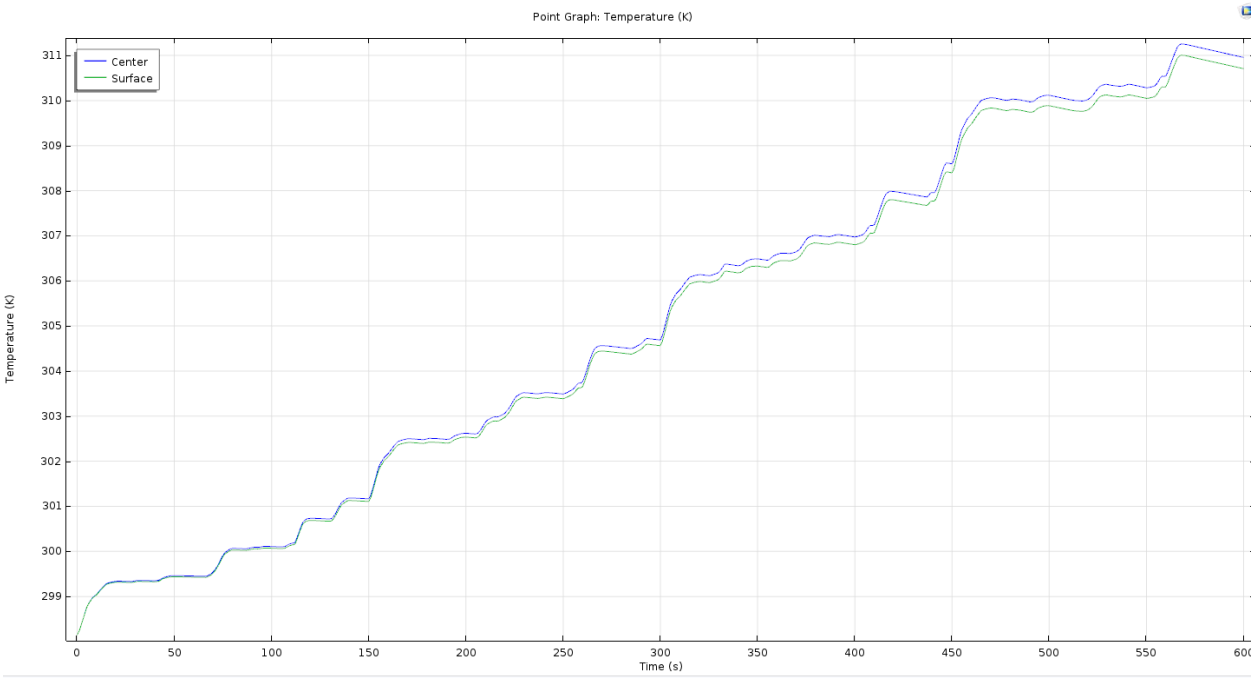

Figure 215 Scenario 2: Temperature at the current collector of the positive electrode (Lithium – ion battery response to HEV driving cycles - Comsol)

- **Scenario 3:**

The cell thickness being the sum of the thicknesses of the two electrodes, of the two current collectors and of the separator is changed from 1.43 to 1.716 * 10^{-4} m (20% increase, negative current collector thickness = 13.56 µm, positive current collector thickness = 20 µm). Despite the fact that the cell thickness affects battery heat capacity, density and the thermal conductivity, this configuration also leads to no significant differences in the response. In scenario 3 the **initial cell voltage** is changed from 3.9 to 4.5 V.

Figure 216 Scenario 3: Cell voltage, OCV, electrode potential (Lithium – ion battery response to HEV driving cycles - Comsol)

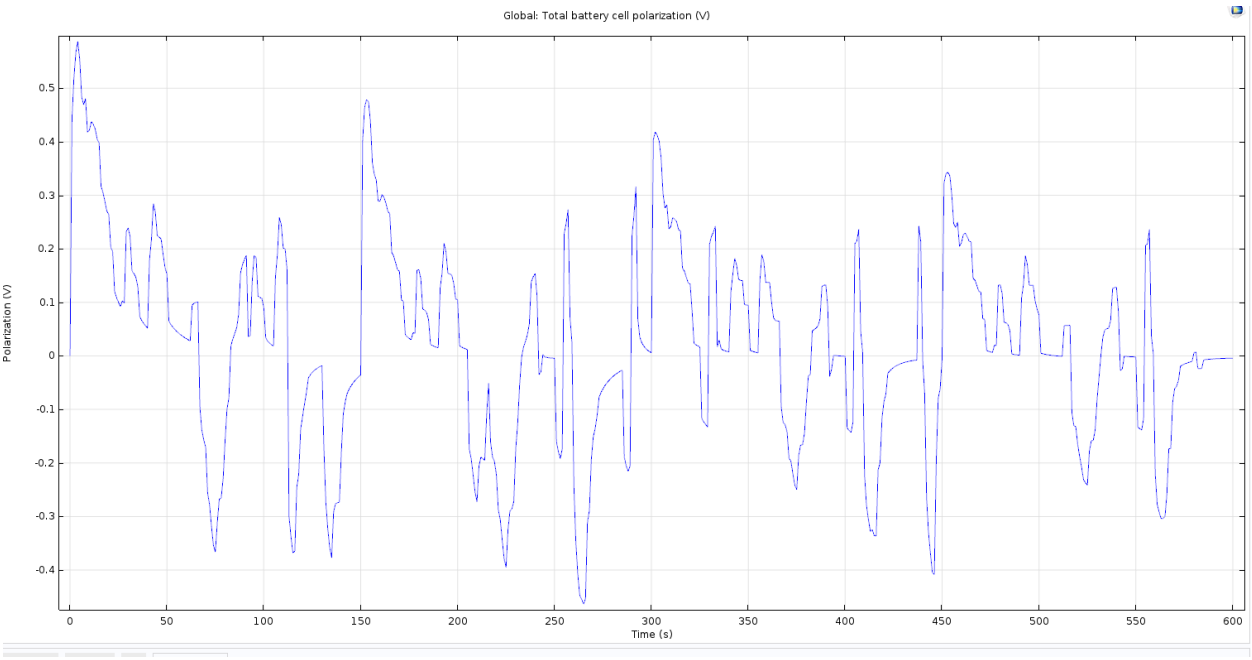

Figure 217 Scenario 3: Total polarization (Lithium – ion battery response to HEV driving cycles - Comsol)

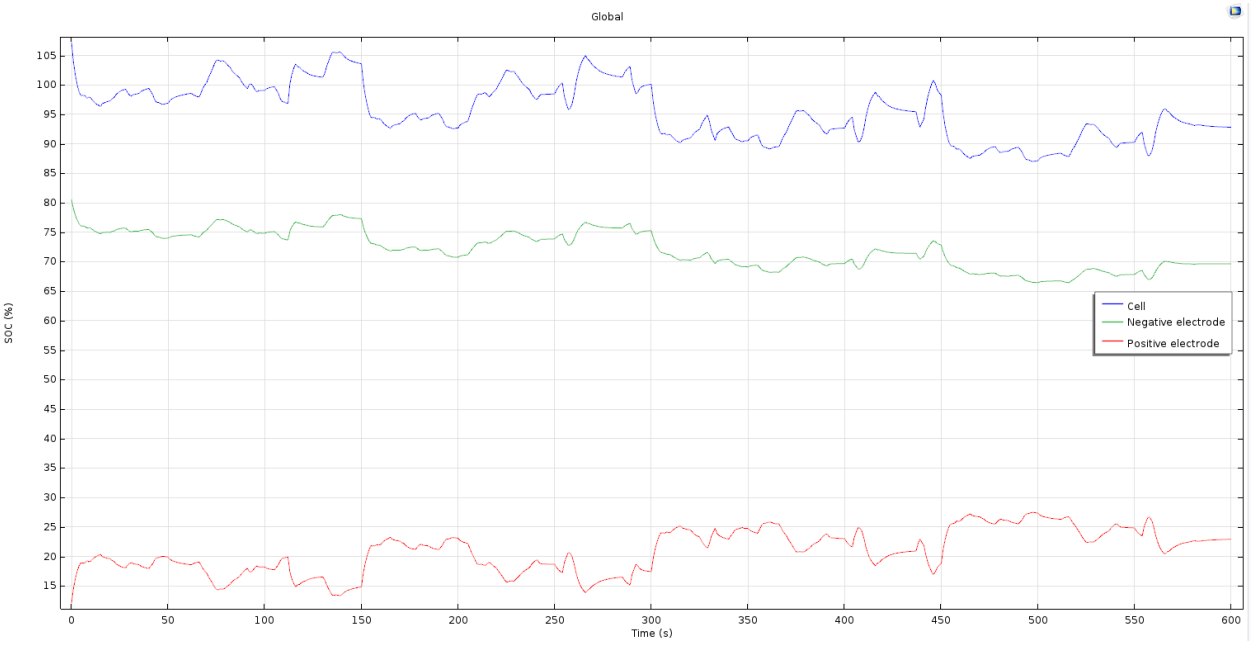

Figure 218 Scenario 3: Cell and electrodes SOC (Lithium – ion battery response to HEV driving cycles - Comsol)

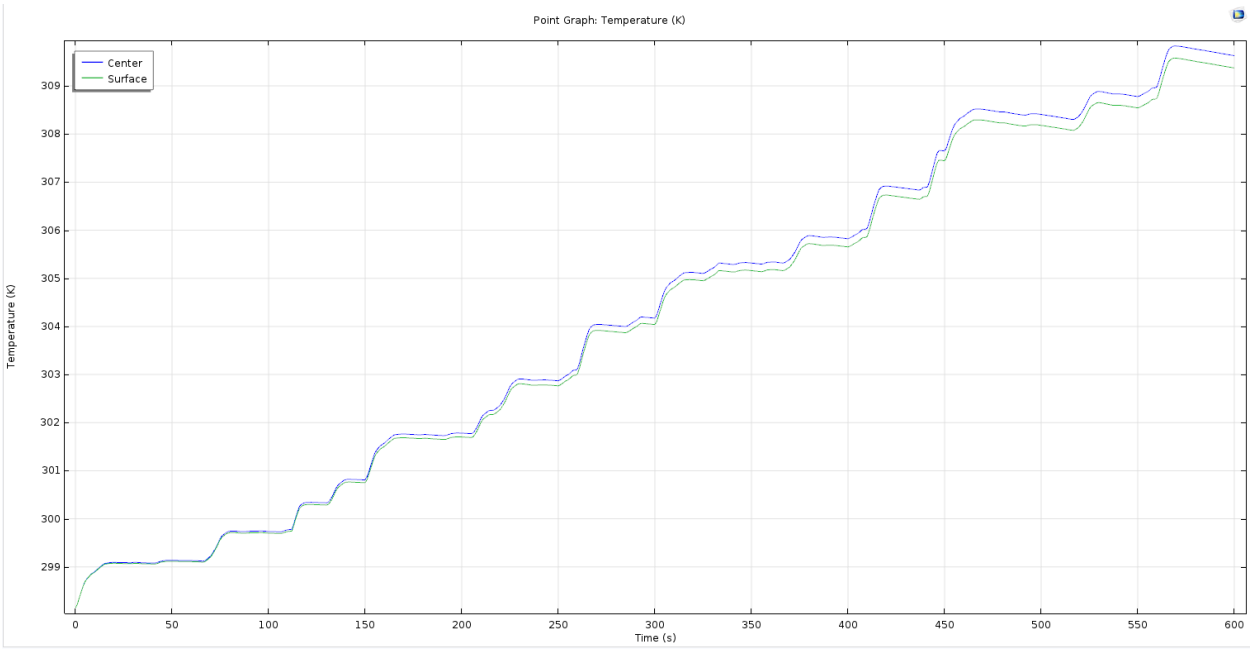

Figure 219 Scenario 3: Temperature at the current collector of the positive electrode (Lithium – ion battery response to HEV driving cycles - Comsol)

The cell voltage varies significantly more than OCV in any case, while the positive electrode potential varies more compared to the negative electrode potential. The battery's lifetime and safety depend on its operation between a specified range of voltage values. Because the range of acceptable voltage values for this chemistry is [3.3, 4.2], the voltage reaching 4.25 V during the cycle has to be reduced [55].

The polarization curve signifies the internal resistance, which means that high values in the polarization curve decrease the battery lifetime by increasing the heat produced. Maintaining SOC at high levels also guarantees the system's stability and reduces thermal stresses on the battery [55].

The trend of the temperature at the current collector of the positive electrode indicate so thermal runaway as aging are possible in the long run, in case no heat dissipation is applied [55]. The temperatures at the center and at the surface being approximately the same indicates that no hot spots are formed due to temperature variations [55].

Except for minor changes in the cell voltage, in the polarization curve, in the SOC of cells and electrodes and in the temperature at the current collector of the positive electrode curves, the changes in the

parameters affecting the battery heat capacity, density and thermal conductivity in scenarios 1 and 2 result in no significant response changes.

In scenario 3 the increase in the voltage along with the other changes resulted in the change of the cell voltage and electrode potentials profiles, in the increase of the cell's SOC such that it is 93% once the cycle finishes (the battery is actually charged higher than its nominal capacity 12 Ah), in considerable changes in the SOC of the electrodes and in the reduction of the temperature at the current collector of the positive electrode by 3 K. That is to say, the increase in the initial cell voltage by 0.6 V considerably improved the battery's performance, extended the battery's lifespan and reduced the risk of thermal runaway.

3.2.13 Case 13 : Parasitic lithium – solvent redox reaction effect on lithium – ion battery response

Fick's first law describes the flux due to diffusion in dilute species transport, where the interaction between the solvent and the solute depends exclusively on the diffusion coefficient [55]. Tortuosity is defined as "the ratio of the actual distance that a molecule covers between two points by following the fluid channel to the straight-line distance between those points" [55]. This means that the concentration of lithium – ions and the parasitic current could increase by increasing the diffusion coefficient, since according to equation (2.17.1) the parasitic current is dependent on the concentration of lithium – ions in the electrolyte. In order for the lithium – ions concentration to be increased in the model, the density of the product of the side reaction is increased (from 2100 kg/m^3), whereas the molar mass of the product of the side reaction (0.1 kg/mol).

- **Reference scenario: Density of the product of the side reaction = 2100 kg/m^3, molar mass of the product of the side reaction = 0.1 kg/mol.**

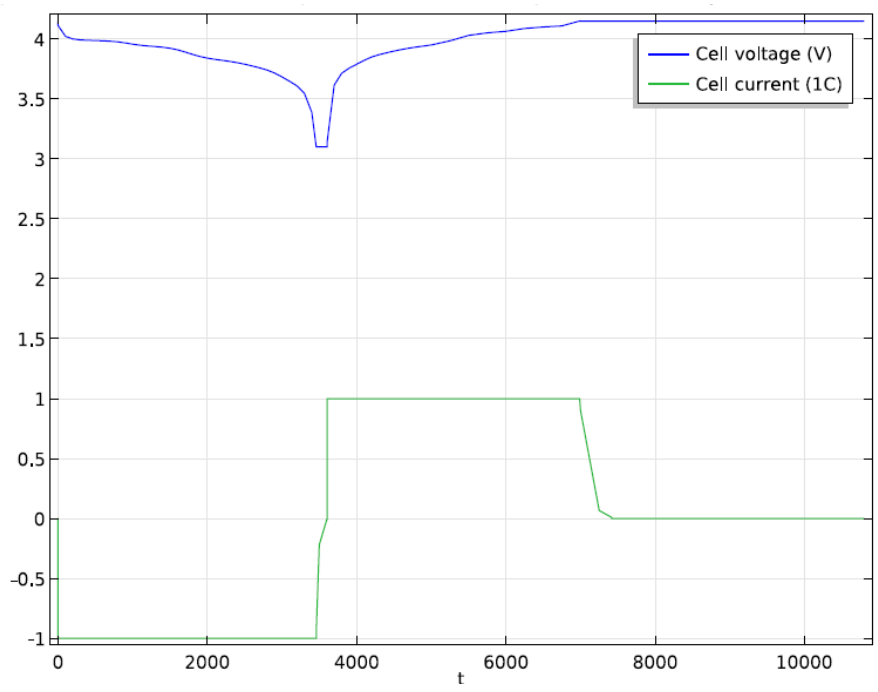

Figure 220 Battery potential and current vs during the 10th cycle (Lithium – ion battery capacity fade model in Comsol Multiphysics) [55]

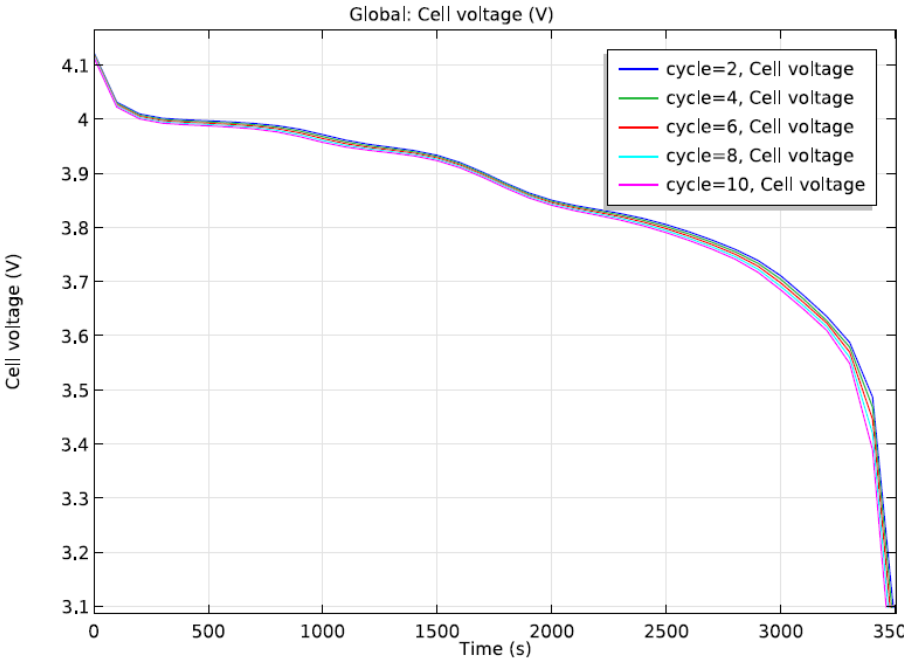

Figure 221 Reference scenario: Cell voltage during several cycles (Lithium – ion battery capacity fade model in Comsol Multiphysics) [55]

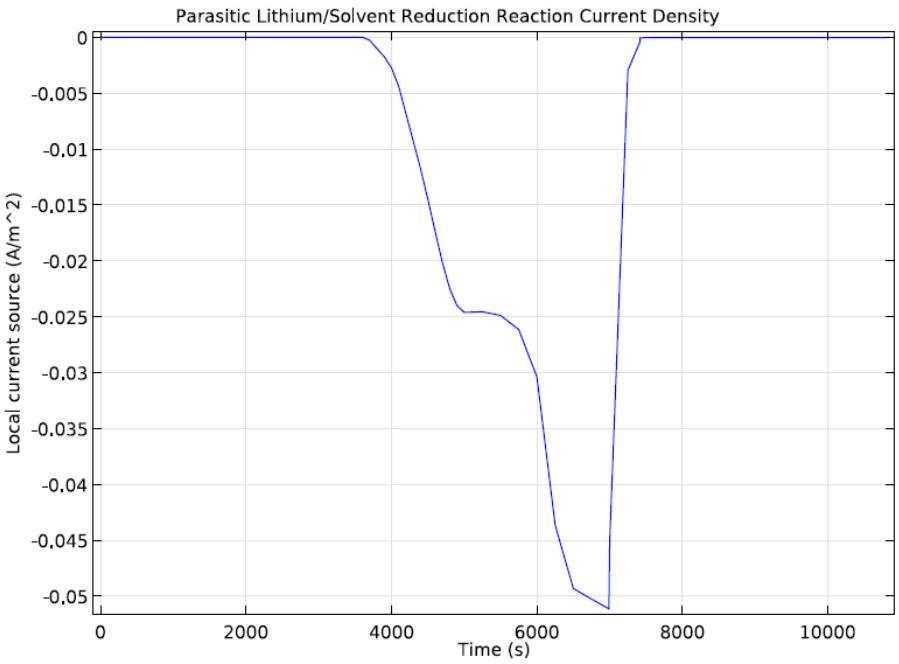

Figure 222 Reference scenario: Parasitic current density during the 10th cycle (Lithium – ion battery capacity fade model in Comsol Multiphysics) [55]

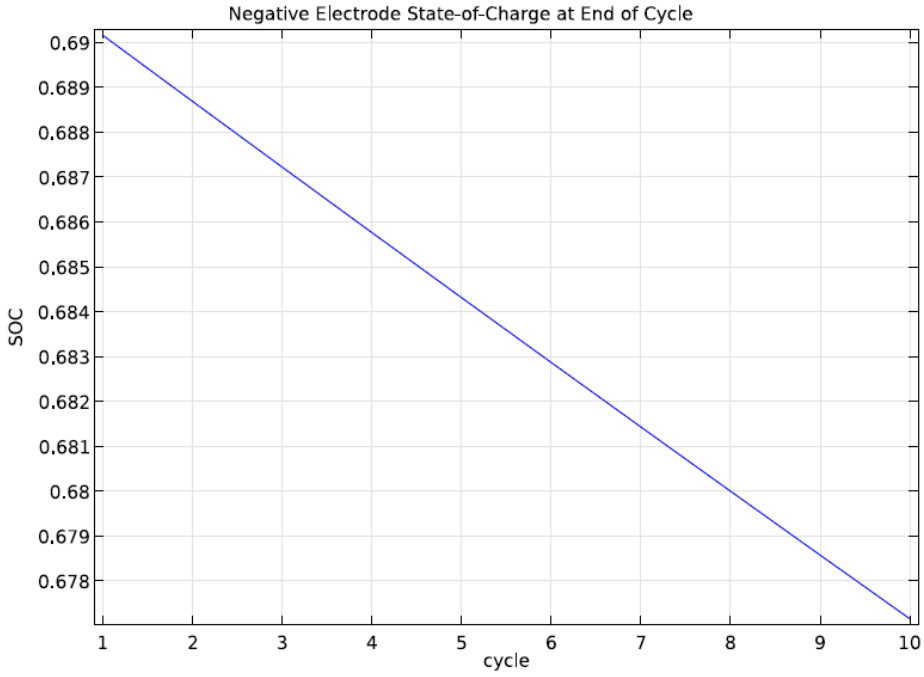

Figure 223 Reference scenario: SOC of the negative electrode at the end of the cycle (Lithium – ion battery capacity fade model in Comsol Multiphysics) [55]

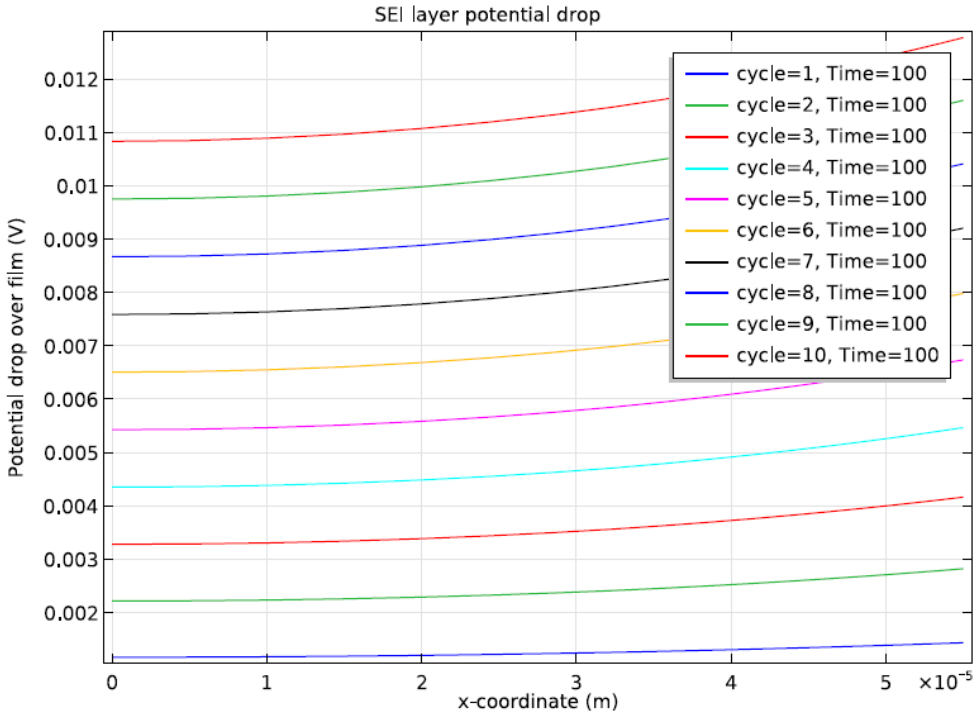

Figure 224 Reference scenario: Potential drop of the SEI layer during constant discharge (Lithium – ion battery capacity fade model in Comsol Multiphysics) [55]

- **Scenario 1: Density of the product of the side reaction = 2730 kg/m^3, molar mass of the product of the side reaction = 0.1 kg/mol**

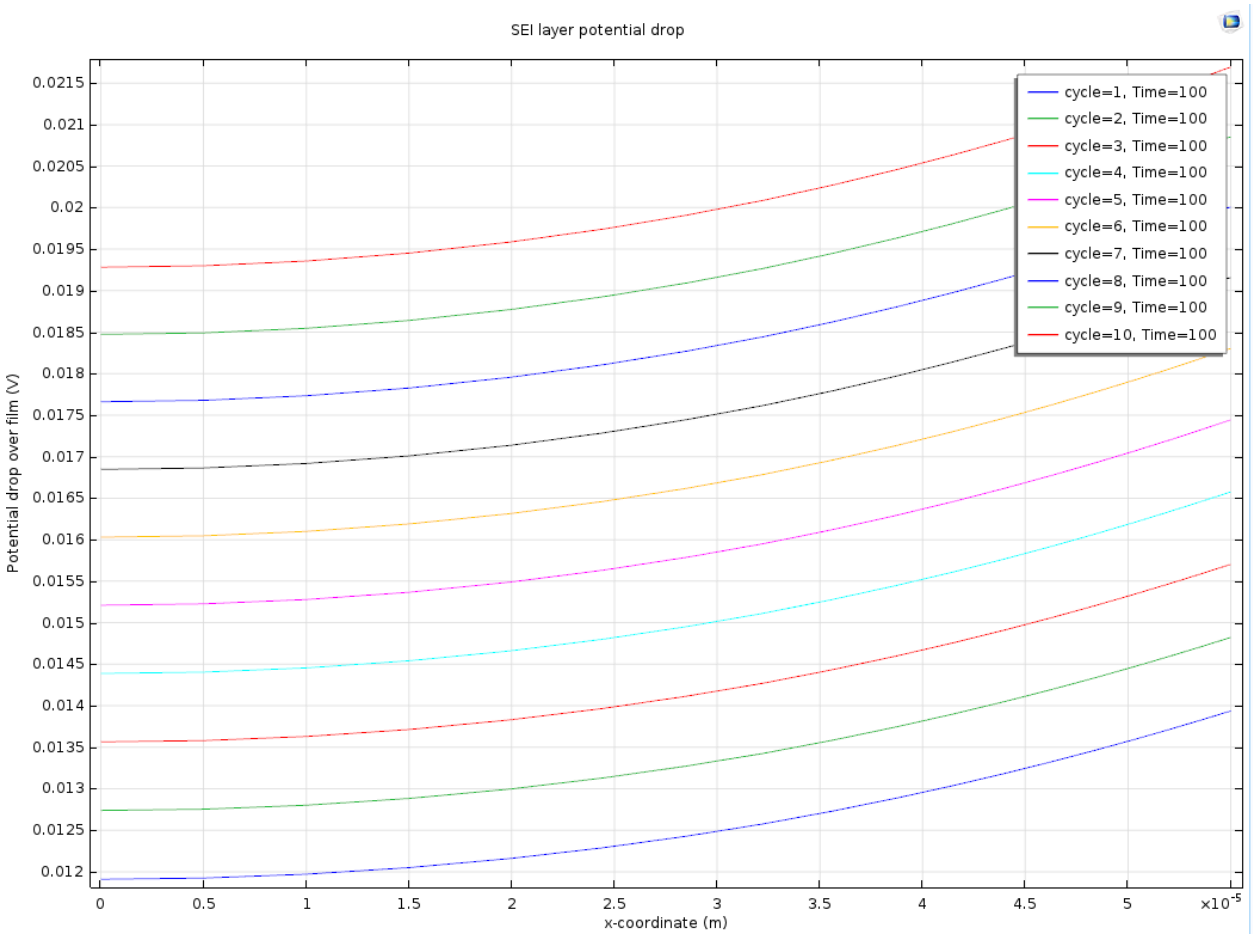

Figure 225 Scenario 1: Potential drop of the SEI layer during constant discharge (Lithium – ion battery capacity fade model in Comsol Multiphysics)

Comparing the constant discharge current curves it is observed that the battery voltage is gradually reduced for each cycle. During the 10th cycle the current magnitude significantly varies during charging due to higher parasitic reaction rates during constant current operation mode and due to lower parasitic reaction rates during constant voltage operation mode, which is attributed to the decreasing equilibrium potential for the lithium particles' insertion during the battery being charged under a low graphite expansion rate due to battery current reduction during the constant voltage operation mode [55].

After ten cycles the capacity loss deriving from the SOC of the negative electrode is approximately 1.3%. The SOC is given by equation (3.2.13.1) [55].

$$SOC = \frac{\int_{neg} c_s dS}{c_{s,max} L_{neg}} \quad (3.2.13.1)$$

Where c_s is the lithium concentration in the negative electrode, $c_{s,max}$ is the maximum intercalated lithium concentration in the negative electrode and L_{neg} is the negative electrode thickness.

It is also observed that the potential drop during all cycles is approximately uniform over the electrode thickness and it increases with cycles. The increase in the density of the product of the side reaction (30%) or in the lithium – ions concentration led to the increase in the potential drops by 0.01 V and to the potential drops not being as uniform over the depth of the electrode as before.

3.2.14 Case 14 : Cooling flow per fin, x,z-axis battery thermal conductivity, electrolyte salt concentration effects on a liquid-cooled lithium – ion battery

The inlet temperature is kept at 310 K in all cases.

- **Reference scenario: Cooling flow per fin = $5*10^{-7}$ m^3/s, electrolyte salt concentration = 1200 mol / m^3 , x,z-axis thermal conductivity = 29.557 W/mK,**

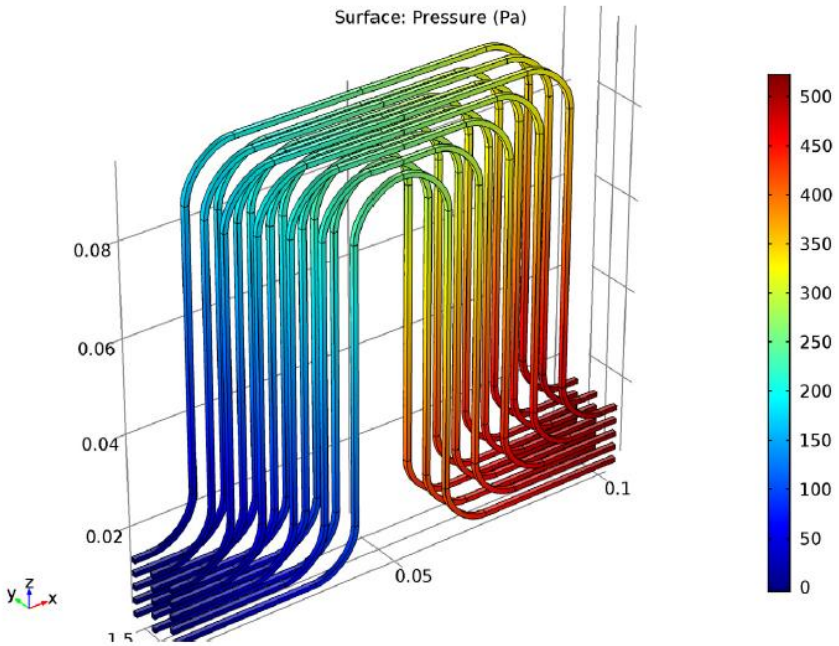

Figure 226 Reference scenario: Pressure inside the flow compartment (Liquid – Cooled Li–on Battery Pack model in Comsol Multiphysics) [55]

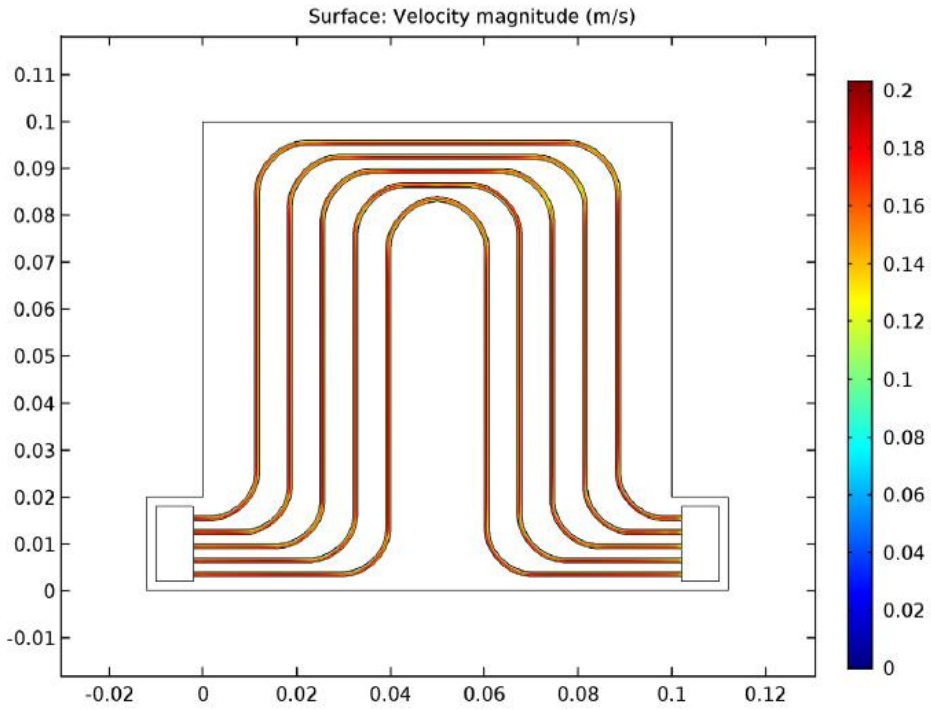

Figure 227 Reference scenario: Velocity magnitude inside the first cooling fin (Liquid – Cooled Li–on Battery Pack model in Comsol Multiphysics) [55]

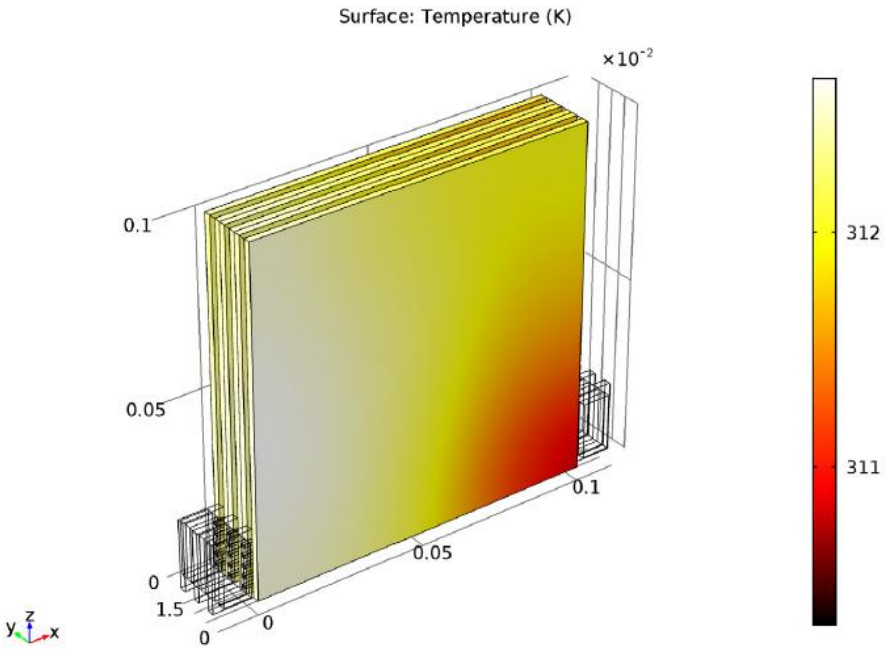

Figure 228 Reference scenario: Battery surface temperature (Liquid – Cooled Li–on Battery Pack model in Comsol Multiphysics) [55]

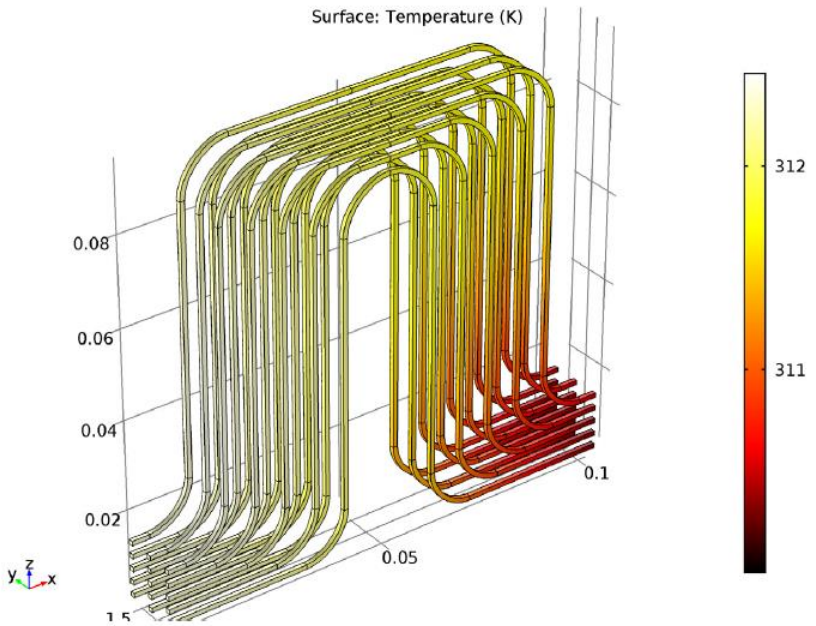

Figure 229 Reference scenario: Cooling liquid temperature (Liquid – Cooled Li–on Battery Pack model in Comsol Multiphysics) [55]

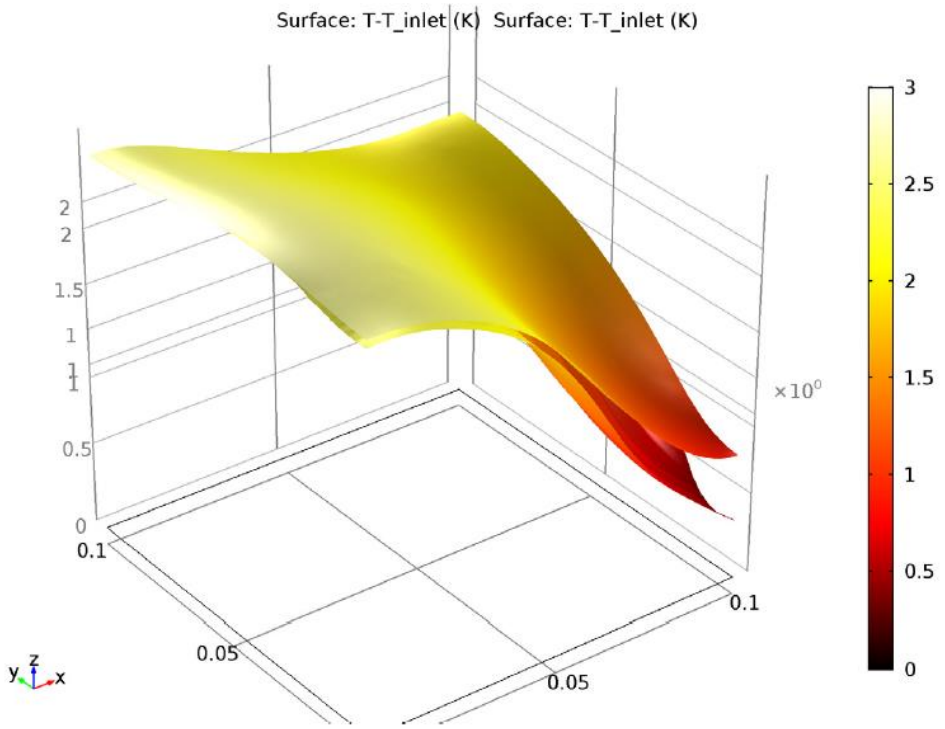

Figure 230 Reference scenario: Temperature increase with respect to the inlet temperature of the second cell at the surface adjacent to the cooling fin (y = 4 mm) and the surface adjacent to the third cell (y = 6 mm) *(Liquid – Cooled Li–on Battery Pack model in Comsol Multiphysics) [55]*

- **Scenario 1: Cooling flow per fin = 10^{-6} m^3/s, electrolyte salt concentration = 1200 mol / m^3 , x,z-axis thermal conductivity = 29.557 W/mK**

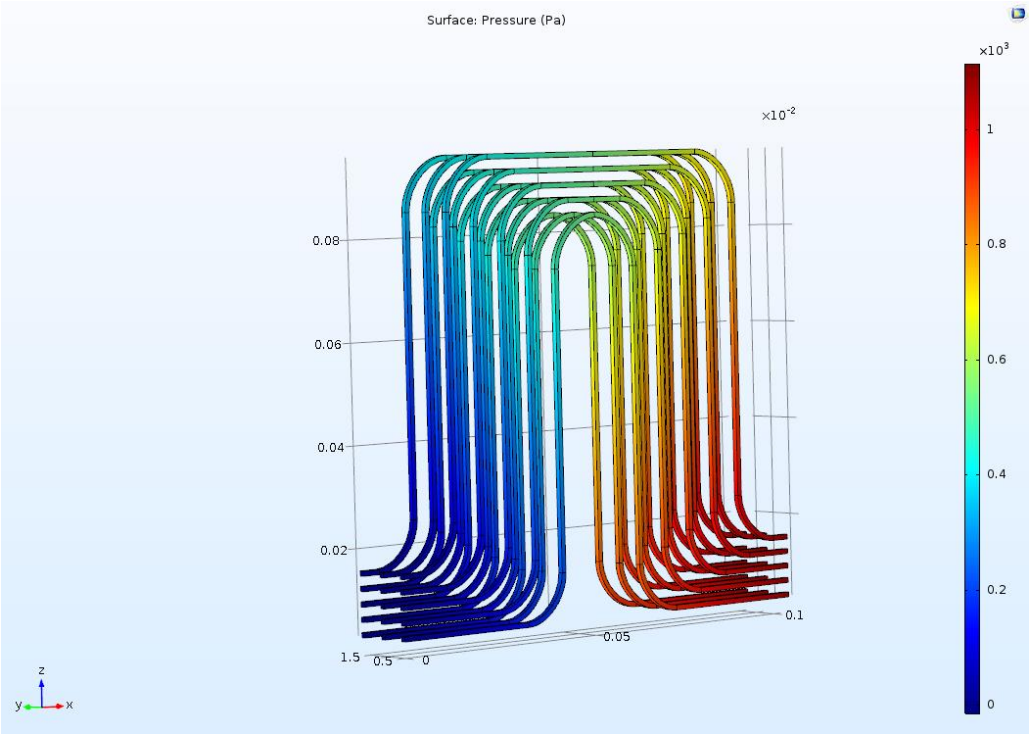

Figure 231 Scenario 1: Pressure inside the flow compartment (Liquid – Cooled Li–on Battery Pack model in Comsol Multiphysics)

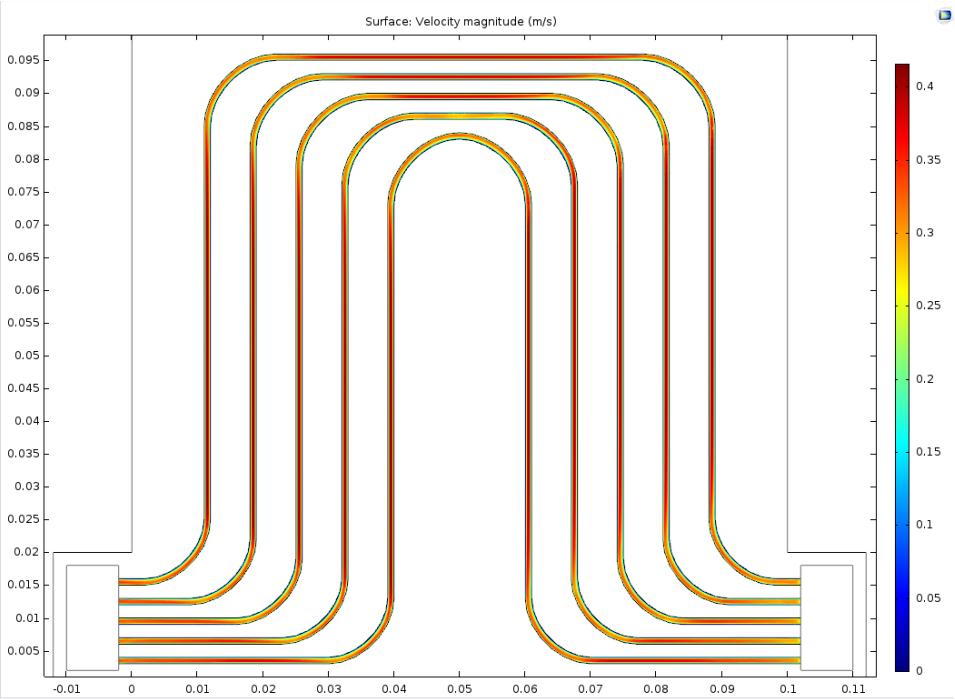

Figure 232 Scenario 1: Velocity magnitude inside the first cooling fin (Liquid – Cooled Li–on Battery Pack model in Comsol Multiphysics)

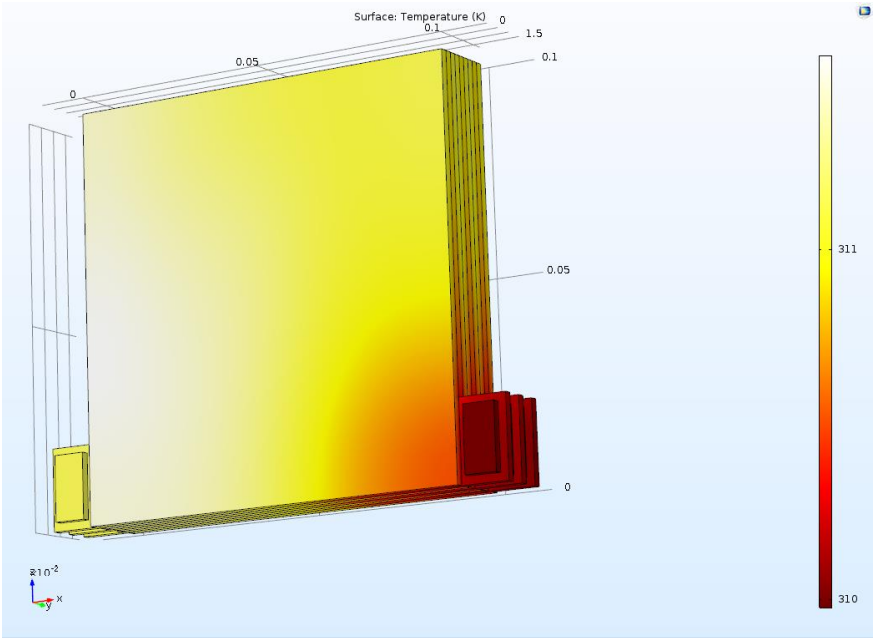

Figure 233 Scenario 1: Battery surface temperature (Liquid – Cooled Li–on Battery Pack model in Comsol Multiphysics)

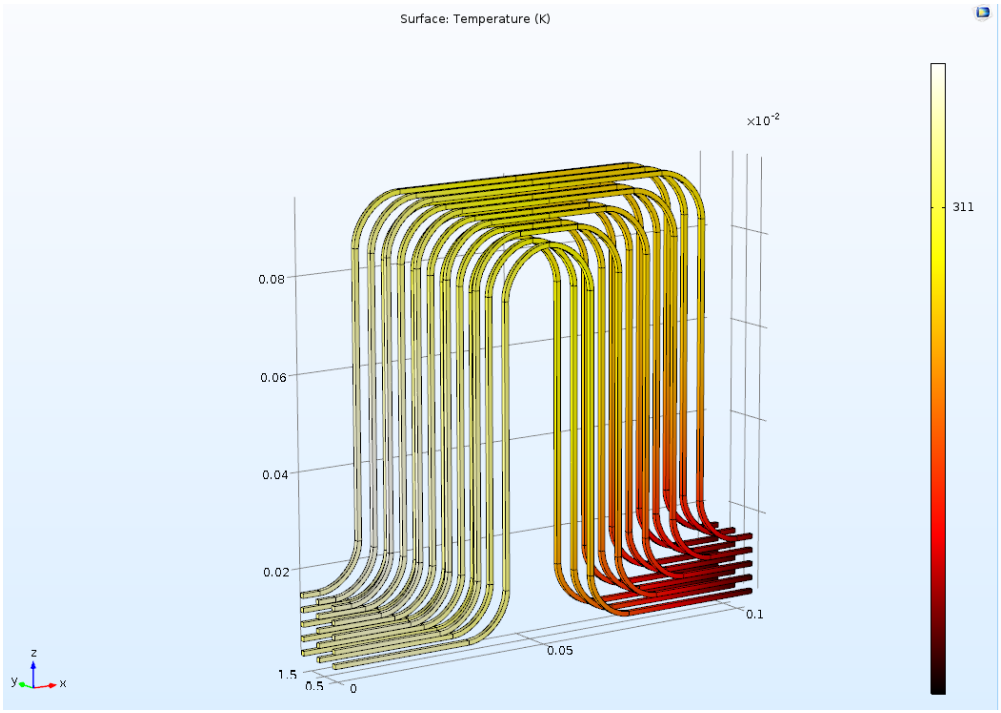

Figure 234 Scenario 1: Cooling liquid temperature (Liquid – Cooled Li–on Battery Pack model in Comsol Multiphysics)

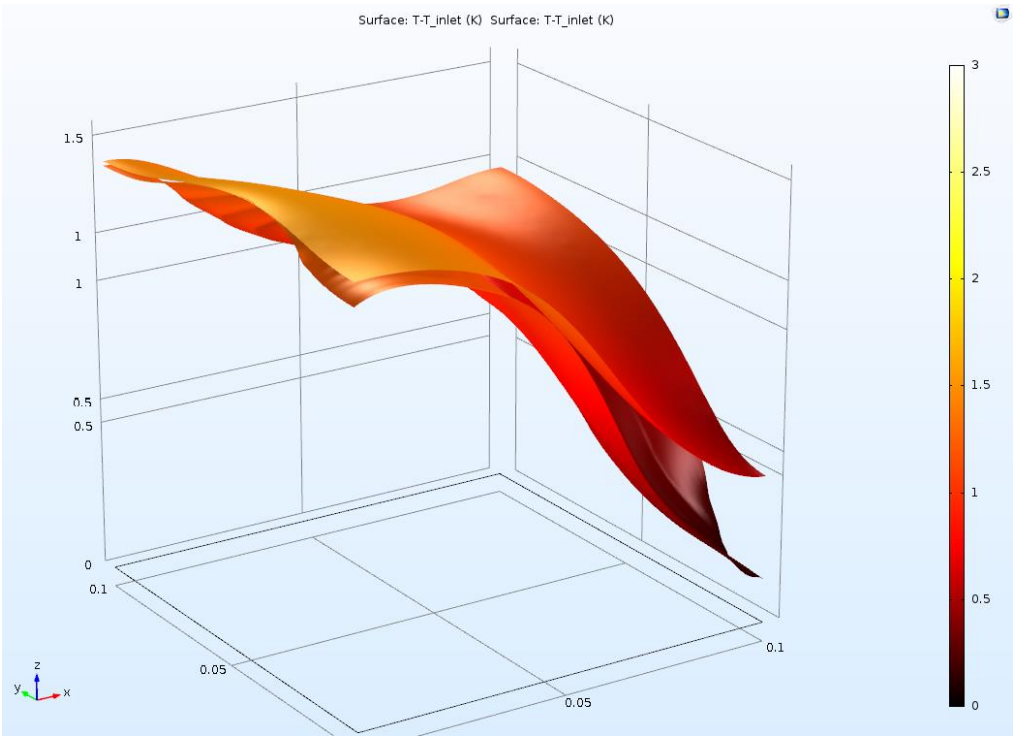

Figure 235 Scenario 1: Temperature increase with respect to the inlet temperature of the second cell at the surface adjacent to the cooling fin (y = 4 mm) and the surface adjacent to the third cell (y = 6 mm) (Liquid – Cooled Li–on Battery Pack model in Comsol)

- **Scenario 2: Cooling flow per fin = $5*10^{-7}$ m^3/s, x,z-axis thermal conductivity = 70.798 W/mK, electrolyte salt concentration = 1200 mol / m^3**

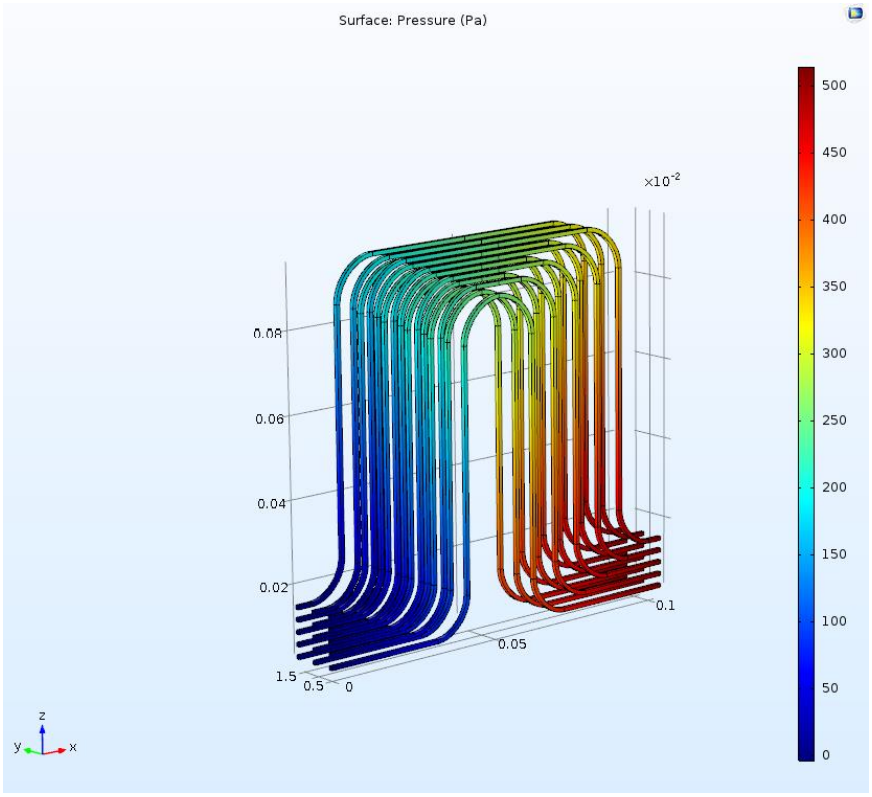

Figure 236 Scenario 2: Pressure inside the flow compartment (Liquid – Cooled Li–on Battery Pack model in Comsol Multiphysics)

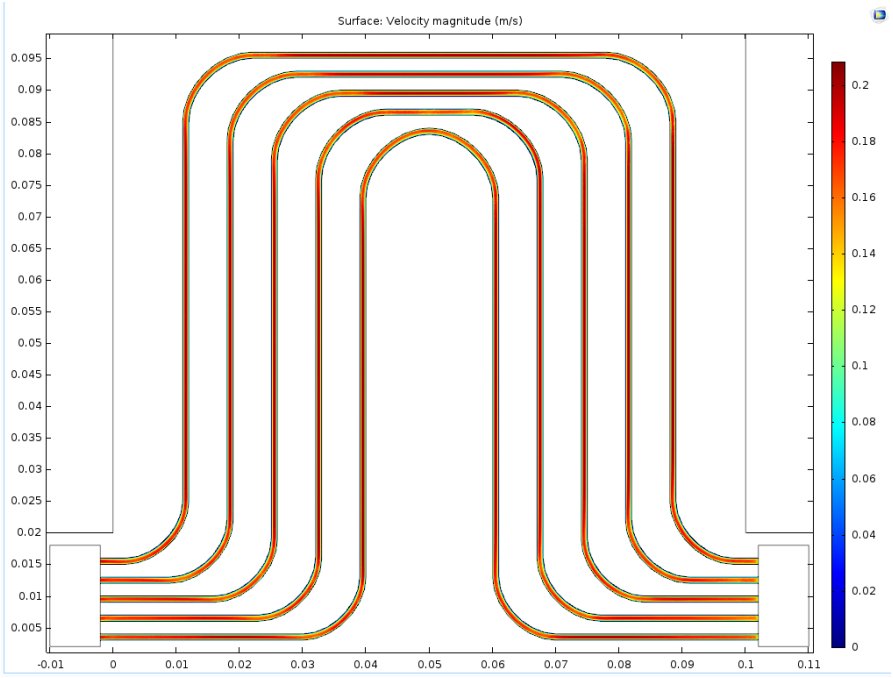

Figure 237 Scenario 2: Velocity magnitude inside the first cooling fin (Liquid – Cooled Li–on Battery Pack model in Comsol Multiphysics)

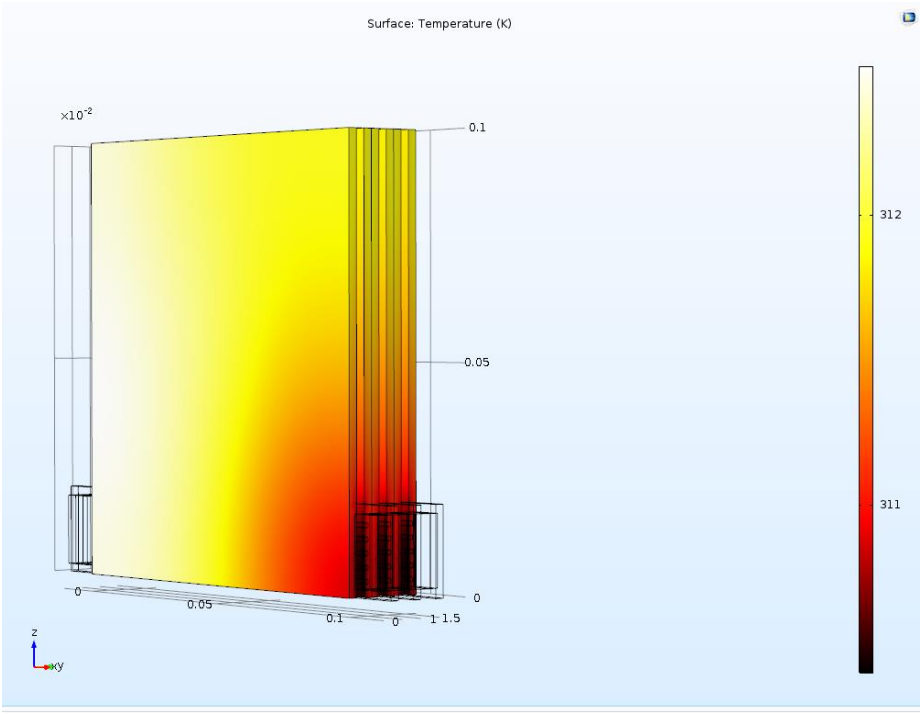

Figure 238 Scenario 2: Battery surface temperature (Liquid – Cooled Li–on Battery Pack model in Comsol Multiphysics)

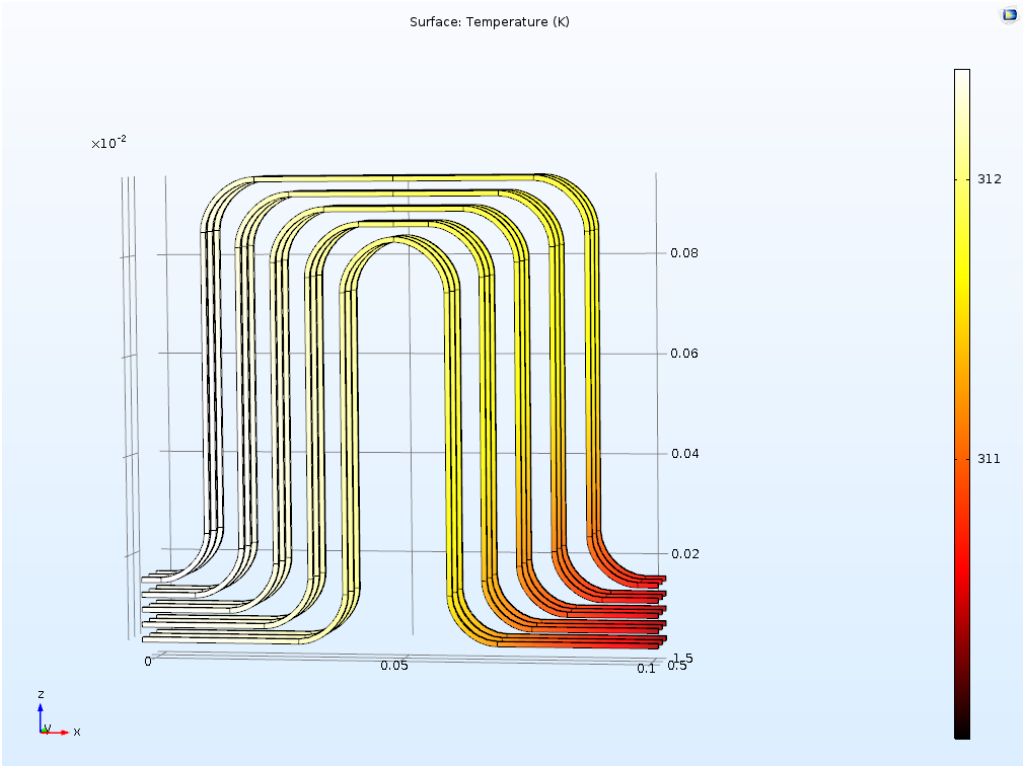

Figure 239 Scenario 2: Cooling liquid temperature (Liquid – Cooled Li–on Battery Pack model in Comsol Multiphysics)

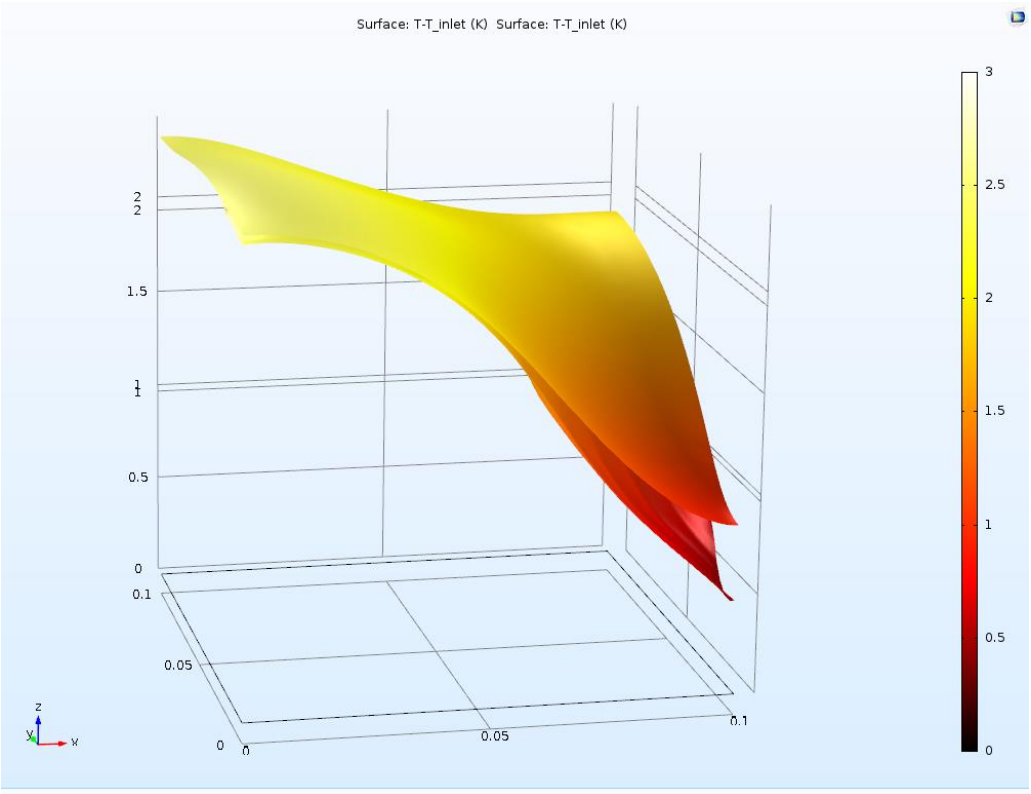

Figure 240 Scenario 2: Temperature increase with respect to the inlet temperature of the second cell at the surface adjacent to the cooling fin (y = 4 mm) and the surface adjacent to the third cell (y = 6 mm) (Liquid – Cooled Li–on Battery Pack model in Comsol)

- **Scenario 3 : Cooling flow per fin = $5*10^{-7}$ m^3/s, x,z-axis thermal conductivity = 29.557 W/mK, electrolyte salt concentration = 2400 mol / m^3**

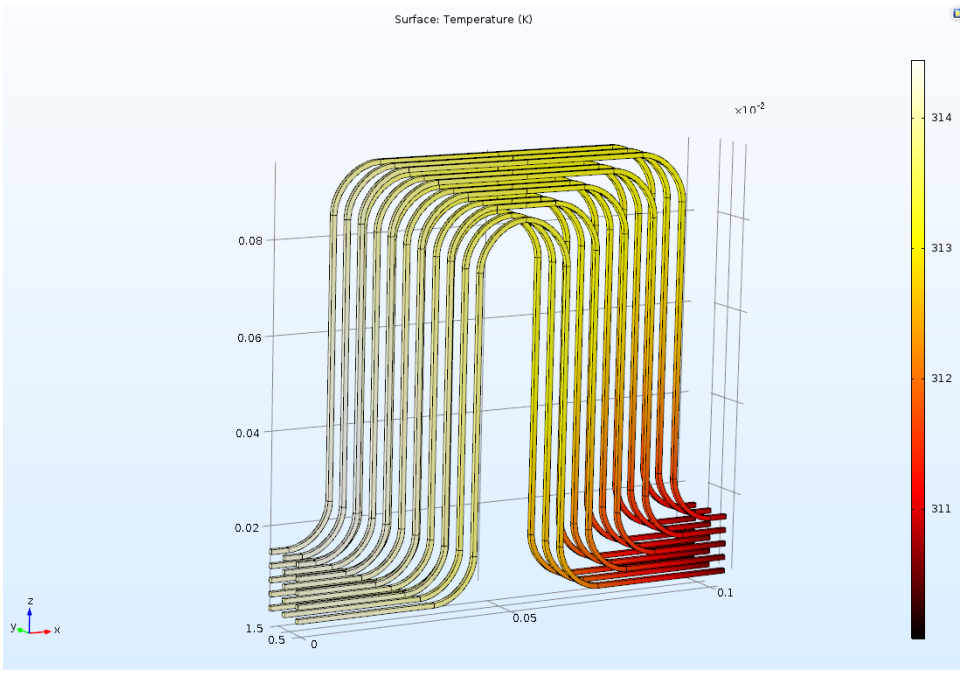

Figure 241 Scenario 3: Cooling liquid temperature (Liquid – Cooled Li–on Battery Pack model in Comsol Multiphysics)

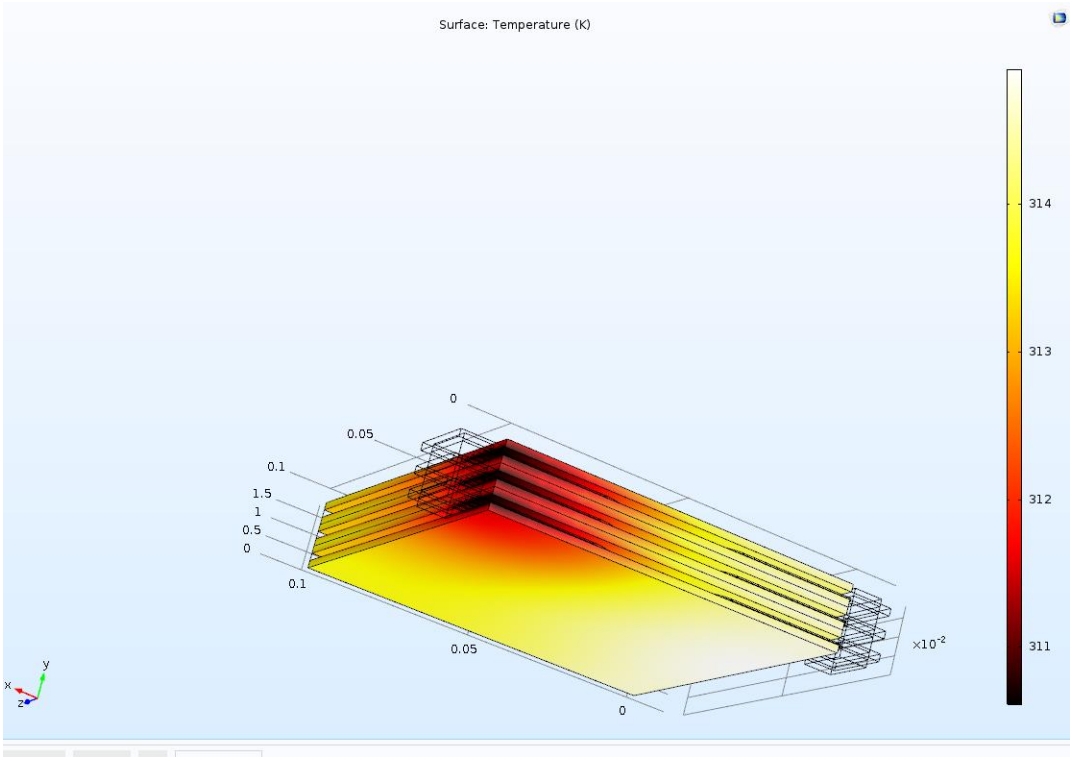

Figure 242 Scenario 3: Battery surface temperature (Liquid – Cooled Li–on Battery Pack model in Comsol Multiphysics)

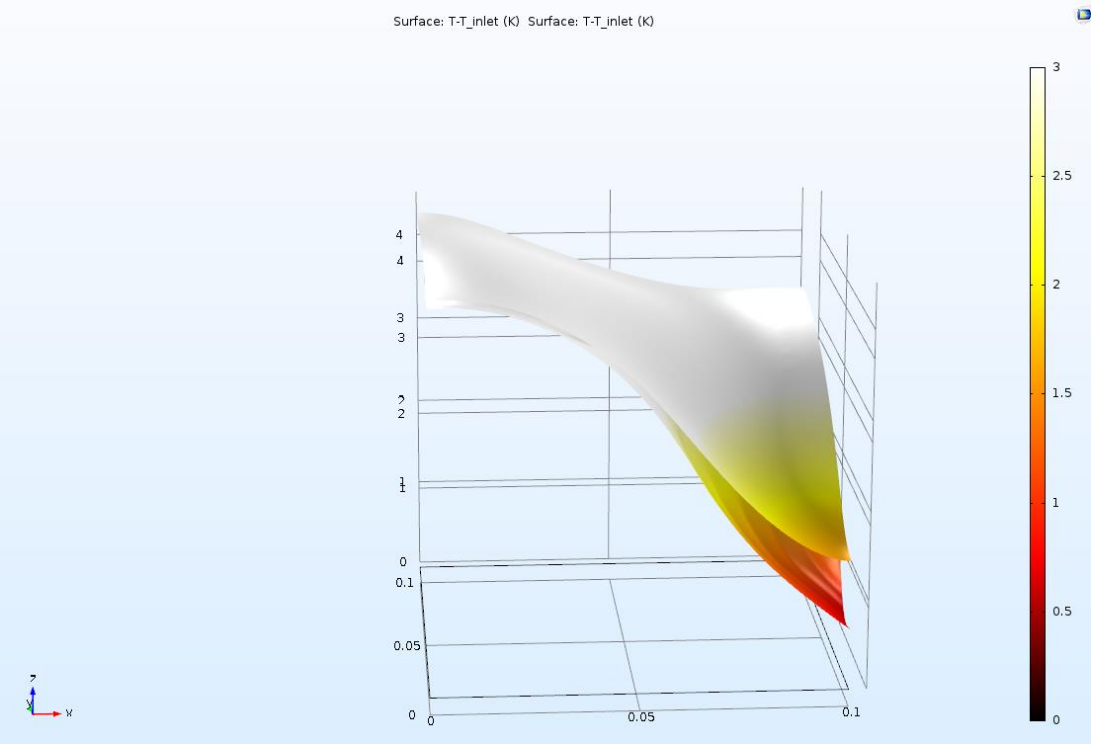

Figure 243 Scenario 3: Temperature increase with respect to the inlet temperature of the second cell at the surface adjacent to the cooling fin (y = 4 mm) and the surface adjacent to the third cell (y = 6 mm) (Liquid – Cooled Li–on Battery Pack model in Comsol)

- **Scenario 4: Cooling flow per fin = $2*10^{-6}$ m^3/s, x,z-axis thermal conductivity = 70.798 W/mK, electrolyte salt concentration = 1200 mol / m^3**

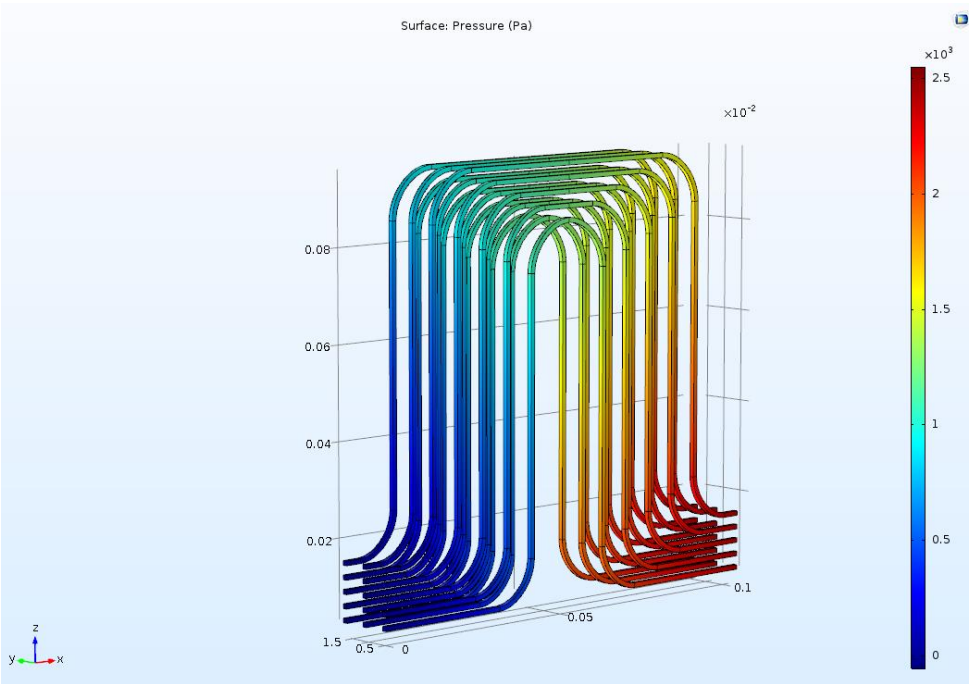

Figure 244 Scenario 4: Pressure inside the flow compartment (Liquid – Cooled Li–on Battery Pack model in Comsol Multiphysics)

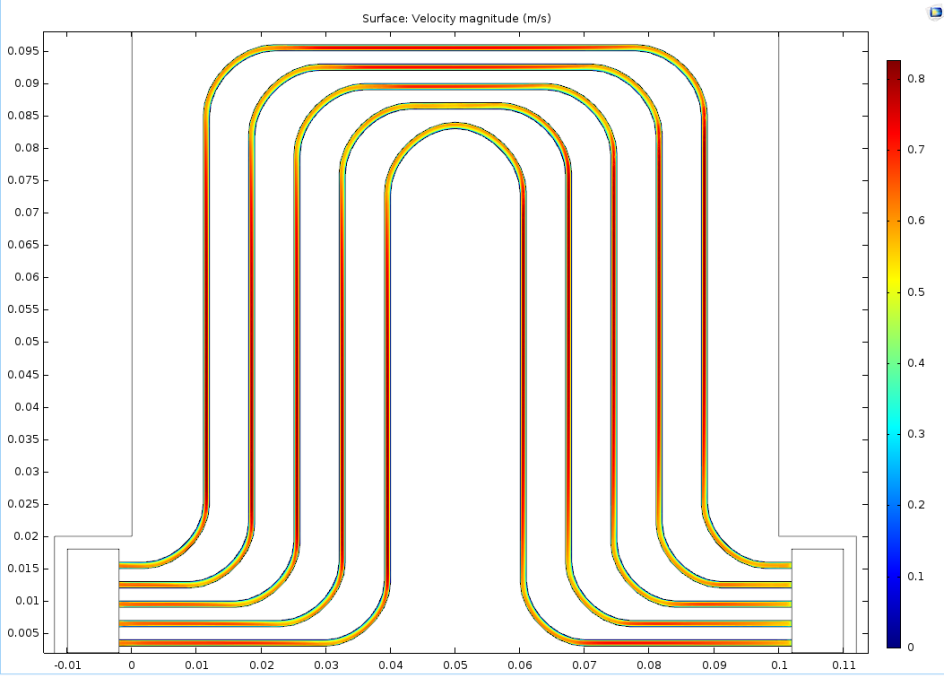

Figure 245 Scenario 4: Velocity magnitude inside the first cooling fin (Liquid – Cooled Li–on Battery Pack model in Comsol Multiphysics)

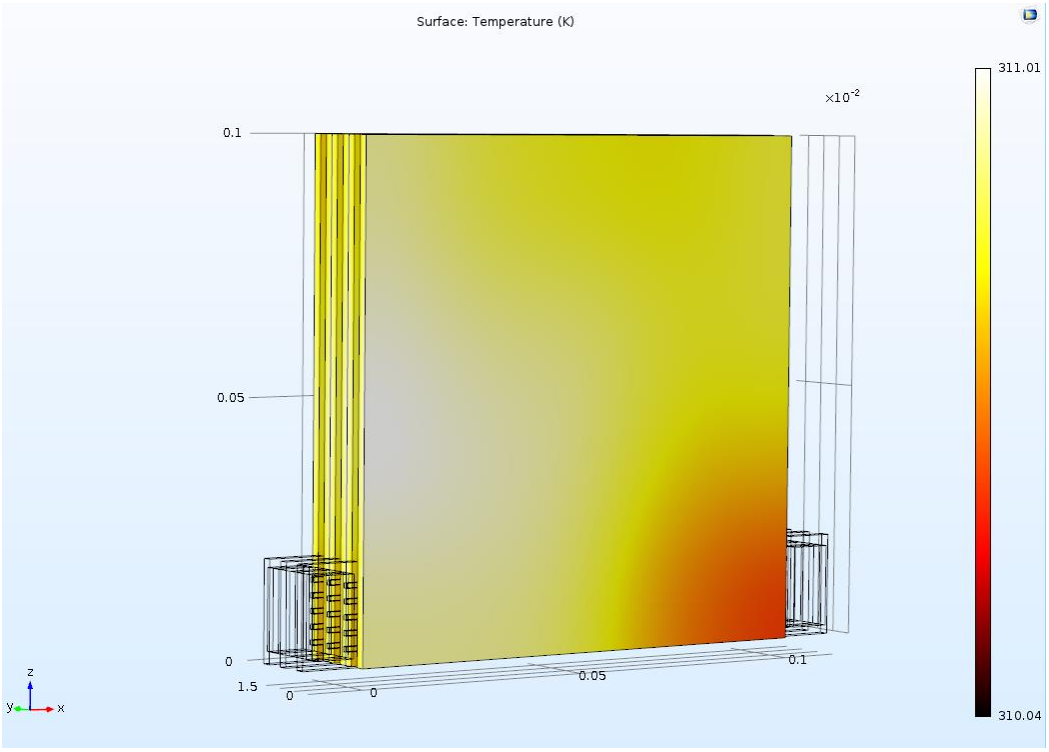

Figure 246 Scenario 4: Battery surface temperature (Liquid – Cooled Li–on Battery Pack model in Comsol Multiphysics)

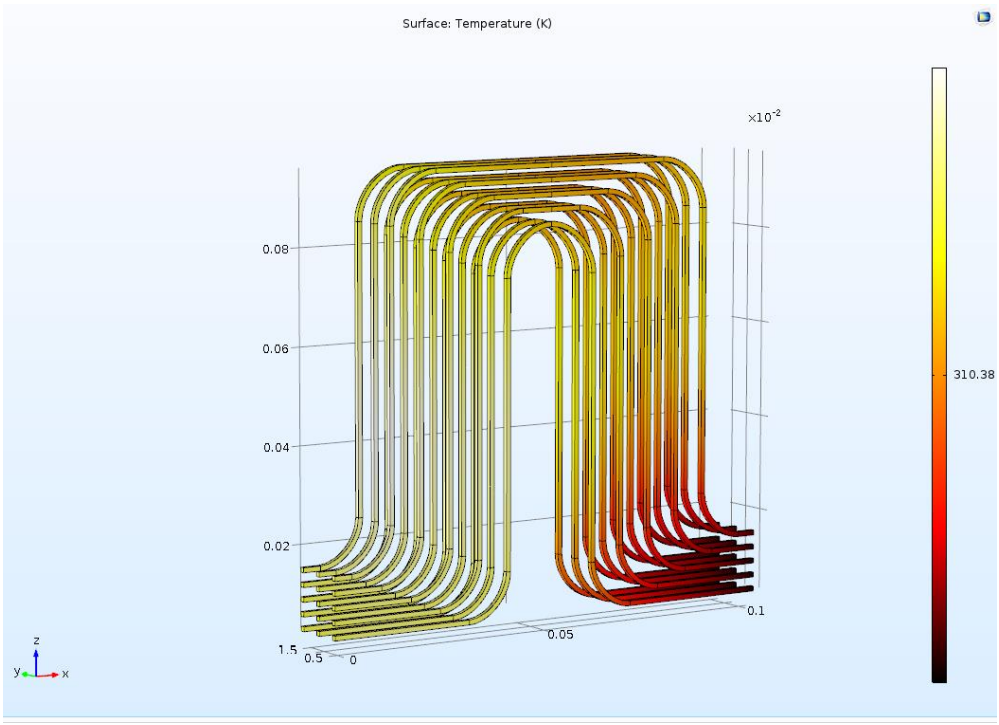

Figure 247 Scenario 4: Cooling liquid temperature (Liquid – Cooled Li–on Battery Pack model in Comsol Multiphysics)

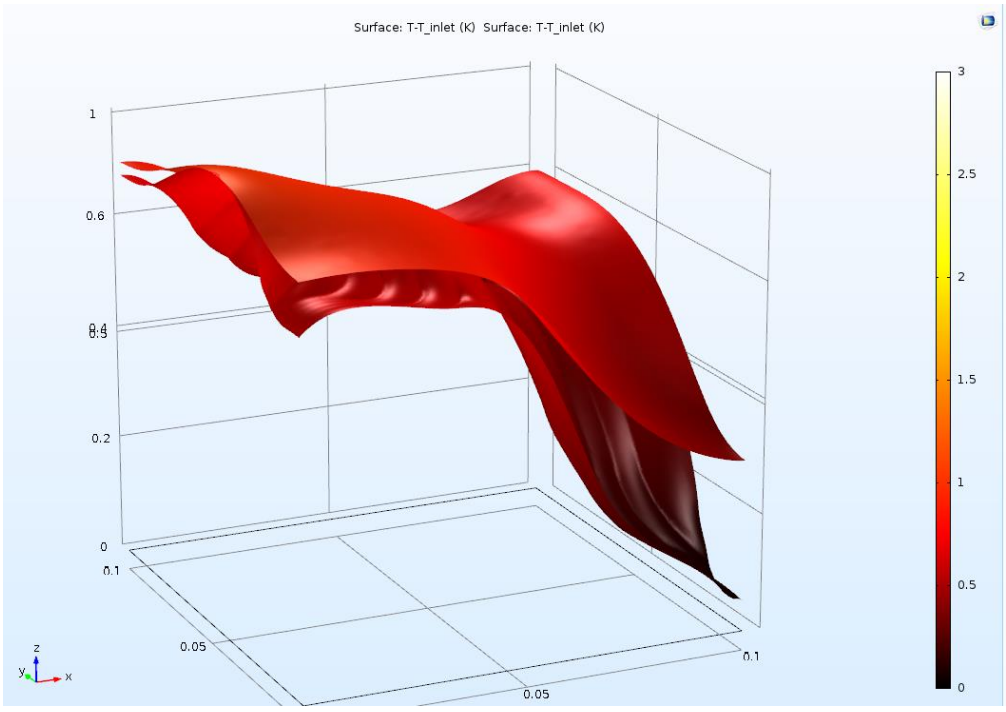

Figure 248 Scenario 4: Temperature increase with respect to the inlet temperature of the second cell at the surface adjacent to the cooling fin (y = 4 mm) and the surface adjacent to the third cell (y = 6 mm) (Liquid – Cooled Li–on Battery Pack model in Comsol)

From the reference scenario simulation results it is observed is that the velocity magnitude approximately 0.2 m/s in the middle of the channels, which means that the fluid remains in the plates for a few seconds. The maximum variation surface temperature of the battery equals 3 K, while the temperature differences along the y – axis are smaller than those on the xz plane. In addition, the cooling fluid temperature values are a bit lower compared to the temperatures in the battery.

The doubling of the cooling flow resulted in the doubling of the pressure in the flow compartment and in the velocity magnitude of the cooling fin. Moreover, the battery surface temperature decreased by 1.5 K, while the temperature gradient at the corner near the inlet slightly increased, whereas the thermal conductivity increase in scenario 3 had no significant impact on the simulation results, except for the minor changes in the battery surface temperature distribution, which can be observed by figures 240 and 230.

As illustrated in the simulation results of scenario 3, the doubling of the electrolyte salt concentration increased the cooling fluid temperature and the battery surface temperature by approximately 2 – 2.5 K and at the same time the surface temperature becomes more uniform. Moreover, in scenario 4 the cooling flow per fin being increased by 4 times raised the pressure at the inlet up to 2500 Pa and at the same time the surface temperature decreased by 2 K and the temperature distribution became homogeneous as depicted in figure 248.

4. Conclusions and future work

This thesis comprised an extensive review of EVs and HEVs touching upon several topics such as their environmental and economic aspects and the requirements for power electronics and regenerative braking. Additional special topics such as the specifics of Formula E, the Atkinson cycle and hybrid configurations were also reviewed.

There are several types of batteries available commercially – even more types can be found at a research level. This thesis focused not only on Lithium-Ion batteries, their technical and performance characteristics but also includes a review of several other types of batteries and means of energy storage such as the Ammonia battery, NiMH and NiZn batteries, Halide and Proton batteries, the Graphene battery, fuel cells and supercapacitors.

Since the lithium – ion battery is a promising energy storage for EVs, its specifications should be optimized so as to meet customers' needs. Previous studies have shown that a decrease of the ambient temperature results in an increase in the internal resistance and a decrease in the power extraction rate of the battery. Optimization of the calendar life and the electrical conductivity, confinement of cell degradation and overheating of the lithium – ion battery are all critical points for enhancing performance and avoiding thermal runaway. A non – uniform thermal distribution in a lithium – ion battery may cause swelling phenomena due to lithium ion intercalation. Water jackets for the electric motor and the motor controller and air cooling system for the battery are often used for the thermal management. The battery's capacity, energy efficiency, internal resistance, SOC loss at storage, cycle life, reliability, temperature change, abuse, thermal shock, vibration, mechanical shock, overcharge and over-discharge protection are all parameters that need to be assessed in the context of validating both the safety and the performance of the battery.

To assess as many critical parameters related to a battery's performance as possible as part of this thesis an extensive review of available models has been carried out. Overall, a total of 18 models already embedded in commercial software such as Matlab/Simulink, Comsol Multiphysics, LMS ImagineLab and ANSYS/FLUENT have been extensively reviewed.

A series of simulations were carried out as part of this thesis using all models reviewed. The cases considered and main findings are summarized in the form of "cause and effect" below.

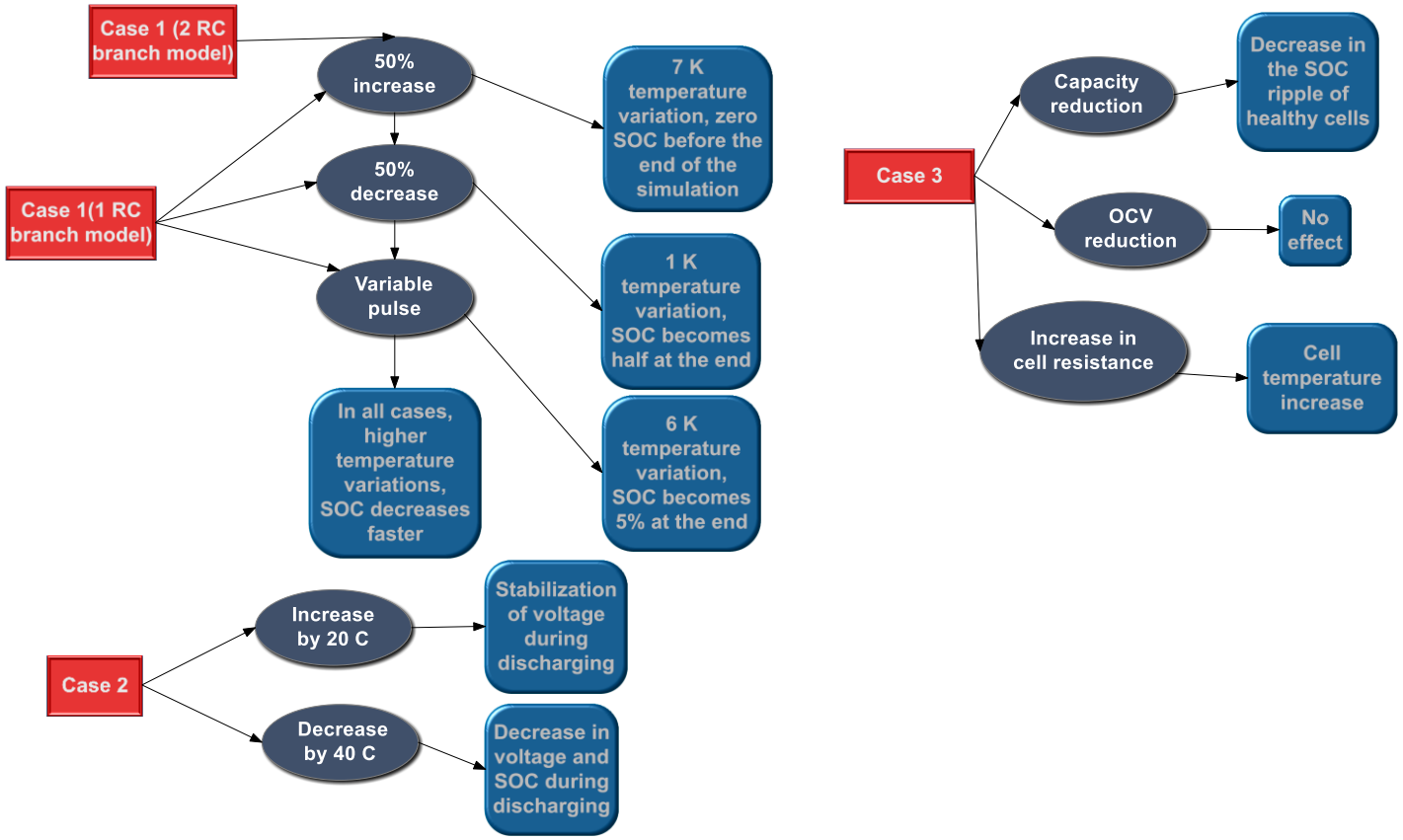

Figure 249 Relationship diagrams of simulation results 1

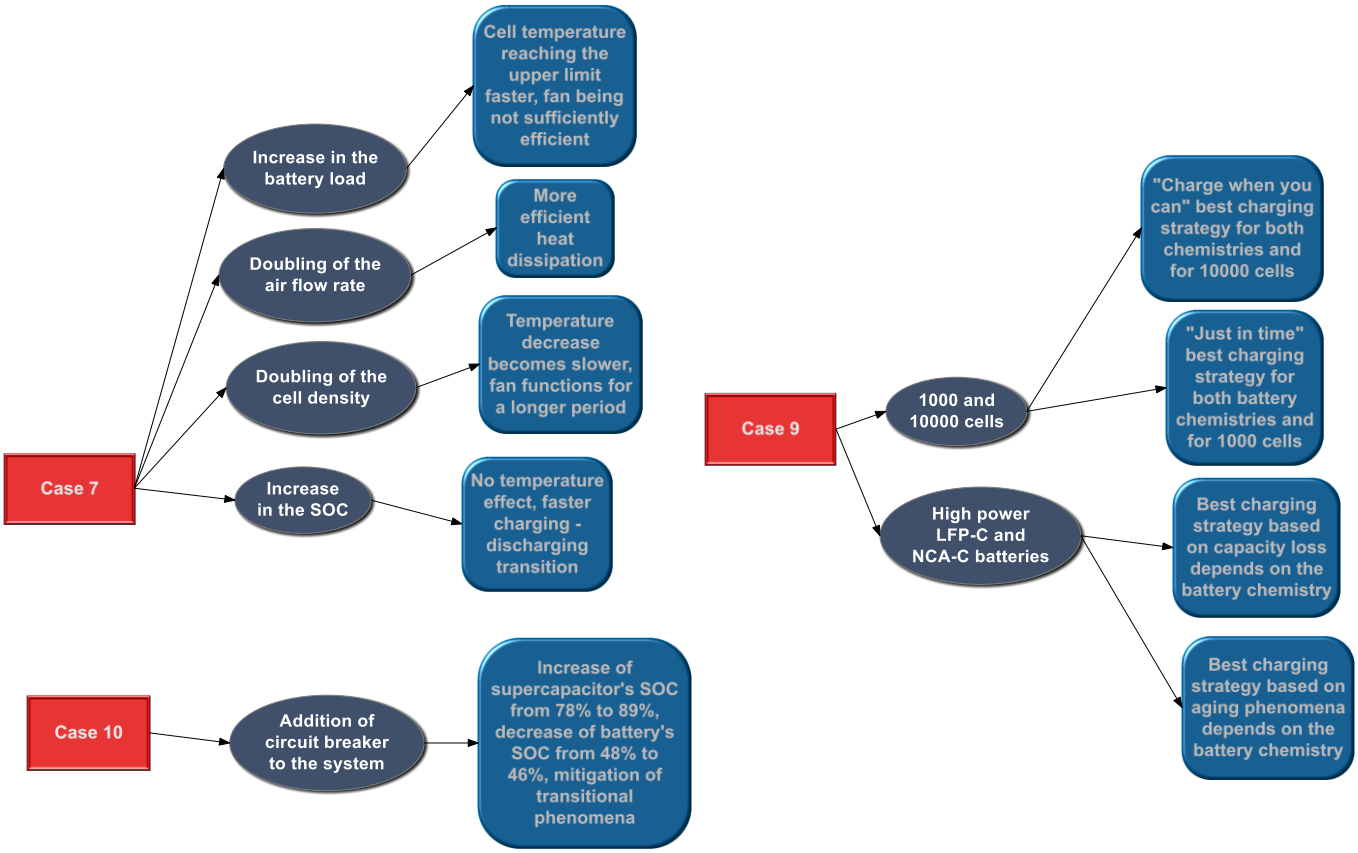

Figure 250 Relationship diagrams of simulation results 2

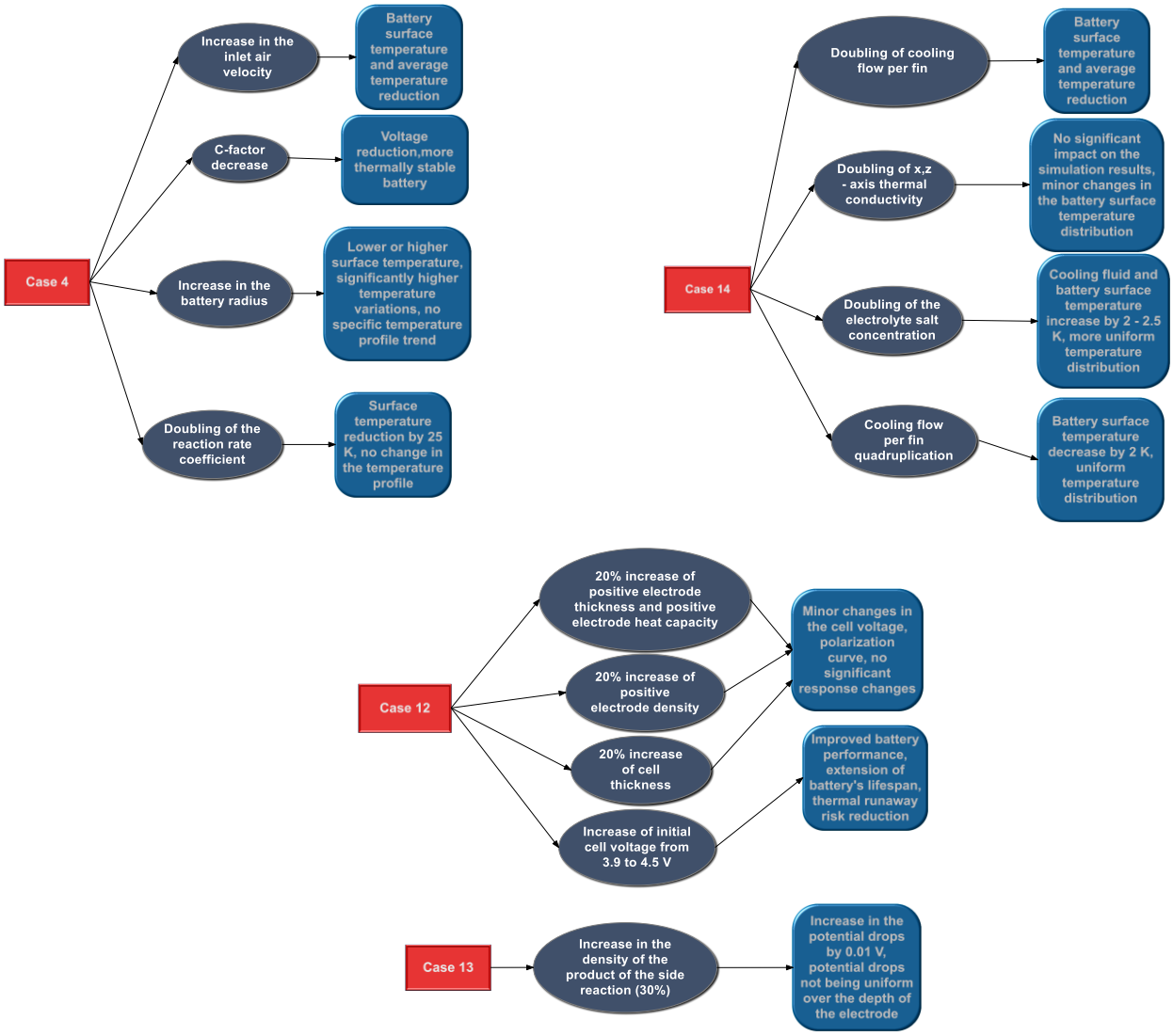

Figure 251 Relationship diagrams of simulation results 3

As the lithium – ion battery is a part of the EV's system, its optimization should be followed by the optimization of every part of the system. Hybrid energy storage systems are also proposed for achieving the previous goals.

5. References

[1] Y. Wu, *Lithium-ion batteries*

[2] R. Yazami, *Nanomaterials for lithium-ion batteries*

[3] F. Zhang, N. LaBarge, W. Yang, J. Liu and B. Logan, "Enhancing Low-Grade Thermal Energy Recovery in a Thermally Regenerative Ammonia Battery Using Elevated Temperatures", *ChemSusChem*, vol. 8, no. 6, pp. 1043-1048, 2015

[4] K. Kordesch, G. Faleschini, G. Koscher, M. Cifrain and V. Hacker, "Ammonia as Hydrogen Source for an Alkaline Fuel Cell–Battery Hybrid System"

[5] "ELECTRIC VEHICLE TECHNOLOGY EXPLAINED", 2012

[6] V. Bagotsky, A. Skundin and Y. Volfkovich, *Electrochemical power sources*

[7] A. González, E. Goikolea, J. Barrena and R. Mysyk, "Review on supercapacitors: Technologies and materials", *Renewable and Sustainable Energy Reviews*, vol. 58, pp. 1189-1206, 2016

[8] "ANSYS Fluent Battery Module Manual", 2013

[9] “Battery specs - Electric Vehicle Wiki", *Electricvehiclewiki.com*, 2016

[10] F. Zhang, J. Liu, W. Yang and B. Logan, "A thermally regenerative ammonia-based battery for efficient harvesting of low-grade thermal energy as electrical power", *Energy Environ. Sci.*, vol. 8, no. 1, pp. 343-349, 2015

[11] E. Heracleous, "Alternative Fuels Lecture Notes", *International Hellenic University*, 2016

[12] J. Wilhelm, H. Janßen, J. Mergel and D. Stolten, "Energy Management for a Fuel Cell/Battery Hybrid System"

[13] S. Patrabansh, Y. El-Sharkh and M. Alam, "Dynamic modeling of transient response of DMFC"

[14] J. Beretta, *Automotive electricity*. London: ISTE Ltd, 2010

[15] G. Pistoia, *Electric and hybrid vehicles*. Amsterdam: Elsevier, 2010

[16] A. Link, A. O'Connor and T. Scott, *Battery technology for electric vehicles*

[17] H. Kim and S. Lee, "Enhanced electrochemical performances of cylindrical hybrid supercapacitors using activated carbon/ Li4-xMxTi5-yNyO12 (M=Na, N=V, Mn) electrodes", *Energy*, vol. 109, pp. 506-511, 2016

[18] A. Perner and J. Vetter, *Lithium-ion batteries for hybrid electric vehicles and battery electric vehicles*. Munich, Germany: BMW Group

[19] G. Martinopoulos, "Solar Energy Systems lecture notes", *IHU*, 2016

[20] P. Corbo, F. Migliardini and O. Veneri, *Hydrogen fuel cells for road vehicles*. London: Springer, 2011

[21] S. Verhelst, "Future vehicles will be driven by electricity, but not as you think [Point of View]", *Proceedings of the IEEE*, vol. 102, no. 10, pp. 1399-1403, 2014

[22] "TOYOTA MOTOR CORPORATION GLOBAL WEBSITE", *TOYOTA MOTOR CORPORATION GLOBAL WEBSITE*, 2016

[23] "VW to Decide on New 700 km Range Battery Technology by July |Electric Vehicle News", *Electric-vehiclenews.com*, 2015

[24] "StoreDot Wants to Charge Your EV in 5 Minutes", *IEEE Spectrum: Technology, Engineering, and Science News*, 2015

[25] J. Jaguemont, L. Boulon and Y. Dube, "Characterization and Modeling of a Hybrid-Electric-Vehicle Lithium-Ion Battery Pack at Low Temperatures", *IEEE Trans. Veh. Technol.*, vol. 65, no. 1, pp. 1-14, 2016

[26] L. Sawa, O. Taya and L. Winston Zhang, "Thermal Management of Lithium-ion Battery Pack with Liquid Cooling"

[27] A. Kumar and S. Anbumalar, "FINITE ELEMENT ANALYSIS OF LITHIUM-ION BATTERY FOR ELECTRIC VEHICLE", 2015

[28] A. Samba, N. Omar, H. Gualous, Y. Firouz, P. Van den Bossche, J. Van Mierlo and T. Boubekeur, "Development of an Advanced Two-Dimensional Thermal Model for Large size Lithium-ion Pouch Cells", *Electrochimica Acta*, vol. 117, pp. 246-254, 2014

[29] K. Oh and B. Epureanu, "Characterization and modeling of the thermal mechanics of lithium-ion battery cells", *Applied Energy*, vol. 178, pp. 633-646, 2016

[30] N. Tamaldin, A. Yamin, M. Abdollah, H. Amiruddin and M. Abdullah, "Design Optimization of Thermal Management System for Electric Vehicle Utilizing CFD Analysis, DFMEA and CES", *Procedia Engineering*, vol. 68, pp. 305-312, 2013

[31] N. Nieto, L. Díaz, J. Gastelurrutia, F. Blanco, J. Ramos and A. Rivas, "Novel thermal management system design methodology for power lithium-ion battery", *Journal of Power Sources*, vol. 272, pp. 291-302, 2014

[32] X. Ying-hao, Y. Hai-jun and L. Chang-dong, "Present Situation and Prospect of Lithium-ion Traction Batteries for Electric Vehicles Domestic and Overseas Standards", 2014

[33] "HCV - Hybrid Commercial Vehicle", *Hcv-project.eu*, http://www.hcv-project.eu

[34] http://www.mclaren.com/technologygroup/news/articles/mclaren-powers-formula-e-beijing

[35] http://www.autoexpo.mahindra.com/images/fomulaE/CarStand_Specs_Mahindra_HR.pdf

[36] https://www.theengineer.co.uk/issues/october-2013-online/electric-formula-inside-the-formula-e-racing-car/

[37] http://fiaformulae.com

[38] A. Wangsupphaphol and N. Idris, "Acceleration-based design of electric vehicle auxiliary energy source", *IEEE Aerospace and Electronic Systems Magazine*, vol. 31, no. 1, pp. 32-35, 2016

[39] F. Machado, J. Trovao and C. Antunes, "Effectiveness of Supercapacitors in Pure Electric Vehicles Using a Hybrid Metaheuristic Approach", *IEEE Trans. Veh. Technol.*, vol. 65, no. 1, pp. 29-36, 2016

[40] A. Castaings, A. Bouscayrol, R. Trigui and W. Lhomme, "Practical control schemes of a battery/supercapacitor system for electric vehicle", *IET Electrical Systems in Transportation*, vol. 6, no. 1, pp. 20-26, 2016

[41] https://avt.inl.gov/sites/default/files/pdf/fsev/fact4500tesla2014.pdf

[42] https://www.toyotaofdecatur.com/blog/toyota-atkinson-cycle-engine/

[43] http://blog.toyota.co.uk/toyota-use-atkinson-cycle-engines

[44] I. Crosby and P. Akbari, "THERMODYNAMIC ANALYSIS OF THE ATKINSON CYCLE", *Scientific Cooperations International Workshops on Engineering Branches*, vol. 2014

[45] Y. Ge, L. Chen, F. Sun and C. Wu, "Performance of an Atkinson cycle with heat transfer, friction and variable specific-heats of the working fluid", *Applied Energy*, vol. 83, no. 11, pp. 1210-1221, 2006

[46] http://doc.utwente.nl/64556/1/BatteryRep4.pdf

[47] A. Fotouhi, D. Auger, K. Propp, S. Longo and M. Wild, "A review on electric vehicle battery modelling: From Lithium-ion toward Lithium–Sulphur", *Renewable and Sustainable Energy Reviews*, vol. 56, pp. 1008-1021, 2016

[48] http://www.eco-aesc-lb.com/en/product/liion_hev/

[49] http://www.mathworks.com/

[50] T. Huria, M. Ceraolo, J. Gazzarri and R. Jackey, "High Fidelity Electrical Model with Thermal Dependence for Characterization and Simulation of High Power Lithium Battery Cells", 2012

[51] http://auto.howstuffworks.com/auto-parts/brakes/brake-types/regenerative-braking.htm

[52] S. Chapman, *Electric machinery and power system fundamentals*. Boston: McGraw-Hill, 2002

[53] O. Tremblay, L. Dessaint and A. Dekkiche, "A Generic Battery Model for the Dynamic Simulation of Hybrid Electric Vehicles", 2007

[54] http://www.ul.com/wp-content/uploads/2016/02/Safety_Issues_for_Lithium_Ion_Batteries1.pdf

[55] https://www.comsol.com

[56] http://batteryuniversity.com/learn/article/types_of_lithium_ion

[57] S. Barua, A. Chowdhury, A. Rahman, S. Banik and S. Tasim, "Modelling and Analytical Studies on Graphene based Supercapacitor Comparing with Traditional Batteries", *2nd Int'l Conf. on Electrical Engineering and Information & Communication Technology*, 2015

[58] P. Goli and A. Balandin, "Graphene-Enhanced Phase Change Materials for Thermal Management of Battery Packs"

[59] Z. Liu and X. Zhou, "*Graphene: Energy Storage and Conversion Applications*"

[60] http://www.nrel.gov/transportation/energystorage/pdfs/long_beach_btm.pdf, 2016

[61] S. MOTAPON, "DESIGN AND SIMULATION OF A FUEL CELL HYBRID EMERGENCY POWER SYSTEM FOR A MORE ELECTRIC AIRCRAFT: EVALUATION OF ENERGY MANAGEMENT SCHEMES", 2013

[62] https://www.plm.automation.siemens.com, 2016

[63] https://www.dieselnet.com/standards/cycles/ftp75.php

[64] http://www.car-engineer.com/the-different-driving-cycles/

[65] https://www.tesla.com/blog/bit-about-batteries

[66]http://waset.org/publications/17181/heat-generation-rate-and-computational-simulation-for-li-ion-battery-module

[67] E. Prada, Y. Creff, V. Moynot and D. Di Domenico, "Towards advanced BMS algorithms development for PHEV and EV by use of a physics-based model of Li-ion battery systems", *EVS27*, 2013

[68] http://graphene-flagship.eu/energy

[69] G. Kapetanakis and P. Karampilas, "*Technology of HEVs and EVs"*, 2008

[70] https://www.prettl.com/

[71] "Drive magazine : ECO edition", http://www.drive.gr, 04/2016

Appendix A

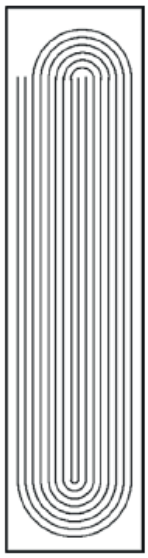

Figure 252 Li - ion cell "jelly rolls"

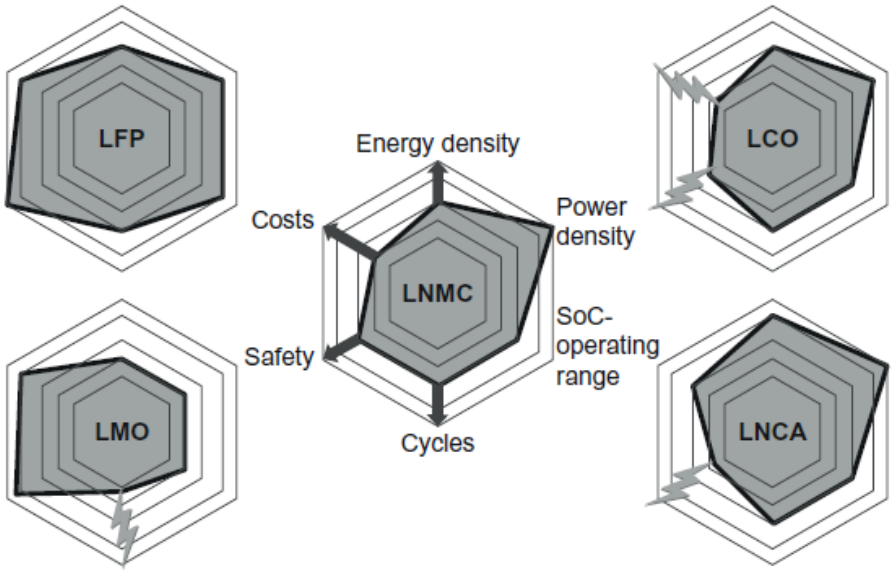

Figure 253 Li - ion cell anode materials vs requirements [18]

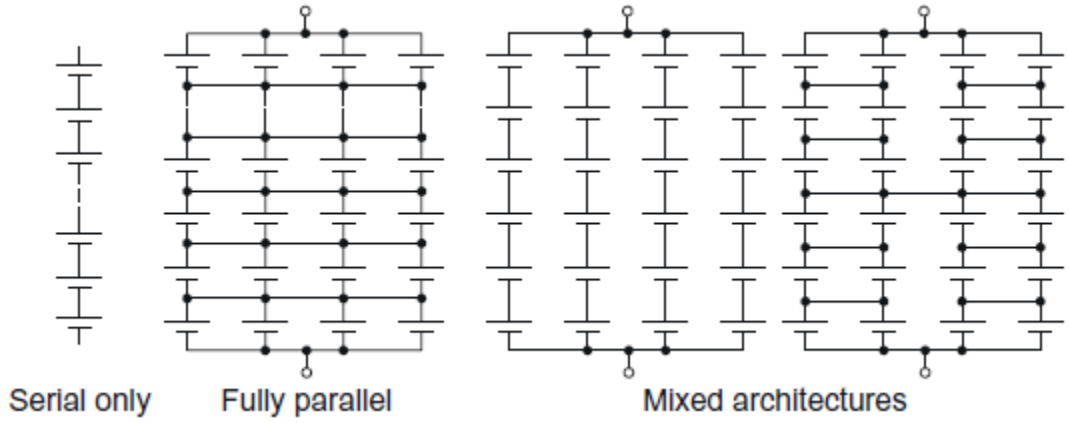

Figure 254 Battery circuit architectures [18]

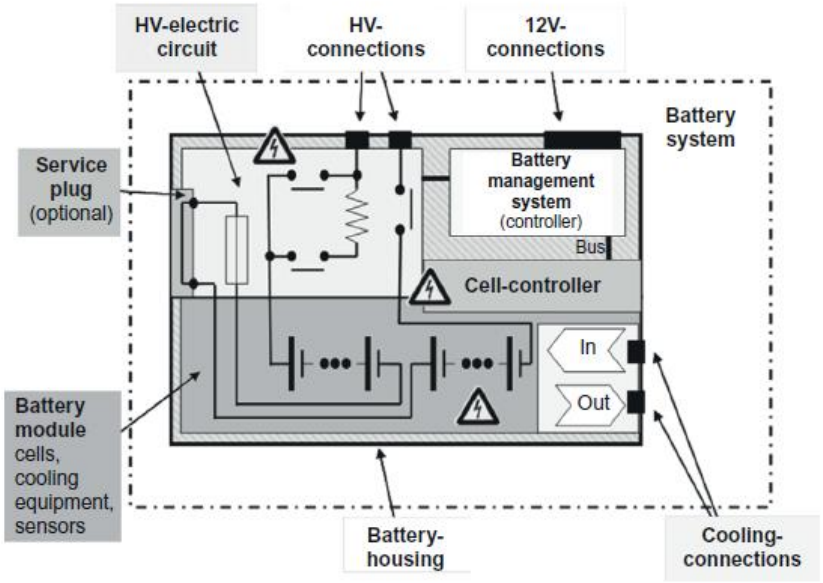

Figure 255 Battery pack architecture [18]

Table 14 Goals to be achieved as to batteries by EV application [18]

	HEV	PHEV	EV
Increase energy content	0	+	++
Increase power	++	+	+
Reduce size	+	++	0
Reduce weight	0	+	++
Increase durability	0	+	+
Increase usability	0	+	+
Maintain safety	++	++	++
Energy density	0	+	++
Power density	++	0	+
Life cycle	++	+	0
Calendar life	0	+	+
Low-temperature performance	0	+	+

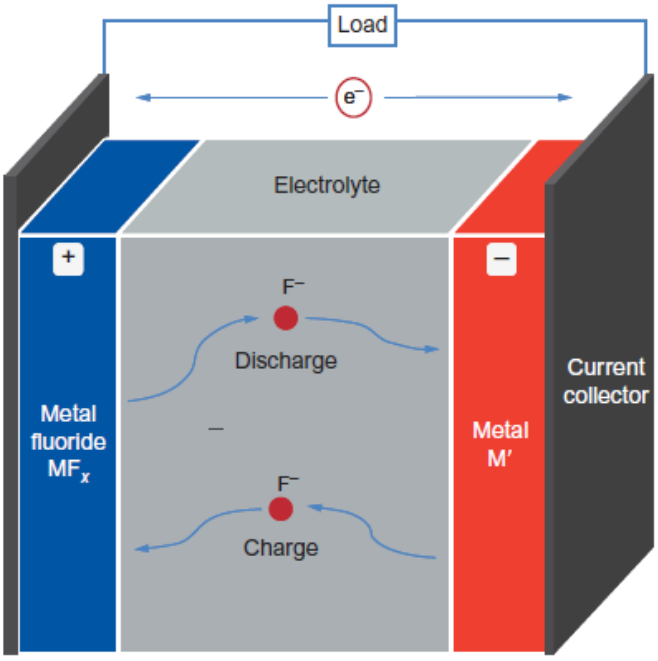

Figure 256 Fluoride battery structure

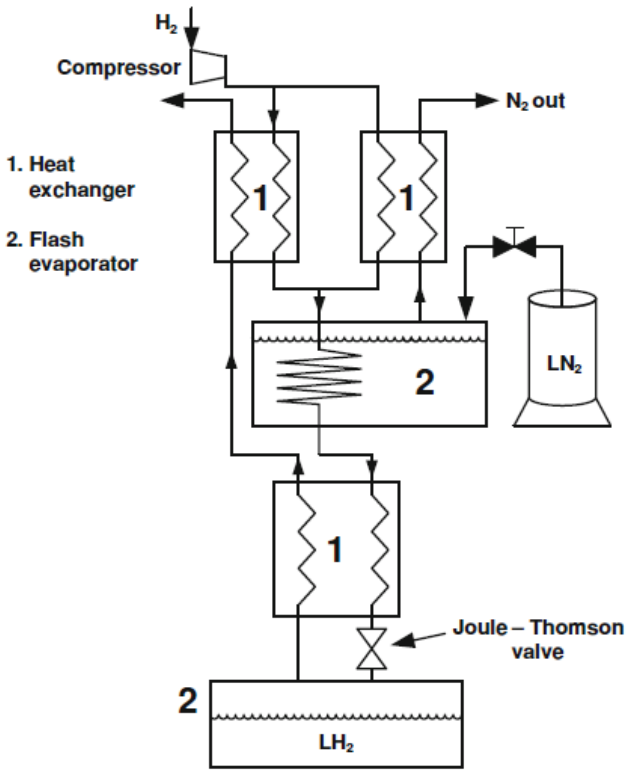

Figure 257 Linde cycle [20]

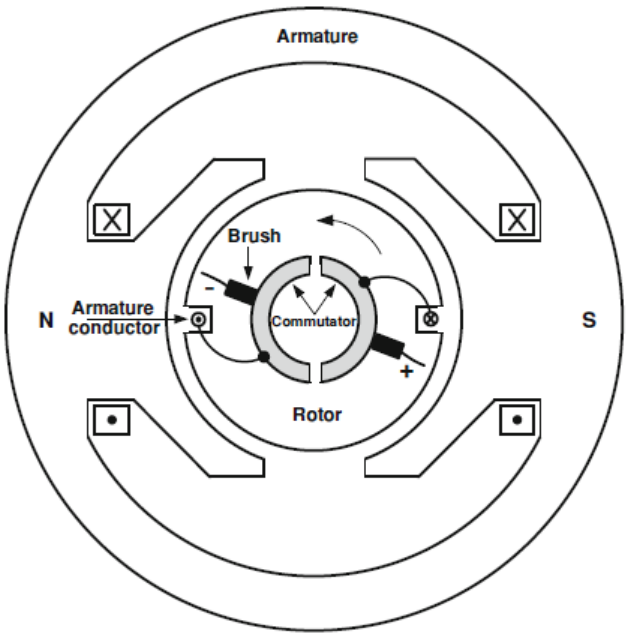

Figure 258 DC electric motor [20]

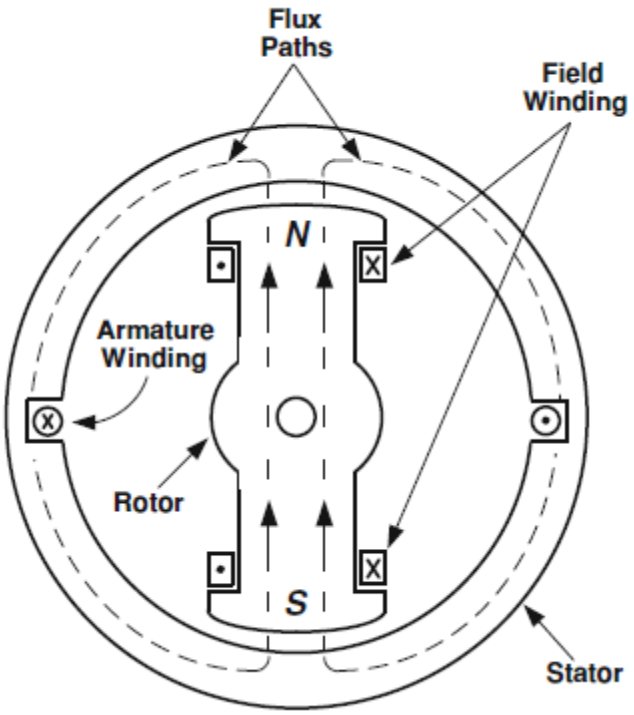

Figure 259 Synchronous AC motor (cylindrical) [20]

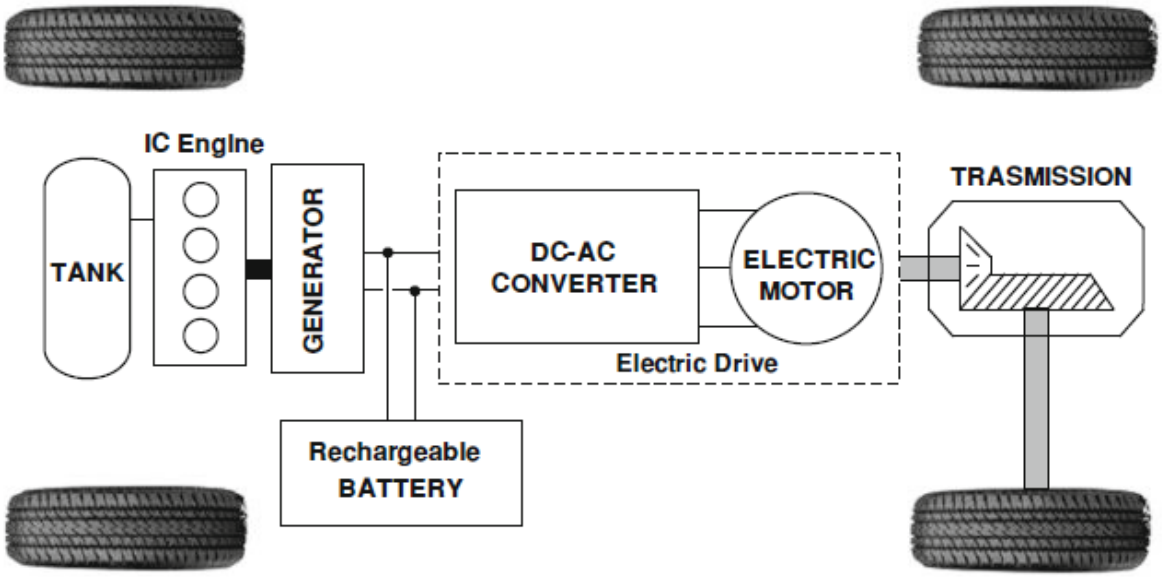

Figure 260 Series hybrid configuration [20]

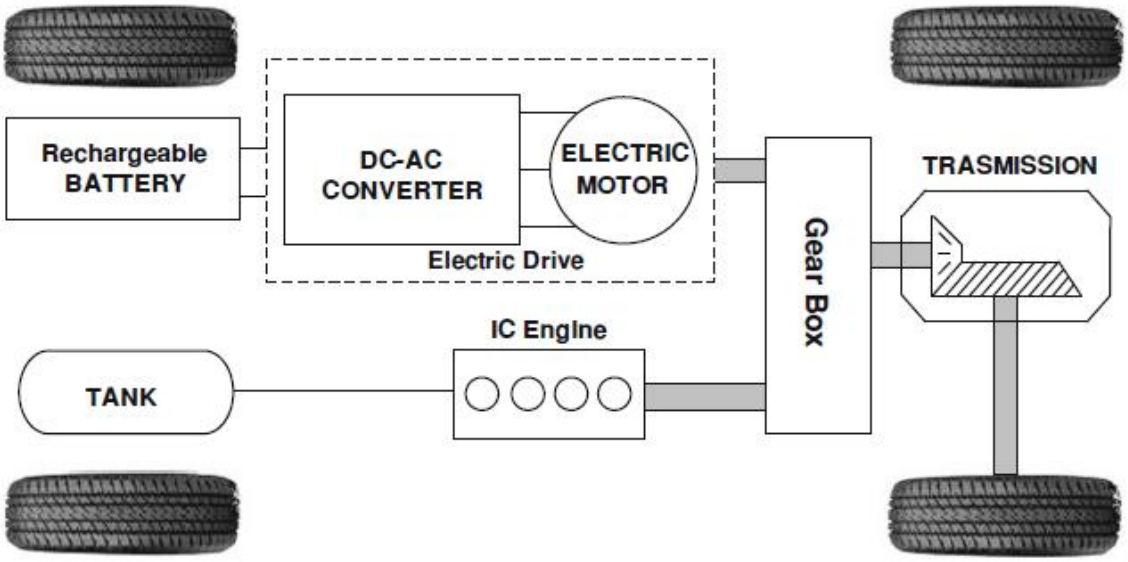

Figure 261 Parallel hybrid configuration [20]

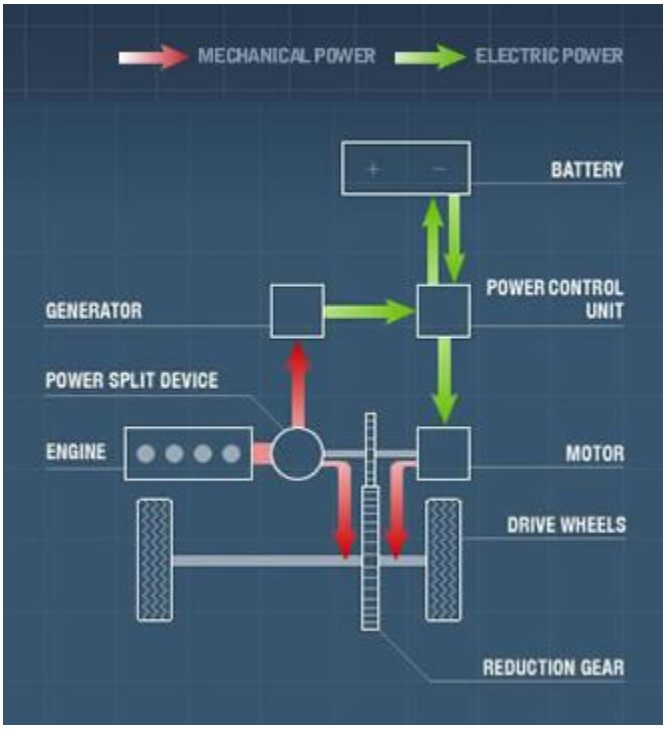

Figure 262 Mixed series/parallel hybrid configuration [22]

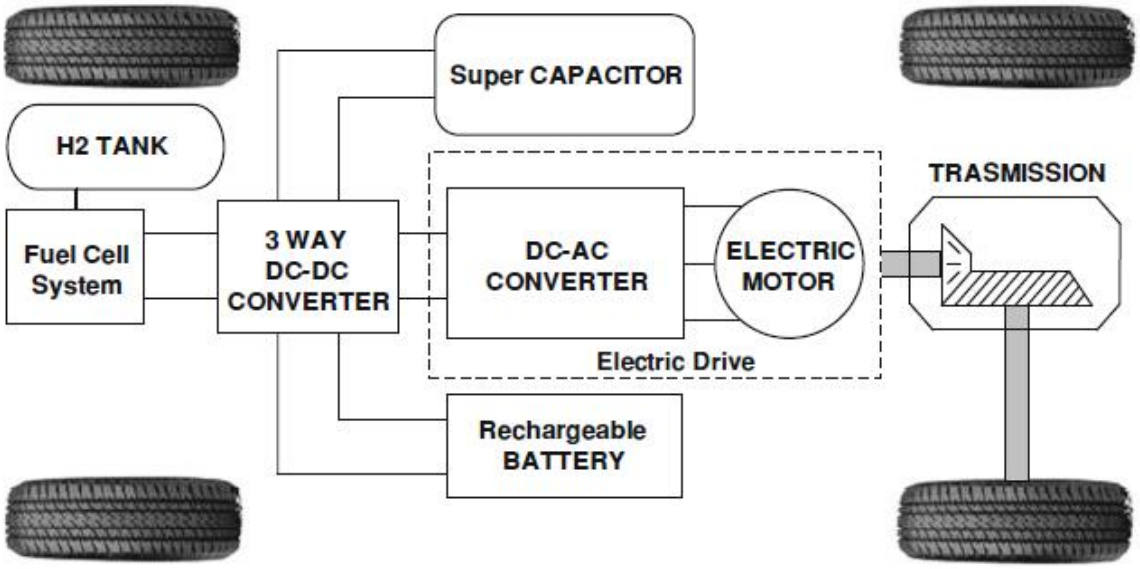

Figure 263 Three power sources hybrid configuration

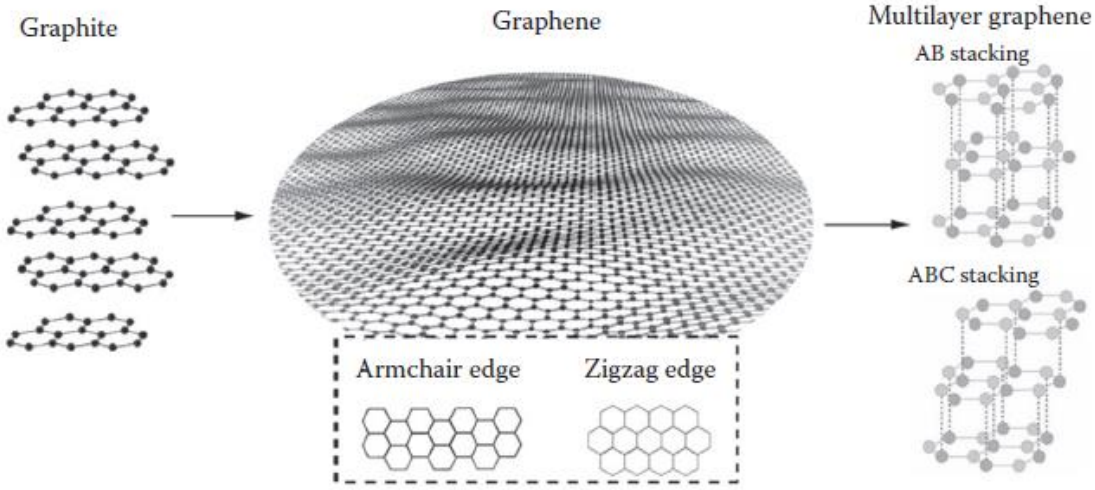

Figure 264 Graphene's structure [59]

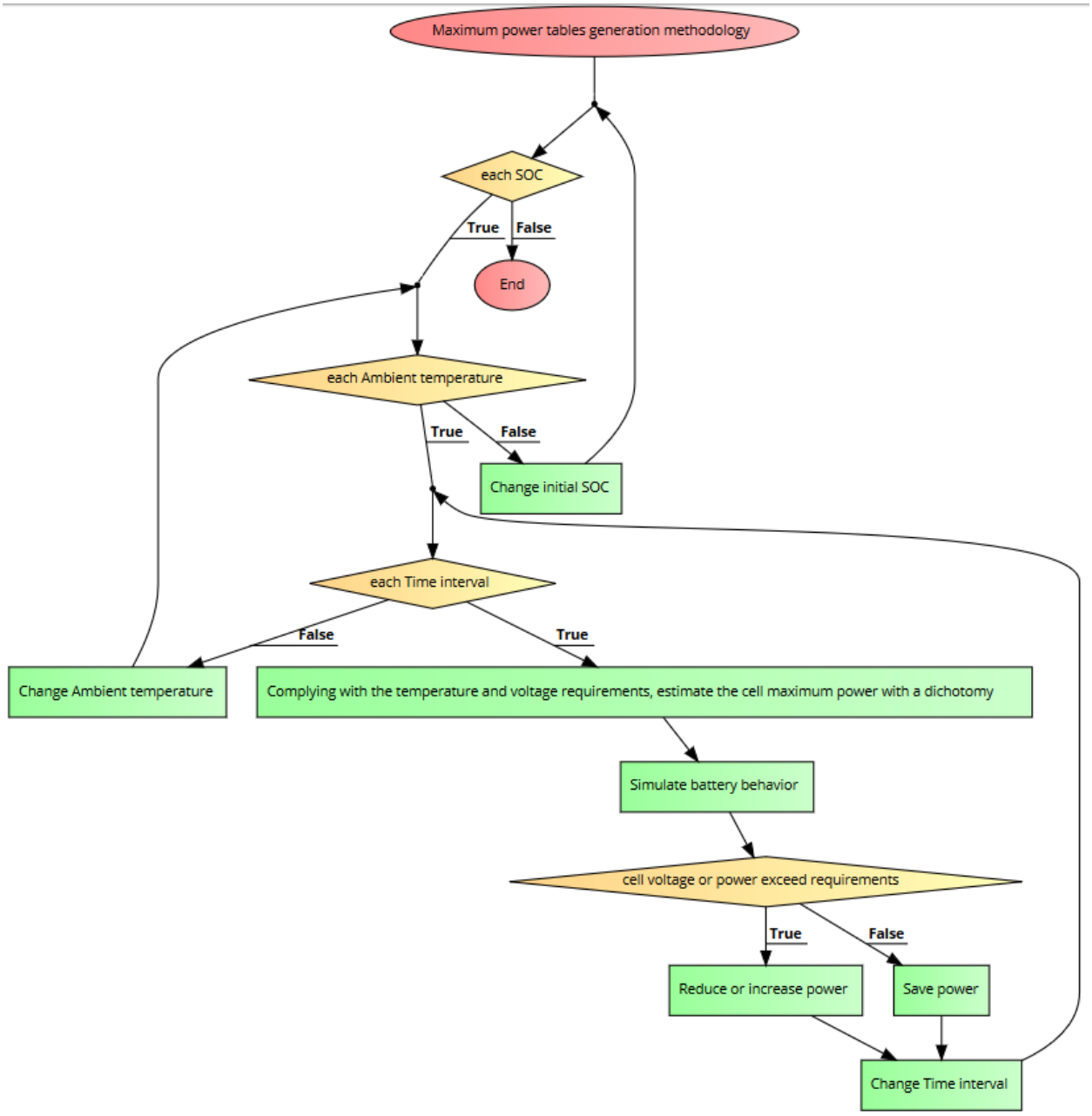

Figure 265 Maximum power tables generation methodology (SCU based on look - up tables model)

APPENDIX B

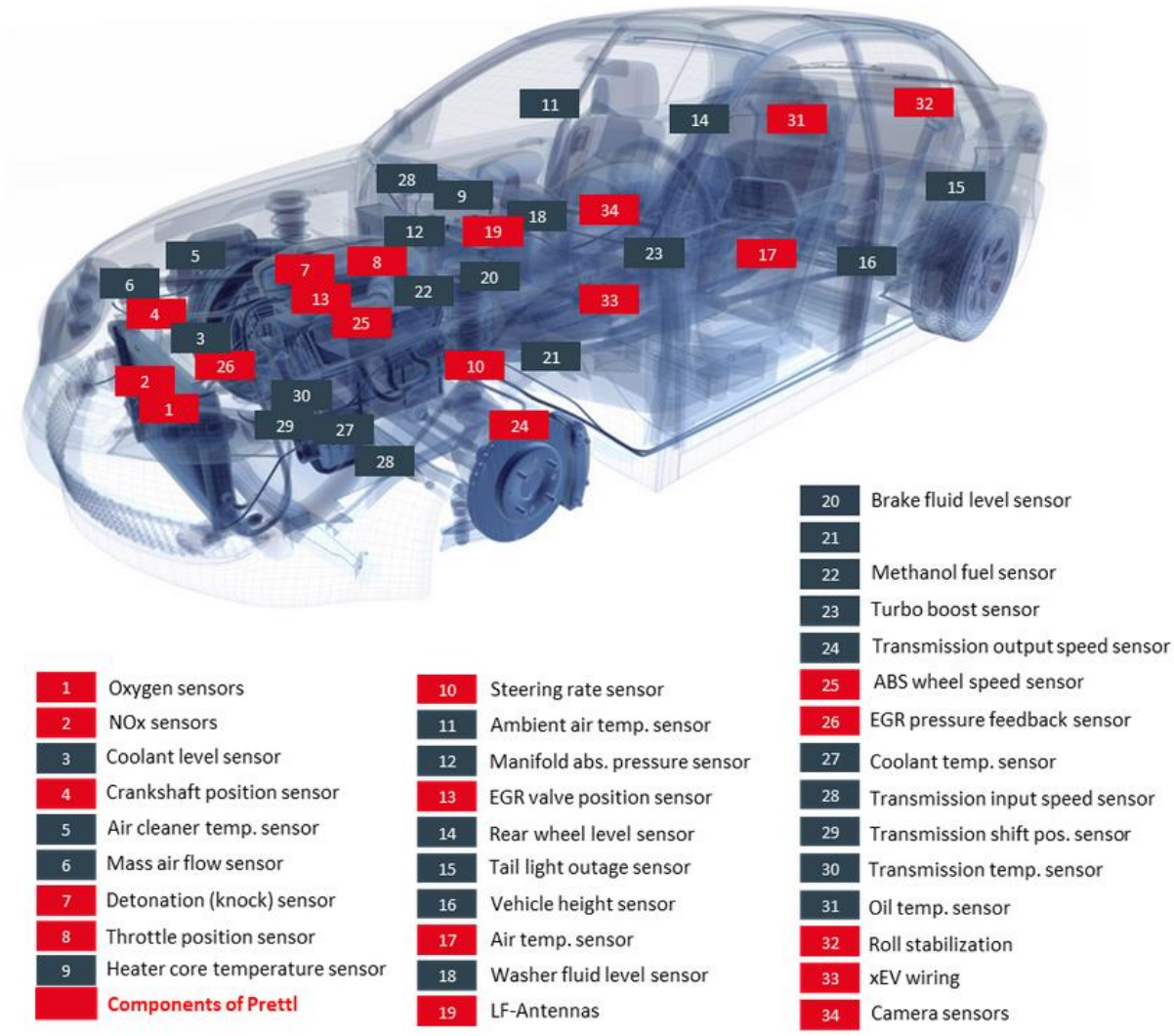

Figure 266 EV's system of sensors [70]